SISSA
Scuola
Internazionale
Superiore di
Studi Avanzati

Physics Area - PhD course in
Astroparticle Physics

Probing scalar particles and forces with compact objects

Candidate:
Mateja Bošković

Advisor:
Prof. Enrico Barausse

Academic Year 2022-23

Abstract

In the highly relativistic regime around compact objects, signatures of new physics may be unravelled. For example, dark matter and dark energy problems may be alleviated by new scalar degrees of freedom. If light scalars are coupled to matter, in relation to the dark energy problem, they generally mediate a fifth force, which could in turn contribute to gravitational phenomenology. In order for this phenomenology to be consistent with existing constraints, it must be suppressed close to matter sources, e.g. through a non-linear screening mechanism. In regard to the dark matter problem, some compact objects may in fact be constructed from beyond Standard Model matter. In particular, boson stars are useful toy models for exotic compact objects that could be produced in the Early Universe or indeed for understanding the behavior of matter under extreme conditions.

First, we consider a two-body problem in shift-symmetric scalar-tensor theories that exhibit kinetic screening. The highly non-linear nature of the theory doesn't allow for an analytical solution away from spherical symmetry. We will present an approximate scheme that allows for a qualitative insight and, in most of the parameter space, very good quantitative agreement with the full numerical results. We will further discuss the partial breakdown of the screening in such systems that could allow for further constraints of these theories.

Second, we consider the most compact boson stars that have a false vacuum in their potential (soliton boson stars), in isolation and in binaries. In the former case, we derive the analytic solutions in spherical symmetry and compare it with the fully numerical ones. In the high-compactness limit we find that these objects present an effectively linear equation of state, thus saturating the Buchdahl limit with the causality constraint. Far from that limit, these objects behave either as flat space-time Q-balls or (in the low-compactness limit) as mini boson stars stabilized by quantum pressure. We establish the robustness of this picture by analyzing a variety of potentials (including cosine, quartic and sextic ones).

Finally, we study the coalescence of two boson stars via numerical evolution of the fully relativistic Einstein-Klein-Gordon equations. Owing to the steep mass-radius diagram, we can study the dynamics and gravitational radiation from unequal-mass binary boson stars with mass ratios up to $q \approx 23$ without the difficulties encountered when evolving binary black holes with large mass ratios. Similar to the previously-studied equal-mass

case, our numerical evolutions of the merger produce either a non spinning boson star or a spinning black hole, depending on the initial masses and on the binary angular momentum. Interestingly, in contrast to the equal-mass case, one of the mechanisms to dissipate angular momentum is now asymmetric, and leads to large kick velocities (up to a few 10^4 km/s) which could produce wandering remnant boson stars. We also compare the gravitational wave signals predicted from boson star binaries with those from black hole binaries, and comment on the detectability of the differences with ground interferometers.

List of publications

The research presented in this thesis is based on the work I have done while being a PhD student in Astroparticle physics at SISSA under the supervision of Prof. Enrico Barausse (SISSA). This Thesis contains material included in the following publications

- Chapter 3:
  M. Bošković and E. Barausse, "Two-body problem in theories with kinetic screening," Phys. Rev. D (Editors' Suggestion, in production) [arXiv: 2305.07725]

- Chapter 4:
  M. Bošković and E. Barausse, "Soliton boson stars, Q-balls and the causal Buchdahl bound," JCAP, vol. 02, no. 02, p. 032, 2022. [arXiv: 2111.03870]

- Chapter 5:
  M. Bezares, M. Bošković, S. Liebling, C. Palenzuela, P. Pani, and E. Barausse, "Gravitational waves and kicks from the merger of unequal mass, highly compact boson stars," Phys. Rev. D, vol. 105, no. 6, p. 064067, 2022. [arXiv: 2201.06113]

Acknowledgements

I would like to thank my supervisor Enrico Barausse for all the discussions, advice and collaborations on Refs. [1, 2, 3] that allowed me to learn a lot on numerical methods, gravitational wave physics, scalar-tensor theories and other topics. The experience and the opportunities that I had by being a member of his GRAMS group have been very valuable. Many thanks are due to my other collaborators on Ref. [2].

I am very grateful to many people with whom I have had the opportunity to discuss the topics in this thesis as well as other related physics topics (some of them being kind enough to also read parts of this manuscript) - foremost Miguel Bezares on numerical methods, soliton stars and kinetic screening, Mario Herrero-Valea on Effective field theories, as well as to Vitor Cardoso, Paolo Creminelli, Marco Crisostomi, Nicola Franchini, Matthias Koschnitzke, Áron Kovács, Steve Liebling, Carlos Palenzuela, Paolo Pani, Rafael Porto, Guilherme Raposo, Claudia de Rham, Nikola Savić, Marko Simonović, Alfredo Urbano, Rodrigo Vicente. It was also a pleasure to interact with many other colleagues from the GRAMS group (Ludovico Capuano, Alexandru Dima, Lotte ter Haar, Guillermo Lara, Sourabh Nampalliwar, Marcelo Rubio, Jam Sadiq, Sebastian Völkel) and the Astroparticle Physics Group at SISSA (Maria Berti, Davide Dal Cin, Giovanni Galati, Jacopo Mazza, Kevin Pardede, Francesco Del Porro). I owe a lot to the experience that I had as a participant, assistant and the coordinator of the Department of Astronomy at Petnica Science Center over the years and recently as one of the organizers of Petnica Summer Institute.

I would like to acknowledge the financial support from SISSA, INFN, European Union's H2020 ERC Consolidator Grant "GRavity from Astrophysical to Microscopic Scales" (Grant No. GRAMS815673) for the work described in this thesis and for the visits to IFAE, Barcelona (2023) and DESY, Hamburg (2023) and the participation in conferences/workshops in Rome (2022), Benasque (2022), Lisbon (2022) and Trieste (2022, 2023). Most of the numerical calculations have been carried out at the Ulysses cluster at SISSA. Finally, without the help of the SISSA Students' Secretariat, navigating the chaos of Italian bureaucracy would have been much harder.

Although working in academia can be difficult at times, and the pandemic didn't help much, all in all I had spent a nice four years in Trst/Trieste, exploring the beauties of Julijska krajina/Venezia Giulia (od Krasa do morja), as well as in Vienna and Belgrade. I would like to thank many friends from home with whom I shared this journey - Ana, Andrej, Anika, Bogdan, Darko, Dušan, Ivan, Lazar, Marko's, Megi, Nemanja, Ognjen, Slobodan's, Srdjan, Stanislav, Steva, Teodora, Vuk and others. All of this wouldn't be possible or made much sense without the support, encouragement and love from my parents Biljana and Vojkan, my sister Ema and my partner Aleksandra. Finally, I would like to thank Jamie and Klara, they don't know why.

Contents

Part I

Introduction

In this Part we will provide a theoretical foundation and phenomenological motivation for the research described in Part II and III. First, in Ch. 1, we will describe effective field theories (EFT) and, in particular, their classical regime, which we will be working with. Secondly, in Ch. 2, we will discuss cosmological problems (dark matter, dark energy) which motivate the particular theories we shall be considering.

Throughout this thesis, we will employ a metric signature $-+++$ and natural units $c = \hbar = 1$, with $M_{\rm Pl}^2 = 1/8\pi G$ and $m_{\rm Pl}^2 = 1/G$. The only exception is Ch. 5 where we will be working with geometrical units $G = c = 1$.

Chapter 1

Theoretical consistency of classical EFTs

All theories considered in this thesis are effective field theories (EFT). In this chapter we will provide an overview of the main aspects of EFTs and discuss the, sometimes subtle, issues regarding their regimes of validity (Sec. 1.2), classical dynamics of the EFT (Sec. 1.3) and what kind of EFTs can have a UV completion (Sec. 1.4).

1.1 Effective field theories

Nature is organized by scales. This has profound consequences on the organization of our understanding of the natural world - in order to understand the behavior of cellular membranes we do not need detailed knowledge of nuclear physics, nor do we need a full theory of quantum gravity to calculate the scattering amplitudes for events at the Large Hadron Collider. *Separation of scales*, in particular low-energy [infra-red (IR)] physics from high-energy scales [ultra-violet (UV)], is the foundation for success of the EFT approach in (quantum) field theory. Although the rise and appreciation of EFT has historically taken place in the context of particle physics (e.g. Fermi theory as a low-energy limit of the electro-weak theory) [4], in this thesis we will focus on EFTs related to gravitational physics in the classical regime.

Any EFT has three key ingredients - relevant *degrees of freedom* which should describe physics at the particular scale; *symmetries* that constrain the form of the effective action and the *expansion parameter* which, together with the *power counting scheme*, sets the hierarchy between the terms in the action [5, 6, 7]. In contrast to renormalizable theories where all infinities that arise in perturbative calculation can, after *regularization*, be absorbed by the redefinition of the finite number of theory parameters (*renormalization*), in the EFT one would need an infinite number of terms to renormalize the theory. Thus, EFTs are *non-renormalizable* theories - even if one starts with a finite number of terms

in the EFT action, all other terms allowed by the symmetry would be generated at the quantum level. However, calculations performed with the EFT are predictive if performed in the regime of validity of the EFT.

We will now provide three examples relevant for this work. First, we consider a complex scalar EFT after integrating out a real scalar. Such a theory can serve as a UV completion of Q-ball/Boson star models from Part III. Secondly, we consider a Goldstone boson EFT from a Higgs potential, theory closely related to k-essence theories that admit screening and are the focus of Part II. Finally, we discuss GR that permeates the whole thesis (as well as the Universe).

1.1.1 Example 1: Integrating out a massive scalar

Let us consider a renormalizable (UV) theory of one complex and one real scalar

$$\mathcal{L} = -\partial_\mu \Phi \partial^\mu \Phi^\dagger - \frac{1}{2}\partial_\mu \psi \partial^\mu \psi - \mu^2 |\Phi|^2 - \frac{1}{2} m_\psi^2 \psi^2 - \alpha |\Phi|^4 - \beta \psi |\Phi|^2 - \frac{1}{2}\gamma \psi^2 |\Phi|^2 \,, \quad (1.1)$$

where $|\Phi|^2 = \Phi^\dagger \Phi$. We will consider the limit of the massive real scalar $m_\psi \gg p$, where p is a typical momentum scale of the low-energy process that we are interested in. The EoM for ψ is from Eq. (1.1)

$$\Box \psi = \beta |\Phi|^2 + m_\psi \psi + \gamma |\Phi|^2 \psi \quad (1.2)$$

As we are interested in $p^2 \ll m_\psi^2$ we can drop the kinetic term and invert for ψ

$$\psi = -\frac{\beta |\Phi|^2}{m_\psi^2} + \frac{\beta\gamma |\Phi|^4}{m_\psi^4} - \frac{\beta \gamma^2 |\Phi|^6}{m_\psi^6} + \mathcal{O}\left(\frac{|\Phi|^8}{m_\psi^8}, \frac{p^2}{m_\psi^2}\right) . \quad (1.3)$$

Substituting this expression back in the Lagrangian (1.1) we obtain the effective action for Φ. In this way, we have *integrated-out* the massive scalar ψ at the classical (tree) level and the effective action for Φ will now contain an infinite number of operators (consistent with $U(1)$ symmetry) that encode the UV physics. For the purposes of Pt. III we will write the effective potential, up to the sixth term, in the following form

$$V_6 = \mu^2 |\Phi|^2 \left(1 - 2\frac{|\Phi|^2}{\sigma_0^2}\right)^2 , \sigma_0^2 = \frac{m_\psi^2}{\gamma} - \frac{2\alpha m_\psi^4}{\gamma \beta^2} \,. \quad (1.4)$$

As $[\alpha] = [\gamma] = 0$ and $[\beta] = 1$, if we assume that $\beta \simeq m_\psi$, then, $\alpha \lesssim 1/2$ and $\gamma > 0$ in order for the matching to make sense.

1.1.2 Example 2: Goldstone boson from the Higgs potential

Consider a complex scalar renormalizable theory with a Higgs potential

$$\mathcal{L}_{\rm H} = -\partial_\mu \Phi \partial^\mu \Phi^\dagger - V_{\rm H}\,, \quad V_{\rm H} = \frac{\lambda}{2}\left(|\Phi|^2 - \frac{v^2}{2}\right)^2\,. \tag{1.5}$$

In the weak-coupling regime $\lambda \ll 1$, the ground state of the theory is given by $|\Phi|^2 = v^2/2$ and it spontaneously breaks the global $U(1)$ symmetry. According to the Goldstone theorem this will lead to massless (gapless) excitations of the vacuum [8, 7]. We can manifest this by performing the field redefinition:

$$\Phi = \frac{v}{\sqrt{2}}\,(1+\rho)\exp\left(i\varphi\right). \tag{1.6}$$

In this way the Lagrangian (1.5) becomes

$$\mathcal{L}_{\rm H} = -v^2\left\{\frac{1}{2}\partial_\mu\rho\partial^\mu\rho + \frac{1}{2}(1+\rho)^2 X + V_\rho\right\} \tag{1.7}$$

$$V_\rho = \frac{M_\rho^2}{2}\left(\rho^2 + \rho^3 + \frac{1}{4}\rho^4\right), \quad M_\rho^2 = \lambda v^2\,, \quad X = \partial_\mu\varphi\partial^\mu\varphi\,. \tag{1.8}$$

In the phase of the non-trivial vacuum, the theory describes a mutually interacting massless scalar φ (Goldstone boson) and a massive and self-interacting scalar ρ.

From the above action (1.7) the equations of motion (EoM) follow:

$$\Box\rho - (1+\rho)X - V'(\rho) = 0 \tag{1.9}$$

$$\partial_\mu[(1+\rho)\partial^\mu\varphi] = 0\,. \tag{1.10}$$

Following [9], we can write the formal solution for the heavy degree of freedom, using the Green function method

$$\rho(x) = -\int d^4x' G(x,x')\left[(1+\rho)\,X + \left(V - \frac{1}{2}M_\rho^2\rho^2\right)\right], \tag{1.11}$$

$$(-\Box + M_\rho^2)G(x,x') = \delta^{(4)}(x-x')\,, \tag{1.12}$$

where all terms in the square bracket on the RHS of Eq. (1.11) are evaluated at x'. Expanding $G(x,x')$ and $\rho(x)$ in powers[1] of M_ρ^{-2} and solving order-by-order we obtain an

[1]Note that, as in Sec. 1.1.1, the dimensionless expansion parameter is p^2/M_ρ^2, where p is the typical momentum of the relevant low-energy process and thus powers of M_ρ^{-2} are associated with the perturbative bookkeeping parameter.

effective action for the Goldstone boson

$$\mathcal{L}_X = -v^2 \left\{ \frac{1}{2} X - \frac{1}{2M_\rho^2} X^2 + \frac{2}{M_\rho^4} \partial_\mu X \partial^\mu X + \mathcal{O}(M_\rho^{-6}) \right\} . \tag{1.13}$$

Note that, as usual, when the symmetry-breaking scale v is larger than the UV scale $M_\rho = \sqrt{\lambda} v$ (as $\lambda \ll 1$), the symmetry of the UV theory is non-linearly realized in the EFT [7] - in this case, as a shift symmetry $\varphi \to \varphi + c$.

1.1.3 Example 3: General Relativity

Historically, GR was developed by Einstein trying to simultaneously find a dynamical generalization of Newtonian gravity (analogously to how Maxwell's electrodynamics generalized electrostatics) and resolve conceptual puzzles of Newtonian mechanics regarding absolute vs. relative motion [10]. Einstein's formulation of GR had, at its heart, the equivalence principle and general covariance as a symmetry of the theory. The subsequent development of quantum physics posed a question of quantization of classical GR (as quantum electrodynamics was formulated by quantizing Maxwell's electrodynamics). Although (quantized) GR can be formulated at the perturbative level [5], a full theory of quantum gravity is yet to be found.

From a modern perspective, classical physics should arise as an approximation of a fundamental quantum description. Indeed, just from unitarity and Poincare invariance one can classify all possible particles by their spin and mass. A natural candidate for the graviton would be a massless boson particle. As massless particles with spin higher than 3 must be non-interacting (and spin-1 particle carries charge of both signs), in order to have a single force carrier one can either have a spin-0 or a spin-2 graviton [11, 12, 13]. Furthermore, as spin-0 particles do not couple to light to and hence contradict e.g. Edington's experiment, gravity should be described by a spin-2 particle (at least to leading order, see Sec. 2.2.3). One can further show that classically GR is a unique non-linear completion of the spin-2 linear theory [14, 15, 13]

$$\mathcal{L}_{\rm GR} = -\sqrt{-g} \frac{1}{2} M_{\rm Pl}^2 R \,, \tag{1.14}$$

where $R(\partial g, \partial^2 g)$ is the Ricci scalar and $g_{\mu\nu}$ is the metric tensor. In this way, GR arises naturally from requiring that the world is both quantum and relativistic. Furthermore, general covariance is just a (useful) gauge redundancy forced on us for using an object that naturally carries five degrees of freedom (spin-2 tensor field) to describe a two degree of freedom particle [16, 17].

Simple power counting (see the next Sec. 1.3) shows that GR is a non-renormalizable theory. One thus expects that the Einstein-Hilbert term is just part of the whole tower of

higher-derivative operators, consistent with general covariance, that encode short-distance (Planckian) physics [7, 18]. In contrast to the previous two examples, UV completion of GR is not known and consequently also the values of the coefficients of higher-derivative corrections (*Wilson coefficients*). After removing redundant operators [2]

$$\mathcal{L}_{\rm GREFT} = -\sqrt{-g}\left\{\Lambda_{\rm cc} + \frac{1}{2}M_{\rm Pl}^2 R + \left[a_1 R^2 + a_2 R_{\mu\nu}R^{\mu\nu}\right] + \mathcal{O}\left(\frac{R^3}{\Lambda}\right)\right\}\,, \tag{1.15}$$

where $\Lambda_{\rm cc}$ is the cosmological constant, Λ is the strong-coupling scale, a_i are dimensionless coefficients $\sim \mathcal{O}(1)$.

1.2 Radiative stability of an EFT

Let us consider a power counting scheme, based on the momentum scaling of the N-point scattering amplitude $\mathcal{A}$ and using the dimensional regularization. By splitting the Lagrangian in the free $\mathcal{L}_0$ and the interaction part $\mathcal{L}_{\rm int}$ [7]

$$\mathcal{L}_0 = -\frac{f^4}{\Lambda^2\nu^2}\left((\partial\psi)^2 + m^2\psi^2\right)\,, \quad \mathcal{L}_{\rm int} = -f^4\frac{c_n}{\Lambda^{d_n}\nu^{f_n}}\mathcal{O}_n \tag{1.16}$$

$$\mathcal{A} \sim f^4\left(\frac{1}{\nu}\right)^N\left(\frac{k\Lambda}{4\pi f^2}\right)^{2L}\left(\frac{k}{\Lambda}\right)^{2+\sum_n(d_n-2)V_n}\,, \tag{1.17}$$

where ψ denotes a low-energy bosonic field of mass m, ν and Λ are typical high-energy scales related to the field and the derivative expansion, f is a typical high-energy density that needs to be set to $f = \Lambda^2\nu^2/2$ in order to have a canonical normalization, the set (f_n, d_n, V_n) counts the number of power of fields, derivatives and vertices in the interaction $\mathcal{O}_n$, N and L represent the number of external lines and loops (all in respective order).

In order to illustrate the above power counting let us first consider a generic shift-symmetric scalar EFT

$$\mathcal{L}_X = K(X) + \Lambda^4\sum_{l=1,k=1}\frac{\partial^l X^k}{\Lambda^{l+k}}\,, \quad K(X) \equiv \Lambda^4\sum_{n=1}c_n\left(\frac{X}{\Lambda}\right)^n \tag{1.18}$$

From Eq. (1.17) it follows

$$\mathcal{A} \sim \Lambda^{4-N}\left(\frac{k}{\Lambda}\right)^{N+4L}\,. \tag{1.19}$$

In other words, loop correction from the terms organized in $K(X)$ cannot change the tree

[2] Inter alia, using the topological nature of the Gauss-Bonnet term $\mathcal{L}_{\rm GB} = R^2 - 4R_{\mu\nu}R^{\mu\nu} + R_{\alpha\beta\gamma\delta}R^{\alpha\beta\gamma\delta}$. Note that in the vacuum GR $R_{\mu\nu}R^{\mu\nu} = R = 0$ and the first higher-curvature correction is cubic in the curvature.

level coefficients c_n as they have too many powers of the momentum. This is an example of the non-renormalization property shared among massless, derivatively coupled theories [19]. Another example of such theory is precisely GR. Expanding the Einstein-Hilbert action around Minkowski as

$$g_{\mu\nu} = \eta_{\mu\nu} + \frac{h_{\mu\nu}}{M_{\rm Pl}}\,, \quad \mathcal{L}_{\rm EH} \sim \sum_{n=0} \left(\frac{h}{M_{\rm Pl}}\right)^n (\partial h)^2 \tag{1.20}$$

we find the same property

$$\mathcal{A} \sim M_{\rm Pl}^{4-N} \left(\frac{k}{M_{\rm Pl}}\right)^{2+2L} . \tag{1.21}$$

This can be checked explicitly for higher-curvature terms.

The non-renormalization property is responsible for the radiative stability of the classical regime of these theories. As the external momentum is set by the typical curvature scale of the background $k^2 \sim \partial^2$ the above results imply for GR that one can be in the classically non-linear (strong-field) regime, but the higher-curvature (quantum) correction will be sub-dominant. As an illustration in the Schwarzschild spacetime, a gauge-invariant object that measures the curvature is the Kretschmann scalar given by

$$\frac{K}{M_{\rm Pl}^4} \equiv \frac{1}{M_{\rm Pl}^4} R_{\alpha\beta\gamma\delta} R^{\alpha\beta\gamma\delta} = 48 \left(\frac{r_S}{r}\right)^2 (M_{\rm Pl} r)^{-4}\,, \quad r_S = \frac{M}{m_{\rm Pl}^2} \tag{1.22}$$

where r is the Schwarzshild coordinate, r_S is the Schwarzshild scale and M is the ADM mass of space-time. For sufficiently heavy black hole (BH) [heavier than $\sim \mu g$] the description of BH horizons is well in the regime of validity of the EFT although certainly a nonlinear phenomena (as is the case of the formation of BH horizons through the stellar collapse or the coalescence of binary compact objects). In contrast, as one approaches the classical singularity $r \to 0$ higher-curvature corrections will become important and the EFT will break down. In this way, singularities are not a consistent prediction and one expects that the full theory of quantum gravity (UV completion of GR) will resolve them.

1.2.1 $K(X)$ theories

The non-renormalization property of $K(X)$ is manifest in the UV-complete example of the Goldstone boson where we found [Eq. (1.13)] that the first correction in X was $\partial^2 X$. In the case of this UV completion, as the heavy mode ρ couples with ϕ through its derivative [Eq. (1.11)], higher-derivative corrections in the EFT will be of the ∂X form. This stays true in the case of an explicit matching at the one loop level [20]. Similarly to GR, the non-renormalization property of shift-symmetric theories allows one to study nonlinear classical solutions of $K(X)$ theories in the EFT regime of validity as long as $\partial \ll \Lambda$.

For future applications, let us thus ignore higher-curvature terms in (1.18) and source the scalar with the trace of the energy-momentum tensor by softly breaking the shift symmetry $\alpha T/M_b$, $M_b \gg \Lambda$. EoM that follow in the non-relativistic limit is given by

$$\partial_i(K_X \partial^i \varphi) = \frac{1}{2}\frac{\alpha}{M_b} T\,, \quad K_P \equiv \frac{\partial K}{\partial P}\,. \tag{1.23}$$

Let us consider an isolated point-particle source (positioned at the origin) and the (finite) polynomial kinetic function

$$T = -m_a \delta^{(3)}(r)\,, \quad K(X) = \Lambda^4 \mathcal{K}_N(X)\,, \quad \mathcal{K}_N(X) = \sum_{n=1}^{N} \frac{c_n}{2n} \mathcal{X}^n\,, \quad \mathcal{X} = \frac{X}{\Lambda^4} \tag{1.24}$$

In the classical nonlinear regime, the highest power of X will dominate and thus

$$\left(\frac{\partial_r \varphi}{\Lambda^2}\right)^{2N-1} \approx \frac{1}{-c_N}\left(\frac{r_{\rm sc}}{r}\right)^2 \tag{1.25}$$

$$r_{\rm sc} = \sqrt{\frac{m\alpha}{4\pi M_b \Lambda^2}}\,, \tag{1.26}$$

where $r_{\rm sc}$ is the kinetic screening radius (analogue to the Schwarazhild radius in the GR example). If we take $c_N < 0$, $\forall N > 2$ and $c_n \sim \mathcal{O}(1)$, $1 < n < N$, the scalar force will be suppressed (screened) with respect to the Newtonian r^{-2} behavior.

In order to understand the condition on which regions of this background are in the EFT regime of validity, we will use the background field method as in Refs. [21, 22, 23]. Let us first be slightly more general and decompose the action around the slowly-varying background $\bar{\varphi}$ as $\varphi = \bar{\varphi} + \pi$ to a quadratic order

$$\mathcal{L}_2 = -\frac{1}{2} Z^{\mu\nu} \partial_\mu \pi \partial_\nu \pi\,, \quad Z^{\mu\nu} = -2\bar{\mathcal{K}}_{\mathcal{X}} \eta^{\mu\nu} - 4\bar{\mathcal{K}}_{\mathcal{X}\mathcal{X}} \partial^\mu \bar{\varphi} \partial^\nu \bar{\varphi}\,, \tag{1.27}$$

where the linear term vanishes from the EoM, $\bar{\mathcal{K}}, \bar{\mathcal{X}}$ are evaluated in the background and we are ignoring the effects of GR. The above formulation suggest introducing an effective metric $\gamma^{\mu\nu}$

$$\sqrt{-\gamma}\gamma^{\mu\nu} \equiv Z^{\mu\nu}\,. \tag{1.28}$$

In general, the transformation $\eta_{\mu\nu} \to \gamma_{\mu\nu}$ is disformal. In the case of the polynomial kinetic function and the static spherically symmetric setting the transformation is approximately conformal to the Minkowski spacetime

$$Z^{\mu\nu} = -\mathcal{X}^{n-1} \mathrm{diag}\left(-1, 1 + 2(n-1), \frac{1}{r^2}, \frac{1}{r^2 \sin\theta}\right) \tag{1.29}$$

We will thus take the metric to be conformal to Minkowski as the correction term will not influence the overall parametric scaling. Using the heat kernel regularization and Barvinsky-Vilkovsky covariant perturbation theory [24, 25, 26, 5], one obtains the following effective action at the one-loop [22]

$$\mathcal{L}_{1-\text{loop}} \sim \sqrt{-\gamma}\left(\Lambda_c^4 + \Lambda_c^2\frac{R}{6} + \frac{1}{240}\left[R_\gamma^2 + (R_\gamma)_{\mu\nu}R_\gamma^{\mu\nu}\right]\right) . \tag{1.30}$$

As power-law divergences are not calculable in the EFT we will assume that they are renormalized in the UV theory and ignore them (technically, they are zero in dimensional regularization) [22]. As curvature-squared terms are of the same order we will just focus on the R_γ^2 term as a representative of the one-loop quantum corrections (see Ref. [22, 23] the full discussion and on the higher-loops). Thus, the the classical background is radiatively stable if

$$\sqrt{-\gamma}R_\gamma^2 \ll K(X) \tag{1.31}$$

As the curvature of the conformally flat space-time defined from Eq. (1.28) is given by [27]

$$R_\gamma = -6\frac{1}{\sqrt{K_X}^3}\frac{1}{\sqrt{-\gamma}}\partial_\mu\left(\sqrt{-\gamma}\gamma^{\mu\nu}\partial_\nu\sqrt{K_X}\right) , \tag{1.32}$$

one finds the scale where the quantum corrections become relevant (as in [22])

$$r_{\text{UV}}^{\text{poly}} \sim \frac{1}{\Lambda}\left(\Lambda r_{\text{sc}}\right)^{-N/(N-1)} . \tag{1.33}$$

Note however that the scalar gradients do not grow arbitrarily, because at some point the radius of the source (e.g. a star) is reached. As demonstrated in Sec. 3.2.3, the maximal value of X is reached at the surface of the object. X then decreases as one progresses towards the center, ultimately entering the linear regime. Thus, a sufficient criterion to assess whether one is in the EFT regime consists of checking whether $r_{\text{UV}} \approx R$, where R is the effective radius of the source. Let us focus for concreteness on quadratic k-essence. From Eqs. (1.25) and (1.33) one has

$$r_{\text{UV}}^{(N=2)} \approx 10^{-43}\text{km}\left(\frac{\alpha}{0.1}\right)^{-1}\left(\frac{\Lambda}{\text{meV}}\right)^{-1}\left(\frac{m}{M_\odot}\right)^{-1} . \tag{1.34}$$

For cosmologically motivated values of $\Lambda \sim$ meV [see Part II] and any astrophysical object, one is clearly in the regime of validity of the EFT.

It needs to be said that the previous discussion, although technically correct, is somewhat at odds with the Wilsonian spirit of the EFT (unequal treatment of different sectors of higher-derivative operators). This construction thus relies heavily on the existence

of an appropriate UV completion - both in order to renormalize the power-law divergences and to provide a specific form of the kinetic function.

1.3 Classical EFT predictivity

EFTs in particle physics are usually used to calculate scattering amplitudes. In this way, the perturbative nature of the EFT is built in from the start and one can explicitly find the scales at which the EFT breaks down. On the other hand, in the classical regime one instead derives the EoM, which are partial differential equations (PDE), usually elliptic or hyperbolic in nature. Then, a boundary/initial value problem (IVP/BVP) is posed on some domain, which may also be the whole space-time. In that way we would treat the EFT as a "fundamental theory", which is obviously not a consistent approach. This is, however, corrected a posteriori by indicating which regions of the classical solution are outside of the regime of validity of the EFT. In the particular elliptic problems considered in Sec. 1.2, these regions can be either "excised" and matched to the interior of the source (both in GR and $K(X)$ theories) or "hidden" inside the horizon (in GR).

Tensions between the EFT approach and the classical description illustrated above are even more pronounced in dynamical scenarios. We will consider two such issues in turn: Ostrogradsky instabilities and well-posedness of the IVP.

1.3.1 Ostrogradsky instability

Higher-derivative terms appear in the EFT expansion by construction, as seen in all three examples analyzed thus far. They generally lead to higher-than-second order EoM. Let us consider an explicit example [28]

$$\mathcal{L}_g = -\frac{1}{2}(\partial\varphi)^2 - V(\varphi) + \frac{a}{2\Lambda^2}(\Box\varphi)^2 + J\varphi\,, \quad a = \pm 1 \tag{1.35}$$

EoM and the propagator structure that follow are

$$\Box\varphi - \frac{a}{\Lambda^2}\Box^2\varphi + V'(\varphi) = J\,, \quad \Pi_0 = \frac{1}{\Box - \frac{a}{\Lambda^2}\Box^2} = \frac{1}{\Box} - \frac{1}{\Box - M_g^2}\,, \quad M_g^{-2} \equiv \frac{a}{\Lambda^2}\,, \tag{1.36}$$

where we have considered the leading order propagator Π_0 in the self-coupling defined by V. The last equality shows that the starting Lagrangian "secretly" describes two degrees of freedom: massless scalar and a massive one with a wrong-sign kinetic term. The degree of freedom with a wrong-sign kinetic term is referred to as a (Ostrogradsky) ghost. Let us see this explicitly by reformulating the original theory with the auxiliary field (modulo the

source)

$$\mathcal{L}_g = -\frac{1}{2}(\partial\varphi)^2 - V(\varphi) + \chi\Box\varphi - \frac{\Lambda^2}{2a}\chi^2\,, \quad \chi = a\frac{\Box\varphi}{\Lambda^2}\,, \tag{1.37}$$

where the equation on the right follows from the EoM. Introducing the field redefinition $\varphi = \psi - \chi$ we find

$$\mathcal{L}_g = -\frac{1}{2}(\partial\psi)^2 + \frac{1}{2}(\partial\chi)^2 - V(\psi,\chi) - \frac{\Lambda^2}{2a}\chi^2\,, \tag{1.38}$$

The presence of the ghost implies the instability of the theory as the Hamiltonian is unbounded from below. Furthermore, if $a = -1$, the ghost is also a tachyon i.e. it has negative mass. Tachyons in and of themselves are not necessarily pathological - they indicate that the perturbation is not performed around the true vacuum of the theory, as in the action (1.5) [29, 30].

A more general analysis, by Ostrogradsky, demonstrates that the instability is present for a generic higher than second order EoM in both mechanical and classical-field systems [30]. From the EFT perspective, ghosts indicate that the cut-off of the the EFT expansion must be lower than the ghost mass M_g [28, 9]. As long as one is in the regime of validity of the EFT, the ghost degree is not excited. Thus, the requirement for a healthy theory would be not to have, for example: a wrong-sign kinetic term in the renormalizable theory; a ghost term in the "principal" sector of theories that can sustain radiatively stable classical nonlinear regimes (GR and $K(X)$). This is also manifest in the first two examples in Sec. 1.1.1, 1.1.2, where the ghost terms are generated in the low-energy expansion of a perfectly healthy UV completion with second-order EoM. Thus, the presence of ghosts is a practical problem of EFT predictivity and not an essential problem of the theory under consideration. In more detail, one needs to identify those solutions in the EFT that are low-energy expansions of the UV theory i.e. the solutions that arise as series in the high-energy scale Λ^{-1} (e.g. in Sec. 1.1.1, 1.1.2) [9, 31]. Furthermore, by use of local field redefinitions and removing total derivatives, terms that would superficially lead to higher order EoM may in fact be *redundant operators*. For example, for shift-symmetric scalar theory one can show that it can be formulated in a ghost-free way up to dimension-11 operators [32].

Finally, let us note that not all of the higher-derivative terms lead to such a ghost-like instability. Aside from the redundant operators, a class of operators invariant under the

generalized shift symmetry (Galileon[3] symmetry)

$$\phi \to \phi + c + b_\mu x^\mu \,, \tag{1.39}$$

also lead to second order EoM [33].

1.3.2 Well-posedness of the IVP

The absence of ghosts does not necessarily imply that the classical dynamics of an EFT are unproblematic. Instead, one needs to understand whether the classical problem, defined by the PDE system and prescribed data (i.e. BVP/IVP), is well-posed (Hadamard criteria) - the problem has a solution; the solution is unique and it depends continuously (with respect to a function space) on the initial/boundary data [34].

Let us first consider most general second-order PDE in $\mathbb{R}^n$

$$\mathcal{D}f = 0 \,, \quad \mathcal{D} \equiv a^{ij}(x)\partial_i\partial_j + b^i(x)\partial_i + c(x) \,, \tag{1.40}$$

where $x = (x_1, ..., x_n)$ is a vector on $\mathbb{R}^n$ and consider a high-frequency plane wave ansatz

$$f = \exp\left(-\frac{k_i x^i}{\epsilon}\right) \,, \quad \epsilon \ll 1 \,. \tag{1.41}$$

To leading order we have

$$\mathcal{D}f = -\frac{1}{\epsilon^2}\sigma^p + \mathcal{O}(\epsilon^{-1}) \,, \quad \sigma^p \equiv a_{ij}k^i k^j \,, \tag{1.42}$$

where the quadratic form σ^p is a principal symbol of the PDE. The real symmetric matrix a_{ij} has real eigenvalues whose sign allows one to classify the PDE type. In more detail, the equation can be elliptic [eigenvalues have the same sign], (ultra)hyperbolic [one (or more) eigenvalues have a different sign] and parabolic [at least one zero eigenvalue] [34]. For example, in the wave equation $-\partial_t^2\phi + \nabla^2\phi = 0$ the quadratic form defines the Minkowski metric in which the waves propagate. Wick rotation of the time variable $t \to it$ makes the problem elliptic (Laplace equation) and the eigenvalues have the same sign.

In the case of the hyperbolic equation, the plane wave Ansatz in the high-frequency limit $\sigma^p \approx 0$ defines a light cone. In general, a surface defined by

$$f(x^i) = 0 \,, \quad a^{ij}\partial_i f \partial_j f = 0 \tag{1.43}$$

is the characteristic hypersurface that describes the propagation of the solution (signal)

[3] In 4-dimesional space-time there are exactly five Galileon operators [33]. These operators have remarkable properties, such as the stronger form of non-renormalization than the one discussed for GR and $K(X)$ theories [19].

from the initial data. Let us focus for simplicity on the $1+1$ case. The implicit definition of the characteristic surface $f(x,t)=0$ implies $x=x(t)$. Thus, one can find the characteristic velocity in the following way

$$\begin{bmatrix}\partial_t f & \partial_x f\end{bmatrix}\begin{bmatrix}a_{00} & a_{01}\\ a_{01} & a_{11}\end{bmatrix}\begin{bmatrix}\partial_t f\\ \partial_x f\end{bmatrix}=0 \implies c\equiv \quad \frac{\partial x}{\partial t}=-\frac{-a_{01}\pm\sqrt{a_{01}^2-a_{00}a_{11}}}{a_{01}}\,. \tag{1.44}$$

In the case of the wave/Laplace equation we have two/zero real characteristic curves, respectively. Furthermore, the characteristic velocity is $c=\pm 1$ for the wave equation - as expected.

As an illustration of how well-posedness is connected to the characteristic analysis, consider paradigmatic examples of mixed-type PDEs in $1+1$

$$\partial_t^2 f + t\partial_x^2 f = 0\,, \quad \partial_t^2 f + \frac{1}{t}\partial_x^2 f = 0\,, \tag{1.45}$$

known as Tricomi and Keldysh equations, respectively [35, 34]. Depending on the sign of the time variable t, the equations change their character. In particular, for $t<0$, $t=0$ and $t>0$, these equations are hyperbolic, parabolic and elliptic, respectively. Their characteristic velocities are given by

$$c_{\rm T}=\pm\sqrt{-t}\,, \quad c_{\rm K}=\pm\frac{1}{\sqrt{-t}}\,, \tag{1.46}$$

where T/K denotes Tricomi or Keldysh. In addition to the change of the character, the characteristic velocity of the Keldysh equation diverges at $t=0$.

As an EFT application, let us consider the $K(X)$ theory and in particular the propagation of the perturbation π on top of some background $\bar{\varphi}$ that follows from (1.27)

$$Z^{\mu\nu}\partial_\mu\pi\partial_\nu\pi=0\,. \tag{1.47}$$

In order for this equation to be hyperbolic, the eigenvalue criteria of the principal symbol coefficient function $Z^{\mu\nu}$ imply that the determinant needs to be negative. Applying Sylvester's determinant identity[4] to Eq. (1.27) it follows

$$1+\frac{2\mathcal{K}_{\mathcal{X}\mathcal{X}}}{\mathcal{K}_{\mathcal{X}}}\mathcal{X}>0 \tag{1.48}$$

Thus, $K(X)$ theory has a mixed-type PDE EoM that describes the propagation of fluctuations. In other words, there may occur a breakdown of the IVP (formation of the elliptic region) depending on the form of the kinetic function and the value of the

[4]If a matrix X is invertible, then $\det(X+AB)=\det(X)\det(I+BX^{-1}A)$, where I is the identity matrix.

kinetic energy X [29, 36, 37, 38, 39, 40, 41]. For example, if one takes a quadratic kinetic function, the previous criteria are not satisfied for all values of the kinetic function X. However, in Sec. 1.1.2 we have seen that such a $K(X)$ EFT may have UV completion. This clearly illustrates that the well-posedness of the IVP is not a measure of whether the EFT is healthy (in contrast to repeated claims in the literature e.g. [29, 42]), but a practical obstacle to EFT predictability [43, 7, 44, 45].

There is an alternative, more physically transparent, way to reach the condition (1.48). The stress-energy tensor of the scalar Lagrangian of the form $K(\varphi, X)$

$$T^{\varphi}_{\mu\nu} = K\eta_{\mu\nu} - 2K_X\partial_\mu\varphi\partial_\nu\varphi\,, \tag{1.49}$$

can be mapped to an ideal fluid (assuming time-like scalar gradient $X < 0$)

$$T_{\mu\nu} = (\rho + p)U_\mu U_\nu + p\eta_{\mu\mu}\,, \tag{1.50}$$

$$U_\mu = \frac{1}{\sqrt{-X}}\partial_\mu\varphi\,, \quad \rho = 2K_X X - K\,, \quad p = K\,. \tag{1.51}$$

Furthermore, requiring $K = K(X)$, makes the fluid barotropic. The speed of sound in a barotropic fluid is given by

$$c_s^2 = \frac{\partial_X p}{\partial_X \rho} = 1 + \frac{2\mathcal{K}_{\mathcal{X}\mathcal{X}}}{\mathcal{K}_{\mathcal{X}}}\mathcal{X} \tag{1.52}$$

Thus, the well-posedness condition in $K(X)$ theories is equivalent to the requirement of hydrodynamic stability $c_s^2 > 0$ [39].

Formally, a dynamical problem is strongly hyperbolic if its principal part has real eigenvalues and a complete set of eigenvectors. This can further be shown to be imply the requirement of well-posedness (in a particular function space) [46]. In EFTs with gauge redundancy, such as GR, the issue of Cauchy problem well-posedness is much more involved as the answer is gauge-dependent [46]. Some of the most important conceptual results (singularity theorems[5]) and conjectures (on cosmic censorship) as well as practical results (simulation of binary coalescence) in GR have followed from the understanding of the causal structure of spacetime [47].

Going beyond GR one often considers scalar-tensor theories (see Sec. 2.2.3). As an illustration, assuming a scalar coupled minimally to GR, shift symmetry and parity invariance, one can construct the following EFT up to six-derivative terms

$$\mathcal{L}_6 = \frac{1}{2}M_{\rm Pl}^2 R - \frac{1}{2}X + \frac{\alpha}{4}X^2 + \lambda\varphi\mathcal{L}_{\rm GB} \tag{1.53}$$

This action leads to second order EoM and in Refs. [48, 49] gauge construction was performed that renders a well-posed IVP as long as the higher-order terms are treated

[5]That also illustrate that the local well-posedness of the IVP does not imply a global one.

perturbativly (weak-coupling regime). The IVP formulation of Refs. [48, 49] (applicable to larger class of scalar-tensor theories that lead to second order EoM) and its subsequent generalizations allowed for numerical evolution of binary systems in such theories [50, 51, 52, 53, 34].

One could hope, by comparing the binary evolution modelled with such scalar-tensor theory with gravitational wave (GW) observations, to put constraints on higher-derivative terms in a similar manner to the parametrized post-Newtonian approach [54] for the solar system or binary pulsars [48]. There are two limitations of such an approach. First, we have seen in Sec. 1.2 that for some theories we may be justified in going beyond the weak-coupling regime in the EFT context[6]. It has been demonstrated in Ref. [41] that in the non-linear regime of k-essence scalar-tensor theory even a locally well-posed[7] IVP can develop a breakdown of hyperbolicity via Keldysh-type instability, although in this particular theory such instability can be successfully gauged away [55]. Secondly, with higher order corrections (akin to a second order parameterized post-Newtonian order) in the EFT, one is bound to have higher than second order EoM [32] and the well-posedness is likely to fail (this may manifest as a ghost instability). As the principal symbol σ^p [Eq. (1.42)] is sensitive to the highest-derivative terms, the well-posedness strongly depends on the highest-derivative term in the action, although such terms in the standard EFT approach are the most suppressed.

In order to perform numerical simulations of the binary coalescence in more general scalar-tensor EFTs an option would be to devise an approximative procedure that would "filter" problematic high-frequency modes [56]. The most popular approach is modifying the EoM and adding a driving term (fixing equations) [43, 57], that has been successfully applied to various theories, including the shift-symmetric EFTs of the type described in Sec 1.1.2 [58, 44]. Another is to perturbatively expand around the theory with a well-posed IVP and then resum secular instabilities, using a dynamical renormalization group [59] (more precisely, its numerical formulation [60]). The development of these methods and their mathematical foundation is an active topic in mathematical and numerical relativity.

1.4 UV consistency of an EFT

We have previously seen in Sec. 1.3 that, although practically important, EFT predictivity cannot be the criterion on whether the theory is "healthy" or not. From the purely Wilsonian perspective, there are no prior constraints on the values of the coefficients.

[6]It should be noted that the issue of radiative stability in the strong-coupling regime is not assessed in most of the scalar-tensor theory parameter space.

[7]Coupling $K(X)$ theory with GR, the condition (1.48) is carried to curved space-time by general covariance. In addition, the initial conditions need to be formulated on a hypersurface that is spacelike with respect to both $g_{\mu\nu}$ and $\gamma_{\mu\nu}$ [38, 39].

However, there may be some "hidden" IR-UV links that impose such constraints. As an illustration, let us consider the first non-linear term in the $K(X)$ EFT

$$\mathcal{L}_X = -\frac{1}{2}X + \frac{\beta}{4\Lambda^4}X^2 + ... \tag{1.54}$$

We have seen that such an EFT can be obtained starting from the explicit UV completion (Sec. 1.1.1), where we found $\beta > 0$. Interestingly, such EFTs can arise from different UV completions. e.g. in the low-energy limit of string theory [Dirac-Born-Infeld (DBI) action] [61]

$$\mathcal{L}_{\rm DBI} = -\Lambda^4\sqrt{1-\Lambda^{-4}X}\,. \tag{1.55}$$

Expanding in Λ, one again finds $\beta > 0$. The same sign is found in other examples as well [61, 62].

We will discuss two approaches of going beyond the standard Wilsonian picture and putting prior constraints on the EFT - the occurrence of superluminality, although intuitive is also more difficult to formulate sharply (although there has been recent progress in that direction) and positivity bounds (plus extensions), which is more formal and sharper but also more limited in its scope.

1.4.1 Superluminality

In theories (including EFTs) with a standard kinetic term (e.g. Sec. 1.1.1), causality implies (sub)luminality i.e. perturbation in the theory can propagate (at most) with the universal speed of massless particles $c = 1$. This is not a necessity when the EFT has a non-trivial kinetic term, as in the case of $K(X)$ theories [29]. Consider again the fluctuation on top of the background (1.27) and the plane-wave Ansatz with a 4-momentum $k_\mu = (k_0, \boldsymbol{k})$ and the phase velocity $v = k_0/|\boldsymbol{k}|$. From (1.47) it follows

$$\bar{\mathcal{K}}_{\mathcal{X}}(-v^2+1) + 2\bar{\mathcal{K}}_{\mathcal{X}\mathcal{X}}(-v\dot{\bar{\varphi}} + \hat{\boldsymbol{k}}\cdot\boldsymbol{\nabla}\bar{\varphi}) = 0\,. \tag{1.56}$$

If the background is time-like, in its rest frame

$$v^2 = \frac{1}{1-\frac{2\bar{\mathcal{K}}_{\mathcal{X}\mathcal{X}}}{\bar{\mathcal{K}}_{\mathcal{X}}}\dot{\bar{\varphi}}^2} \approx 1 - \frac{8\beta}{\Lambda^4}\dot{\bar{\varphi}}^2\,, \tag{1.57}$$

where in the last equality we have assumed that the background is weak i.e. $\dot{\bar{\varphi}}/\Lambda^2 \ll 1$. As the non-interacting scalar is "living" on the null cone, a non-linear perturbation in the kinetic term can kick the scalar to different sides of the cone. Imposing $\beta > 0$, one has $v < 1$.

At the classical level this result is somewhat at odds with the conclusion on the well-posedness condition of IVP of $K(X)$ theories, given in (1.48), while the condition (1.57) implies a stronger criteria $2K_{\mathcal{X}\mathcal{X}}\mathcal{X}/K_{\mathcal{X}} \geq 0$. Using hydrodynamic language, the stability condition (1.52) is $c_s^2 \geq 0$ and not $c_s \leq 1$. Although the subluminality criteria in $K(X)$ theories are not necessary for a well-posed IVP, it has been argued in Ref. [61] that superluminality would lead to a breakdown of the global hyperbolicity by the formation of closed timelike curves, that would in turn give rise to various causal paradoxes. One should note that such solutions can be found in GR as well (e.g. Gödel spacetime) [38]. An additional structure is thus needed in order to prevent the formation of such pathologies in the physical Universe (Hawking's chronology protection conjecture) and the backreaction of the quantum effects serves as a natural candidate [63]. Hawking's conjecture could then be extended to a more broader class of scalar-tensor theories. Careful analysis of the examples presented in Ref. [61] shows that all such examples rest on the particular construction of the external source, whose origin and backreaction are not under control. These effects could then prevent the formation of closed time-like curves [39]. Indeed, numerical evolution has been successfully performed in $K(X)$ scalar-tensor theories that can develop superluminal modes, even in the non-linear regime [41, 58, 55].

As the ill-posedness of the IVP may be just an artefact of EFT truncation, one can think that the same may apply for the superluminality and that in the UV (sub)luminality is restored. However, from the QFT perspective, superluminality is more worrisome. One can formulate at the S-matrix level time delay between the signal, of frequency ω, propagating in the vacuum and a background such as the one in Eq. (1.56) [64, 65, 66, 67]. If this delay can be calculated in the regime of validity of the EFT

$$\Delta T \gtrsim -\frac{1}{\omega} \tag{1.58}$$

it would imply that an asymptotically Lorentz-invariant light cone is not unique in clear contradiction to the foundations of QFT [64, 65, 66, 67]. In the above $K(X)$ example, the widening of the light cone that follows from Eqn. (1.57)

$$\Delta r \equiv \int^{\Delta t} dt|v-1| \approx 4(-\beta)\frac{\dot{\bar{\varphi}}^2}{\Lambda^4}\Delta t\,, \tag{1.59}$$

can in principle be made arbitrarily large, and thus resolvable $\Delta r \gg \lambda$ (λ is the wavelength of the fluctuation), if Δt is made large (observation time) [64, 65]. This would in turn discard the possibility of $\beta > 0$, consistently with explicit examples of UV completion. Note that the time-delay causality criteria depend explicitly on the construction of a non-trivial background and it being in the regime of validity of the EFT [68].

1.4.2 Positivity bounds

A much sharper relation between the IR and the UV originates from a powerful theorem, known as *positivity bounds* on the Wilson coefficients, formulated in Ref. [61]. Assuming only that (partial) UV completion of the EFT is local, unitary, causal and Lorentz-invariant (we will denote this set of properties as standard UV completion), one derives inequalities on Wilson coefficients which must be obeyed by the scattering amplitudes calculated with the EFT. This provides a necessary condition for an EFT to have a standard UV completion. On the flipside, finding observational signatures of the EFT which violate positivity bounds would provide evidence of much more exotic physics in the UV than is commonly expected.

Let us sketch the derivation of this theorem. The standard and simplest formulation assumes $2 \to 2$ scattering in a scalar self-interacting theory. From Lorentz invariance it follows that the amplitude of the process can only depend (modulo coupling constants) on the Mandelstam variables (s, t, u), which encode the center-of-mass energy and the transferred momentum

$$s \equiv -(p_1 + p_2)^2 \,, \quad t \equiv -(p_1 + p_3)^2 \,, \quad u \equiv -(p_1 + p_4)^2 \tag{1.60}$$

$$s + t + u = 4m^2 \,. \tag{1.61}$$

The concept of causality is implemented by means of analyticity of the amplitude. Let us first illustrate the connection between causality and analyticity in classical physics. Considering an external source $s(t)$ acting on a system at $t = 0$ (e.g. the force in a driven harmonic oscillator), the response function in the time domain $y(t)$ is given by

$$y(t) = \int dt' G_{\rm ret}(t - t') s(t') \tag{1.62}$$

The retarded Green function $G_{\rm ret}$ must satisfy $G_{\rm ret}(t) = 0$ for $t < 0$ in order for causality to be respected. Transitioning to the Fourier space we have

$$G_{\rm ret}(t) = \int \frac{d\omega}{2\pi} \tilde{G}_{\rm ret}(\omega) e^{-i\omega t} \tag{1.63}$$

The condition $t < 0$ implies that we need to close the contour in the upper-half of the complex plane as $e^{-i(i\infty)t} \to 0$ if $t < 0$. By the Cauchy residue theorem, the RHS of the previous Eq. will be equal to the sum of the residues of $\tilde{G}_{\rm ret}(\omega)$. However, if the LHS needs to be zero, this implies that there are no residues i.e. $\tilde{G}_{\rm ret}(\omega)$ is analytic in the upper half plane.

The classical connection carries over to the quantum realm. In particular, it can be shown that micro-causality implies the analyticity of $\mathcal{A}_s(s, t)$ in the complex s plane, for

fixed t and $\text{Im}(s) \neq 0$ [69]. On the real axis, however, there are poles and branch cuts that correspond to the spectrum of physical states of the theory.

Let us now assume analyticity in both IR and UV i.e. in the whole complex plane, modulo the real axis, and consider the following integral

$$I = \frac{1}{2\pi i} \oint_C d\mu \frac{\mathcal{A}_s(\mu, t)}{(\mu - s)^{n+1}} \,, \tag{1.64}$$

where the curve C encircles the pole $\mu = s$. By the Cauchy integral formula

$$I = \frac{1}{n!} \frac{\partial^n \mathcal{A}_s(s, t)}{\partial s^n} \tag{1.65}$$

Now, let us deform the contour as in Fig. 1.1 and break the integral into several terms[8]

$$I = \left(\int_{-\infty}^{-t} + \int_{4m^2}^{\infty} \right) \frac{d\mu}{\pi} \frac{\text{Im}\mathcal{A}_s(\mu)}{(\mu - s)^{n+1}} + C_\infty + \text{s.p.} \,, \tag{1.66}$$

$$C_\infty = \frac{1}{\pi} \oint d\mu \frac{\mathcal{A}_s(\mu, t)}{\mu^{n+1}} \tag{1.67}$$

where s.p. denotes the simple poles at m^2 and $4m^2$ and C_∞ the arcs at infinity. If we further assume *locality*, then the Martin-Froissart bound [65, 69]

$$\lim_{s \to \infty} |\mathcal{A}_s(s, t)| < s^2 \tag{1.68}$$

implies that $C_\infty = 0$ for $n \geq 2$. Furthermore, the assumption of *crossing symmetry* allows one to further simplify the expression and obtain [69]

$$\frac{1}{n!} \frac{\partial^n \mathcal{A}_s(s, t)}{\partial s^n} - \frac{1}{\pi} \int_{2m^2 - t/2}^{s_b} d\mu P_n(\mu, s, t) - \text{s.p.} = \frac{1}{\pi} \int_{s_b}^{\infty} d\mu P_n(\mu, s, t) \,, \tag{1.69}$$

$$P_n(\mu, s, t) = \frac{\text{Im}\mathcal{A}_s(\mu)}{(s - \mu)^{n+1}} - \frac{\text{Im}\mathcal{A}_u(\mu)}{(u - \mu)^{n+1}} \,, \tag{1.70}$$

where s_b denotes the scale at the regime of validity of the EFT. Note that the LHS of Eq. (1.69) is completely calculable within the EFT.

The last step follows from unitarity, where the optical theorem [8] in the forward $t \to 0$ limit implies [69]

$$\frac{1}{\pi} \int_{s_b}^{\infty} d\mu P_n(\mu, s, t) \geq 0 \tag{1.71}$$

The loop correction in the weak-coupling limit are subdominant and one can calculate the

[8]There are two contours, on each side of the real axis, infinitesimally shifted from it, contributing to the numerator in the integrand $2i\text{Disc}\mathcal{A}_s(s, t) \equiv \mathcal{A}_s(s + i\epsilon, t) - \mathcal{A}_s(s - i\epsilon, t)$. Using the Schwarz reflection principle $\mathcal{A}_s(s^\star, t) = \mathcal{A}_s^\star(s, t)$ one find $2i\text{Disc}\mathcal{A}_s(s, t) = \text{Im}\mathcal{A}_s(s, t)$.

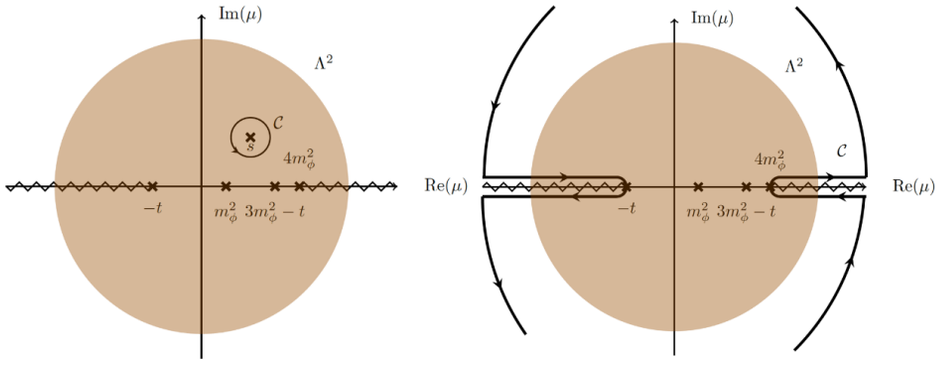

Figure 1.1: Analytic structure of the forward $2 \to 2$ scattering amplitude $\mathcal{A}_s$. Ref: [69]

tree-level leading order contribution. For $n = 2$

$$\partial_s^2 \mathcal{A}_s\big|^{\text{tree}}_{s=0,t=0} > 0 \tag{1.72}$$

Let us illustrate on our $K(X)$ toy problem (1.54) how positivity bounds work. The 2-to-2 scattering amplitude is given by

$$\mathcal{A}_{2\to 2} = \frac{\beta}{8}\frac{1}{\Lambda^4}\left(s^2 + t^2 + u^2\right) \tag{1.73}$$

Applying the Eq. (1.72) we find $\beta > 0$ i.e. the same conditions as in the subluminality constraints (Sec. 1.4.1) as well as the one that is found in all explicit UV completions [61, 62]. Note that, in contrast with subluminality constraints, the positivity bound argument does not depend on the construction of the classical background.

The argument above just provides a sketch of the basic positivity bound argument. This approach has been further extended in various directions: including loop-effects [70], going beyond the forward limit [71], including higher-spin states [67] and massless particles [72, 73] etc. Finally, there have been recent efforts to formulate the positivity bounds for EFTs with spontaneously broken Lorentz symmetry [74, 69, 75].

Chapter 2

Challenges of the standard cosmological model

The turn of the century has transitioned cosmology to the phase of precision science. The standard cosmological model, known as ΛCDM, assumes that the matter content of the Universe is at present dominated by the dark energy (DE) that behaves as a cosmological constant (Λ) and the dark matter (DM). Together with the standard thermal history and the spectrum of primordial fluctuations that follow from the inflationary paradigm, ΛCDM model provides a succinct explanation for the evolution of the Universe, consistent with observational probes sensitive to the different stages of its evolution [76]. However, this model necessitates new matter content - DM, DE and inflaton field(s), whose nature is not understood. This chapter gives a short description of how the subject matter of this thesis relates to the nature of DM and DE. In the end, we will mention a few speculative ideas of relics from the Early Universe that may be detected with the novel GW astronomy probes.

Let us summarize, for future reference, the dynamics of the homogenous ΛCDM Universe. Assuming the cosmological principle (i.e. spatial homogeneity and isotropy), from the Friedmann–Lemaître–Robertson–Walker (FLRW) metric

$$ds^2 = -dt^2 + a(t)^2 \left[\frac{dr^2}{1 - kr^2/R_0^2} + r^2 d\Omega^2 \right] , \tag{2.1}$$

where a is the scale factor, k is the spatial curvature and R_0 is the curvature scale, the Friedmann and Raychaudhuri equation follow, respectively [27, 77]

$$\left(\frac{\dot{a}}{a} \right)^2 = \frac{1}{3} \frac{\rho}{M_{\rm Pl}^2} - \frac{k}{a^2 R_0^2} , \quad \frac{\ddot{a}}{a} = -\frac{1}{6M_{\rm Pl}^2} (\rho + 3p) . \tag{2.2}$$

Knowing the matter content, these equations allow one to describe the dynamics of the homogeneous Universe.

2.1 Scalar dark matter

Cosmological observations are consistent with the presence of an effective cold DM component on large scales [78, 79, 80, 81]. There are a plethora of models providing a microphysical explanation for this component, although none have yet been confirmed experimentally [81, 82].

In addition, there are tensions between the cold DM matter model and the observations on small scales [83]. A simple illustration is the "core-cusp" problem, where pure CDM simulations produce steeper density profiles in galaxy centers than are observed. However, on small scales the feedback effects of complex astrophysical processes take place and it may be the case that such tensions will be resolved as one develops a more realistic description of the baryonic feedback effects in cosmological simulations. On the other hand, an at least partial resolution of these tensions may originate from the departure from the CDM model on small scales. Let us consider two examples of such microphysics.

2.1.1 Example 1: Solitons from wave DM

If the mass of the DM particle is smaller than $m \lesssim 30\text{eV}$ a simple estimate indicates $\mathcal{O}(1)$ occupancies in the DM halo [84]. Light DM of this type is necessarily bosonic due to the Fermi exclusion principle [85]. Consequently, one can use classical field theory to describe such classical-wave DM. On the particle physics side, there are several natural candidates for wave DM: from axions that are leading candidate to solve the strong CP problem in Quantum Chromodynamics [86, 87], to a plethora of light axion-like particles that are expected to arise in string theory [88].

The standard scenario for generating scalar DM of this type is the misalignment mechanism, where in the very early universe a homogeneous scalar field has some primordial value ϕ_0. The Klein-Gordon eq. in the FLRW metric for such a field is given by

$$\ddot{\phi} + 3H\dot{\phi} + \partial_\phi V = 0 \tag{2.3}$$

The effective equation of state of such a cosmological fluid is [from Eq. (1.51), with $K = -X/2 - V(\phi)$]

$$w \equiv \frac{\rho}{p} = \frac{\frac{1}{2}\dot{\phi}^2 - V}{\frac{1}{2}\dot{\phi}^2 + V} \tag{2.4}$$

Initially, a large Hubble parameter that acts like a friction keeps the scalar slowly rolling down the potential V and $w \approx -1$. When $H \sim m$, the scalar rolls down the potential well and when reaching the minimum it will start oscillating as $\phi \sim \cos(mt)$. It follows from (2.4) that $\langle w \rangle \approx 0$ and from Eqns. (2.2) that $\rho \sim a^{-3}$. In this way, this component behaves like DM.

The above is a standard argument for having a scalar field that exhibits cold DM

behavior on large scales. If the scalar mass is sufficiently light (fuzzy DM range, $m \sim 10^{-22}$eV) scalars in the DM halo will further relax to the self-gravitating pseudo-soliton structure - the axion star [89]. The stability of the star stems from the interplay of the kinetic term in the Lagrangian ("quantum pressure") and gravity. Microscopically, quantum pressure originates from Heisenberg's uncertainty principle. Let R be the characteristic size of the configuration and $v_{\rm vir} \sim \sqrt{M/(m_{\rm Pl}^2 R)}$ its virialized velocity. From the uncertainty principle, one has

$$mM \sim \frac{m_{\rm Pl}^2}{mR}. \tag{2.5}$$

The maximum mass, when $R \sim R_{\rm Sch}$, corresponds to the Kaup limit [90]

$$M_{\rm Kp} \sim \frac{m_{\rm Pl}^2}{m}. \tag{2.6}$$

Note that the quantum pressure is not a polytropic radial pressure, but rather an anisotropic non-local stress [91]. These axion stars are not strictly speaking solitons (localized, finite-energy and stable solutions of the equations of motion of a field theory), as prohibited by Derrick's theorem (e.g. [92]), and both the energy-momentum tensor and metric are time dependent [93, 94, 95]. However, owing to the large number of particles, their decay is exponentially suppressed [96, 97, 98].

Pseudo-soliton configurations in the fuzzy DM scenario are dilute and large $\sim$ 100pc, located at the center of the DM halo. Such configurations would make a DM halo profile more cored and provide a resolution of the core-cusp problem from the DM side. However, the presence of fuzzy DM solitons is in tension with the data [99, 100, 101]. Different particle properties (heavier axion masses, stronger self-interactions) and particular early Universe conditions or DM production mechanisms could also lead to cosmological formation of more compact axion stars [102, 103, 104]. Such objects may be discovered with present and future GW astronomy probes and depending on the strength of the axion coupling to the SM sector, even with broader multimessenger probes [105].

2.1.2 Example 2: Fifth forces from superfluid DM

An early alternative to DM was the phenomenological proposal of modifying Newtonian gravity, known as Modified Newtonian Dynamics (MOND) [106, 107], that had some success on galactic scales [108]. Possible relativistic generalizations of MOND [109, 110, 111, 112] seem to be disfavored by LIGO/Virgo observations [113, 114] and are yet unsuccessful at explaining the structure of the Universe on large scales [115]. However, some proposals have also attempted to combine cold DM's success on extra-galactic scales with MOND's advantages on galactic scales. If these models are viable, a MOND-like phenomenology

would arise from the fifth force operating on galactic scales.

Let us illustrate the main idea of a cold DM-MOND hybrid model, known as superfluid DM [116, 117, 42]. The simplest realization of this model is to have a complex scalar of mass m that on cosmological scales behaves just like cold DM (see previous example). However, in galaxies, a phase transition occurs and the scalar is in the superfluid phase. Superfluid phonons φ mediate a force between baryons $\rho_{\rm b}$ that need to be described by a non-analytic function in order to reproduce the MOND-ian phenomenology

$$\mathcal{L}_{\rm SF} = K(X) + \frac{\Lambda}{M_{\rm Pl}}\theta\rho_b\,, \quad K(X) \sim \Lambda m^{3/2} X\sqrt{X}\,, \quad X = \dot{\varphi} - m\phi_{\rm N} - \frac{1}{2m}(\nabla\varphi)^2\,, \quad (2.7)$$

and $\phi_{\rm N}$ is the external Newtonian gravitational potential. Similarly to the fifth force that develops screening (Sec. 1.4.1), superfluid DM also allows for superluminal propagation [42].

2.2 Cosmological constant problem and the accelerated expansion of the Universe

2.2.1 Accelerated expansion of the Universe

The cosmological constant problem is one of the central puzzles of contemporary physics. The core of the puzzle is related to the (quantum) nature of the vacuum. If we imagine that the vacuum is Lorenz-invariant and has non zero energy density one has

$$T_{\mu\nu} = -\rho_{\rm vac} g_{\mu\nu}\,. \quad (2.8)$$

Mapping this to the form of the stress-energy tensor of the perfect fluid (1.50) we find

$$w \equiv \frac{p_{\rm vac}}{\rho_{\rm vac}} = -1 \quad (2.9)$$

The existence of such a fluid has cosmological consequences. Assuming vacuum dominance, with respect to the other matter source, from the Friedmann equations (2.2) the accelerated expansion follows

$$a = a_0 \exp\{H(t-t_0)\}\,, \quad H^2 = \frac{1}{3}\frac{\rho_{\rm vac}}{M_{\rm Pl}^2} \quad (2.10)$$

The Cosmic Microwave Background measurement, together with distance supernovae, indicate that the Universe is spatially flat and has an accelerated expansion [118]. Furthermore, from the cosmological measurements [79]

$$\Omega_{\rm vac} \equiv \frac{\rho_{\rm vac}(a_0)}{\rho_{\rm crit}} = 0.67 \pm 0.006\,, \quad w = -1.03 \pm 0.03\,, \quad (2.11)$$

implying $\rho_{\rm vac}(a_0) \approx (3 \cdot 10^{-3}{\rm eV})^4$.

2.2.2 Cosmological constant problem(s)

Let us formulate the cosmological constant problem in the EFT spirit, following Refs. [119, 120, 7]. Let us first imagine that we integrate out all heavy states below $\sim$ meV scales and measure the cosmological value $\rho_{\rm vac}(\mu_0)$. Now, let us consider a heavy scalar $m \gg$ meV in $\lambda\phi^4$ theory. We can calculate the (Coleman-Weinberg) effective 1-loop action e.g. by using the heat kernel methods as in Sec. 1.2. The renormalized vacuum energy density in this theory is

$$\rho_{\rm vac}(\mu) = \rho_{\rm vac}(\mu_0) + \frac{m^4}{64\pi^2} \log\left(\frac{\mu_0^2}{\mu^2}\right) . \tag{2.12}$$

The value of the cosmological constant at high energies $\mu \gg \mu_0$ is now dominated by the scalar mass. Thus, its UV value $\rho_{\rm vac}(\mu)$ needs to be fine tuned in such way to cancel the quantum fluctuation contribution and "arrive" on the renormalization-group flow at $\mu = \mu_0$. In the real Universe, this fine tuning becomes even more pronounced as there are plethora of SM (and presumably beyond SM) particles whose quantum fluctuations will contribute to the vacuum energy, along with the phase transition contributions. Somehow, the UV value needs to "know" about all of these contributions and to cancel them appropriately.

A natural explanation for the smallness of the term in the Lagrangian can be found if there is an approximate symmetry. For example, in the Goldstone boson case, small mass is technically natural [1] if the breaking of the shift-symmetry is soft ('t Hooft naturalness) [7]. Analogously, the present value of the cosmological constant would be natural if e.g. the supersymmetry is spontaneously broken at the meV scale as the boson and fermion quantum contributions would cancel out [121]. However, this is clearly not the case.

The difficulty of the cosmological constant problem then follows from the fact that its resolution needs to somehow "modify" the contribution to the quantum vacuum even from well-tested low energy physics [119]. In addition, a satisfactory solution to the cosmological constant problem should not generate new fine tunings or contradict well-established experimental results. Several theoretical ideas have been pursued to solve the problem, but it is hardly surprising that none has succeeded as of yet [119, 120]. An exception could be found in an *anthropic* approach that relies on having a landscape of vacua in the UV theory [122]. Only in the "small" set of vacua a near-cancellation described in (2.12) occurs. However, these vacua are precisely the ones where the value of the cosmological constant is consistent with structure formation. This kind of consistency reasoning was used by Weinberg a decade before the measurement of the accelerated expansion of the Universe to find the range of values of $\Lambda_{\rm cc}$ that would be anthropically consistent [123].

[1] This is the case with axions, where the non-perturbative effects brake the shift symmetry and generate a small mass [86, 87].

Aside from the obvious epistemological difficulties of such a solution (falsifiability) and challenges with defining the statistics on the landscape (measure problem), one still does not have an example of a UV theory that can generate SM, DM, GR and a positive cosmological constant in the low-energy regime [118, 119].

An alternative approach is to assume that, for some reason yet to be understood, the cosmological constant is zero ("old cosmological constant problem") and that there is some other matter that drives the accelerated expansion of the Universe ("new cosmological constant problem"[2]). The simplest example of non-cosmological constant dark energy (DE) is a cosmic scalar on a slow-roll potential (2.4) where $w \approx -1$. Indeed, such a component is commonly assumed to drive the accelerated expansion of the Early Universe to solve the horizon and flatness problems. Notwithstanding the "old cosmological constant problem" that needs to be solved, scalar DE generates a new fine-tuning question: if DE is dynamical, why does matter contribute to the energy budget of the Universe at present at the same order as DE (coincidence problem). The latter question can be addressed by "tracking" scenarios, the simplest one being the quintessence model [120]. Scalar DE provides a testable alternative to the cosmological constant as one can look for the departure from $w_{\rm DE} - 1$ in the cosmological observables [124].

2.2.3 Scalar-tensor theories

Even if the signatures of scalar DE were found, this would still leave the "old" cosmological constant problem unsolved. If this scalar is somehow also responsible for the solution of the "old" cosmological problem it would need to couple to loops of SM fields like in Fig. 2.1 (left) [30]. However, from the optical theorem, such a coupling would induce the fifth force (Fig. 2.1 - right). This simple argument suggests broadening the scope of search for cosmological scalars, also to the ones that couple universally to matter. As this coupling would phenomenologically contribute to the gravitational force, one considers together the scalar and graviton degrees of freedom as a scalar-tensor theory that extends GR. It should be noted that so far no model has been constructed to solve both "old" and "new" cosmological constant problems [120]. The relevance of scalar-tensor theories is foremost in their testability both with the cosmological and novel GW astronomy probes [124].

For example, the simplest way of extending GR is to introduce a massless scalar conformally coupled to matter, which leads to the Fierz-Jordan-Brans-Dicke (FJBD) theory [125, 126, 127]. As the scalar does not couple to light, light and matter will interact with a different gravitational constant. Consequently, FJBD theory is strongly constrained in the solar system, e.g. by the Cassini flyby [128]. In order for the fifth force to be consistent with these local experimental constraints, it must be suppressed close to matter sources, e.g. through a non-linear "screening" mechanism [129, 130, 131, 30]. In contrast

[2]The terminology stems from the fact that before 1998. when it was generally believed that $\Lambda_{\rm cc} = 0$. [121]

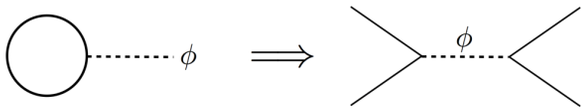

Figure 2.1: Unitarity implies that the scalar that couples universally to the matter loops must mediate a fifth force. Ref: [30].

to GR, whose coupling to matter and self-coupling are completely determined by unitarity and Poincaré invariance [8], massless scalars allow for different screening mechanisms, e.g. through scalar or derivative self-interactions [30]. Let us consider a general action that describes scalar fluctuations (decoupled from gravitons for simplicity) around the non-trivial background. As in Sec. 1.2.1 we have[3] $\varphi = \bar{\varphi} + \pi$ and

$$\mathcal{L} = -\frac{1}{2}\bar{Z}^{\mu\nu}\partial_\mu\pi\partial_\nu\pi - \frac{1}{2}\bar{m}^2\pi^2 + \bar{g}T + ... \tag{2.13}$$

where the barred quantities depend on the background. Let us for illustrative purposes take a conformal inertia factor $\bar{Z}^{\mu\nu} \sim \bar{Z}\eta^{\mu\nu}$ (as we have seen in Sec. 1.2.1 this is approximately the case in $K(X)$ theories and spherical symmetry). After field redefinition $\hat{\pi} = \sqrt{\bar{Z}}\pi$, to leading order we have a massive scalar theory that gives rise to a Yukawa potential

$$\hat{\pi} \sim \frac{\bar{g}}{\sqrt{\bar{Z}}}\frac{\exp\left(-\frac{\bar{m}}{\sqrt{\bar{Z}}}r\right)}{r} \tag{2.14}$$

Thus, one can suppress the scalar-mediated force by environmentally suppressing the coupling (symmetron mechanism [134]) or increasing the mass (chameleon mechanism [135]). Alternatively, by increasing "inertia" $\bar{Z}$ one can effectively suppress the coupling. Implementing this mechanism with first derivatives (i.e. the Newtonian acceleration) is known as kinetic screening (or k-mouflage) [130], while the implementation with second derivative (i.e. curvature) is known as Vainshtein screening [129, 131].

For the purposes of phenomenological applications, scalar-tensor theories are usually organized as the most general action that leads to second order equations of motion (Horndeski class [136]) or generalizations that are engineered to propagate $2+1$ degrees of freedom and evade ghosts (beyond Horndeski [137], DHOST theories [138]). The reason behind such a choice is that cosmological non-linearities are expected to excite the ghost degree of freedom and thus lead to loss of predictability [139]. As discussed in Sec. 1.3, such theories are not consistent EFTs and, indeed, the consistent power coupling would generate higher-derivative operators that would need to be considered at the same order

[3]Here we consider only conformal coupling to matter (in the Einstein frame). The disformal one does not mediate any tree-level interaction between matter particles [132]. If both the conformal and the disformal coupling are present, the latter one can induce a correction to gravitational phenomenology [133].

as some of the Horndeski terms [32]. However, a subclass of (beyond) Horndeski theories can be made structurally robust (Weakly Broken Galileon theories) [140, 139].

GW astronomy and, in particular, electromagnetic follow-up of the event GW170817 [114, 141] and a requirement for DE not to decay to GW have imposed strong constraints on a class of operators in Horndeski theories [142, 143, 144, 139]. In this framework, the only term that survives is the k-essence scalar-tensor theory

$$S = \int d^4x\sqrt{-g}\left[\frac{M_{\rm Pl}^2}{2}R + K(X)\right] + S_m\left(\Psi_i, \frac{g_{\mu\nu}}{\Phi(\varphi, X)}\right) . \tag{2.15}$$

It would thus be important to understand whether the $K(X)$ term can be probed. In particular, to establish whether the screening mechanism breaks down or is less effective beyond spherical symmetry and stationarity.

2.3 Solitons from the early Universe

As we have seen previously, novel GW probes may shed light on or at least constrain some of the DM and DE models. However, GW astronomy can also reveal relics from the early Universe. Two of the most discussed relics are signatures of the phase transition in the stochastic GW background and solitons formed in the early Universe [145].

From a more general phenomenological perspective, one of the target objects of GW astronomy are compact objects that do not have a standard astrophysical formation scenario - exotic compact objects (ECO) . In particular, ECOs with compactness $\mathcal{C} \equiv GM/(Rc^2) > 1/3$ (M and R being respectively the mass and radius of the body), also referred to as "ultra-compact objects", may be hard to distinguish from BHs if they present a light ring [146]. However, toy models for ECOs (such as wormholes [147], gravastars [148], anisotropic fluid stars [149] etc) have pointed to a rich range of possible observational features distinguishing these objects from BHs, e.g. non-vanishing Love numbers [150, 151], distinct post-merger phase for binary systems coalescence [152], GW echoes [153, 154, 155, 146] etc.

Many ECO toy models, however, are not realistic candidates, as they contradict some of the following reasonable requirements: stability (on relevant astrophysical/cosmological scales); existence of possible production mechanisms and astrophysical/cosmological formation channels; consistency with known and tested physics and embedding in a plausible beyond-SM theory. A more promising way to construct realistic ECO models is to consider solitons. Derrick's theorem (e.g. [92]) is a powerful constraint on the existence of these solutions, as it prohibits static non-trivial solutions for a set of real scalar fields in $D \geq 2$, where D is the number of space dimensions. In order to evade Derrick's theorem, one must either consider topologically non-trivial configurations (topological solitons) or

consider a theory with conserved charge (non-topological solitons) [156, 92].

The simplest examples of non-topological solitons are boson stars (BS): configurations made from complex scalars Φ minimally coupled to gravity and admitting a $U(1)$ symmetry [157, 158, 159, 146, 160]. Boson stars generally satisfy the soundness checks that we mentioned above. Non-rotating boson stars have at least one stable branch in the low-compactness (MBS) limit [161, 159]. Although rotation can lead to instabilities [162], it has been recently shown that sufficiently strong self-interactions can sustain it [163, 164]. These objects are constructed from covariant Lorentz-invariant actions and the modelling of their dynamics is in principle accessible. Boson stars can form from scalar collapse, with the excess field "evaporating" (gravitational cooling) [165]. Once a population of non-rotating boson stars is formed, it can reproduce in binaries through the channel BS + BS $\rightarrow$ BS [166].

If the BS admits a false/degenerate vacuum in its potential, it is known as a solitonic boson star [167] (SBS). SBS have a bubble-like structure in the most compact part of the parameter space, where the accumulation of energy near the surface gives rise to a surface tension between different vacua, which in turn allows for developing massive and highly compact configurations (see Ch. 4). In this way, the configuration is stabilized even in the absence of gravity $M_{\rm Pl} \rightarrow \infty$. In that limit, SBSs are also referred to as Q-balls [168]. SBSs are the simplest representatives of non-topological solitons that exist in the $M_{\rm Pl} \rightarrow \infty$ limit and admit a false or degenerate vacuum in one of the bosonic degrees of freedom[4]. Other examples may also include a second boson or a fermion [171, 173, 174, 175, 176].

Besides simplicity, there are also at least two additional reasons to be interested in these kinds of objects. First, Q-balls/SBSs can be formed in the early Universe, through scalar fragmentation after inflation [177, 178], thermal phase transitions [179] or solitosynthesis [180, 181]. Therefore, the possible observation of SBSs or similar ECOs can shed light on beyond-SM physics - from baryogenesis to dark matter [182]. The charge of these objects could be protected by an approximate, low-energy global symmetry [183], and depending on the specific model a fraction of the compact-object population of the universe could be in this form [184]. Note that even if SBSs are low-compactness at formation, their subsequent interaction and merger could lead to the formation of more compact configurations.

SBSs could also be considered as a proxy for similar self-gravitating structures made from (real) bosons unprotected by a symmetry. Among the latter are axion stars [94], but also oscillatons [185], moduli stars [183, 186] etc. Notwithstanding their pseudo-solitonic nature, these objects have macroscopic properties qualitatively similar to the corresponding boson star models. For example, the M-R curve of scalar stars with a mass-term potential

[4]The study of these objects was initiated by T. D. Lee and collaborators in the 1980s [169, 170, 167, 171, 172, 156].

(oscillaton) differs only by (at most) a few percent from the corresponding MBS model, and only in the most compact branch [187]. Axion stars and similar objects are expected to form in a wider variety of settings - through cosmological evolution of axion dark matter (Sec. 2.1.1), as inflation relics [188, 189, 104] or through other early Universe processes similar to those giving rise to complex configurations [183, 177, 178, 190]. Although an exact parallel between boson star models and pseudo-solitonic configurations warrants a more in-depth study, in particular when a false/degenerate vacuum exists, the static nature of boson star spacetimes allows for a technically easier preliminary analysis of these objects.

Part II

Aspects of kinetic screening

Chapter 3

Two-body problem in theories with kinetic screening

3.1 Introduction

In this Chapter we will focus on $K(X)$ theories (k-essence), introduced in Ch. 1, motivated by the DE/DM problems described in Ch. 2. Self-acceleration of the universe can be obtained with models of the type $K(X, \varphi)$ [191, 192], although those generically do not lead to screening [193]. Purely kinetic models $K(X)$ can also serve as DE, although with some degree of fine tuning [194, 195]. Models that produce a MOND-like phenomenology on galactic scales are also of this type, sometimes featuring complex scalar fields and additional non-derivative self-interactions [116, 117, 42]. The class of $K(X)$ models can also generate "anti-screening", where the fifth force increases near matter [196]. An interesting feature of these models is that they do not violate the positivity bounds, and therefore they are expected to have a standard UV completion.

In the non-linear regime, k-essence theories are non-trivial to work with. Recently, significant effort has been directed at producing numerical simulations of the full non-linear dynamics in both k-essence [197, 35, 41, 198, 58, 55, 44, 199] and in theories with Vainshtein screening [200, 56] (in the flat spacetime limit)[1]. These breakthroughs allowed for studying stellar oscillations [58, 199], gravitational collapse [58] and neutron star mergers [55]. These simulations, as well as numerical results for the two-body problem in the stationary limit [203, 204, 205] (see also Ref. [206]), indicate that the phenomenology of screening in dynamical regimes and beyond spherical symmetry presents non-trivial differences from the static and spherically-symmetric case. This modified phenomenology may include a partial breakdown of the screening mechanism [58, 55] and allow for further constraints on the parameter space of these theories. In addition to the inherent difficulties

[1]Simulations have also been performed in other scalar-tensor theories in the Hordenski class that do not exhibit screening [48, 201, 53, 51, 202, 34].

of k-essence theories, a further obstacle in a fully numerical approach arises for the cosmologically motivated models where $\Lambda \sim (H_0 M_{\rm Pl})^{1/2}$, as the latter implies a huge separation between the cosmological scales and the local scales relevant for the solar system or compact object binaries. It is thus important to understand in more detail, analytically as much as possible, the physics of kinetic screening.

In this work, we will focus on the two-body problem in theories with kinetic screening. We consider this problem first analytically, providing a decomposition of the scalar equation and solving it with various approximation techniques, and we then numerically check their validity. In particular, we will discover a partial breakdown of the screening mechanism in the regime where one would expect it to operate. We will consider the two-body problem for different choices of the kinetic function $K(X)$, including a modification of DBI theory that allows for "opposite" DBI screening [207], i.e.

$$K(X) = \Lambda^4 \sqrt{1 - \Lambda^{-4} X}\,. \tag{3.1}$$

Phenomenologically, the two-body problem is relevant in several astrophysical scenarios, e.g. in the solar system and in binary pulsars, where tests of gravity have historically been performed [208, 128, 209, 210, 211, 52], and more recently in the merging binaries of compact objects detected by gravitational wave (GW) experiments [209, 210, 212]. While the calculations of this Ch. are only at leading post-Newtonian (PN) order and are clearly inadequate to quantitatively describe binary mergers, they do nevertheless allow for a qualitative insight into the dynamics of binary systems beyond GR.

This Ch. is organized as follows. In Sec. 3.2 we will provide the field equations of k-essence, show how they can be reformulated, using the Hodge-Helmholtz decomposition, review kinetic screening and illustrate it in the case of isolated objects. In Sec. 3.3 we will describe the analytical approximations and the numerical formalism that we use to study the two-body problem in k-essence at leading PN order in the scalar sector. In Sec. 3.3.3 we will focus on a specific finding of our investigation - the appearance of pockets of linear dynamics inside a region that would be in a non-linear regime in the absence of the second object. Thus far, our results will be either general or focused on a polynomial k-essence model. In Sec. 3.4 we will instead explore other models, including "opposite" DBI screening and anti-screening. We will summarize our results in Sec. 3.5. Some details on the regime of validity of EFTs in theories with kinetic screening and on the regularization of point-particle divergences are presented in Appendices A.1 and A.2, respectively. In App. A.3 we comment on the parallel between the Hodge-Helmholtz decomposition and classical dual reformulation of self-interacting theories developed in Refs. [213, 214]. Finally, validations of our numerical code are described in App. A.4.

3.2 Setup

3.2.1 k-essence equations of motion

The action for a k-essence scalar-tensor theory is given by Eq. (2.15). Matter is assumed to be minimally coupled to the conformal metric[2] $\tilde{g}_{\mu\nu} = \Phi^{-1} g_{\mu\nu}$, for whose conformal factor we consider the following expansion at leading order $\varphi/M_{\rm Pl}$:

$$\Phi^{-1} \approx 1 + \frac{\alpha}{M_{\rm Pl}}\varphi \,. \tag{3.2}$$

In spherical symmetry, screening is a robust consequence of this action [for appropriate choices of $K(X)$], even when considering higher order corrections to this expansion [216]. From the action, the equations of motion are

$$G_{\mu\nu} = \frac{1}{M_{\rm Pl}^2}(T_{\mu\nu} + T^{\varphi}_{\mu\nu}) \,, \tag{3.3}$$

$$T_{\mu\nu} = \frac{2}{\sqrt{-g}}\frac{\delta S_m}{\delta g_{\mu\nu}} \,, \tag{3.4}$$

$$T^{\varphi}_{\mu\nu} = K(X) g_{\mu\nu} - 2K_X \partial_\mu\varphi\partial_\nu\varphi \,, \tag{3.5}$$

$$\nabla_\mu(K_X \nabla^\mu\varphi) = \frac{1}{2}\frac{\alpha}{M_{\rm Pl}} T \,, \tag{3.6}$$

where $G_{\mu\nu} = R_{\mu\nu} - R g_{\mu\nu}/2$ and $R_{\mu\nu}$ are the Einstein and Ricci tensors for the metric $g_{\mu\nu}$, $T_{\mu\nu}$ (with $T = g_{\mu\nu}T^{\mu\nu}$) and $T^{\varphi}_{\mu\nu}$ are the matter and the scalar energy-momentum tensors, and $K_X \equiv \partial K/\partial X$.

Let us start by defining

$$\chi_\mu \equiv K_X \nabla_\mu\varphi \,. \tag{3.7}$$

In the absence of matter sources, this vector is covariantly conserved and represents the Noether current associated with the shift symmetry $\varphi \to \varphi + c$. Let us then perform a Hodge-Helmholtz decomposition of this current into a longitudinal component $\partial_\mu\psi$ and a transverse component B_μ:

$$\chi_\mu = -\frac{1}{2}\nabla_\mu\psi + B_\mu \,, \tag{3.8}$$

$$\nabla_\mu B^\mu = 0 \,. \tag{3.9}$$

To check that this decomposition is unique and well-defined, one can compute the divergence $\nabla_\mu\chi^\mu = \Box\psi$, with $\Box = \nabla_\mu\nabla^\mu$. One can then conclude that ψ is uniquely determined if

[2] One can also perform a field redefinition and work with the conformal metric directly [215]. This is usually referred to as "Jordan frame", as opposed to the Einstein frame used in this Ch.

the D'Alembertian is invertible, which is the case if ψ is given appropriate initial and boundary conditions. B_μ can then be determined unambiguously[3] from Eq. (3.8).

By replacing the decomposition (3.8) in Eq. (3.6), one then gets the following Klein-Gordon equation for the longitudinal mode:

$$\Box\psi = -\frac{\alpha}{M_{\rm Pl}}T\,. \tag{3.10}$$

As for B_μ, taking a covariant derivative of Eq. (3.7) and anti-symmetrizing we obtain

$$\nabla_{[\nu}B_{\mu]} = K_{XX}\nabla_{[\nu}X\nabla_{\mu]}\varphi\,, \tag{3.11}$$

where the antisymmetric part of a tensor $S_{\mu\nu}$ is defined as $S_{[\mu\nu]} = (S_{\mu\nu} - S_{\nu\mu})/2$. This equation can be put in manifestly hyperbolic form by taking a divergence [using also Eq. (3.9)], which leads to

$$\Box B^\mu - R^\mu_{\ \nu}B^\nu = J^\mu\,, \tag{3.12}$$

$$J_\mu = 2\nabla^\nu[K_{XX}\nabla_{[\nu}X\nabla_{\mu]}\varphi]\,. \tag{3.13}$$

Note that this is formally the same as the equation for the relativistic vector potential in electromagnetism. In particular, in FJBD theory $K_{XX} = 0$, and this equation therefore implies $B^\mu = 0$ and $\varphi = \psi$. [This can also be seen directly from Eqs. (3.7)–(3.8), recalling that $K_X = -1/2$ in FJBD theory]. Thus, we will refer to ψ as the FJBD field.

By squaring Eq. (3.7), one obtains $\chi^\mu\chi_\mu = K_X^2 X$. In order to express X as a function of $\chi^\mu\chi_\mu$, $K_X^2 X$ needs to be a monotonic function of X. This therefore requires $1+2XK_{XX}/K_X$ being sign definite. One can obtain the same condition by requiring invertibility of $\partial_\mu\varphi$ in terms of χ_μ from the transformation (3.7). That requires the Jacobian of Eq. (3.7), i.e.

$$\mathcal{J}_{\mu\nu} = K_X g_{\mu\nu} + 2K_{XX}\partial_\mu\varphi\partial_\nu\varphi\,, \tag{3.14}$$

to be sign-definite [218]. Since $\det\mathcal{J}_{\mu\nu} \propto 1 + 2XK_{XX}/K_X$,[4] this yields again the same condition. By requring additionally invertibility for small values of X, one finally obtains the condition

$$1 + \frac{2K_{XX}X}{K_X} > 0\,. \tag{3.15}$$

Remarkably, this is the same condition that is found by requiring that the field equations

[3]More generally, the decomposition (3.8) is a consequence of the Hodge decomposition theorem, which states that any p-form ω on a compact, Riemannian manifold can be uniquely decomposed as $\omega = d\Psi + d^\dagger\beta + \gamma$, where $d^\dagger$ denotes a codifferential and γ is a harmonic form defined by $\Delta\gamma = 0$ with $\Delta = (d + d^\dagger)^2$ [217]. In coordinates, this statement leads to (3.8), provided that the harmonic component γ vanishes. This will indeed be the case for appropriate boundary/initial conditions.

[4]This can be easily proven for generic $g_{\mu\nu}$ by projecting the Jacobian (3.14) on a tetrad basis.

of k-essence are strongly hyperbolic [36, 38, 39, 40, 41].

3.2.2 Non-relativistic and static limit

Let us now consider the scalar equation of motion at leading PN order, i.e. at leading order in $1/c$. To this purpose, let us note that if $c \neq 1$ is reinstated, then $g_{\mu\nu} = \eta_{\mu\nu} + \mathcal{O}(1/c^2)$ and $\Box = \nabla^2 + \mathcal{O}(1/c^2)$ (with $\nabla^2 = \delta^{ij}\partial_i\partial_j$). The scalar equation (3.6) at leading PN (i.e. Newtonian) order is therefore simply

$$\partial_i(K_X \partial^i \varphi) = \frac{1}{2}\frac{\alpha}{M_{\rm Pl}} T \,. \tag{3.16}$$

For a binary system of point particles and again up to higher order corrections in $1/c$, one has

$$T = -m_a \delta^{(3)}(\boldsymbol{r} - \boldsymbol{r}_a(t)) - m_b \delta^{(3)}(\boldsymbol{r} - \boldsymbol{r}_b(t)) \,, \tag{3.17}$$

where $\boldsymbol{r}_{a,b}(t)$ are the two trajectories. It is then easy to check that if we find a solution $\varphi_{\rm static}(\boldsymbol{r}, \bar{\boldsymbol{r}}_a, \bar{\boldsymbol{r}}_b)$ for the static problem (with the two particles at rest at positions $\bar{\boldsymbol{r}}_a, \bar{\boldsymbol{r}}_b$), the solution to Eq. (3.16) for two particles in motion with velocities $\ll c$ can be obtained simply as $\varphi(t, \boldsymbol{r}) = \varphi_{\rm static}(\boldsymbol{r}, \boldsymbol{r}_a(t), \boldsymbol{r}_b(t))$. In the following we will therefore restrict, with no loss of generality (at least as long as one is working at Newtonian order), to the case of two static point particles.

In terms of the (three-dimensional) Helmholtz decomposition[5]

$$\boldsymbol{\chi} = -\frac{1}{2}\boldsymbol{\nabla}\psi + \boldsymbol{B} \,, \tag{3.18}$$

Eq. (3.10) for ψ therefore becomes the Poisson equation

$$\nabla^2 \psi = -\frac{\alpha}{M_{\rm Pl}} T \,. \tag{3.19}$$

This equation can be solved for an N-body system simply by linear superposition. If one could assume $\boldsymbol{B} = 0$, one would have to invert Eq. (3.18) in order to find φ, i.e., by squaring that equation, one would have to invert

$$K_X^2 X = \frac{1}{4} X_\psi \,, \tag{3.20}$$

with $X_\psi = (\nabla\psi)^2$. This is possible if Eq. (3.15) is satisfied. The implicit assumption $\boldsymbol{B} = 0$ was made, in the DBI case, in Ref. [207]. However, it is not a priori clear that the

[5]This decomposition was also introduced for k-essence in Ref. [40], although the solenoidal component was set to zero in spherical symmetry (see Sec. 3.2.3). In the context of MOND, the decomposition was introduced in Ref. [219], while the behavior of the two components was discussed for a particular type of $K(X)$ and in particular regions of space in a binary problem in Ref. [220] (see Sec. 3.3.3).

solenoidal component $\boldsymbol{B}$ can be ignored. In the rest of the Ch., we will discuss the role and importance of this component.

In $\mathbb{R}^3$ the decomposition that we are using, i.e. one into a longitudinal component (irrotational vector field) and a transverse component (solenoidal vector field), is further strengthened by the Helmholtz theorem [221], which states that if all involved functions have appropriate asymptotic behavior, the decomposition (3.18) is unique and

$$\psi = -\frac{1}{4\pi M_{\rm Pl}} \int d^3\boldsymbol{r}' \frac{\alpha T(\boldsymbol{r}')}{|\boldsymbol{r}-\boldsymbol{r}'|}\,, \tag{3.21}$$

$$\boldsymbol{B} = \boldsymbol{\nabla} \times \frac{1}{4\pi} \int d^3\boldsymbol{r}' \frac{\boldsymbol{C}(\boldsymbol{r}')}{|\boldsymbol{r}-\boldsymbol{r}'|}\,, \tag{3.22}$$

$$\boldsymbol{C} \equiv \boldsymbol{\nabla} \times \boldsymbol{\chi}\,. \tag{3.23}$$

From the definition of the vector $\boldsymbol{\chi}$ [see Eq. (3.7)], one has

$$\boldsymbol{C} = K_{XX} \boldsymbol{\nabla} X \times \boldsymbol{\nabla}\varphi = 2K_{XX}\epsilon_{ijk}\partial_l\varphi\partial_j\partial_l\varphi\partial_k\varphi\,, \tag{3.24}$$

where ϵ_{ijk} is the totally antisymmetric Levi-Civita symbol. It is clear that the solenoidal component will be highly suppressed (or zero) in highly symmetric regions/scenarios where $\boldsymbol{\nabla} X$ and $\boldsymbol{\nabla}\varphi$ are parallel, or when non-linearities are suppressed.

Note that the total gravitational force (at leading PN order) between two bodies, separated by a distance D, is the sum of the Newtonian/GR force and the scalar fifth force. In FJBD theory the scalar force has a Newtonian-like behavior and just renormalizes the gravitational constant:

$$F_{\rm g} = F_{\rm N} + F_{\rm FJBD} = \left(G_N + \frac{\alpha^2}{4\pi M_{\rm Pl}^2}\right) \frac{m_a m_b}{D^2}, \tag{3.25}$$

where the term in brackets defines the effective gravitational constant. In theories with screening, the fifth force will exhibit a different behavior. In the following, we will ignore the usual Newtonian/GR component and focus on the scalar force.

3.2.3 Isolated object

Let us first briefly review the solution for an isolated object, extensively discussed elsewhere [193, 40, 222, 198, 58, 216], from the perspective of the Helmholtz decomposition. In the case of a point particle or a spherically symmetric object, spherical symmetry implies that both $\boldsymbol{\nabla}\varphi$ and $\boldsymbol{\nabla} X$ must be parallel to the radial vector $\boldsymbol{r}$. Thus, from the discussion in Sec. 3.2.2 [and particularly Eq. (3.24)], the solenoidal component must vanish. The solenoidal component will vanish also in other highly symmetric configurations, if there is only one vector in the problem that all quantities need to be proportional to.

Consider a point particle at the origin with mass m. For a quadratic choice of the kinetic function

$$K(X) = K_2(X) \equiv -\frac{1}{2}X - \frac{1}{4\Lambda^4}X^2 \tag{3.26}$$

the full solution to Eq. (3.16) can be expressed in terms of the generalized hypergeometric function as [204]:

$$\varphi = -\frac{1}{4\pi r} m \frac{\alpha}{M_{\rm Pl}} \, {}_3F_2\Big[\frac{1}{4}, \frac{1}{3}, \frac{2}{3}; \frac{5}{4}, \frac{3}{2}; -\Big(\frac{r_{\rm sc}}{r}\Big)^4\Big] \,, \tag{3.27}$$

$$\begin{aligned} r_{\rm sc} &= \frac{1}{\Lambda}\left(\frac{27}{4}\right)^{1/4} \sqrt{\frac{m\alpha}{4\pi M_{\rm Pl}}} \\ &= 3 \times 10^{11}{\rm km} \times \left(\frac{\alpha}{0.1}\right)^{1/2} \left(\frac{\Lambda}{1.9 \times 10^{-3}{\rm eV}}\right)^{-1} \left(\frac{m}{M_\odot}\right)^{1/2} . \end{aligned} \tag{3.28}$$

The length scale that controls the solution is the kinetic screening radius $r_{\rm sc}$ [130]. Fixing the value of $r_{\rm sc}$ determines the profile of $\varphi(r)/(m\alpha)$, although there is degeneracy among the individual parameters $\{m, \alpha, \Lambda\}$. One can compare this "screened" solution to the FJBD one [Eq. (3.21)]. For a point particle, the latter diverges at the particle's location, while the scalar field φ, as a result of the non-linear term in the kinetic function $K(X)$, remains finite, i.e. at small radii one has

$$\varphi \approx -3.7\Lambda \sqrt{\frac{m\alpha}{4\pi M_{\rm Pl}}} + 3\Lambda^{4/3} \left(\frac{m\alpha}{4\pi M_{\rm Pl}}\right)^{1/3} r^{1/3} \,. \tag{3.29}$$

The screening therefore acts as a physical "UV regulator" for the field. Expanding the full result (3.27) around $\Lambda \to \infty$, one instead obtains

$$\varphi = -\frac{m\alpha}{4\pi M_{\rm Pl}} \frac{1}{r} + \frac{1}{5}\left(\frac{m\alpha}{4\pi M_{\rm Pl}}\right)^3 \frac{1}{\Lambda^4 r^5} + \mathcal{O}(\Lambda^{-8}) \,, \tag{3.30}$$

which demonstrates that screening is a non-perturbative effect appearing only in the regime $X/\Lambda^4 \gg 1$, i.e. in order to recover it one needs to resum all the terms in the perturbative expansion [74].

Note that although the scalar field is finite at the origin, the scalar gradient still diverges. This is, however, simply an artifact of the point particle approximation, i.e. the scalar gradient goes to zero at the origin for a spherical star [198]. In the following, when solving for the scalar field in a two body system, we will therefore have to resolve (or "regularize") the Dirac deltas in order to allow for a numerical treatment of the problem.

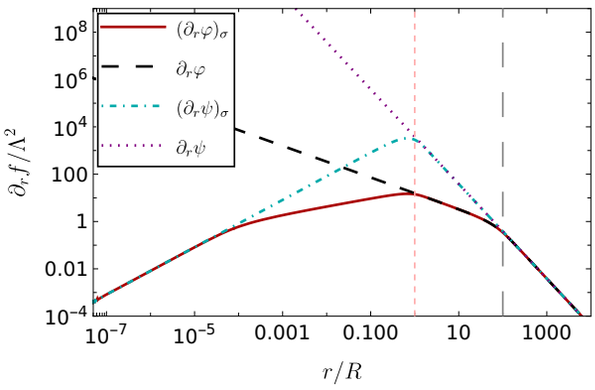

Figure 3.1: Scalar gradients for the quadratic k-essence theory described by Eq. (3.26) and for an isolated object located at $r = 0$. The screening radius is $r_{\rm sc} = 100R$ (gray long dashed vertical line) and the effective radius of the Gaussian source is $R = 2\sigma$ (pink short dashed vertical line). $f = \{\varphi, \psi\}$ are respectively the k-essence scalar field and its irrotational component (which matches the FJBD gradient). Profiles are computed for a Gaussian source (index σ) and a Dirac delta (no index).

We will do so by utilizing a Gaussian density model for each point particle, i.e.

$$T_i = -\frac{m_i}{(\sqrt{2\pi}\sigma)^3} \exp -\frac{(\boldsymbol{r} - \boldsymbol{r}_i)^2}{2\sigma^2}\,, \tag{3.31}$$

where σ is the width of the Gaussian and $\boldsymbol{r}_i$ is the position of the particle. The solution of Eq. (3.16) with this source cannot be expressed in closed form, even for a single particle, although Eq. (3.20) provides a closed form expression for $\partial_r\varphi$ [see Eq. (3.47) below]. This expression, however, needs to be integrated in order to find the scalar profile $\varphi(r)$ for a single point particle.

To test this regularization, we show in Fig. 3.1 the scalar gradient, calculated with a Dirac delta and a Gaussian source. As expected, the two profiles coincide outside the effective radius of the object ($R = 2\sigma$). The same figure also shows the gradient of the FJBD field ψ, again for both sources. As expected from previous studies [130, 198, 58], the gradients of φ (which can be physically interpreted as the fifth force) are suppressed with respect to the FJBD gradients $\partial_r\psi$, even inside the effective radius R. As the radial coordinate approaches the origin, both gradients tend to zero for the regular Gaussian source, as dictated by spherical symmetry and regularity [198, 58]. Further details on the Gaussian regularization will be presented in App. A.2.

3.3 The two-body problem: polynomial k-essence

Unlike the isolated object case of Sec. 3.2.3, the two-body problem is only axially symmetric, around the direction that connects the two particles. Let us define the coordinate system such that the particles (of masses m_i) are located on the z axis at $z_i = \pm D/2$, where D

is the separation and i is an index running on the two particles a and b. We will work in cylindrical coordinates (ρ, ϑ, z), with $\rho = \sqrt{x^2 + y^2}$ and $\vartheta = \arg(x, y)$. In principle, the scalar field could depend on ϑ, but because the source on the right-hand side of Eq. (3.16) does not, the dependence must be linear, i.e. $\varphi = L\vartheta + \bar{\varphi}(\rho, z)$ for some constant L. This would ensure that the left-hand side of Eq. (3.16) is independent of ϑ. However, asymptotic flatness requires φ approaching zero far from the two-body system, which in turn imposes $L = 0$.

Let us then solve the scalar equation (3.16) with the source (3.17) and the polynomial kinetic function

$$K(X) = \Lambda^4 \mathcal{K}_N(X)\,, \quad \mathcal{K}_N(X) = -\sum_{n=1}^{N} \frac{1}{2n}\Big(\frac{X}{\Lambda^4}\Big)^n\,, \tag{3.32}$$

which allows for screening as long as the leading order term has a negative coefficient [74]. Note that the choice of the dimensionless series coefficient was made simply for computational convenience, and is not expected to qualitatively impact our results (see also Sec. 3.4.1). In App. A.1 we argue, based on Ref. [22], that the non-linear regime of the above theory is in the EFT regime of validity for generic astrophysical scenarios and every $N > 1$.

From the analysis of the scalar profile around an isolated object in the previous section, we have seen that the screening starts operating when $X \gtrsim \Lambda^{-4}$, and that the field strength is governed by $\{m, \alpha, \Lambda\}$. For a generic polynomial function, in the region of deep screening the highest power of X^N will dominate. For an isolated point particle, we then have, from Eq. (3.16),

$$\left(\frac{\partial_r \varphi}{\Lambda^2}\right)^{2N-1} \approx \left(\frac{m\alpha}{4\pi M_{\rm Pl}\Lambda^2}\right)\frac{1}{r^2}\,. \tag{3.33}$$

Thus, the lengthscale that controls the scalar field profile for an isolated object is parametrically the same as for quadratic k-essence, i.e.

$$r_{\rm sc} = c_N \sqrt{\frac{m\alpha}{4\pi M_{\rm Pl}\Lambda^2}}\,, \tag{3.34}$$

up to a numerical coefficient c_N [for a quadratic kinetic function one has e.g. $c_2 = (27/4)^{1/4}$]. In particular, for $N = 2$, from Eq. (3.33) one finds the small-radius expansion given by Eq. (3.29), i.e. $\varphi \approx \text{const} + \mathcal{O}(r^{1/3})$.

Let us now turn to the binary problem and define $m_a \equiv m$ and $m_b \equiv m/q$, $q \geq 1$.

Motivated by the previous discussion, we introduce the rescaled dimensionless variables

$$\mathsf{x}_i = \lambda x_i\,, \quad \kappa = \frac{m\alpha}{4\pi M_{\rm Pl}}\left(\frac{\lambda}{\Lambda}\right)^2\,, \quad \phi = \frac{\varphi\lambda}{\Lambda^2}\,, \tag{3.35}$$

$$\mathcal{X} = \frac{X}{\Lambda^4}\,, \quad \Psi = \frac{\psi\lambda}{\Lambda^2}\,, \quad \mathcal{B} = \frac{B}{\Lambda^2}\,, \quad \boldsymbol{\mathcal{C}} = \frac{\boldsymbol{C}}{\lambda\Lambda^2(4\pi)}\,, \tag{3.36}$$

where the constant λ (which has dimensions of a mass) is for the moment left free. Note that the rescaling of the Cartesian coordinates implies in particular the rescaling $\varrho = \lambda\rho$. Moreover, from now on the spatial derivatives will be assumed to be taken with respect to the rescaled coordinates x_i unless otherwise specified. With these rescalings, the scalar equation (3.16) takes the form

$$\boldsymbol{\nabla}\cdot\left(\boldsymbol{\nabla}\phi\sum_{n=1}^{N}\mathcal{X}^{n-1}\right) = 4\pi\kappa\left[\delta^{(3)}\left(\mathbf{r}-\frac{\mathsf{D}}{2}\hat{\boldsymbol{z}}\right)+\frac{1}{q}\delta^{(3)}\left(\mathbf{r}+\frac{\mathsf{D}}{2}\hat{\boldsymbol{z}}\right)\right] \tag{3.37}$$

We will from now on use the scale invariance of Eq. (3.37) to set $\mathsf{D} = 1$, and thus $\lambda = D^{-1}$, without loss of generality. Thus, the parameter space of the problem is defined by the (square of the) ratio of the screening radius of the more massive object and the inter-particle separation,

$$\kappa = \frac{m\alpha}{4\pi M_{\rm Pl}\Lambda^2}\frac{1}{D^2} \propto \left(\frac{r_{\rm sc}}{D}\right)^2\,, \tag{3.38}$$

and by the mass ratio q. As mentioned earlier, to solve the two-body problem numerically we will need a finite representation for the Dirac deltas, i.e. Eq. (3.31) for both sources, centered at $\mathsf{z} = \pm 1/2$. The appearance of a resolution length scale σ now extends the dimension of the parameter space from two to three: κ, q and R, where $\mathsf{R} = R/D = (2\sigma)/D$.

In the following, for concrete calculations we will focus on a quadratic model ($N = 2$), which makes Eq. (3.20) solvable analytically. However, we will also provide analytic arguments supporting the (qualitative) applicability of these results to more general polynomial functions.

3.3.1 To B or not to B

As discussed in Sec. 3.2.3, a perturbative treatment of the dynamics is only useful outside the screening region(s). In that regime, the solenoidal component is suppressed relative to the irrotational one, as $\mathcal{K}'' \ll 1$ [see Eq. (3.24)]. Inside the screening region(s), the equation of motion is highly non-linear, and an exact solution cannot be found for the two-body problem. We will therefore attempt two approximations, whose validity we will

evaluate by self-consistency and by comparing to our fully numerical results[6].

As the Helmholtz decomposition (3.18) breaks the problem into a straightforward part (irrotational component) and a complicated one (solenoidal component), most of our focus will be on understanding the solenoidal component. Let us then outline its vectorial structure. As elaborated in the introduction of this Section, from axial symmetry and asymptotic flatness one has $\phi = \phi(\varrho, \mathsf{z})$, and thus from the Helmholtz decomposition (3.18) one can conclude that $\mathcal{B}^\vartheta = 0$. As the source $\boldsymbol{\mathcal{C}}$ is proportional to $\boldsymbol{\nabla}\phi \times \boldsymbol{\nabla}\mathcal{X}$, and these two vectors are spanned by $\{\hat{\boldsymbol{\varrho}}, \hat{\mathbf{z}}\}$, the only non-zero component of the source vector will be $\mathcal{C}^\vartheta$. From Eq. (3.22) it then follows

$$\begin{aligned} \mathcal{B}_\varrho &= -\int d\mathsf{V}' \partial_\mathsf{z} \left(\frac{1}{|\mathbf{r} - \mathbf{r}'|} \right) \mathcal{C}^\vartheta(\varrho', \mathsf{z}') \,, \\ \mathcal{B}_\mathsf{z} &= \int d\mathsf{V}' \frac{1}{\rho} \partial_\varrho \left(\frac{\varrho}{|\mathbf{r} - \mathbf{r}'|} \right) \mathcal{C}^\vartheta(\varrho', \mathsf{z}') \,. \end{aligned} \tag{3.39}$$

It is clear that these two components satisfy the zero-divergence condition (3.9)

$$\frac{1}{\varrho} \frac{\partial(\varrho \mathcal{B}_\varrho)}{\partial \varrho} = -\frac{\partial \mathcal{B}_\mathsf{z}}{\partial \mathsf{z}} \,. \tag{3.40}$$

If the source $\mathcal{C}^\vartheta$ is non-zero, as generically expected, the solenoidal component is expected to be non-vanishing, unlike in the example given in Sec. 3.2.3.

3.3.1.1 Linear superposition approximation

A very simple approximation is to consider the *linear superposition* of the *full* single particle solutions [given by Eq. (3.27) for the quadratic kinetic function], i.e.

$$\phi = \phi_a + \phi_b \,, \tag{3.41}$$

where $\phi_{a,b}$ are the two solutions. We expect this ansatz to work well when the screening regions of the individual bodies do not overlap, i.e. in the limit $\kappa \ll 1$. In that situation, non-linearities are strong only in the vicinity of each body, and are sourced by the body itself (in isolation). These non-linearities are therefore already captured by Eq. (3.27). This approximation will however receive non-trivial and a priori uncontrolled corrections

[6] One can perform a field rescaling [223, 224, 225] or introduce an auxiliary field at the level of action (dual formulation) that replaces the self-interacting terms [213, 214] in order to obtain a well-defined perturbative expansion in the screening region. In App. A.3 we show that the dual formulation is in fact equivalent to the Helmholtz decomposition. We have not been able to solve the equation for the solenoidal component (3.12) in a binary problem even after such a reformulation. Other analytic approaches, based e.g. on perturbing the scalar field around the background field generated by a fictitious isolated body located at the center of mass of the system [226], or on a sort of effective one-body approach [204], have also failed to solve the two-body problem in a controlled perturbative manner in theories with kinetic/Vainshtein screening.

when the screening regions of the individual bodies overlap.

Note that even when $\kappa \ll 1$, the solenoidal component $\boldsymbol{\mathcal{B}}$ will be non-zero. In this regime, we can just insert the ansatz (3.41) into Eq. (3.18) and get a (complicated) expression for $\mathcal{B}^2 = \boldsymbol{\mathcal{B}} \cdot \boldsymbol{\mathcal{B}}$. The latter can be simplified on the plane $\varrho = 0$, where both the solenoidal and irrotational components present maximal amplitudes:

$$\begin{aligned} \mathcal{B}^2(\varrho = 0, z) &= \frac{64}{3} f(a)^2 f(b)^2 \big[s(b) f(a) + s(a) f(b)\big]^2 , \\ f(i) &\equiv \sinh\left[\frac{1}{3} \operatorname{arcsinh}\left(\frac{\mathsf{r}_{\mathrm{sc},i}}{\mathsf{z} - \mathsf{z}_i}\right)^2\right] , \qquad (3.42) \\ s(i) &\equiv \operatorname{sgn}(\mathsf{z} - \mathsf{z}_i) . \qquad (3.43) \end{aligned}$$

In the regime where the superposition approximation is valid ($\kappa \ll 1$), we find that the irrotational component dominates upon the solenoidal one, as the dimensionless ratio between their kinetic energies is

$$\frac{\mathcal{X}_\Psi(0, \mathsf{z})}{\mathcal{B}^2(0, \mathsf{z})} \sim \frac{81 q^2}{16 \kappa^4} (1 - 2\mathsf{z}) , \qquad (3.44)$$

when $\kappa \to 0$. Note that this is a non-trivial result, as it is valid not only in the perturbative regime (outside the screening regions of the individual bodies), but also in the screening region of each body. Indeed, near the body positions $\mathsf{z} = \pm 1/2$, one recovers (by construction) the isolated object solutions, at leading order. Similarly, the isolated object solution can be recovered in the extreme mass ratio limit. Indeed, expanding for $q \gg 1$ we find

$$\mathcal{B}^2(0, \mathsf{z}) \sim \mathcal{O}(q^{-2}) , \quad \mathcal{X}_\Psi(0, \mathsf{z}) \sim \mathcal{O}(q^0) , \qquad (3.45)$$

which shows that the solenoidal component is suppressed, as expected.

3.3.1.2 Irrotational approximation

Motivated by the previous discussion, one can start from the Helmholtz decomposition (3.18), ignore the solenoidal component and invert Eq. (3.20) to find X. We will refer to this approach as the *irrotational (or longitudinal) approximation*. Let us consider first a general kinetic function $K(X)$, and emphasize that the kinetic energy X obtained in this way is an infinite series in Λ^{-2} (although this scale is absorbed in the parameter κ). Indeed, in the case of an isolated object or other highly symmetric configurations, this result matches the full result, as shown in Sec. 3.2.3. Once found X, one can reconstruct

the field by integrating Eq. (3.18) (with $\boldsymbol{B} = 0$), i.e.

$$\phi(\varrho, \mathsf{z}) = -\frac{1}{2}\int_{\infty}^{\varrho} d\tilde{\varrho}\frac{\partial_{\tilde{\varrho}}\Psi}{\mathcal{K}'(\mathcal{X})}\,. \tag{3.46}$$

(Note that the general solution would include an additional arbitrary function of z, which is however forbidden by requiring that ϕ vanishes far from the source.) For example, for the quadratic function of Eq. (3.26), one finds the following closed form for $\mathcal{X}$:

$$\begin{aligned} \mathcal{X} &= \frac{1}{3}\left(Y^{1/3} + Y^{-1/3} - 2\right)\,, \\ Y &= \frac{3\sqrt{3}\,(27\mathcal{X}_{\Psi}^2 + 4\mathcal{X}_{\Psi})^{1/2} + 27\mathcal{X}_{\Psi} + 2}{2}\,. \end{aligned} \tag{3.47}$$

[from Eq. (3.20); see Fig. 3.10].

Once determined $\mathcal{X}$ and ϕ in this irrotational approximation, one can check the validity of the latter by computing the solenoidal component from Eq. (3.24). In this way, one could devise an iterating scheme in order to solve the problem self-consistently. We will however try to understand if there are regimes where the solenoidal component is parametrically suppressed and the irrotational approximation is valid to leading order. We are thus interested in comparing $\mathcal{B}$ with $-\boldsymbol{\nabla}\Psi/2$. As the same derivative power will act on the radial distance in the denominator on the right-hand side of Eq. (3.21) as in Eq. (3.39), it follows that if the source of the solenoidal component $\mathcal{C} \equiv |\boldsymbol{\mathcal{C}}| = \mathcal{C}^{\theta}$ is parametrically suppressed with respect to the irrotational one, i.e.

$$S_{\Psi} = -\frac{1}{2}\kappa\left[\delta^{(3)}\left(\mathbf{r} - \frac{1}{2}\hat{\boldsymbol{z}}\right) + \frac{1}{q}\delta^{(3)}\left(\mathbf{r} + \frac{1}{2}\hat{\boldsymbol{z}}\right)\right]\,, \tag{3.48}$$

this will be also true for the magnitudes of the components themselves.

The magnitude of the source of the solenoidal component in the irrotational approximation is given by

$$\mathcal{C} \approx \mathcal{N}_K G_{\boldsymbol{\nabla}}\,, \tag{3.49}$$

$$\mathcal{N}_K = -\frac{1}{8\pi}\frac{\mathcal{K}_{\mathcal{X}\mathcal{X}}}{\mathcal{K}_{\mathcal{X}}}\frac{d\mathcal{X}}{d\mathcal{X}_{\Psi}}|\boldsymbol{\nabla}\mathcal{X}_{\Psi}|\sqrt{\mathcal{X}_{\Psi}}\,, \tag{3.50}$$

$$G_{\boldsymbol{\nabla}} = \sqrt{1 - \frac{(\boldsymbol{\nabla}\mathcal{X}_{\Psi}\cdot\boldsymbol{\nabla}\Psi)^2}{(\boldsymbol{\nabla}\mathcal{X}_{\Psi})^2\mathcal{X}_{\Psi}}}\,, \tag{3.51}$$

where the kinetic function and its derivatives are functions of $\mathcal{X} = \mathcal{X}(\mathcal{X}_{\Psi})$. As can be seen, the source $\mathcal{C}$ depends on the non-linear terms of the function (encoded in $\mathcal{N}_K$) and on the "misalignment" between $\boldsymbol{\nabla}\mathcal{X} \propto \boldsymbol{\nabla}\mathcal{X}_{\Psi}$ and $\boldsymbol{\nabla}\phi \propto \boldsymbol{\nabla}\Psi$ (encoded in $G_{\boldsymbol{\nabla}}$). In order for the solenoidal component to be significant, there must be an overlap between the supports of $\mathcal{N}_K$ and $G_{\boldsymbol{\nabla}}$.

Let us first consider $G_{\boldsymbol{\nabla}}$. Since it depends only on the FJBD fields Ψ and $\mathcal{X}_\Psi$, this quantity is independent of the screening radius and only depends on the mass ratio q. From the definition (3.51), it is also clear that $0 \leq G_{\boldsymbol{\nabla}} \leq 1$, with $G_{\boldsymbol{\nabla}} = 1$ when $\boldsymbol{\nabla}\mathcal{X}_\Psi$ and $\boldsymbol{\nabla}\Psi$ are orthogonal. In Fig. 3.2, we plot the support of $G_{\boldsymbol{\nabla}}$, defined as the region where $G_{\boldsymbol{\nabla}} \geq 0.1$, for various mass ratios. In the equal mass case, the support is symmetric around the center of mass of the system. As q increases, the support shrinks and gets shifted towards the smaller object (located at $\mathsf{z}_b = 1/2$). In the limit $q \to \infty$ we find that $G_{\boldsymbol{\nabla}} \to 0$, i.e. we recover the spherically symmetric solution and the solenoidal component vanishes, as expected.

The prefactor $\mathcal{N}_K$ has instead support in the screening region, where the non-linearities dominate and which is centered on the objects themselves, encoded in $\kappa \propto (r_{\rm sc}/D)^2$ and q. Let us first demonstrate two cases where the overlap between $\mathcal{N}_K$ and $G_{\boldsymbol{\nabla}}$ is small. Consider first the equal mass limit $q \approx 1$ and $\kappa \ll 1$: the support of $\mathcal{N}_K$ shrinks (because the screening radii of the two objects shrink) and the small overlap with the support of $G_{\boldsymbol{\nabla}}$ suppresses the source of the solenoidal component. When instead $q \gg 1$, the support of $\mathcal{N}_K$ is mostly around the more massive body a, while the support of $G_{\boldsymbol{\nabla}}$ is closer to the lighter body b (see Fig. 3.2), resulting again in a small overlap between $\mathcal{N}_K$ and $G_{\boldsymbol{\nabla}}$ and thus in a small source magnitude $\mathcal{C}$. Note that both of these cases ($q \approx 1$ and $\kappa \ll 1$; $q \gg 1$) are consistent with the intuition from the linear superposition approximation (for the quadratic k-essence), but the arguments presented here extend their validity to a generic kinetic function.

To gain some insight on the remaining case ($\kappa \gg 1$ and $q \approx 1$), let us specialize to the polynomial form (3.32) for the kinetic function. In the deep screening regime $\kappa \gg 1$, the highest power in the series dominates, and from (3.20) one therefore concludes that

$$\mathcal{X} \approx \mathcal{X}_\Psi^{1/(2N-1)}\,, \tag{3.52}$$

and consequently

$$\mathcal{N}_K \approx -\frac{\kappa}{8\pi}\frac{N-1}{(2N-1)}\frac{|\boldsymbol{\nabla}\hat{\mathcal{X}}_\psi|}{\sqrt{\hat{\mathcal{X}}_\Psi}}\,, \tag{3.53}$$

$$\mathcal{X}_\Psi \equiv \kappa^2\hat{\mathcal{X}}_\Psi(q)\,. \tag{3.54}$$

For $N = 1$, one recovers the FJBD theory result ($\mathcal{X} = \mathcal{X}_\Psi$ and $\mathcal{N}_K = 0$). Since $G_{\boldsymbol{\nabla}}$ does not depend on κ, one can therefore conclude that $\mathcal{C} \approx \mathcal{N}_K G_{\boldsymbol{\nabla}} \propto \kappa$.

Let us now compare the source of irrotational and the solenoidal components. As both S_Ψ [see Eq. (3.48)] and $\mathcal{C}$ scale linearly with κ, their ratio will depend only on the mass ratio q. Since $-\boldsymbol{\nabla}\Psi/2$ and $\boldsymbol{\mathcal{B}}$ [Eqs. (3.21), (3.39)] depend on the volume integrals of their respective sources and both sources have a compact support, let us then compute

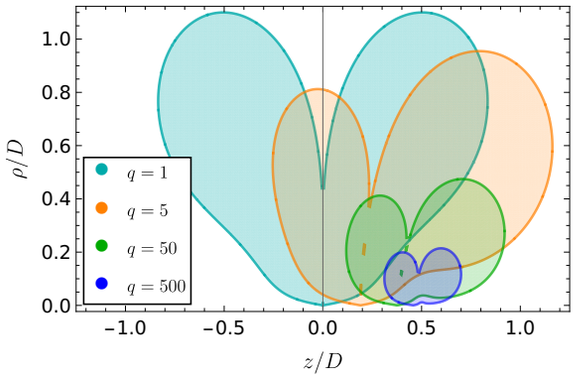

Figure 3.2: Support of the function $G_{\boldsymbol{\nabla}}$, which encodes the geometry of the source (3.51), defined by $G_{\boldsymbol{\nabla}} > 0.1$, for four choices of the mass ratio $q = m_a/m_b$. The cylindrical coordinates (ρ, z) are rescaled by the inter-particle separation, and the particles are located at $z_i = \pm D/2$.

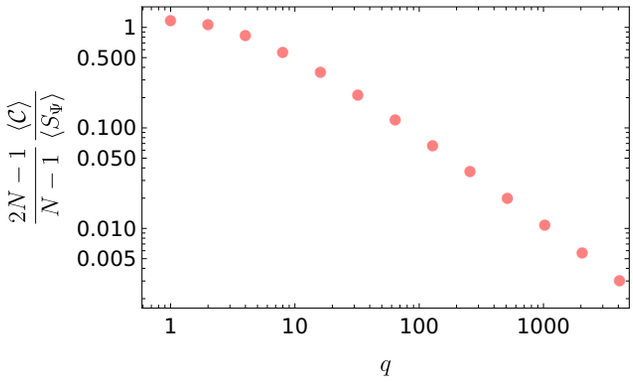

Figure 3.3: The ratio between the volume-averaged source of the irrotational component in the Helmholtz decomposition (3.18), $\langle S_\Psi \rangle$, and the (averaged) source of the solenoidal component, $\langle C \rangle$, as function of the mass ratio q in the deep screening regime $\kappa \gg 1$. The ratio is multiplied by the factor $(2N-1)/(N-1)$, which depends on the choice of the kinetic function (in polynomial form).

the spatial averages of $\mathcal{C}$ and S_Ψ. For the irrotational component, Eq. (3.48) yields the average $\langle S_\Psi \rangle = -\kappa(1+q^{-1})/(2V)$, where V is the volume (larger than the individual supports of $\mathcal{C}$ and S_Ψ) over which the average is peformed. For $\mathcal{C}$, we calculated the average numerically for a set of values of q. In Fig. 3.3, we show the ratio $\langle \mathcal{C} \rangle / \langle S_\Psi \rangle$, multiplied by $(2N-1)/(N-1)$ to eliminate the dependence on N [see Eq. (3.53)]. For instance, for $q = 1$ and $N = 2$, the ratio is $\langle \mathcal{C} \rangle / \langle S_\Psi \rangle \approx 0.38$ (Also note that the ratio is independent of the volume V). These results demonstrate that the solenoidal component is always suppressed with respect to the irrotational one even in the deep screening regime, although when $q \approx 1$ this suppression is less evident.

In conclusion, the analytic arguments of this section indicate that the solenoidal component will be significantly suppressed relative to the irrotational one when $\kappa \ll 1$ and/or $q \gg 1$ (for a generic kinetic function). The suppression also holds in the deep screening regime $\kappa \gg 1$ (for a polynomial kinetic function), although it becomes less pronounced for comparable masses ($q \approx 1$).

3.3.2 Numerical solution

3.3.2.1 Formulation

In order to validate the analytic approximations of Sec. 3.3.1 and to understand the full behavior of the two-body dynamics, we have performed numerical simulations for the

case of a quadratic kinetic function[7]. The scalar equation of motion (3.37), together with appropriate boundary conditions (to be described below), defines an elliptic boundary value problem. We have represented Eq. (3.37) in cylindrical coordinates, and we have discretized it using a second-order finite difference scheme, regularizing the Dirac deltas with the Gaussian source of Eq. (3.31).

Our integration domain is the rectangle $[0, \varrho_{\rm out}] \times [-\mathsf{z}_{\rm out}, \mathsf{z}_{\rm out}]$, where the boundary values $\varrho_{\rm out}$ and $\mathsf{z}_{\rm out}$ are chosen to be larger than or at most comparable to the screening radii of the constituent object. On the $\varrho = 0$ plane, regularity requires the boundary condition $\partial_\varrho \phi|_{\varrho\to 0} = 0$. Defining our grid as $\varrho = i\mathsf{h}$ and $\mathsf{z} = j\mathsf{h}_\mathsf{z}$ (with h and h_z the grid steps), regularity is then implemented by introducing the ghost point $i = -1$ and taking $\phi(-1, j) = \phi(1, j)$. In order to regularize the coordinate singularity of Eq. (3.37) at $\varrho = 0$, we apply the L'Hôpital rule

$$\lim_{\varrho\to 0} \frac{1}{\varrho}\frac{\partial\phi}{\partial\varrho} = \frac{\partial^2\phi}{\partial\varrho^2} \tag{3.55}$$

to modify the scalar equation at $i = 0$ [227].

On the other sides of the grid, we have used two implementations of Dirichlet boundary conditions. First, we have used the superposition of the FJBD potentials to set the scalar field on the boundary, as long as the latter is sufficiently far from the screening radius. Moreover, after establishing that Eq. (3.46) provides a good approximation away from the objects, but inside the screening region, we have used it to set the boundary scalar field in the case when the size of the domain is comparable to the screening radius, in order to reduce the size of the grid for the highly non-linear cases.

After discretization, Eq. (3.37) yields the non-linear system

$$G_{ij}[\{\phi(i', j')\}_{i'=i-1,i,i+1,j'=j-1,j,j+1}] = 0\,, \tag{3.56}$$

where G_{ij} is a (non-linear) function of the discretized field at the neighboring points i' and j'. We solve this non-linear system by using a Newton-Raphson method and an LU decomposition to compute the inverse of the Jacobian. We have set a tolerance of 10^{-5} on the scalar field profile. In all runs grid size was several times smaller than the effective radius of the Gaussian source. As initial guess for scalar profile in the Newton-Raphson method, we adopt several choices including the superposition of FJBD potentials (A.6) and the single particle solutions (Sec. 3.3.1). However, as the non-linearities become more important, corresponding to the growth of κ in our units, we use Eq. (3.46) as initial

[7]The same problem was also studied numerically in Ref. [204]. However, that analysis focused only on the binary's energy. Here we discuss several other aspects, and in particular the behavior of the scalar gradients. In addition, we use a different numerical method and provide a more refined code validation (see App. A.4).

guess. Moreover, to speed up the calculation we occasionally replace the Newton-Raphson method iteration with one computed with a Broyden method [228].

A description of our code's validation, including a comparison with the semi-analytic solution in the single particle case and convergence tests, is left for App. A.4.

3.3.2.2 Results

Consider first an equal-mass system where the screening regions of the constituent objects do not overlap, i.e. $\kappa < 1$. In Fig. 3.4 (left), we show the numerical solution for the scalar's kinetic term on the plane $\rho = 0$, $\mathcal{X}_{\rm num}$, vs the same quantity for FJBD theory $\mathcal{X}_{\Psi}$, and two approximations described in Sec. 3.3.1 (with a Gaussian source). In more detail, both the linear superposition of the two one-particle solutions $\mathcal{X}_{\rm sup}$ and the irrotational approximation $\mathcal{X}_{\rm irr}$ provide an excelent agreement with the numerical results. Furthermore, the difference between these approximations and the numerical solutions, and hence the importance of the solenoidal component, is of the order of the numerical error in this regime. The comparison with FJBD theory demonstrates that the screening is active inside the screening region of the individual objects (shaded region), and that outside the individual screening regions the scalar gradient is not suppressed. Note also that the kinetic term is significantly suppresed (although not zero in contrast to the isolated object, Sec. 3.2.3), and thus the theory is in the linear regime, near the center of the source.

More interesting is a scenario where $\kappa > 1$. In Fig. 3.4 (right) we show the same quantities as for the previous case. In order to appriciate the full spatial behaviour of the scalar kinetic energy we also present in Fig. 3.5 a contour plot of $\mathcal{X}_{\rm num}$ for one such case (bottom), together with the same plot for the corresponding one-particle case (top). Consider the region around $z = \rho = 0$, which is inside the single-particle screening region. In the binary problem, this region corresponds to the saddle point of the scalar profile, where the fifth forces cancel each other and thus the scalar gradient is suppressed (see the next Sec. 3.3.3 for further discussion). This can be clearly seen in the bottom panel, where the contour lines get deformed to allow for near zero gradients in the saddle region. On the "outer" side of the binary, the profile is much closer to the expectation from the single-particle case, although both the scalar gradients and the screening radius become larger. This is expected, as sufficiently far away from the constituent objects, the system behaves as a composite single object $m_a + m_b$. Both the irrotational and linear superposition approximations considered earlier capture the essential characteristics of how the screening operates in a binary system as is clear from Fig. 3.4 (right). The superposition ansatz $\mathcal{X}_{\rm sup}$ tends to overcorrect the difference between the one-particle case and the two-body by drastically reducing the peaks inside the binary and enhancing those outside it. On the other hand, the irrotational approximation $\mathcal{X}_{\rm irr}$ makes these adjustments closer to the true (numerical) solution.

Consider now a case with $\kappa > 1\,, q \gg 1$, shown in Fig. 3.6. As discussed in Sec. 3.3.1, both approximations are much closer to the numerical result than in the case of equal-mass systems. In particular, the discrepancy between the analytic approximations and the numerical result is most pronounced in the vicinity of the smaller object. Again, the irrotational approximation is outperforming the simple linear superposition of the one-body solutions.

In order to compactly describe the two approximations across the mass ratio parameter space, we define the following L^2 norm

$$||\Delta y||_2 \equiv \sqrt{\int d\mathcal{V}(y_{\rm num} - y_{\rm an})^2} \tag{3.57}$$

where $y = \{\phi, \mathcal{X}\}$, with subscripts $\{\rm num, an\}$, denote the numerical result and the analytic approximation, respectively, and the integral is taken over whole grid. The estimate is sensitive to the non-linear regime, because in the linear regime both approximations give a very good description of the numerical results. Results are shown in Fig. 3.7 for a scenario representative of the deep screening regime $\kappa \gg 1$. We find that the irrotational approximation is outperforming the superposition approximation for all mass ratios, although the relative error of both approximations increases as $q \to 1$. This is completely in line with the conclusions from Sec. 3.3.1. We also find that the relative error of the kinetic energy saturates at $\sim 10\%$ for $q = 1$. Thus, even in the case of equal masses, the irrotational approximation provides a decent quantitative description of the scalar profile. It is also apparent that, for a given approximation, the error is smaller for the field than for X. A similar phenomenon is observed in the two-body problem for cubic Galileons (where the Vainshtein screening operates [33, 215, 226, 222, 30]), when comparing the superposition approximation and numerical results [205].

3.3.3 Descreened bubbles

In systems where only attractive forces act, there may be special points where all the forces cancel. For spherical objects in isolation, one such point is the center, while in N-body systems these are the saddle points, where the gradient of the potential vanishes. In theories where the screening is activated by the magnitude of the scalar gradient, these saddle points (and their neighborhoods) are therefore in the perturbative regime, which leads to a possible breakdown of the screening (Fig. 3.5). This, in turn, suggests that saddle points and their vicinities may be useful testing grounds for theories with screening mechanisms. This was recognized for MOND [220], and it was even suggested that LISA Pathfinder could be used to probe the MOND interpolating function if directed towards the saddle point of the solar system [229].

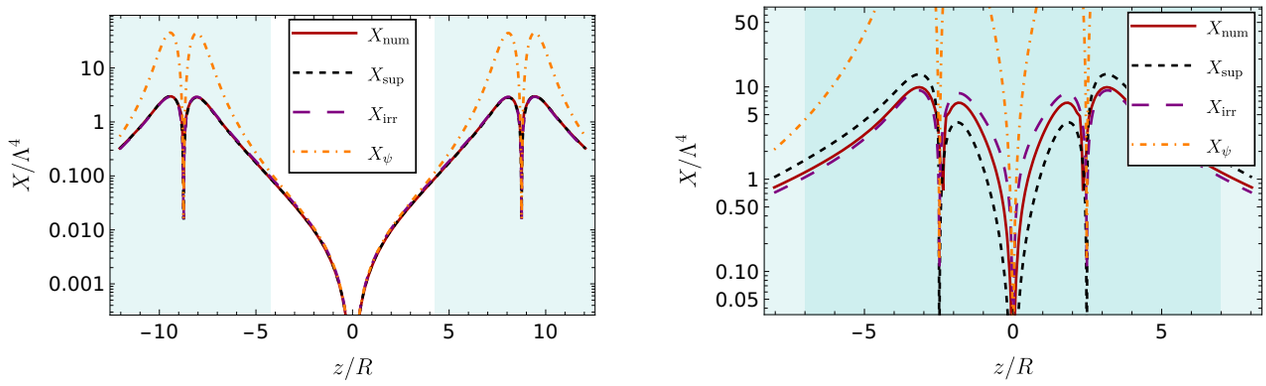

Figure 3.4: Scalar kinetic energy on the plane $\rho = 0$ for quadratic k-essence, calculated from our numerical results ($X_{\rm num}$, red solid line), with the linear superposition approximation ($X_{\rm sup}$, black dashed line), and with the irrotational approximation ($X_{\rm irr}$, purple long-dashed line). Also shown for comparison is the FJBD result (X_ψ, orange dot-dashed line). Two equal-mass ($q = 1$) binary systems are considered: $r_{\rm sc} = 4.5R$, $D = 17.5R$ (left) and $r_{\rm sc} = 9.5R$, $D = 5R$ (right), with the origin placed at the geometric center. The cyan shaded areas represent the individual screening regions of each body in isolation (ignoring the descreening in the vicinity of the object's center), and the darker shade in the right panel denotes the overlap of these individual screening regions.

Following Ref. [220], let us then consider a region where the theory dynamics is in the linear regime near the saddle point. Therefore, we can use the superposition of the FJBD scalar gradients (along the axis that connects the two bodies) to compute fifth force (per unit mass) as (restoring physical units)

$$(\boldsymbol{\nabla}\psi)_z = \frac{\alpha}{4\pi M_{\rm Pl}}\frac{m}{(z+D/2)^2} - \frac{\alpha}{4\pi M_{\rm Pl}}\frac{mq^{-1}}{(z-D/2)^2}\,, \tag{3.58}$$

The (saddle) point where the total scalar gradient is zero is given by

$$z_{\rm SP} = \frac{D}{2}\frac{\sqrt{q}-1}{\sqrt{q}+1}\,. \tag{3.59}$$

Taylor-expanding the scalar gradient around this saddle point, we find the force in its vicinity[8] to be

$$\boldsymbol{\nabla}\psi_{\rm SP} \approx A\left((z-z_{\rm SP})\hat{\boldsymbol{z}} - \frac{1}{2}\rho\hat{\boldsymbol{\rho}}\right)\,, \tag{3.60}$$

$$A \equiv -\frac{\alpha}{2\pi M_{\rm Pl}}\frac{mq^{-3/2}}{D^3}(1+\sqrt{q})^4\,. \tag{3.61}$$

The condition $|\boldsymbol{\nabla}\psi_{\rm SP}| = \sqrt{X_\psi}|_{\rm SP} \lesssim \Lambda^2$ then defines the region where the screening may

[8]One can further verify that the Hessian matrix is indefinite and thus $(0, z_{\rm SP})$ is indeed a saddle point. For a general discussion see Ref. [230] (we thank Áron Kovács for pointing out this reference).

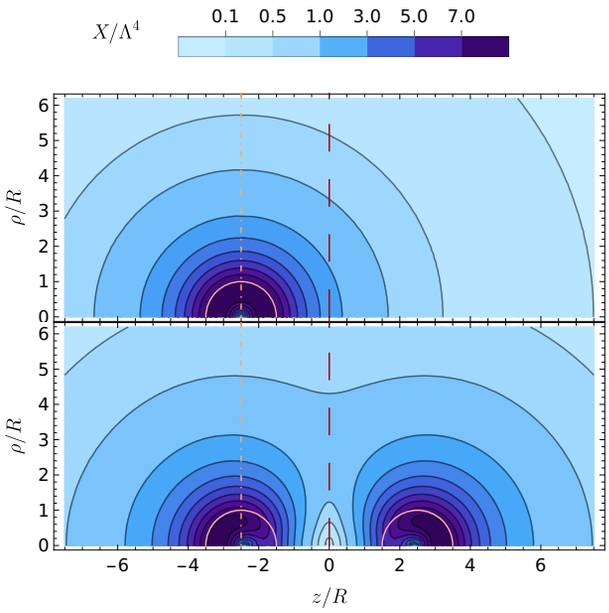

Figure 3.5: Contour plot of the scalar kinetic energy X in the (ρ, z) place. The bottom panel is for an equal-mass binary with $r_{\rm sc} = 9.5R$ and $D = 5R$. The top panel is for just one of the two bodies. The pink semicircles denote the effective radii of the Gaussian source model for the point particles. The orange dot-dashed line connects the geometric center of the left object in the two subplots, while the red dashed line connects the origins (which are placed at the center of mass of the binary).

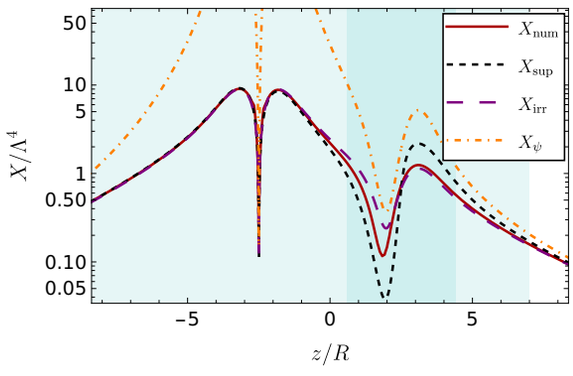

Figure 3.6: The same as in Fig. 3.4 (right), but for $q = 25$. The two bodies are placed at $z = \pm 2.5R$.

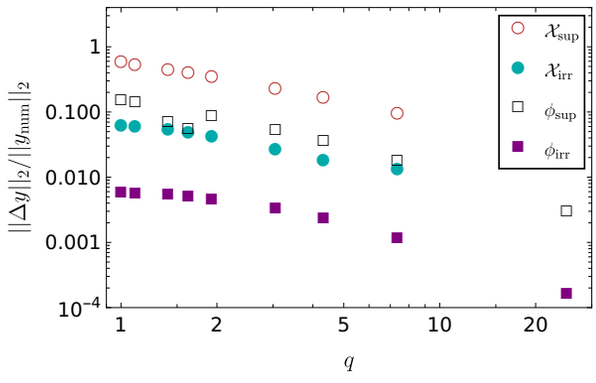

Figure 3.7: Relative difference of the linear superposition and irrotational approximations from the numerical results, in terms of the L^2 norm defined in the text and as a function of the mass ratio q. The differences are shown for the scalar field ϕ and ist kinetic energy X, in the deep screening regime. The system considered is an $r_{\rm sc} = 9.5R$ and $D = 5R$.

break down. From this condition, one obtains that the size δ of this region is given by

$$\frac{\delta}{D} \simeq \frac{1}{\kappa} \frac{q^{3/2}}{(1+\sqrt{q})^4} \,, \tag{3.62}$$

i.e. this region shrinks in both the deep screening regime ($\kappa \gg 1$) and in the extreme mass ratio limit ($q \to \infty$).

Although both the GR Newtonian force and the scalar fifth force go to zero precisely at the saddle point, in their vicinity they are both non-vanishing, with their precise ratio depending on the value of α. Note that constraints on the time-variation of the effective gravitational constant (in the Jordan frame) from Big Bang nucleosynthesis and Lunar Laser Ranging experiments require $\alpha \lesssim 0.1$ [231]. Considering three representative binary systems, i.e. Earth and Moon, Sun and Earth, and Sun and Jupiter, taking $\Lambda \approx 2 \times 10^{-3}$eV and $\alpha = 0.1$, we obtain $\delta \approx 0.2$km, $\delta \approx 1$km and $\delta \approx 2800$km, respectively. As $\delta \propto \alpha^{-2}$, by reducing α the size of the "descreening" region grows, but the correction to the GR Newtonian force from the fifth force decreases by the same amount.

Precise modeling of the dynamics near the saddle point of the solar system is challenging, as it would require accurate ephemeris data [232, 52] and even account for the effect of the spacecraft carrying the accelerometer itself. While this is outside the scope of this work, let us comment on a few parallels with MOND, where these problems have been analyzed to some extent [220, 229]. First, note that if we had used $\alpha = 1$ in our estimates for δ for the Earth and Moon, Sun and Earth, and Sun and Jupiter systems, they would have differed only by a factor $\sim$ a few from the estimate for MOND in Ref. [220]. The reason is that the scale of the MOND critical acceleration is $a_o \approx H_0/6$, thus leading to the same parametric scaling as the cosmologically motivated k-essence. In more detail, the MONDian behavior is triggered by the condition $a_0 \simeq a_{\rm N}$ [where $a_{\rm N} \simeq m/(D^2 M_{\rm Pl}^2)$], which is equivalent to the k-essence $\partial_r \psi \simeq \Lambda^2$ deep screening condition.

Note that although MOND is not a well-defined theory by itself, several attempts have been directed at constructing a field theory that can develop a MONDian phenomenology [107], including hybrid models such as superfluid DM [117]. Implementations that are of $K(X)$ type combine both screening around matter sources and anti-screening (i.e. enhancement of the scalar gradient, see Sec. 3.4.3) in the low-acceleration regime. Thus, MOND saddle point regions can be larger than the simple estimate given above, and the fifth force may even dominate the Newtonian force inside them [220]. This makes saddle points a potentially better probe of MOND than k-essence (although not all MOND interpolating functions can be further constrained in this way [233]).

3.3.4 Two-body energy and the fifth force

In a time-independent system such as the one that we consider, the Hamiltonian (density) is given by $\mathcal{H} = -\mathcal{L}$, where the Lagrangian (density) $\mathcal{L}$ is obtained from Eq. (2.15) [specializing to Minkowski space]. From this, one can find the potential energy $E = \int dV\mathcal{H}$ as a function of the system's parameters and the inter-particle separation (see Sec. 3.3.1). From the energy, the magnitude of the fifth force between the two particles can then be found as

$$F = \frac{\partial E}{\partial D}\,. \tag{3.63}$$

Let us consider the polynomial kinetic function of Eq. (3.32), which yields

$$E = -\int dV\Big[-\Lambda^4\sum_{n=1}^{N}\frac{1}{2n}\left(\frac{X}{\Lambda^4}\right)^n + \frac{\alpha}{M_{\rm Pl}}\varphi T\Big]\,. \tag{3.64}$$

Using the equation of motion (3.37), we can rewrite this integral as

$$\mathcal{E} \equiv \frac{E}{D^3\Lambda^4} = -\int d\mathsf{V}\sum_{n=1}^{N}\Big(\frac{2n-1}{2n}\Big)\mathcal{X}^n\,, \tag{3.65}$$

where we have also used the rescaling of Eq. (3.35). Noting that in the deep screening regime the highest power of $\mathcal{X}$ dominates the integral and using the irrotational approximation, one can apply Eq. (3.52) and obtain that the energy $\mathcal{E}_{\rm sc}$ of the screened regions (sc) is given by

$$\mathcal{E}_{\rm sc} \approx -\kappa^{\frac{2N}{2N-1}}\Big(\frac{2N-1}{2N}\Big)\int_{\rm sc} d\mathsf{V}\hat{\mathcal{X}}_\Psi^{N/(2N-1)}\,. \tag{3.66}$$

The total energy is then obtained by adding the subdominant term $\approx -\int_{\rm un-sc} d\mathsf{V}\mathcal{X}_\Psi/2$ that corresponds to the 'unscreened' region $\mathrm{un}-\mathrm{sc}$. [Note indeed that the integral in Eq. (3.66) diverges in the unscreened region]. One can observe that for $N = 1$, we recover the FJBD scaling $E \propto D^{-1}$, while for $N = 2$ we obtain $E \propto D^{1/3}$, as expected on dimensional grounds and from the single particle limit. Note also that in contrast to the Newtonian/FJBD case, the scalar self-energy does not diverge in the point-particle limit thanks to the screening. From the scaling of the source of the solenoidal component [Eq. (3.53)], we find that $\mathcal{B} \propto \kappa$ when $\kappa \gg 1$. Thus, including the solenoidal component in Eq. (3.65) does not change the overall scaling of the energy with κ in the deep screening regime, as given by Eq. (3.66).

The amplitude of the fifth force [from Eqs. (3.63) and (3.66)] is then given by

$$\begin{aligned} \mathcal{F}_{\rm sc} &\equiv \frac{F_{\rm sc}}{D^2\Lambda^4} \approx -\kappa^{\frac{2N}{2N-1}} I_N(q)\,, \\ I_N(q) &\equiv \frac{1}{2}\int_{\rm sc} d\mathcal{N}\hat{\mathcal{X}}_\Psi^{(1-N)/(2N-1)}\partial_{\mathsf{D}}\hat{\mathcal{X}}_\Psi\big|_{\mathsf{D}=1}\,. \end{aligned} \tag{3.67}$$

This indicates a clear suppression when $N > 1$ in comparison to the FJBD limit $N = 1$. For instance, for $N = 1$ one has $F_{\rm sc} \propto D^{-2}$ (Newton's law), while for $N = 2$ one ontains $F_{\rm sc} \propto D^{-2/3}$. Unlike the energy, the fifth force diverges in the limit $D \to 0$. However, this is simply an artifact of the point-particle model, i.e. it disappears for extended sources (see e.g. Ref. [198] and the discussion in our Sec. 3.2.3, App. A.2). The details of the calculation of $I_N(q)$ are presented in App. A.2.1.

In order to verify the internal consistency of our irrotational approximation (in both the deep screening and FJBD regimes), we have calculated the fifth force [from Eqs. (3.63) and (3.65)] semi-analytically in quadratic k-essence (see App. A.2.1 for details). In Fig. 3.8, we show how the magnitude of the fifth force depends on the mass ratio and on the inter-particle separation in units of the object's radius (although we stress that our results do not depend on the details of the object's internal structure, as long as one focuses on the object's exterior). For $q = 1$, we also show, for comparison, the FJBD limit F_ψ and the deep screening limit given by Eq. (3.67) (which suppresses the fifth force relative to FJBD theory). As can be seen, the change between the two regimes is abrupt, for all mass ratios, and the two approximations provide a very good description of the scaling of the fifth force with distance in a piecewise fashion.

Having established that the deep screening limit of Eq. (3.67) is valid in the context of the irrotational approximation, we can compare that limit with the full numerical result of Ref. [204] for quadratic k-essence. Let us define the force in the test-mass limit by performing the standard Newtonian reformulation of a two body problem into the motion of a fictitious particle with the reduced mass $\mu = m_a m_b/(m_a + m_b)$ around a particle with the total mass $m_a + m_b$ (see e.g. Ref. [54]). The amplitude of the force is then given by $F_{\rm tm} = (\alpha/M_{\rm Pl})\mu\,\partial_r\varphi|_{r=a}$. Thus, from Eq. (3.33) [and using the rescaling of Eq. (3.35)] we obtain

$$\frac{\mathcal{F}_{\rm tm}}{4\pi} = \left[\frac{\kappa^4}{q(q+1)^2}\right]^{1/3}\,. \tag{3.68}$$

From the irrotational approximation, it follows that the force in the deep screening regime [Eq. (3.67)] has the same scaling with κ as the test-mass limit (and the solenoidal component does not change this scaling, as argued above). Therefore, the ratio of $F_{\rm sc}$ and $F_{\rm tm}$ depends only on the mass ratio q. The same conclusion was reached in Ref. [204]

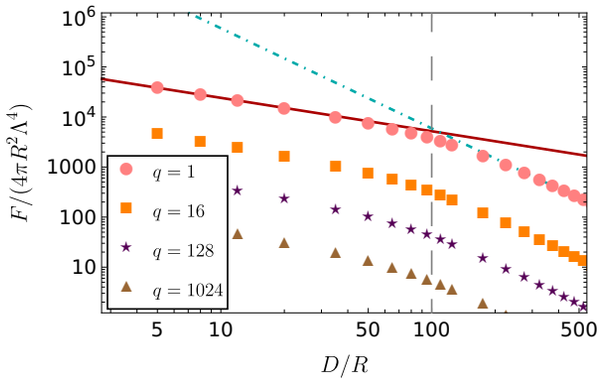

Figure 3.8: Fifth force F for four values of the mass ratio q, calculated using the irrotational approximation and various values of D/R, for fixed $r_{\rm sc}/R = 100$ (denoted by the gray dashed line). For $q = 1$, we also show the FJBD limit [Eq. (A.5), cyan dot-dashed line] as well as the deep screening approximation [Eq. (3.67), solid red line].

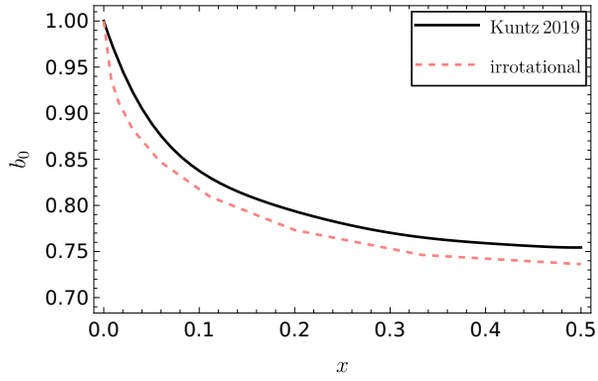

Figure 3.9: Ratio of the fifth force amplitudes between the two point particles and in the test-mass limit, in quadratic k-essence, calculated from the numerical simulation of Ref. [204] (black) and using the irrotational approximation in the deep screening regime (pink, dashed).

using an effective-one-body approach. Following Ref. [204], let us define

$$F_{\rm sc} = b_0(x) F_{\rm tm}\,, \quad x = \frac{1}{1+q}\,, \tag{3.69}$$

where we expect that $\lim_{x\to 0} b_0 \to 1$. We have found $b_0(x)$ [from $I_2(q)$] semi-analytically, and we have compared it with the fit of the full numerical result from Ref. [204] (Eq. 46) in Fig. 3.9. As can be seen, this comparison confirms the observation from Ref. [204] that the screening is more efficient in equal-mass systems than in the extreme-mass ratio limit. (This implies a breakdown of the weak equivalence principle, as further elaborated in Ref. [204]). Note that the relative enhancement of the screening relative to the extreme mass-ratio limit is at most $\sim 25\%$. Also note that our findinds confirm that the irrotational approximation is in good agreement with the full numerical results, differing only by a few percent from the latter.

Finally, let us emphasize that the breakdown of screening in the descreened bubbles (see Sec. 3.3.3) is a *local* phenomenon, which can be probed with a third test body. Descreened bubbles can in principle affect the two-body energy and the fifth force, since the latter are expressed as integrals over all space. For a given κ, Eq. (3.62) predicts that the largest descreened bubbles appear for $q \approx 9$. However, as clear from Fig. 3.9, in the deep screening regime this does not significantly impair the efficiency of the screening mechanism.

3.4 Other theories

Thus far, we have focused on the polynomial form of the k-essence kinetic functon, given by Eq. (3.32). Let us now broaden the scope of the possible kinetic functions, and investigate again the non-relativistic limit for single bodies and for binary systems. We will employ the same notation as in the previous sections. Note that while in polynomial k-essence a generic astrophysical system is in the regime of validity of the EFT when the screening operates, this may not be the case for some theories considered in this section, and in particular opposite DBI and anti-screening theories (see App. A.1).

3.4.1 Beyond (simple) polynomial k-essence

One may wonder how values of the polynomial coefficients different from those in Eq. (3.32) impact our previous discussion and results. Since the highest power of X dominates upon the others in the deep screening regime, our results should be qualitatively unchanged (as long as the coefficient of the highest power of X has the sign leading to screening in the first place). We have performed simple numerical experiments to check this, e.g. we have considered a sextic polynomial $\mathcal{K}_6 = -\mathcal{X}/2 + c_2\mathcal{X}^2 + c_4\mathcal{X}^4 - \mathcal{X}^6/12$, with randomly generated values of the coefficients $\{c_2, c_4\}$ in the interval $-5 \leq c_i \leq 5$ but requiring that the condition of Eq. (3.15) is satisfied. We have calculated the suppression factor $\mathcal{X}/\mathcal{X}_\psi$ for the isolated Gaussian source as in Sec. 3.2.3 for several such realizations. Comparing with our default model $\mathcal{K}_6 = -\mathcal{X}/2 - \mathcal{X}^6/12$, we have found that outside the object but within the screening region, the suppression factor varies by at most a few percent. The differences between the various realizations peak around the screening radius, where they reach $\sim 10\%$, as this is the transition region where the effect of the subleading terms $\mathcal{X}^2, \mathcal{X}^4$ is maximized. The relative difference is further suppressed outside the screening region, when the FJBD limit is asymptotically approached. We expect this conclusion to hold also for the two-body problem.

If one relaxes the assumption of a polynomial kinetic function, one can also engineer particular functions passing different cosmological and solar system constraints while still providing a viable scalar-tensor theory of gravity [40, 231]. One such model was considered in Ref. [231] and is given by

$$\mathcal{K}_{\tan^{-1}} = -1 - \frac{\mathcal{X}}{2} - \mathcal{K}_\star \left[\mathcal{X} - \mathcal{X}_\star \arctan\left(\frac{\mathcal{X}}{\mathcal{X}_\star}\right)\right] , \tag{3.70}$$

where $\{\mathcal{X}_\star, \mathcal{K}_\star\}$ are free parameters of the model. Note that $\mathcal{K}'(\mathcal{X}) \to \mathcal{K}_\star$ as $\mathcal{X} \to \infty$ (see Ref. [23] for the quantum aspects of this model). In the irrotational approximation, one cannot invert Eq. (3.15) exactly, although in the deep screening regime the relation is approximately linear, $\mathcal{X} \approx \mathcal{X}_\Psi/(1+\mathcal{K}_\star)^2$, and the suppression of the fifth force is realized

through a large value for $\mathcal{K}_\star$. We show a numerical solution $\mathcal{X}(\mathcal{X}_\Psi)$ for $\mathcal{X}_\star = -2$, $\mathcal{K}_\star = 10^3$ (model I from Ref. [231]) in Fig. 3.10.

In the context of the two-body problem, let us assess the importance of the solenoidal component using the arguments of Sec. 3.3.1. The quantity that characterizes the non-linearities, i.e. $\mathcal{N}_K$ [Eq. (3.50)], is given in the deep screening regime by

$$\mathcal{N}_K \approx \kappa^{-3}\mathcal{K}_\star(1+\mathcal{K}_\star)^3\mathcal{X}_\star^2\frac{|\boldsymbol{\nabla}\hat{\mathcal{X}}_\Psi|}{\hat{\mathcal{X}}_\Psi^{5/2}}\,. \tag{3.71}$$

As the screening arises in this model from a large factor $\mathcal{K}_\star$, the relative strength of the solenoidal and irrotational components is controlled by $(\mathcal{K}_\star/\kappa)^4$ [we remind the reader that $S_\Psi \propto \kappa$, see Eq. (3.48)]. This scaling makes the solenoidal component much more suppressed than in the case of a polynomial kinetic function, for the parameter values considered in Ref. [231].

3.4.2 "Opposite" DBI

Let us consider a class of models where the scalar gradient $\mathcal{X}$ saturates in the strongly interacting regime. A particularly interesting model is the (opposite) DBI one [234, 207, 22]

$$\mathcal{K}_{\rm DBI} = \sqrt{1-\mathcal{X}/2}\,. \tag{3.72}$$

Standard DBI theory (obtained by flipping the overall sign of the Lagrangian and the sign in front of $\mathcal{X}$) can be embedded in string theory, but does not allow for screening [193, 40]. However, the "opposite DBI" kinetic function in Eq. (3.72) may appear naturally in higher dimensions and possesses a higher symmetry group than the standard shift-symmetric $K(X)$ theory analyzed thus far [22, 207].

Like in the case of quadratic k-essence, the solution for a single point-particle source can be expressed in terms of the hypergeometric function:

$$\phi \;=\; 1.85\mathsf{r}_{\rm sc} - \mathsf{r}\;{}_2F_1\Big[\frac{1}{4},\frac{1}{2};\frac{5}{4};-\Big(\frac{\mathsf{r}}{\mathsf{r}_{\rm sc}}\Big)^4\Big]\,. \tag{3.73}$$

This exact solution features a screening radius $\mathsf{r}_{\rm sc} = \sqrt{\kappa}$. Like in Sec. 3.2.3, we show the scalar gradient for an isolated Gaussian source and for a point particle in Fig. 3.11. In contrast with the polynomial k-essence, now even in the point-particle case the scalar gradient does not diverge at the particle's location, and the point-particle and Gaussian models are much closer even inside the source, down to very small radii. We also find that the screening in opposite DBI is more efficient than in quadratic k-essence (see Figs. 3.1 and 3.11, and also Fig. 3.10).

Away from spherical symmetry (or other highly symmetric configurations), the solenoidal

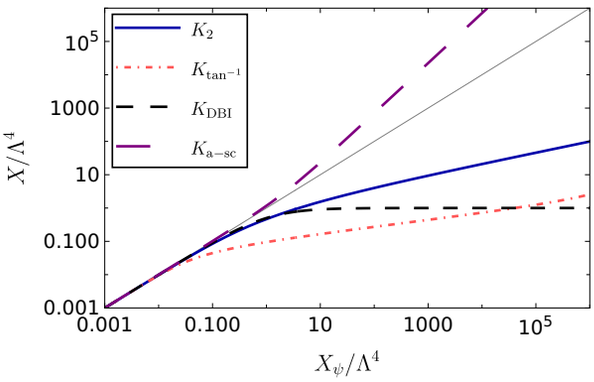

Figure 3.10: Relation between the kinetic energy X and the FJBD kinetic energy X_ψ in the irrotational approximation, for several choices of the kinetic function. The latter include quadratic k-essence K_2 [Eq. (3.26)]; the arctan model $K_{\tan^{-1}}$ [Eq. (3.70); $\mathcal{X}_\star = -2$, $\mathcal{K}_\star = 10^3$]; opposite DBI theory $K_{\rm DBI}$ [Eq. (3.72)]; and the anti-screening model $K_{\rm a-sc}$ [Eq. (3.76); $p = 5/6$]. The thin solid line corresponds to $X = X_\psi$.

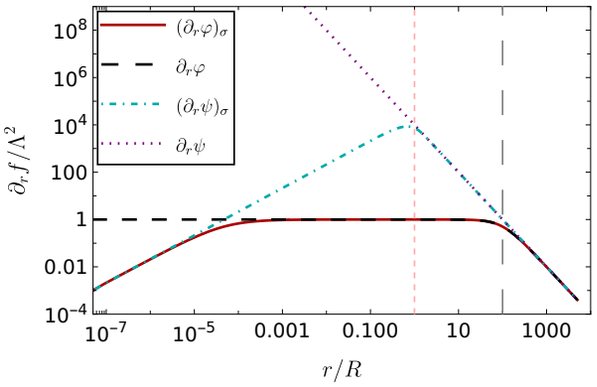

Figure 3.11: The same as in Fig. 3.1, but for (opposite) DBI theory.

component is in general not zero in opposite DBI, unlike what was implicitly assumed in Ref. [207]. However, we can consider the irrotational approximation described in Sec. 3.3.1 (see Fig. 3.10) and obtain

$$\mathcal{X} = \frac{\mathcal{X}_\Psi}{1 + \mathcal{X}_\Psi} \,. \tag{3.74}$$

We can then calculate the source of the solenoidal field that encodes non-linearities in the two-body problem [see Eq. (3.50)], obtaining

$$\mathcal{N}_K \approx \frac{1}{4}\sqrt{\mathcal{X}(1-\mathcal{X})} \,. \tag{3.75}$$

One can see that as X flattens in the deep screening regime, $\mathcal{N}_K \to 0$. Thus, the solenoidal component in opposite DBI is even more suppressed than for a polynomial kinetic function.

3.4.3 Anti-screening

As noted in Sec. 3.1, a drawback of generic k-essence models is the absence of a standard UV completion [61, 62]. Thus, in Ref. [196] a class of shift-symmetric theories that do not violate positivity bounds[9] and which are thus expected to admit such a completion were

[9]These models were unfortunately advertized in Ref. [196] as causal modifications of gravity, as opposed to superluminal models that allow for screening. However, as elaborated in Sec. 3.1, causality is not an issue in superluminal k-essence theories [36, 38, 39, 40, 41, 44].

considered. Those are described by

$$\mathcal{K}_{\rm a-sc} = -\frac{1}{p}\left[(1+\mathcal{X}/2)^p - 1\right] , \tag{3.76}$$

where $1/2 \leq p < 1$ ($p = 1/2$ corresponding to the standard DBI theory, see Ref. [40], while $p = 1$ yields FJBD theory). These theories, however, lead to *anti-screening* i.e. an enhancement of the fifth force near matter sources (see Fig. 3.10). These theories, like FJBD theory, are then only relevant if the coupling of the scalar to matter satisfies the Cassini bound. The anti-screening phenomenon could then provide additional constraints in the solar system and in the strong gravity regime [196].

The Helmholtz decomposition and the arguments of Sec. 3.2.2, 3.3.1 can also be applied to theories with anti-screening. In particular, in spherical symmetry the solenoidal component is zero, and $\mathcal{X}(\mathcal{X}_\Psi)$ can be found from Eq. (3.20) (see Fig. 3.10). Away from spherical symmetry, from Eq. (3.50) one finds (e.g. for the special case $p = 5/6$)

$$\mathcal{N}_K \approx \frac{\kappa}{8}\frac{|\boldsymbol{\nabla}\hat{\mathcal{X}}_\psi|}{\sqrt{\hat{\mathcal{X}}_\Psi}} , \tag{3.77}$$

i.e. the same as in Eq. (3.53) for $N = 5/6$. Therefore, the details of the anti-screening model are captured in a dimensionless prefactor, and the dependence on κ and q is the same as in polynomial k-essence (see Fig. 3.3).

3.5 Conclusions

We have shown that shift-symmetric scalar-tensor theories, involving only first derivatives in scalars, can be reformulated by covariantly splitting the scalar gradient into a longitudinal $\partial_\mu\psi$ and a transverse component B_μ (Hodge-Helmholtz decomposition; Sec. 3.2.1). The longitudinal component reduces to a (free) Klein-Gordon field, while the transverse component obeys a hyperbolic equation with a non-linear source. We have shown that for spherical and static sources, the transverse component identically vanishes (Sec. 3.2.2, 3.2.3). In this situation, the problem reduces to solving a linear elliptic equation and then an algebraic one.

In general, and also in the case of two-body non-relativistic systems that we consider in this Ch., the solenoidal component does not vanish (unlike what was implicitly assumed e.g. in Refs. [213, 207]). Outside the screening region of a two-body system (which is controlled by the ratio between the screening radius of the more massive objects $r_{\rm sc}$ and the inter-particle separation D, as well as by the mass ratio q), the solenoidal component is perturbativly suppressed and the superposition approximation provides a good description of the full results (see Sec. 3.3.1 and 3.3.2). Inside the screening region, we have developed

an approximate 'irrotational' scheme that starts by ignoring the solenoidal component and finds the scalar gradients X by solving an algebraic problem. This approach was validated by checking self-consistency (Sec. 3.3.1), by solving the full system numerically (Sec. 3.3.2) and by comparing with the previous results of Ref. [204] (Sec. 3.3.4). We have shown in Sec. 3.3.1 that irrespective of the form of the kinetic function, the irrotational field dominates upon the solenoidal one when $D \gg r_{\rm sc}$ and/or $q \gg 1$. In these regimes, ignoring the solenoidal component will introduce only small errors in the description of the scalar gradients. Furthermore, we have shown that even when $r_{\rm sc} \gg D$ and $q \approx 1$, the irrotational approximation will introduce only percent-level errors in the binary fifth force, in comparison with the full numerical results for quadratic k-essence (Sec. 3.3.4). Kinetic functions whose growth is suppressed in the deep screening regime will have even more suppressed solenoidal components (Sec. 3.4.1, 3.4.2). The irrotational approximation can also be applied for theories that exhibit anti-screening (Sec. 3.4.3).

At the physical level, our results, both analytic and numerical, show that the absence of spherical symmetry in a binary system does not make screening necessarily inefficient. On the one hand, the non-linear nature of k-essence generally renders screening slightly *more efficient*, relative to the test-body limit, in equal-mass systems (Sec. 3.3.4). This has already been established numerically, and its consequences on violations of the weak equivalence principle elaborated, in Ref. [204]. However, we show that binaries also produce "descreened" regions near the system's saddle point (Sec. 3.3.3). These regions may in principle be probed in the solar system with sufficiently precise accelerometers. A natural continuation of this work would be to assess the validity of the irrotational approximation in N-body systems. In relation to k-essence probes in the solar system (e.g. with these descreened regions), such an irrotational approach could alleviate the numerical difficulty and cost of full multi-body simulations (for a related numerical study of the Sun-Earth-Moon system in the cubic Galileon theory, see Ref. [205]).

As the Hodge-Helmholtz decomposition can be implemented in a covariant way, it is an interesting question to consider whether it can be helpful in dynamical problems. For instance, stellar collapse in k-essence leads to a breakdown of screening [58]. Indeed, due to black-hole no-hair theorems [235, 236, 237, 238, 239], the star's scalar "charge" must be radiated away [58], producing a potentially observable gravitational-wave signal. Another interesting problem is a binary neutron star's inspiral. In scalar-tensor theories, the orbital energy of a binary decreases because of the emission of both scalar and tensor gravitons. In FJBD, and related perturbative theories where the screening does not operate, the binary inspiral can be systematically studied within the PN formalism [240, 241, 242, 243, 244, 54]. However, in theories with screening, such an approach is not straightforward. Thus far, in theories with strong non-linearities the inspiral has been studied by perturbing the scalar field around the background field generated by a fictitious isolated body located at the

center of mass of the system [245, 200, 196]. On the other hand, numerical simulations have been performed in cubic k-essence (including GR), scanning the $r_{\rm sc}/D \approx 1-6$ range [55]. Both of these problems may benefit from (a more systematic) analytic approach based on the Hodge-Helmholtz decomposition.

Part III

Soliton boson stars as compact objects

Chapter 4

Soliton boson stars, Q-balls and the causal Buchdahl bound

4.1 Introduction

In this Ch., we focus on self-gravitating objects made from complex scalars (gravitating Q-balls/soliton boson stars), introduced in Ch. 2 and their structural properties. Besides the rich literature on Q-balls (starting from the seminal paper by Coleman [168]; see also [246] for a recent review), the structure of relativistic SBSs has been investigated for the simplest potential [167, 247, 248, 155, 163],

$$V = \mu^2|\Phi|^2\Big(1 - 2\frac{|\Phi|^2}{\sigma_0^2}\Big)^2, \tag{4.1}$$

for more general sextic potentials [249, 250, 163] and for related potentials, such as the cosine one [251, 163]. Quasi-normal modes and geodesics around SBSs have also been studied [248], their Love numbers have been calculated [150, 252], and they have been simulated in binary systems [155, 253, 166, 254, 255, 2].

The relation between Q-balls and SBSs has been at least partially discussed previously [256, 257, 258, 259] and the most dramatic effects of gravity are non-perturbative in $\sigma_0/M_{\rm Pl}$. In this regime, as $M_{\rm Pl} < \infty$, Q-ball limit is not realized. However, there is no major qualitative difference between Q-balls and SBSs in the part of the parameter space where the effects of gravity are not important and perturbative. For clarity, in the rest of the Ch. we will refer to the $M_{\rm Pl} \to \infty$ limit as Q-balls and to the gravitating case as SBSs.

Notwithstanding all these studies, to the best of our knowledge some basic aspects of SBSs and non-topological solitons that admit degenerate vacua in general have not been appropriately addressed in the literature. In this work we aim to fill this gap by constructing analytic descriptions of SBSs for the simplest potential (4.1) in the sub-Planck limit $\sigma_0/M_{\rm Pl} \ll 1$, by understanding the physics that sets the maximal compactness of

these objects, and by illuminating the non-trivial connection with the Q-ball limit. We will establish the robustness and the limits of this picture by exploring the parameter space in $\sigma_0/M_{\rm Pl}$, and also by considering cosine, sextic and quartic potentials. We will show that diverse choices of the potential do not correspond to dramatically distinct macroscopic behaviours of SBSs, and that the structure of SBSs mostly depends on the distance between the central field and the scalar false vacuum, and on whether the false vacuum is sufficiently deep.

This Ch. is organized as follows. In Sec. 4.2 we will provide a brief review of Q-balls, upon which we build up description of SBS structure and properties in Sec. 4.3. In Sec. 4.4 we will explore the parameter space of these objects and the effect of the scalar potential on their structure. The technical details of our numerical methods are presented in App. B.1, while in App. B.2 we discuss various definitions of the SBS radii and in App. B.3 we provide some additional details on the analytic construction of SBSs.

4.2 Q-balls: a review

The Lagrangian of a scalar field with $U(1)$ symmetry in flat space-time is given by

$$\mathcal{L}_\Phi = -\partial_\mu \Phi^\dagger \partial^\mu \Phi - V(|\Phi|)\,. \tag{4.2}$$

The scalar field can be decomposed in Fourier modes as

$$\Phi = \phi(r) e^{-i\omega t}\,, \tag{4.3}$$

with time translations corresponding to a change in phase. Because of the $U(1)$ symmetry, and as long as only one Fourier mode is excited, this superficial time dependence does not propagate to any observable quantity, such as thermodynamics parameters: the density $\rho = -T^t_t$, the radial pressure $P_{\rm rad} = T^r_r$ etc., and Derrick's theorem is circumvented.

Varying the action (4.2) with respect to ϕ, one obtains the Klein-Gordon equation

$$\phi'' + \frac{2}{r}\phi' = -\frac{dU_\omega}{d\phi}\,, \tag{4.4}$$

$$U_\omega = \frac{1}{2}(\omega^2\phi^2 - V(\phi))\,. \tag{4.5}$$

Note that this equation can be interpreted as the equation of motion of a Newtonian particle under a friction term and an effective potential U_ω. The energy of the Newtonian particle is

$$\mathcal{E} = \frac{1}{2}(\phi')^2 + U_\omega\,, \tag{4.6}$$

and it is conserved only in $D = 1$ dimensions, when the friction is absent.

In order for the field energy (i.e. the integrated energy density) $E = \int dV\rho$ to be finite, one must have $\phi(r \to \infty) \to 0$, which implies that the Q-ball is a localized object. Let us assume that at infinity the scalar is free, with leading mass term in the potential $V = \frac{1}{2}\mu^2\phi^2 + \mathcal{O}(\phi^4)$. As $U_\omega \sim (\omega^2 - \mu^2)\phi^2\,,\ \phi \to 0$, we require $\omega < \mu$ for the scalar to converge to the vacuum state at infinity. The leading order behaviour is of the form $\phi \sim \exp\left(-\sqrt{\mu^2 - \omega^2}r\right)$, which implies zero "velocity" ϕ' at infinity and $\mathcal{E}(\infty) = 0$. The asymptotic Yukawa-like behaviour implies that the Q-ball radius is ill defined. We follow the common practice (e.g. [248]) and arbitrarily define the radius as that enclosing 99% of the total mass R_{99}. (Note however that different conventions and definitions can be found in the literature, see App. B.2).

At the initial point (in the particle perspective), in order for the friction to be overcome one must have $\phi'(r \to 0) \propto r^{1+\epsilon}\,, \epsilon > 0$ i.e. $\phi'(0) = 0$. As $U_\omega(0) = 0$, the particle needs to be released at some point $\phi_c | U_\omega(\phi_c) > 0\,, U'_\omega(\phi_c) > 0$ in order to overcome the friction and arrive at infinity with finite energy. The last condition implies that U_ω must admit an additional hill, or more formally there must be a non-trivial minimum of V/ϕ^2 at some point $\phi_0 \neq 0$ and $\omega \geq \omega_0 \equiv \min[V/\phi^2]$ [168]. The simplest potential is thus of the form

$$V = \mu^2|\Phi|^2\Big(1 - 2\frac{|\Phi|^2}{\sigma_0^2}\Big)^2\,, \tag{4.7}$$

with $\phi_0 = \sigma_0/\sqrt{2}$. A theory with this potential is non-renormalizable, and thus must interpreted in the context of effective or thermal field theories[1].

A sketch of the corresponding U_ω is shown in Fig. 4.1. In the limit $\omega = \omega_0$, the fictitious particle is at the second hill $\phi_c \to \phi_0$, and the scalar would need an infinite amount of time to travel to the first hill (trivial vacuum). This scenario, in the Q-ball perspective, corresponds to an infinitely large configuration. The impact of the friction in this case can be neglected, as it is proportional to $1/R \to 0$. For a small but non-zero value of ω , the traveling time/Q-ball radius becomes finite, but still large (thin-wall regime). In the opposite case when $\omega \to \mu$, the impact of friction is pronounced and the transition to the origin is smoother (thick-wall regime). The particle picture also demonstrates how one can construct these solutions numerically - through a shooting algorithm (see Sec. 4.3.2 and App. B.1 for the numerical formulation). If one releases the particle on the left of ϕ_c (e.g. somewhere around the valley for $\omega/\mu = 0.5$), it will not have enough energy to reach the first hill. However, releasing the particle sufficiently near the second hill will let it reach the trivial vacuum with an excess of energy. In this way, one can iteratively find the true solution.

[1]If one considers non-Abelian groups, instead, renormalizable potentials can also admit stable Q-balls [260].

From the invariance under internal $U(1)$ symmetry, the Noether current and charge can be found as

$$j^\mu = -i(\Phi^\dagger \partial^\mu \Phi - \Phi \partial^\mu \Phi^\dagger)\,, \tag{4.8}$$

$$Q \equiv -\int dV j^t = 4\pi\omega \int dr\, r^2 \phi^2\,. \tag{4.9}$$

In order for the Q-ball not to decay to constituent scalars, the energy per unit charge should be lower than the particle mass:

$$E < \mu Q\,. \tag{4.10}$$

In [168], Coleman proved the stability of Q-balls, under the above restrictions on the form of the potential in classical field theory (necessary condition) and the requirement (4.10) . Other aspects of stability are discussed in [261, 262].

To obtain a rough understanding of the Q-ball properties, let us consider the potential (4.1). When the central field is near the degenerate vacuum σ_0 (thin-wall regime), the main contribution to the mass of the object comes from the bulk $\sigma_0^2 R^3$ and the surface tension $\delta^{-1}\sigma_0^2 R^2$, where $\delta \sim \mu^{-1}$ is the size of the potential wall. In equilibrium one has [with $(\Phi \sim \sigma_0 \exp i\omega t)$]

$$R \sim \frac{\mu}{\omega^2}\,. \tag{4.11}$$

This rough argument provides the leading order behaviour of Q-balls in the thin-wall limit.

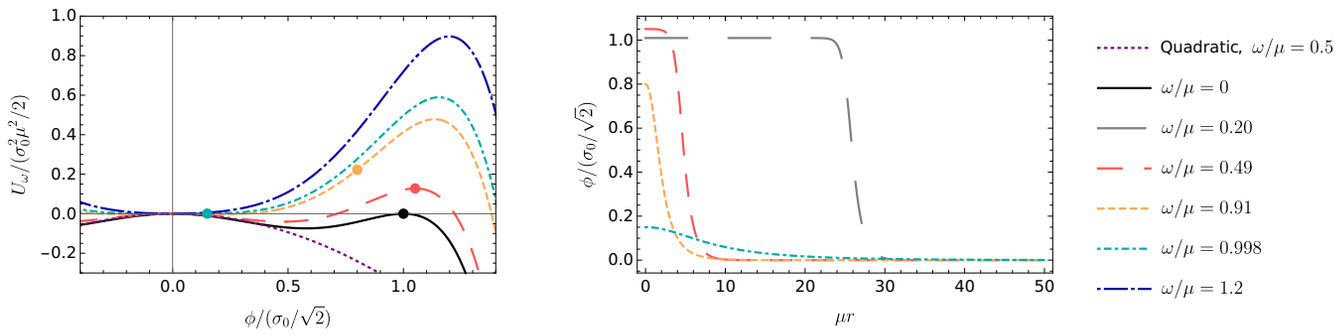

Figure 4.1: (Left) Effective particle potential U_ω for various values of the field frequency ω. The dots correspond to initial field values for physical configurations and all curves represent the potential (4.1), except for the purple one which represents the quadratic potential $V = \mu^2|\Phi|^2$ (that doesn't allow for solitonic solutions in flat space-time). (Right) Radial field profile (numerical results) for several physical configurations. Note that the $\omega/\mu = 0$ case corresponds to the infinitely large Q-ball with scalar $\phi = \sigma_0/\sqrt{2}$.

4.2.1 Simplest Q-ball potential: analytic description

We will now focus on the simplest potential with a global $U(1)$ symmetry and which admits stable Q-balls (4.1). For this potential, we can use the following scaling:

$$\mathsf{r} = \mu r\,, w = \frac{\omega}{\mu}\,, \varphi = \phi/(\sigma_0/\sqrt{2})\,, \tag{4.12}$$

which makes the equations of motion dimensionless.

In [263], analytic profiles for Q-balls have been constructed (building on [261, 264]) by matching solutions in three regimes – interior (perturbative solution around φ_c), boundary (expansion around the radius) and exterior (asymptotic). Here, we only mention these results, as we will partially review them (together with their curved space-time generalization) in the next section:

$$\varphi_< \approx \varphi_+\Big(1 - c_<\frac{\sinh(\alpha\mathsf{r})}{\mathsf{r}}\Big)\,, \tag{4.13}$$

$$\varphi_B \approx \varphi_+\frac{1}{\sqrt{1+2e^{2(\mathsf{r}-\mathsf{R}^*)}}}\,, \tag{4.14}$$

$$\varphi_> \approx \frac{\varphi_+ c_>}{\mathsf{r}}e^{-\sqrt{1-w^2}\mathsf{r}}\,, \tag{4.15}$$

where

$$\alpha^2 = \frac{4}{3}\big(1+3w^2+2\sqrt{1+3w^2}\big)\,, \quad \varphi_+^2 = \frac{1}{3}(2+\sqrt{1+3w^2})\,.$$

Here, φ_+ corresponds to the maximum of U_ω. For $w \ll 1$, the maximum of U_ω lies close to the degenerate vacuum $\varphi \approx 1$; $\mathsf{R}^* = \mu R^*$ is the inflection point of the field $\varphi''(\mathsf{R}^*) = 0$, taken as the estimate of the size of the Q-ball. We confirm the observation from [263] that the function (4.14) does a good job at describing the numerical profile of the Q-ball, even outside its range of validity, in contrast with the interior and asymptotic approximants, which only work sufficiently close/far to the centre, respectively.

By matching the fields (4.13)-(4.15) and their derivatives at $\{\mathsf{r}_<, \mathsf{r}_>\}$, one finds [263]:

$$c_< \approx \mathsf{R}^* e^{-2\mathsf{R}^*}\,, \quad c_> \approx \sqrt{2}\mathsf{R}^* e^{\mathsf{R}^*}\,. \tag{4.16}$$

However, this matching is not sufficient to close the system. One needs also the energy balance condition

$$\mathcal{E}(\infty) - \mathcal{E}(0) = -\int_0^\infty dr\big[\frac{2}{r}(\phi')^2\big]\,. \tag{4.17}$$

In summary, we have five equations in five unknowns $\{c_<, c_>, \mathsf{R}^*, \mathsf{r}_<, \mathsf{r}_>\}$ as functions of ω, or equivalently $\varphi_c(\omega) = \varphi_+(1-c_<)$. From Eq. (4.16) we see that in the thin-wall regime (large Q-balls), the deviation of the field from the central value in the interior zone is

exponentially suppressed. In the outer zone, the field itself is exponentially suppressed, and thus the integral on the right hand side of Eq. (4.17) is dominated by the boundary zone.

From invariance under time reversal, we expect R^* to be a Laurent polynomial in even powers of ω. From Eq. (4.17) and introducing $z = \mathsf{r} - \mathsf{R}^*$, we then have

$$\begin{aligned}&\left(e^{-2\mathsf{R}^*}\mathsf{R}^* - 1\right)^2 (2 + \sqrt{1+3w^2}) \times \left[w^2\mathsf{R}^* - \mathsf{R}^*\Big(1 - \frac{1}{3}\big(e^{-2\mathsf{R}^*}\mathsf{R}^* - 1\big)^2(\sqrt{3w^2+1}+2)\Big)^2\right] \\ &= 4\varphi_+ \int_{-\infty}^{+\infty} \frac{dz}{1+\frac{z}{\mathsf{R}^*}} \frac{4e^{4z}}{(1+2e^{2z})^3}\,. \end{aligned} \tag{4.18}$$

If we take the $\mathsf{R}^* \to \infty, \omega \to 0$ limits, the integral on the right hand side is convergent. In order for the left hand side (i.e. the term in square brackets) to be finite, we must have

$$R\omega^2 = 1 + \sum_{n=0}^{\infty} c_{2n}\omega^{2n+2}\,, \tag{4.19}$$

which confirms the preliminary expectation given by formula (4.11), i.e. $R^* \propto \omega^{-2}, \omega \to 0$. By expanding the denominator for $z \ll \mathsf{R}^*$ and ignoring exponentially suppressed terms, we find

$$c_0 = \frac{1}{4}(2\log 2 - 1)\,, \qquad c_2 = \frac{1}{48}\left(4\pi^2 - 27\right) \tag{4.20}$$

for the leading order behaviour.

In order to connect R^* to the mass-based radius $R \equiv R_{99}$, we must numerically solve $4\pi\int_0^R dr\, r^2\rho(r) = 0.99M$ for R. Here, we construct an analytic approximate solution by considering the density support of the Q-ball. By construction of the profile, $\mathsf{R} - \mathsf{R}^* \equiv \lambda > 0$ and we will assume that $\lambda \equiv \mathsf{R} - \mathsf{R}^*$ corresponds to the tail of the boundary zone[2]. The width of the boundary zone can be found by taking the derivative of the field (4.14) and computing the standard deviation of that symmetric function, which we generalize by changing $2z \to \delta z$ in the exponent, having in mind the inclusion of gravity in Sec. 4.3. This yields

$$\lambda = 3\frac{1}{2}\sqrt{-\int_{-\infty}^{+\infty} z^2 d\Big(\frac{1}{\sqrt{1+2e^{\delta z}}}\Big)} = \frac{3}{2}\frac{2.66}{\delta}\,. \tag{4.21}$$

The prefactor arises from the fact that $\int_{-3\delta}^{+3\delta} d(1+2e^{\delta z})^{-1/2} \approx 0.99\int_{-\infty}^{+\infty} d(1+2e^{\delta z})^{-1/2}$. For Q-balls (in Minkowski space) $\delta = 2$ and

$$\mathsf{R} \approx \mathsf{R}^* + \lambda\,, \lambda = 2.66. \tag{4.22}$$

[2]The most compact regime corresponds to $\omega \to 0$ when $\lambda \to 0+$. All other, physically reasonable, profiles would present a smoother decay of the scalar i.e. fatter tails. Thus, they would reach the inflection point well before most of 99% of the energy density has been accumulated. We have checked this explicitly, for all of the models considered in this work, both with and without gravity.

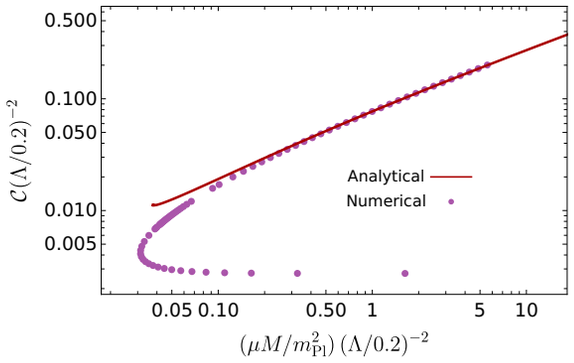

Figure 4.2: Mass-compactness relations for Q-balls. Dots correspond to numerical configurations, while the solid line is found from the analytic expressions (4.22), (4.24).

From the solution, other macroscopic parameters can also be calculated, such as the energy (mass) $E = M$ and the Noether charge Q [263] :

$$\bar{Q} \equiv \frac{\mu^2 Q}{m_{\rm Pl}^2} \approx \frac{\Lambda^2}{6}(\mathsf{R}^*)^3 w\Big[1 - \frac{3\ln 2}{2\mathsf{R}^*} + \mathcal{O}\big((\mathsf{R}^*)^{-2}\big)\Big]\,, \tag{4.23}$$

$$\bar{M} \equiv \frac{\mu M}{m_{\rm Pl}^2} \approx w\bar{Q} + \frac{\Lambda^2}{24}(\mathsf{R}^*)^2\Big[1 + \frac{1-\ln 2}{\mathsf{R}^*} + \mathcal{O}\big((\mathsf{R}^*)^{-2}\big)\Big], \tag{4.24}$$

where we have introduced

$$\Lambda = \frac{\sigma_0}{M_{\rm Pl}}\,, \tag{4.25}$$

anticipating the connection with the curved space-time case in the next section. Note that the previous relations imply the following scaling of the compactness in the thin-wall regime

$$\mathcal{C} \propto \Lambda^2 \frac{1}{\omega^2}\,. \tag{4.26}$$

In Fig. 4.2 we show the $\mathcal{C} - M$ curve from both the numerical and analytic calculations. From the plots, we also see that the analytic approximation for R agrees well with the numerically calculated value. The strong gravity regime is expected to be attained for values of $\mu\,, M\,, \sigma_0$ such that $\mathcal{C} \lesssim 0.1$:

$$\begin{aligned}\Big(\frac{\mathcal{C}}{0.1}\Big) &\approx 1.6 \times \Big(\frac{\mu}{10^{-8}\text{eV}}\Big)^{1/2}\Big(\frac{M}{1M_\odot}\Big)^{1/2}\Big(\frac{\sigma_0}{10^{17}\text{GeV}}\Big)^{-1} \\ &\approx 1.6 \times \Big(\frac{\mu}{10^{-14}\text{eV}}\Big)^{1/2}\Big(\frac{M}{10^6 M_\odot}\Big)^{1/2}\Big(\frac{\sigma_0}{10^{17}\text{GeV}}\Big)^{-1}\,.\end{aligned}$$

The threshold frequency between the stable and the unstable branch can be found from Eqs. (4.10), (4.23) and (4.24), and is given by [263]

$$w < w_{\rm Qb-s} \approx 0.82\,. \tag{4.27}$$

4.3 Soliton boson stars

Turning gravity on introduces a new scale Λ in the problem, with both perturbative and non-perturbative effects. In the low-compactness limit, SBSs effectively "see" a quadratic potential and are thus stabilized by quantum pressure (Sections 4.3.1 and 4.4.2). In the high-compactness limit, Eq. (4.26) shows that for any given Λ there exists a sufficiently low ω such that at some point the Schwarzschild compactness will be reached, and the scalar will collapse to a BH, simply because of the hoop conjecture [265, 146]. Thus, from the one stable and the one unstable branch in the flat space-time limit, we expect two stable and two unstable branches for *any* value of $\Lambda \ll 1$. This has already been established numerically and using catastrophe theory arguments [258, 250]. In the following, we will confirm previous results and supplement them with a physical interpretation and also an analytic model, focusing on the compact stable branch in the perturbative regime $\Lambda \ll 1$.

4.3.1 Scaling arguments

The structure of macroscopic objects is determined by the physics that stabilizes them. In this section, partially inspired by [172, 266, 267], we will provide rough scaling arguments to demonstrate what kind of configuration properties are to be expected.

A polytropic equation of state $P \sim \kappa \rho_{\rm m}^{\gamma}$, $[\kappa] = [M]^{-n}$ provides pressure support counteracting the attractive gravitational force. In equilibrium, one has

$$M^{2-\gamma} \sim \kappa m_{\rm Pl}^2 R^{4-3\gamma} \,. \tag{4.28}$$

If these configurations can reach the Schwarzshild compactness scale $R_{\rm Sch} \sim M/m_{\rm Pl}^2$, where strong-gravity effects are important, the maximum Chandrasekhar mass is given by

$$M_{\rm Ch}^{2\gamma-2} \sim \kappa m_{\rm Pl}^{6\gamma-6} \,. \tag{4.29}$$

Self-interacting boson stars (SIBSs) are pressure-supported by the repulsive interaction $P \sim \lambda|\Phi|^4$ for sufficiently large values of $\lambda > 0$. As the matter density is given by $\rho_{\rm m} \sim \mu^2|\Phi|^2$ (with μ the scalar mass), the equation of state is $P \sim \frac{\lambda}{\mu^4}\rho_{\rm m}^2$. SIBSs thus have the same mass-radius scaling as fermionic pressure-supported objects [scaling (4.28)], and the maximum mass is given by the Chandrasekhar limit

$$M_{\rm Ch} \sim \sqrt{\lambda}\frac{m_{\rm Pl}^3}{\mu^2} \,. \tag{4.30}$$

Pressure-supported nature of the SIBS is also the reason why the maximal attainable compactness for this model $\mathcal{C}_{\rm max}[\text{SIBS}] \approx 0.16$ [268] is very close to the neutron star value $\mathcal{C}_{\rm max}[\text{NS}] \approx 0.19$ [269].

In contrast to Mini boson stars (MBSs), discussed in Sec. 2.1.1, and SIBSs, SBSs are stabilized already in flat space-time, as discussed in Sec. 4.2. We can estimate the maximum mass by equating expression (4.11) with the Schwarzschild scale, which gives the Lee limit [167, 172]

$$M_{\rm Lee} \sim \frac{m_{\rm Pl}^4}{\sigma_0^2 \mu}. \tag{4.31}$$

4.3.2 Structure equations in GR

The action (4.2) can be generalized to curved space-time via a minimal coupling to gravity:

$$S = \int d^4x\sqrt{-g}\left(\frac{M_{\rm Pl}^2}{2}R + \mathcal{L}_\Phi\right). \tag{4.32}$$

We will consider spherically symmetric and static space-times of the form

$$ds^2 = -e^v dt^2 + e^u dr^2 + r^2 d\Omega^2 . \tag{4.33}$$

The radial profile of the metric coefficients follows from the Einstein field equations, which together, with the Klein-Gordon equation for the scalar, describe the full structure of the object:

$$\frac{1}{r^2}\left(r\, e^{-u}\right)' - \frac{1}{r^2} = -\frac{1}{M_{\rm Pl}^2}\rho\,, \tag{4.34}$$

$$e^{-u}\left(\frac{v'}{r} + \frac{1}{r^2}\right) - \frac{1}{r^2} = \frac{1}{M_{\rm Pl}^2}P_{\rm rad}\,, \tag{4.35}$$

$$\phi'' + \left(\frac{2}{r} + \frac{v'-u'}{2}\right)\phi' = e^u\left(\frac{dV}{d|\Phi|^2} - \omega^2 e^{-v}\right)\phi, \tag{4.36}$$

with the density ρ, the radial pressure $P_{\rm rad}$ and the tangential pressure $P_{\rm tan}$ defined by

$$\rho = e^{-v}\omega^2\phi^2 + e^{-u}(\phi')^2 + V\,, \tag{4.37}$$

$$P_{\rm rad} = e^{-v}\omega^2\phi^2 + e^{-u}(\phi')^2 - V\,, \tag{4.38}$$

$$P_{\rm tan} = e^{-v}\omega^2\phi^2 - e^{-u}(\phi')^2 - V\,. \tag{4.39}$$

We will now focus on the simplest potential (4.1) and adopt the rescaling

$$\mathsf{r} = \mu r\,, \quad \bar{m}(\mathsf{r}) = \frac{\mu m(r)}{m_{\rm Pl}^2}\,, \quad w = \frac{\omega}{\mu}\,, \quad \varphi = \phi/(\sigma_0/\sqrt{2}) \tag{4.40}$$

[c.f. relations (4.12)]. With this parameterization, the structure equations become dimensionless. We further assume that $' \equiv d/d\mathsf{r}$ unless we state otherwise.

Note that a shift $v \to \tilde{v} = v - v(0)$ corresponds to a rescaling of the time coordinate and thus to a redefinition of the scalar frequency $\tilde{\omega} = \exp(-v(0)/2)\omega$. Fixing $\varphi(0) \equiv \varphi_c$ and $\varphi(\infty) = 0$, let us use this gauge freedom to also set $\tilde{v}(0) = 0$. This specifies[3] a boundary value problem, with eigenvalue $\tilde{\omega}$, which we determine with a shooting method. Once that the configuration is calculated in this gauge, we can rescale the time coordinate at will, so that $v(\infty) \equiv v_\infty = 0$. More details on the numerical method are given in the App. B.1.

The Arnowitt-Deser-Misner (ADM) mass [273] can be extracted from the asymptotic behaviour of the metric functions:

$$\exp[-u(\mathsf{r})] = 1 - \frac{2\bar{M}}{\mathsf{r}} + \mathcal{O}\Big(\frac{1}{\mathsf{r}^2}\Big)\,. \tag{4.41}$$

From Eq. (4.35), one can also obtain the integral representation

$$\bar{M} = 4\pi \int d\mathsf{r}\, \mathsf{r}^2 \frac{\rho(\mathsf{r}')}{\mu^2 \sigma_0^2}\,. \tag{4.42}$$

Finally, the Noether charge is given by

$$Q \;\equiv\; -\int dV j^t = 4\pi\omega \int dr d\theta \sqrt{-g} e^{-v} \phi^2\,. \tag{4.43}$$

4.3.3 Representative configurations

In the rest of this Section, we will set $\Lambda = 0.186$ in order to illustrate our results. In the gauge $\tilde{v}(0) = 0$, the fictitious particle initially does not feel the impact of gravity, and consequently, in the thin-wall regime, we should expect that the central field is close to φ_+.

Like in the flat space-time case, in curved space-time numerical results produce two types of configurations - thin-wall ones for small w, and thick-wall ones for larger w. Unlike in the Q-ball case, the thin-wall regime of SBSs has two sub-classes, one perturbatively close to the flat space-time case, and a non-perturbative one close to the maximum compactness configuration. In Fig. 4.3 we show the $w - \varphi_c$, $\tilde{w} - \varphi_c$ and $\mathcal{C} - \varphi_c$ curves for our choice of Λ.

Various authors have used catastrophe theory arguments to assess the (local) stability of Q-balls and boson stars [262, 257, 258, 250]. We will not review these arguments here, but let us mention that they show that stability can be checked by analyzing the position of the turning points, for fixed Λ, in the $\bar{M} - \varphi_c$ curve, up to a final (unstable) "spiral" that occurs for $\varphi_c \gtrsim 1$ in the gravitating case. Thus, one can start from the stable MBS limit

[3]We are here focusing on the ground state (nodeless) solutions. It has been previously established that the excited solutions in various boson star models decay to the ground state [270, 271]. However, there are recent indications that sufficiently strong self-interactions can stabilise excited states over long time scales at least for SIBSs [272].

	$\phi(0)/(\sigma_0/\sqrt{2})$	$\tilde{\omega}/\mu$	ω/μ	$\tilde{v}(\infty)$	μR	$\mu M/m_{\rm Pl}^2$	$\mathcal{C}$
I	1.05	0.488	0.454	0.147	7.243	0.188	0.026
II	1.014	0.241	0.146	1.009	29.821	5.719	0.192
III	1.032	0.380	0.088	2.924	41.182	13.84	0.336

Table 4.1: Parameters of the representative configurations of SBSs: thick-wall regime (I); thin-wall regime perturbatively close to the Q-ball limit (II); strong gravity, thin-wall non-perturbative branch (III). Configuration III has also the maximal value of mass for $\Lambda = 0.186$ and thus is at the border between the compact stable and the unstable branch.

and track the turning points as φ_c increases. Already from Fig. 4.3, we see two turning points that mark the boundaries of a middle stable branch, with two unstable branches on the left and on the right of it (a low compactness stable branch is not shown on this plot, see Fig. 4.14). Note however that the turning point in the $\bar{M} - \varphi_c$ parameter space does not map exactly to the same point in the $\mathcal{C} - \varphi_c$ parameter space. We have established that the most massive configurations, which separate the compact stable branch from the unstable one, have compactnesses slightly bellow the maximum one. For example, for our representative case, the maximum mass configuration has $\mathcal{C} = 0.336$, while the maximally compact one has $\mathcal{C} = 0.346$.

We will now focus on the three representative configurations for each of the three aforementioned (sub-)classes: the thick-wall regime (I); the thin-wall regime perturbatively close to the Q-ball limit (II); and the thin-wall regime close to the non-perturbative $\mathcal{C}_{\rm max}$ cut-off (III) for our $\Lambda = 0.186$. Configuration III is also the maximally massive one for our Λ. The parameters of these configurations are given in Table 4.1. The field and density profiles are shown in Figs. 4.5 and 4.6, while the metric coefficients are displayed in Fig. 4.7.

4.3.4 Origin of maximum compactness

The maximum compactness of an object is usually discussed in the context of Buchdahl's theorem [274]. The latter states, in its most general form, that GR self-gravitating objects with energy density monotonically decreasing outwards $\rho' \leq 0$ and positive (or vanishing) pressure anisotropy (i.e. radial pressure larger than or equal to the tangential one) $P_{\rm rad} \geq P_{\rm tan}$ must have $C \leq 4/9$ [274, 275]. In the case of fluid stars, isotropic "normal matter" (i.e. one satisfying the weak energy condition $\rho \geq 0 \wedge \rho + P \geq 0$ and the micro-stability condition $P \geq 0 \wedge dP/d\rho \geq 0$) is consistent with these assumptions. However, Buchdahl's limit is not a robust concept, as it can be easily evaded by violating the theorem's assumptions, producing even more compact objects. A discussion of the parameterized bounds on $\mathcal{C}$ can be found in [276], and various toy models that exceed the Buchdahl bound have been constructed in the literature [146].

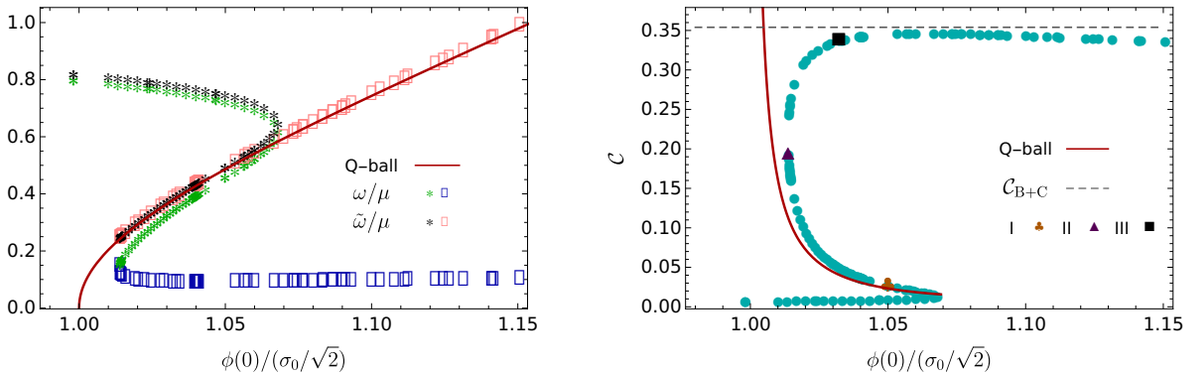

Figure 4.3: (Left) Frequency vs central field $\varphi_c \equiv \phi(0)/(\sigma_0/\sqrt{2})$ for $\Lambda = 0.186$, in two gauges $\omega\,, \tilde{\omega}$ compared to the Q-ball prediction appropriate in the $\tilde{v}(0) = 0$ gauge (dark red line). Note that two almost identical segments of the thin-wall regime in the $\tilde{v}(0) = 0$ gauge, denoted by the pink rectangles and the black stars, correspond to separate segments in the $v(\infty) = 0$ gauge, denoted by the blue rectangles and the green stars, respectively. (Right) Compactness vs central field for $\Lambda = 0.186$ (cyan circles) and the Q-ball result (dark red line). The three representative configurations (denoted by the orange club for I, purple triangle for II and black square for III) are indicated.

Buchdahl's theorem can be additionally strengthened by requiring that the equation of state be consistent with causality. In [275] (see also [277]), it has been shown that a useful toy model for understanding the maximally compact and causal configurations is given by objects described by a linear equation of state (LinEoS)

$$\rho = \rho_c + \frac{P}{c_s^2}\,, \tag{4.44}$$

where $c_s^2 \equiv \partial P/\partial\rho > 0$ (the speed of sound) and ρ_c are constant. Hence, allowing for $c_s^2 > 1$ accounts for violations of causality. The limit $c_s^2 \to \infty$ corresponds to constant density stars, whose maximum compactness $\mathcal{C}_{\rm B} = 4/9$ follows from Buchdahl's theorem. For a given c_s^2, the LinEoS describes the stiffest possible matter, and consequently it yields the most compact configurations. Maximally compact and causal configurations consistent with the assumptions of Buchdahl's theorem cannot surpass $\mathcal{C}_{\rm B+C} = 0.354$ when $c_s^2 = 1$. The dependence of the compactness of LinEoS configurations on c_s^2 is approximately given (to within a 3.6% error) by the fitting formula [275]

$$\frac{4}{9\mathcal{C}_{\rm LinEoS}} - 1 \approx \frac{0.77 + 0.51c_s^2}{c_s^2(4.18 + c_s^2)}\,. \tag{4.45}$$

SBSs in the thin-wall regime are a physical example of objects with a LinEoS[4], because in the bulk of the star $\varphi \approx 1$ and hence $\varphi' \approx V \approx 0$, making in turn $P_{\rm rad} \approx \rho$. This

[4]This is, as far as we know, original insight. A comparison between SBSs and constant density stars ($c_s^2 \to \infty$) was discussed in Ref. [248].

argument implies that the maximal compactness of SBS is $\mathcal{C}_{\rm max} \lesssim \mathcal{C}_{\rm B+C}$, which is consistent with our numerical results and the values reported in the previous work [167, 247, 155, 160]. Now we address two apparent loopholes in the previous argument. First, SBSs do *not* have monotonic energy density profiles in their surface regions (Fig. 4.6, right), which violates the assumptions of Buchdahl's theorem [275]. The region where this violation occurs, however, is parametrically smaller than the size of the SBS bulk in the thin-wall regime, and thus it does not affect $\mathcal{C}_{\rm B+C}$ significantly. Secondly, although SBSs have anisotropic pressure, the radial pressure is larger than the tangential one [Eqns. (4.38), (4.39)], which does not allow for violating the Buchdahl compactness bound (unlike the opposite case in which the tangential pressure is larger than the radial one [149, 277]).

In more detail, we can estimate how well the LinEoS describes the matter inside the SBS in the thin wall regime. Assuming the Q-ball results (c.f. Section 4.3.5 for a justification) we will ignore exponentially suppressed scalar derivatives [Eq. (4.16)] and approximate Eqns. (4.37), (4.38) to obtain

$$\frac{\rho}{\frac{\mu^2\sigma_0^2}{2}} \approx w_+^2\varphi_c^2 + V(\varphi_c)\,, \quad \frac{P_{\rm rad}}{\frac{\mu^2\sigma_0^2}{2}} \approx w_+^2\varphi_c^2 - V(\varphi_c)\,,$$

from where it follows that

$$(c_s^2)_a \approx \frac{\varphi_c^2\,(3\varphi_c^2-2)}{6\varphi_c^4 - 6\varphi_c^2 + 1}\,, \tag{4.46}$$

with w_+ being the inverse of Eq. (4.16) and $\varphi_+ \approx \varphi_c$. For $\varphi_c = 1.032$ (configuration III) from Eq. (4.46) we find $(c_s)_a = 0.95$. Using this value in Eq. (4.45) we get $\mathcal{C}_{\rm LinEoS} = 0.350$, close to $\mathcal{C}_{\rm III} = 0.336$. Taking the limit $\varphi_c \to 1$, Eq. (4.46) implies $(c_s^2)_a \to 1$ and hence $\mathcal{C}_{\rm max} \to \mathcal{C}_{\rm B+C}$. Note however that the exact limit $\varphi_c = 1$ in the thin-wall regime is attainable only in the Minkowski space-time ($\Lambda = 0$). This is a singular limit as the absence of gravity implies $\mathcal{C} \to \infty$ when $\varphi \to 1$, as elaborated in Section 4.2.1.

In order to scrutinize previous analysis further, we have calculated (for our representative $\Lambda = 0.186$) numerically the average

$$\langle c_s^2 \rangle = \frac{1}{R_<}\int_0^{R_<} dr \frac{\partial P_{\rm rad}}{\partial \rho} \tag{4.47}$$

over several configurations [with $R_<$ the boundary of the bulk, c.f. expression (4.64)], and we have compared the compactness predicted by Eq. (4.45) with the actual one. The results are shown in Fig. 4.4 , and clearly indicate good agreement in the thin wall regime (i.e. at high compactnesses). We have also presented results for the position dependence of c_s^2 in Fig. 4.5 , for two specific configurations (I and III). Note that negative and seemingly non-causal values of c_s^2 appear in the boundary zone, signaling a breakdown of

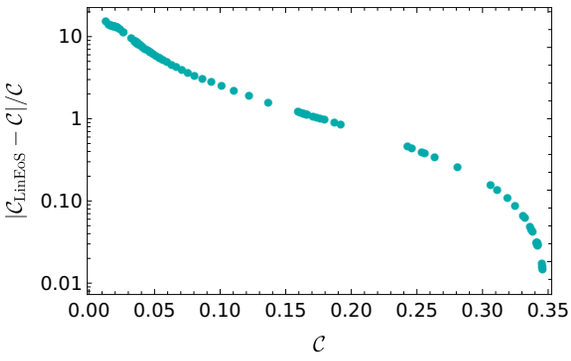

Figure 4.4: Relative difference between the numerically determined compactness $\mathcal{C}$ and the prediction from the LinEoS $\mathcal{C}_{\rm LinEoS}$ (4.45) [using the numerically found average speed of sound (4.47)].

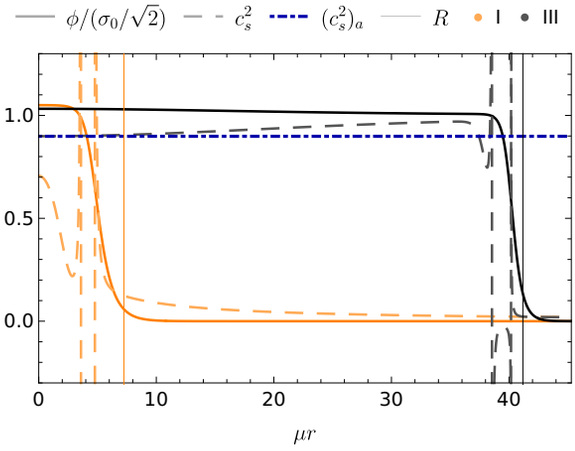

Figure 4.5: Scalar field $\varphi \equiv \phi/(\sigma_0/\sqrt{2})$ and the speed of sound c_s^2 radial profile for the two representative configurations: I (orange) and III (black). The blue dot-dashed line represents the estimate of the speed of sound (for III) $(c_s^2)_a$ from Eq. (4.46).

the hydrodynamic description. This breakdown also occurs in flat space-time [246].

Finally, in the thick-wall regime, commensurability between the bulk and the boundary does not allow for an effective LinEoS description (Fig. 4.5). As a result, in this regime $\mathcal{C} \ll \mathcal{C}_{\rm B+C}$.

4.3.5 Analytic construction

As already mentioned, the structure of SBSs can also be interpreted in light of the dynamics of a fictitious Newtonian particle in a time dependent potential, with r playing the role of time[5], as can be seen from the Klein-Gordon equation

$$\begin{aligned} &\varphi'' + \left(\frac{2}{\mathsf{r}} - \frac{W'}{W}\right)\varphi' = \left[\mathsf{m}^2(1 - 4\varphi^2 + 3\varphi^4) - W^2\right]\varphi\,, \\ &\mu W = \omega e^{(u-v)/2}\,, \quad \mu\mathsf{m} = \mu e^{u/2}\,, \end{aligned} \tag{4.48}$$

Equations (4.34) and (4.35) can be formulated as dynamical equations for "time-dependent" frequency μW and scalar mass $\mu\mathsf{m}$. Their dynamics depends on φ through ρ and $P_{\rm rad}$. However, in certain regimes we can approximately evaluate W, m without knowing the full behaviour of φ.

If we work in the gauge where $\tilde{v}(0) = 0$, the Q-ball does not "feel" the gravitational

[5]This interpretation was mentioned in [259] at the qualitative level, but without exploring its implementation and consequences. A similar approach was also applied to (Minkowski) Q-balls with gauged $U(1)$ symmetry while this work was well into preparation [278].

field initially (i.e. at the centre). Like in the flat space-time case, for a given φ_c we need to find $W(0) = w$ such that the "SBS-particle" rolls over the time-dependent potential and reaches $\varphi = 0$ in an infinite time ($\mathsf{r} \to \infty$) with $\mathcal{E} = 0$. Note that W is a gauge invariant object (i.e. it is left unaffected by a change of the time coordinate).

The particle analogy sheds light, already at the qualitative level, on some of the properties of SBSs: as Q-balls have a unique thin-wall regime, for SBSs this regime will be described by a curve in the $\tilde{w} - \varphi_c$ space, very close to the Q-ball result. However, for some SBS configurations, the effective particle will exhibit the thin-wall regime perturbatively close to the Q-ball one (like for configuration II), while others will be in the non-perturbative part of the parameter space (like in the case of configuration III). Thus, the thin wall regime in the $\tilde{w} - \varphi_c$ representation consists of two almost degenerate curves (denoted by black stars and pink rectangles in Fig. 4.3). For example, there are configurations where the difference in $\tilde{w}$ can be as low as $\sim 10^{-51}$, with the corresponding difference in w $\sim 10^{-6}$. These curves split into two separate curves in the $w - \varphi_c$ parameter space, one close to the Q-ball line, while the other is the horizontal asymptote, represented by green stars and blue rectangles on Fig. 4.3, respectively.

In the following subsections, we will give an analytic description of the scalar in the strong-field regime in three zones (analogous to the flat-spacetimes ones introduced in Sec. 4.2), starting from the simplest one.

4.3.5.1 Exterior zone

The simplest regime is the asymptotic one, where the space-time is to a good approximation Schwarzschild, owing to the fast decay of the scalar:

$$u_> = -\log\left(1 - \frac{2\bar{M}}{\mathsf{r}}\right), \tag{4.49}$$

$$\tilde{v}_> = \tilde{v}_\infty + \log\left(1 - \frac{2\bar{M}}{\mathsf{r}}\right). \tag{4.50}$$

The evolution of the scalar is found by solving the Klein-Gordon equation (4.36) with these u, v, expanding in powers of $1/r$:

$$\begin{aligned} &[\mathcal{O}_{\rm L} + \mathcal{O}_{\rm NL}]\varphi(\mathsf{r}) = 0\,, \\ &\mathcal{O}_{\rm L} = \frac{d^2}{d\mathsf{r}^2} + \frac{2}{\mathsf{r}}\frac{d}{d\mathsf{r}} - \left(1 - e^{-\tilde{v}_\infty}\tilde{w}^2 + \frac{2\bar{M}}{\mathsf{r}}\left(1 - 2e^{-\tilde{v}_\infty}\tilde{w}^2\right)\right), \\ &\mathcal{O}_{\rm NL} = \frac{\bar{M}}{\mathsf{r}}\left(6\varphi^5 - 8\varphi^3\right) + 3\varphi^5 - 4\varphi^3\,. \end{aligned} \tag{4.51}$$

Note that the non-linear terms can be treated as a perturbation. While it appears that there is no simple analytic estimate of these corrections, the leading term gives a good description of the asymptotic behaviour, because the scalar is suppressed (more than

exponentially).

Requiring $\varphi \to 0$ as $r \to \infty$, we obtain the solution in terms of hypergeometric functions, or equivalently in terms of the Wittaker function [279]

$$\varphi_\infty = \frac{\mathcal{A}}{2\mathsf{r}\sqrt{1-e^{-\tilde{v}_\infty}\tilde{w}^2}} \times W\left[\bar{M}\frac{2e^{-\tilde{v}_\infty}\tilde{w}^2-1}{\sqrt{1-e^{-\tilde{v}_\infty}\tilde{w}^2}}, -\frac{1}{2}, 2\sqrt{1-e^{-\tilde{v}_\infty}\tilde{w}^2}\right]. \tag{4.52}$$

This asymptotic solution is parameterized by $\tilde{v}_\infty$, $\bar{M}$, $\tilde{w}$ and the normalization amplitude $\mathcal{A}$. The linear equation $\mathcal{O}_{\rm L}\varphi(\mathsf{r}) = 0$ is invariant under the rescaling $\varphi \to \mathsf{C}\varphi$, but the matching condition breaks the invariance and selects $\mathsf{C} = \mathcal{A}$. Expanding the Whittaker function in $1/\mathsf{r}$, the leading behaviour gives

$$\varphi_\infty \simeq \frac{\mathcal{A}}{\mathsf{r}^{1+\beta_>}} e^{-\alpha_> \mathsf{r}}\,, \tag{4.53}$$

$$\alpha_> = \sqrt{1-e^{-\tilde{v}_\infty}\tilde{w}^2}\,, \tag{4.54}$$

$$\beta_> = \frac{\bar{M}}{\alpha_>}(1-2e^{-\tilde{v}_\infty}\tilde{w}^2)\,. \tag{4.55}$$

Note that for $\Lambda \to 0$, $\bar{M} \to 0$ and we recover the Q-ball result (4.15). We show a comparison between the numerical and the asymptotic field behaviour in Fig. 4.6.

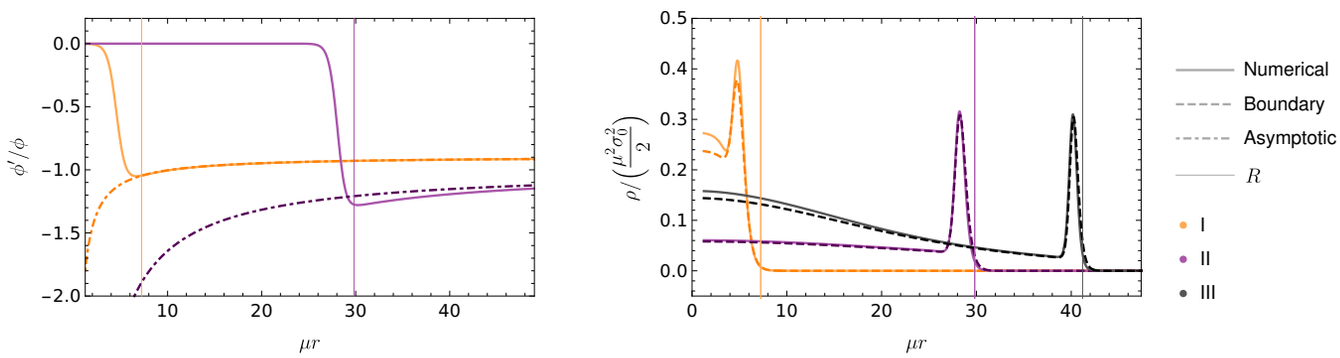

Figure 4.6: (Left) Numerical results vs asymptotic approximation for the ratio between the field radial profile and its derivative ϕ/ϕ' for configurations I, II. (Right) Numerical results vs boundary zone analytic approximation for the field energy density radial profile $\rho/(\frac{\mu^2\sigma_0^2}{2})$ for configurations I, II, III. Numerically determined parameters are used as input.

4.3.5.2 Interior zone

In the gauge $\tilde{v}(0) = 0$, the flat space-time result (4.16) should be valid sufficiently close to the origin, and the scalar field derivative is suppressed by $\tilde{w}$. Thus, we will calculate the metric coefficients in the interior perturbatively in $\tilde{w}$, and approximate $\varphi' \approx 0$ and $V_< \approx V(\varphi_c)$. This description provides a good approximation for configurations similar to II in the strong-field and the thin-wall regime and close to the Q-balls limit, where $\tilde{w}$ is

small and controls the size of the star.

The perturbative expansion in $\tilde{w}$ must be appropriately resummed (or performed from the start in a suitable form) so that it can be matched with the exterior. Taking

$$\tilde{u}_< = \log[\tilde{\mathsf{u}}_0(r) + \tilde{\mathsf{u}}_2(r)\tilde{w}^2 + \tilde{\mathsf{u}}_4(r)\tilde{w}^4 + \mathcal{O}(\tilde{w}^6)]\,, \tag{4.56}$$

$$\tilde{v}_< = \log[\tilde{\mathsf{v}}_0(r) + \tilde{\mathsf{v}}_2(r)\tilde{w}^2 + \tilde{\mathsf{v}}_4(r)\tilde{w}^4 + \mathcal{O}(\tilde{w}^6)]\,, \tag{4.57}$$

from Eqns. (4.34) and (4.35) one gets

$$\tilde{\mathsf{u}}_0 = 1\,,\ \tilde{\mathsf{u}}_2 = \frac{1}{6}\Lambda^2 r^2\,, \tilde{\mathsf{u}}_4 = \frac{1}{360}\left(45\Lambda^2 r^2 - 2\Lambda^4 r^4\right) \tag{4.58}$$

$$\tilde{\mathsf{v}}_0 = 1\,, \tilde{\mathsf{v}}_2 = \frac{1}{3}\Lambda^2 r^2\,, \tilde{\mathsf{v}}_4 = \frac{1}{120}\left(15\Lambda^2 r^2 + 4\Lambda^2 r^4\right)\,. \tag{4.59}$$

In Fig. 4.7 we show the numerical results and the interior and asymptotic approximations for the metric coefficients.

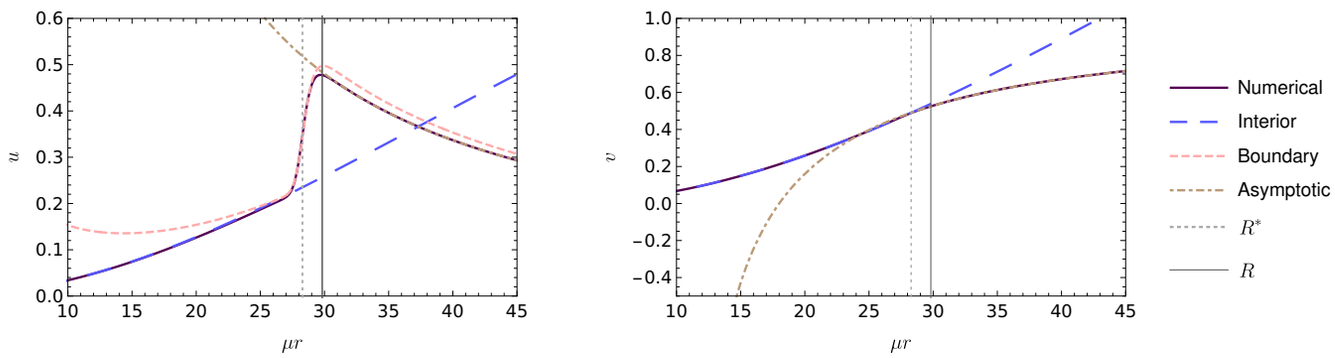

Figure 4.7: (Left) Numerical vs. approximate analytic (interior, boundary, asymptotic) results for the u metric coefficient radial profile for II. (Right) Numerical vs. approximate analytic (interior, asymptotic) results for the v radial profile metric coefficient for II. Numerically determined parameters are used as input.

4.3.5.3 Boundary zone

In the transition region, let us expand around $(\mathsf{R}^*)^{-1}$ as in Ref. [263]. Thus, we neglect the friction $1/R^*$ term in the Klein-Gordon equation (4.36). We can estimate the contribution from the time-dependent frequency as

$$\frac{W'}{W} \sim \frac{1}{1-\frac{2\bar{M}}{\mathsf{R}^*}}\frac{2\bar{M}}{(\mathsf{R}^*)^2} \sim \frac{2}{\mathsf{R}^*(\mathcal{C}^{-1}-1)}\,. \tag{4.60}$$

As $\mathcal{C}_{\max} \sim 0.35$ (cf. Sec. 4.3.4), we find that this term is of the order of $1/R^*$ and can be neglected. Now, neglecting friction and assuming in the first iteration $W \approx W_* \equiv W(\mathsf{R}^*)\,, \mathsf{m} \approx \mathsf{m}_* \equiv \mathsf{m}(\mathsf{R}^*)$ (as we are interested only in a tiny strip around of the thin wall),

we can use the conservation of energy and the fact that $\mathcal{E}(\infty) = 0$ to reduce the equations of motion to [263]

$$\varphi' = \pm\varphi\sqrt{\left[\mathsf{m}_*^2(1-\varphi^2)^2 - W_*^2\right]}\,. \tag{4.61}$$

In the thin-wall regime, the expectation $W_*^2 \ll 1$ leads to

$$\varphi_B = \frac{1}{\sqrt{1+2\exp\left[2\mathsf{m}_*(\mathsf{r}-\mathsf{R}^*)\right]}}\,, \tag{4.62}$$

where we have specified the integration constant by requiring $\varphi''(\mathsf{R}^*) = 0$. Note that the second integration constant is determined by the value of the energy and the requirement that the function is monotonously decreasing. Furthermore, [263] includes an *ad hoc* prefactor φ_+ in φ_B for Q-balls [formula (4.14)], because it slightly improves the analytic description in the thick-wall limit. (Note that in the thin-wall regime $\varphi_+ \approx 1$ in any case.) We have not included this prefactor in the SBS context, as it tends to worsen the model.

From the analysis around Eq. (4.21), we find the estimate of the width of the density support in the boundary zone to be

$$\lambda = \frac{3}{4}\frac{2.66}{\mathsf{m}_*}\,, \tag{4.63}$$

$$\mathsf{R}_{>/<} = \mathsf{R}^* \pm \lambda \tag{4.64}$$

In the flat space-time limit $\mathsf{m}_* = 1$ and we recover Eq. (4.14).

A plot of the field density is given in Fig. 4.6, where the metric coefficients are taken from the interior zone perturbative series (4.56), (4.57). Note that the boundary-zone solution works (somewhat surprisingly) even far from its region of a priori validity, down to the transition region (like in the flat space-time case). The worst agreement occurs for the configuration I, as expected since this configuration is in the thick-wall regime.

Having a preliminary understanding of the field behaviour in the boundary zone, as well as of the radial profile of the metric coefficients in the internal and external zones, we can understand the junction conditions for the metric coefficients. From expression (4.62):

$$\bar{\rho}_{\rm kin} = e^{-v}\tilde{w}^2\varphi^2 \approx \frac{e^{-v_*}\tilde{w}^2}{2e^{2\mathsf{m}_* z}+1} \tag{4.65}$$

$$\bar{\rho}_{\rm st} = e^{-u}(\varphi')^2 \approx \frac{4e^{4\mathsf{m}_* z}}{\left(2e^{2\mathsf{m}_* z}+1\right)^3} \tag{4.66}$$

$$\bar{\rho}_{\rm pot} = V \approx \frac{4e^{4\mathsf{m}_* z}}{\left(2e^{2\mathsf{m}_* z}+1\right)^3}\,, \tag{4.67}$$

with $z = \mathsf{r} - \mathsf{R}^*$ and $\bar{\rho}_i = \left(\frac{\mu^2\sigma_0^2}{2}\right)^{-1}\rho_i$. In the thin wall limit one has $\bar{\rho}_{\rm kin} \to H(-z)$, where H is the Heaviside step function, while $\bar{\rho}_{\rm st} \to \delta(z)$. From Eqns. (4.34), (4.35) and

the limiting cases, we can expect that u will have a step-like behaviour at R^*, while v will present a smoother transition. This type of behaviour was noted already in [167]. Solving Eq. (4.34) we find a complicated expression that we report in App. B.3.1. For the configuration II we show u_B in Fig. 4.7 (Left).

4.3.5.4 Energy balance

Like in the flat space-time case [Eq. (4.17)], we can determine the inflection point in the case of SBSs by using energy balance arguments. We now need to account for the "time" dependence of the potential parameters as

$$\frac{dU_\omega}{dr} = \frac{\partial U_\omega}{\partial \phi}\phi' + \frac{\partial U_\omega}{\partial r}\,. \tag{4.68}$$

One then finds

$$\frac{2}{\mu^2\sigma_0^2}\mathcal{E}(0) = \int_0^\infty d\mathsf{r}\big[\frac{2}{\mathsf{r}}(\varphi')^2 - \frac{W'}{W}(\varphi')^2 + \mathsf{m}'\mathsf{m}\varphi^2(1-\varphi^2) - W'W\varphi^2\big]\,.$$

Note that in the last expression, only the first term is present in the Minkowski limit (4.17), because $\mu W \to \omega$, $\mu\mathsf{m} \to \mu$ and ω, μ do not run in "time". Like the first one, the other terms are also dominant in the particular zones, as can be inferred from their form. The second and third terms are important in the boundary zone where the field interpolates between φ_c and the exponential tail, while the fourth term receives important contributions both from the interior and the boundary zone. The leading order behaviour of all these terms is provided separately by

$$A_\mathcal{E} \equiv \int_{\mathsf{R}_<}^{\mathsf{R}_>} d\mathsf{r}\frac{2}{\mathsf{r}}(\varphi')^2 \approx \frac{\mathsf{m}_*}{2\mathsf{R}^*}\,, \tag{4.69}$$

$$B_\mathcal{E} \equiv -\int_{\mathsf{R}_<}^{\mathsf{R}_>} d\mathsf{r}\frac{W'}{W}(\varphi')^2 \approx -\frac{\mathsf{m}_*}{\mathsf{R}^*}\Big[\frac{1-\mathsf{m}_*^2}{4} + \frac{1}{80}\mathsf{m}_*^2\Lambda^2\mathsf{R}^{*2}\Big]\,, \tag{4.70}$$

$$C_\mathcal{E} \equiv \int_{\mathsf{R}_<}^{\mathsf{R}_>} d\mathsf{r}\mathsf{m}'\mathsf{m}\varphi^2(1-\varphi^2) \approx \frac{\mathsf{m}_*}{\mathsf{R}^*}\Big[\frac{1-\mathsf{m}_*^2}{8} + \mathsf{m}_*^2\Lambda^2\mathsf{R}^{*2}\Big(\frac{1}{80} + \frac{1}{48}w^2e^{-v_*}\Big)\Big]\,, \tag{4.71}$$

$$D_{\mathcal{E}<} \equiv -\int_0^{\mathsf{R}_<} d\mathsf{r}W'W\varphi^2 \approx \frac{w^2\varphi_c^2}{2}\big[1 - e^{u_<(\mathsf{R}_<)-v_<(\mathsf{R}_<)}\big]\,, \tag{4.72}$$

$$D_{\mathcal{E}\,B} \equiv -\int_{\mathsf{R}_<}^{\mathsf{R}_>} d\mathsf{r}W'W\varphi^2 \approx -2\frac{\mathsf{m}_*}{\mathsf{R}^*}w^2e^{-v_*}\Big[\frac{1}{2}\log\Big(\frac{3}{2}\Big)(1-\mathsf{m}_*^2) + \frac{7}{648}\mathsf{m}_*^2\Lambda^2\mathsf{R}^{*2}\Big] \tag{4.73}$$

The left hand side of Eq. (4.69) is therefore given as in Eq. (4.18), i.e., neglecting exponentially suppressed terms, by

$$\bar{\mathcal{E}}(0) \approx \frac{\big(\sqrt{3w^2+1}+2\big)}{27}\Big(3w^2 + \sqrt{3w^2+1} - 1\Big)\,. \tag{4.74}$$

From the numerical results of Fig. 4.3, it is clear that the effect of (strong) gravity is to introduce a new branch. As a result, for a subset of $\varphi_c \sim 1$ we have two different stable configurations [and possibly one more (un)stable one] for the same φ_c. For the class of configurations that contains I and II, we expect the Q-ball result $\mathsf{R}^* \sim 1/\tilde{w}^2$. For the most compact configurations, from Eqns. (4.49), (4.56) and ignoring the jumping conditions, one naively gets

$$\mathsf{R}^* \sim \frac{\sqrt{12\mathcal{C}_{\rm max}}}{\Lambda\tilde{w}} \sim \frac{2}{\Lambda\tilde{w}}\,. \tag{4.75}$$

where we assumed in the last relation $\mathcal{C}_{\rm max} \approx \mathcal{C}_{\rm B+C}$. Although this expectation is too simplistic, it suggests the useful variable

$$T \equiv \mathsf{R}^*\Lambda\tilde{w}\,. \tag{4.76}$$

Because of the aforementioned degeneracy, $T(\tilde{w})$ is not a single-valued function. Instead, it is more useful to look for $\tilde{w} = \tilde{w}(T)$. The minimum of this curve, $\tilde{w}_\cup$, separates the Q-ball-like branch from the non-perturbative strong-gravity one, and provides the lowest $\tilde{w}$ for a given Λ. In flat space-time, one has $\tilde{w}_\cup = 0$ ($\mathsf{R}^* \to \infty$), so we expect $\tilde{w}_\cup \sim \mathcal{O}(\Lambda)$.

Approximating the complicated algebraic expressions in R^* we find (see App. B.3.2 for the details)

$$\tilde{w} \approx \Lambda\frac{\sqrt{-\frac{T^4}{5}+6T^2+36}\,(T^4+10T^2+30)}{T\,(-T^4+30T^2+180)}\,. \tag{4.77}$$

The minimum of this function corresponds to $\tilde{w}_\cup/\Lambda \approx 1.1$, while for $T \to 0$ we recover the Q-ball asymptotics $\tilde{w} \sim \Lambda/T$. From there the approximate behaviour of w follows:

$$\frac{w}{\tilde{w}} \approx \left(1+\frac{5T^2\,(3\tilde{w}^2+4)-(2/3)T^4}{(2\sqrt{30})^2}\right)^{-1/2} \times \left(1+\frac{5T^2\,(3\tilde{w}^2+8)+4T^4}{(2\sqrt{30})^2}\right)^{-1/2}, \tag{4.78}$$

which we show in Fig. 4.8. Our rough approximations have therefore given us a simple analytic description that predicts the horizontal branching off of the $w-\varphi$ curve for any $\Lambda \ll 1$ (corresponding to the non-perturbative effect of strong-gravity), with $\mathcal{C}$ getting close to LinEoS limit discussed in Sec. 4.3.4.

4.3.5.5 Finale: Semi-analytic solution

Instead of ignoring sub-leading terms, which led us to Eq. (4.78), we can also solve the full master (algebraic) Eqns. (4.69)-(4.74) numerically, using expression (4.77) as a guess for each T. Now, we use u_B when calculating m_* in Eqns. (4.69)-(4.73), except in u_B itself [expression (B.15)], where we iteratively take $\mathsf{m}_* \approx \exp\left(u_<(\mathsf{R}^*)/2\right)$. In contrast to the

costly numerical solution of the boundary-value Einstein-Klein-Gordon system (App. B.1), the semi-analytic approach provides a solution in a few seconds on a laptop computer.

This procedure leads to a very good description of the configurations in the stable compact branch, as shown in Fig. 4.8. The semi-analytic results are in excellent agreement with the numerical ones for $\bar{M}$, v_∞, and consequently for w. For both R^* and R, the agreement is almost perfect in the Q-ball-like strong-gravity branch (i.e. for configurations similar to II), while in the non-perturbative strong-gravity branch (similar to III), there is a systematic deviation, up to a few percent relative error. This error increases as φ increases, but note that this occurs mostly in the unstable branch, for which accurate approximations are not of crucial importance. We elaborate more on the reason for the systematic error in App. B.3.3.

Once the parameters are determined in the described way, one can use the expansions from the previous Subsections to reconstruct both the scalar and the gravitational field throughout the space-time, as well as the thermodynamic functions: density, pressure(s), speed of sound etc.

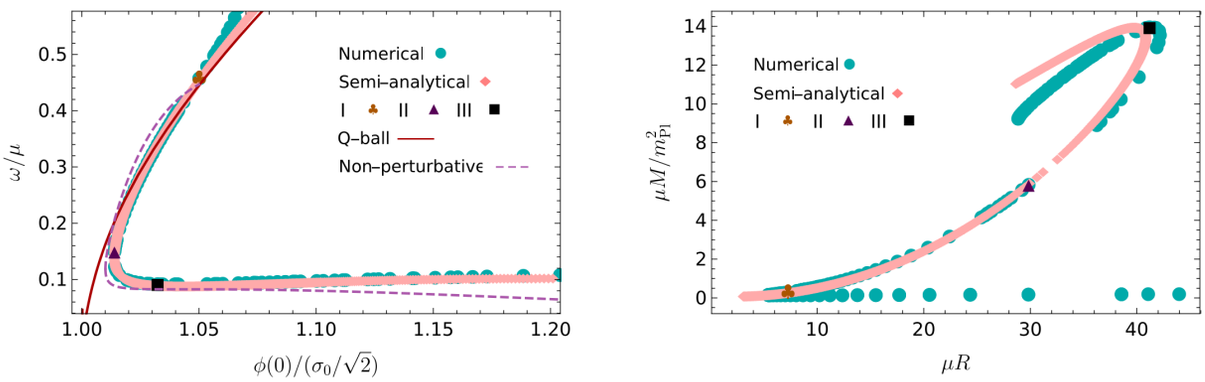

Figure 4.8: (Left) Approximate analytic, semi-analytic (pink diamonds) and numerical calculations (cyan circles) of the $w-\varphi$ behaviour for SBSs. The purple dashed line shows both branches from expression (4.78), while the dark red line represents the the Q-ball limit [expression (4.19), using expansion (4.56), (4.57)]. (Right) Semi-analytic vs. numerical calculation of the $M-R$ curves. Both plots correspond to the benchmark scenario $\Lambda = 0.186$. Three representative configurations from Table 4.1 are also shown.

4.4 Parameter space of Soliton boson stars

In this Section, we will move away from the benchmark scenario of Sec. 4.3, where we only considered the compact stable branch of SBSs with the simple potential (4.1) for $\Lambda \ll 1$. We will now consider the Planck limit $\Lambda \sim 1$ in Sec. 4.4.1 and the low-compactness stable branch (for generic Λ) in Sec. 4.4.2. We will then adopt potentials with multiple degenerate vacua in Sec. 4.4.3, ones with a false vacuum instead of a degenerate one

in Section 4.4.4, and we will test the robustness of our conclusions in Sec. 4.4.5, by considering a non-polynomial effective potential.

4.4.1 Planck scale regime

To understand the qualitative impact of a large "control parameter" Λ, let us assume that the Q-ball description is valid up to $\mathcal{C}_{\rm B+C}$ i.e. $\mathcal{C}_{\rm max} \sim \frac{\Lambda^2}{16\pi}\varphi_c^2 \mathsf{R}^2 w^2 \propto \Lambda^2/w_{\rm min}^2 < \mathcal{C}_{\rm B+C}$. As Λ increases, in order for $\mathcal{C}_{\rm max}$ to asymptote to $C_{\rm B+C}$ in the thin wall regime, $w_{\rm min}$ has to increase. However, as $w_{\rm min}$ increases, the thin wall regime is superseded by the thick wall one, and when $w_{\rm min} \simeq w_{\rm Qb-s}$ [cf. Eq. (4.27)] the stable branch inherited from the flat space-time limit disappears.

We have presented numerical results for $\tilde{w}\,, w$ as functions of Λ in Fig. 4.9. Note that the dip in the $w(\varphi_c)$ curve increases with Λ. This corresponds to the growth of the height of the horizontal asymptote of the $w(\varphi_c)$ and hence minimal possible w as argued above. Consequently the Planck scale regime leads to *less* compact configurations (Fig. 4.11). As strong deviations from the Q-ball description occur in the compact stable branch at $\Lambda \simeq 0.4$, we cannot make quantitative predictions for when the compact stable branch will disappear, but numerically we find that this occurs at $\Lambda \simeq 1.1$. The mass-radius relation is shown in Fig. 4.10, while Fig. 4.11 represents how the maximum achievable compactness changes[6] from $C_{\rm B+C}$ to $C_{\rm MBS} \approx 0.11$ over $\Lambda \sim 0.1 - 1$ range.

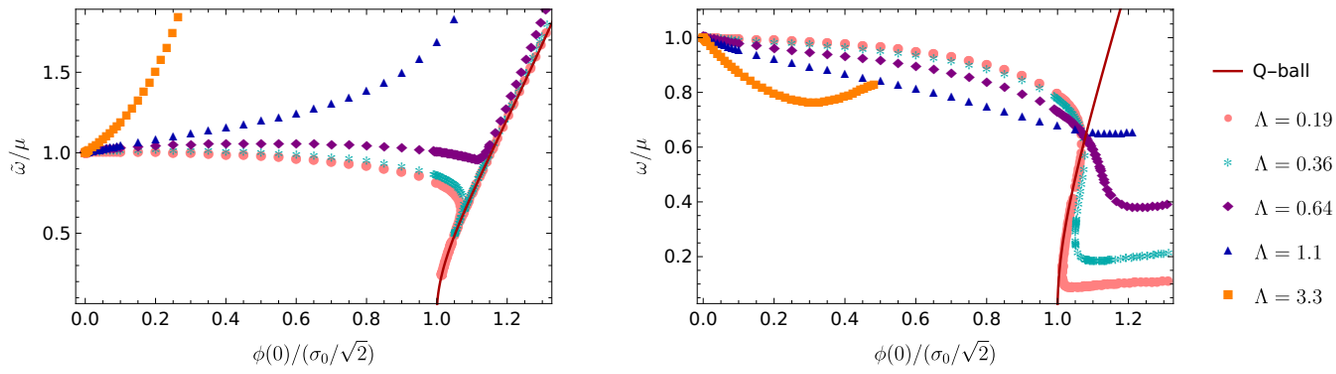

Figure 4.9: (Left) Frequency vs central scalar field value in $\tilde{v}(0) = 0$ gauge and (Right) in the $v(\infty) = 0$ gauge, for SBSs with different values of Λ, along with the (gauge-independent) analytical result for Q-balls (4.16).

[6]It is interesting to note that scalar stars in Horndeski's theory have been recently constructed and present very similar a behaviour for $\mathcal{C}$ (c.f. Fig. 10 in [280]). However, we are not aware of a simple mapping between SBSs in GR and this kind of configurations.

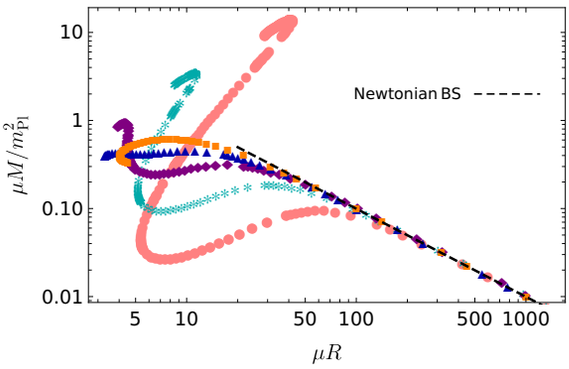

Figure 4.10: Mass-radius relation for SBSs with different values of Λ. The dots represent numerical results, while the dashed black line represents the analytic result for NBS (4.83). The shapes and colours of dots are the same as in Fig. 4.9.

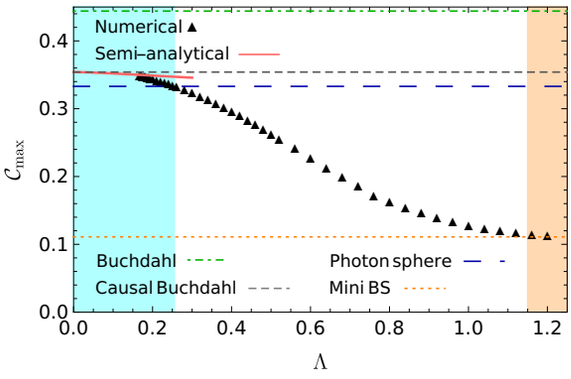

Figure 4.11: Maximum compactness of SBSs for given Λ. We have also indicated the Buchdahl bound $\mathcal{C}_{\rm B} = 0.44$, the causal Buchdahl bound $\mathcal{C}_{\rm B+C} = 0.354$, the condition for the photon sphere $\mathcal{C} = 0.33$ and the maximal compactness for MBSs $\mathcal{C} = 0.11$. In the ultra-compact domain (cyan region), the numerical results are supplemented with semi-analytical ones. Note that for $\Lambda = 0$: $\mathcal{C}_{\rm max} \to \infty$ (Q-ball limit). The orange region represents the MBS part of the parameter space and extends to $\Lambda \to \infty$.

4.4.2 Low compactness stable branch

The low compactness stable branch of SBSs is supported by quantum pressure, and as a result in this limit SBSs behave as MBSs. The exact MBS limit of SBSs is $\Lambda \to \infty$, and the appropriate field parametrization is

$$\varphi_{\rm MBS} = \phi/M_{\rm Pl}\,, \tag{4.79}$$

as there are no scales on which the structure equations depend, except for the Planck scale. These configurations were thoroughly studied in the original paper by Kaup [90] and are reviewed in [159, 158]. The numerical procedure to obtain MBSs is analogous to the SBS case (App. B.1).

In the SBS setting, at $\Lambda \simeq 1.1$ the compact stable branch of SBS vanishes, and only the MBS one is left. For small Λ, the low compactness stable branch is replaced by the unstable Q-ball branch in the weak field regime. As the control parameter increases from $\Lambda \simeq 0.7$, more and more configurations in the low compactness stable branch develop *higher* compactness, up to the MBS limit of $C_{\rm MBS} \approx 0.11$. The low compactness branch presents different behaviour than the compact one, where the Planck scale regime leads to lower compactness. Note that the highest compactness is achieved in the unstable branch,

while in the stable one $C^{(s)}_{\rm MBS} \approx 0.08$.

In the weak-field approximation of MBSs, the Einstein-Klein-Gordon system reduces to the Schrödinger-Poisson system (Newtonian boson stars) [161, 281, 159, 279, 95, 282]

$$e\phi = -\frac{1}{2\mu}\nabla^2\phi + \mu\phi\Omega\,, \tag{4.80}$$

$$\nabla^2\Omega = \frac{1}{2}M_{\rm Pl}^{-2}\mu^2\phi^2\,, \tag{4.81}$$

where $e^v \approx 1+2\Omega$, $\omega \approx \mu + e$ and $\Omega \ll 1$, $e \ll \mu$. Like in the general discussion, the scalar mass can be factored out, and in addition system admits a scaling symmetry

$$\phi \to k^2\phi\,, \quad e \to k^2 e\,, \quad r \to r/k\,, \quad \Omega \to k^2\Omega\,. \tag{4.82}$$

This allows for a universal description of these objects, and for performing the numerical integration only once (for the analytic solution see [279, 283]).

Fixing the scale with $-k^2 = e/2$, we can find several useful relations between the macroscopic parameters, which will be compared with the relativistic numerical results, e.g.

$$\bar{M} = \frac{\beta Z}{\bar{R}}\,, \tag{4.83}$$

$$\bar{M} = \sqrt{2\beta^2\Big(1-w\Big)}\,, \tag{4.84}$$

$$\varphi_c = \frac{2s_0}{\Lambda}\frac{1}{\sqrt{w}}\Big(1-w\Big)\,, \tag{4.85}$$

where $s_0 = 1.022$ and $\beta = 1.753$ [279] and we find the scale-invariant radius (that encloses 99% of the BS mass) to be $Z = 5.6741$.

In Fig. 4.10, we see that the Newtonian boson star scaling gives a good description of SBS configurations in the $\varphi_c \to 0$ limit.

4.4.3 Cosine potential

In axionic physics, a cosine potential $V \sim \cos(a/f_a)$, where a is the axion field and f_a is a decay constant, is often considered. This potential arises from non-perturbative effects that generate small masses for the (initially massless) Goldstone boson associated with the spontaneous breaking of the Peccei-Quinn symmetry [**?** 89, 94]. In the strong gravity context, an axion potential can produce non-trivial effects on the stability of axion stars [94].

Inspired by axion star solutions with the axion potential, some authors have considered boson star models with similar potentials [251, 284, 163]. Note that in the absence of

beyond standard model physics that could motivate such potentials for complex scalars with $U(1)$ symmetry, one should consider these models only as proxies to understand (pseudo-real) axion stars (and only if different minima are physically sensible). As these potentials develop multiple minima and having in mind the Taylor expansion of the cos function, our previous discussion would imply that "axion boson stars" would periodically replicate SBSs for the different values of Λ corresponding to different minima, up to the Planckian threshold.

For concreteness we will consider a specific form of the potential, from [251]:

$$V = \frac{2\mu^2 f_a^2}{B}\Big[1 - \sqrt{1 - 4B\sin^2\Big(\frac{|\Phi|}{2f_{\rm a}}\Big)}\Big]\,, \tag{4.86}$$

where B is a model dependent constant [taken to be $B \approx 0.22$ in [251]]. The minimum of potential (4.86) occurs at

$$\phi_{\rm min} = f_a 2n\pi\,, n \in \mathbb{N}\,. \tag{4.87}$$

This gives an n-dependent Λ scale

$$\Lambda_n = \frac{f_a}{m_{\rm Pl}} 2n\pi\sqrt{16\pi}\,, n \in \mathbb{N}\,. \tag{4.88}$$

In Fig. 4.12, we have compared numerical results from [251] with a set of SBSs specified by the potential (4.1) and the control parameter (4.88). It is clear that the periodic features for the "axion boson stars" occur for the appropriate field values given by (4.87). The $\bar{M} - \phi(0)$ plot for the first minimum is in excellent quantitative agreement with the SBS results. The agreement, however, is not perfect as cos can only locally be approximated with the sextic polynomial. As we progress in n, the agreement worsens. This should come as no surprise, because in the analogue perspective an axion boson star "particle" has to go through an effective potential that has several peaks and troughs, unlike in the SBS case. Finally, a sufficiently large n field is in the Planck scale regime, and the final unstable branch is reached, like in the SBS case (Sec. 4.4.1).

The cosine potential example is illustrative also for the following reason: the sextic potential is non-renormalizable and thus not valid for arbitrary field values (as one needs to be within the limit of validity of the effective field theory). Close to this limit, higher-dimensional operators become relevant. The cosine potential illustrates that such terms do not modify qualitatively the macroscopic behaviour, as long as degenerate vacua (and even false ones, as we will argue next) are present.

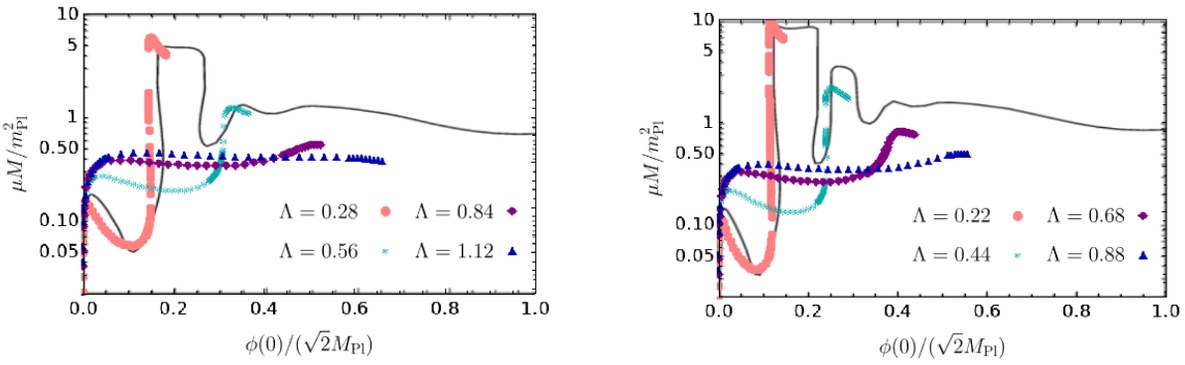

Figure 4.12: Mass-central field dependence for the cosine potential (4.86). The black line represents numerical results from [251], while dots correspond to a set of SBSs with Λ_n from Eq. (4.88) and $n = 1, 2, 3, 4$. The left panel represents cosine potential boson stars with $f_a/m_{\rm Pl} = 10^{-2.2}$, while the right one assumes $f_a/m_{\rm Pl} = 10^{-2.3}$, with the other parameters set to the values used in [251]. Note the different rescaling of the scalar with respect to the rest of this work, in accordance with the conventions of [251].

4.4.4 General sextic potential

The case of degenerate vacua is somewhat special, while a more generic scenario would allow for a non-zero false vacuum:

$$V = \mu^2|\Phi|^2 - \beta|\Phi|^4 + \xi|\Phi|^6\,, \qquad \beta > 0\,, \quad \xi > 0\,. \tag{4.89}$$

There are two useful reparametrizations of this potential. The first one, used in [263], parametrizes the potential as a deviation from the degenerate vacuum case:

$$V_6 = \phi_0^2\Big[(\mu^2 - \omega_0^2)\varphi^2(1-\varphi^2)^2 + \omega_0^2\varphi^2\Big]\,, \tag{4.90}$$
$$\varphi = \frac{|\Phi|}{\phi_0}\,, \quad \phi_0 = \sqrt{\frac{\beta}{2\xi}}\,, \quad w_0 = \frac{\omega_0}{\mu} = \sqrt{1 - \frac{\beta^2}{4\xi\mu^2}}$$

The parameter choices $\beta = 4\mu^2/\sigma_0^2$, $\xi = 4\mu^2/\sigma_0^4$ imply $\omega_0^2 = 0$ and $\phi_0 = \sigma_0/\sqrt{2}$ and reproduce the potential (4.1) i.e. the benchmark scenario of this work, while ω_0 parametrizes deviation from the simplest potential (4.1). Another useful approach is to relate ω_0 to the ratio between the potential barrier $\phi_{\rm B}$: $dV/d\phi|_{\rm B} = 0$, $d^2V/d\phi^2|_{\rm B} < 0$ and the non-trivial

minimum (false vacuum) $\phi_{\rm F}$:

$$\begin{aligned} V_6 &= \frac{\mu^3}{6\sqrt{3\xi}}\frac{\varphi_x^2}{x^3}\left(6x^2+\left(-3x^2-3\right)\varphi_x^2+2\varphi_x^4\right), \\ \varphi_x &\equiv \frac{\phi}{\phi_{\rm B}}, \quad \phi_{\rm F/B}=\frac{1}{\sqrt{3\xi}}\sqrt{\beta\pm\sqrt{\beta^2-3\xi\mu^2}}, \\ x &\equiv \frac{\phi_{\rm B}}{\phi_{\rm F}}=\sqrt{\frac{2-\sqrt{1-3\mathsf{w}_0^2}}{2+\sqrt{1-3\mathsf{w}_0^2}}}, \quad \mathsf{w}_0=\frac{\omega_0}{\sqrt{\mu^2-\omega_0^2}}. \end{aligned} \tag{4.91}$$

In this parameterization, the limits $x=1/\sqrt{3}$ ($\mathsf{w}_0=0$) and $x=1$ ($\mathsf{w}_0=1/\sqrt{3}$) interpolate between the degenerate vacua case and the scenario where the potential develops an exact stationary inflection point. Allowing for $x<1/\sqrt{3}$ (and hence imaginary w_0) makes $\varphi_{\rm F}$ a true vacuum, but we will not consider that scenario in this work[7]. In principle, Coleman's (necessary) stability criterion (c.f. Sec. 4.2) $w_0\leq w<1$ allows even for the cases where the second minimum disappears $\mathsf{w}_0>1/\sqrt{3}$ ($w_0>1/2$) and the parametrization given in Eq. (4.91) is not applicable. However, such configurations are in the deep thick wall regime, as we will argue below. Thus, defining the class of non-topological solitons that we have examined in this work by the presence of the false/degenerate vacuum in the potential is not completely rigorous. However, not only does that describe the largest part of the parameter space, but also the region where the phenomenology of these objects differs most significantly from "normal matter".

We can define (as in [263])

$$\varkappa^2=\frac{w^2-w_0^2}{1-w_0^2}, \tag{4.92}$$

so that the Minkowski Klein-Gordon equation has the same form as in Sec. 4.2.1 if one substitutes $w\to\varkappa$ and $\mathsf{r}\to\sqrt{\mu^2-\omega_0^2}r$. One can thus use both analytic and numerical results for the scalar profile of Q-balls with the simplest potential. The macroscopic properties $R, M, Q...$, however, depend explicitly on w_0 (see [263] for the relevant expressions). As w_0 increases from 0 to 1, the length scale of the boundary $\propto(1-w_0^2)^{-1/2}$ increases even if $\varkappa\ll 1$. Thus, as the false vacuum departs from 0, the thick-wall regime increasingly dominates the Q-ball behaviour.

In curved spacetime, the Klein-Gordon equation is not invariant under the above

[7] See [262] for the flat space-time case and [258] for the gravitating case.

reparametrization[8]. Instead, the system (4.34) - (4.36) can be formulated as:

$$\frac{1}{\mathsf{r}^2}\left(\mathsf{r}\, e^{-u}\right)' - \frac{1}{\mathsf{r}^2} = -\frac{\Lambda^2}{2} \times \tag{4.93}$$

$$\left[e^{-v}\varkappa^2\varphi^2 + e^{-u}(\varphi')^2 + \varphi^2(1-\varphi^2)^2 + \mathsf{w}_0^2\varphi^2(1+e^{-v})\right], \tag{4.94}$$

$$e^{-u}\left(\frac{v'}{\mathsf{r}} + \frac{1}{\mathsf{r}^2}\right) - \frac{1}{\mathsf{r}^2} = \frac{\Lambda^2}{2} \times \tag{4.95}$$

$$\left[e^{-v}\varkappa^2\varphi^2 + e^{-u}(\varphi')^2 - \varphi^2(1-\varphi^2)^2 - \mathsf{w}_0^2\varphi^2(1-e^{-v})\right],$$

$$\varphi'' + \left(\frac{2}{\mathsf{r}} + \frac{v'-u'}{2}\right)\varphi' = \tag{4.96}$$

$$e^{u}\left[(1-4\varphi^2+3\varphi^4) - \varkappa^2 e^{-v} + \mathsf{w}_0^2(1-e^{-v})\right]\varphi\,,$$

where

$$\mathsf{r} = \sqrt{1-w_0^2}\,\mu r\,, \quad \bar{m}(\mathsf{r}) = \frac{\sqrt{1-w_0^2}\mu m(r)}{m_{\rm Pl}^2}\,, \quad \Lambda = \frac{\sqrt{2}\phi_0}{M_{\rm Pl}}$$

and the other conventions from Eqs. (4.90), (4.91) and (4.92) apply, while the prime $'$ denotes spatial derivatives with respect to r. In the Minkowski limit, one has $u \to 0, v \to 0$, and the explicit dependence on w_0^2 disappears in the Klein-Gordon equation.

Self-gravitating configurations with the potential (4.89) have been considered for particular values of the coefficients in [249, 258, 250, 163]. The parameterization outlined here allows us to perform a systematic exploration of the parameter space, by varying w_0 from 0 to 1 in discrete steps using the same numerical approach as in the rest of this work (App. B.1). In Fig. 4.13 (left) we show how the compactness decreases (for fixed Λ) from the most compact configurations $w_0 = 0$ to $w_0 \to 1$. This is represented in the $w - \varphi$ parameter space by the growth of the height of the horizontal asymptote, or by that of the tipping point of the two branches in the $\tilde{\omega} - \varphi$ parameter space, as demonstrated in Fig. 4.13 (right).

The interpretation of these results is straightforward: increasing the height of the false vacuum implies thicker walls and hence larger minimal frequency/smaller maximal mass and compactness. The picture outlined in Sec. 4.3.5, where the analogue particle in the $\tilde{v}(0) = 0$ gauge does not initially feel the presence of gravity, is valid also for the general sextic potential. Henceforth, the curve $\tilde{w} - \varphi$ in the thin-wall regime is given by Eq. (4.16) (with $w \to \varkappa$):

$$\tilde{w}^2 = (1 - 4\varphi_c^2 + 3\varphi_c^4)(1 - w_0^2) + w_0^2\,. \tag{4.97}$$

The compactness dependence on w_0 can also be understood in terms of the LinEoS. Using an arguments analogous to those that lead to Eq. (4.46) one gets, for the general

[8]This is expected from the equivalence principle: in Minkowski space it is enough to know the energy difference between the two vacua, while in GR information about both vacua is needed.

sextic potential, the following estimate of the speed of sound

$$(c_s^2)_a = \frac{\varphi_c^2\left(w_0^2\left(3\varphi_c^2-4\right)+6\varphi_c^2-4\right)}{2+4\left(w_0^2-3\right)\varphi_c^2-3\left(w_0^2-4\right)\varphi_c^4}\,. \tag{4.98}$$

This equation predicts that even for $\varphi_c = 1$, the speed of sound will be subluminal when $w_0 \neq 0$. For example, the compactness of the maximum mass configuration with $w_0 = 0.24$ is numerically found to be $\mathcal{C} = 0.321$, while Eqns. (4.98) and (4.45) predict a similar value for the corresponding $\varphi_c = 1.083$: $\mathcal{C}_{\rm LinEoS} = 0.326$.

In agreement with the discussion in Sec. 4.4.2, for $\Lambda \gtrsim 1$ the configurations exhibit a MBS-like behaviour, irrespective of the value of w_0.

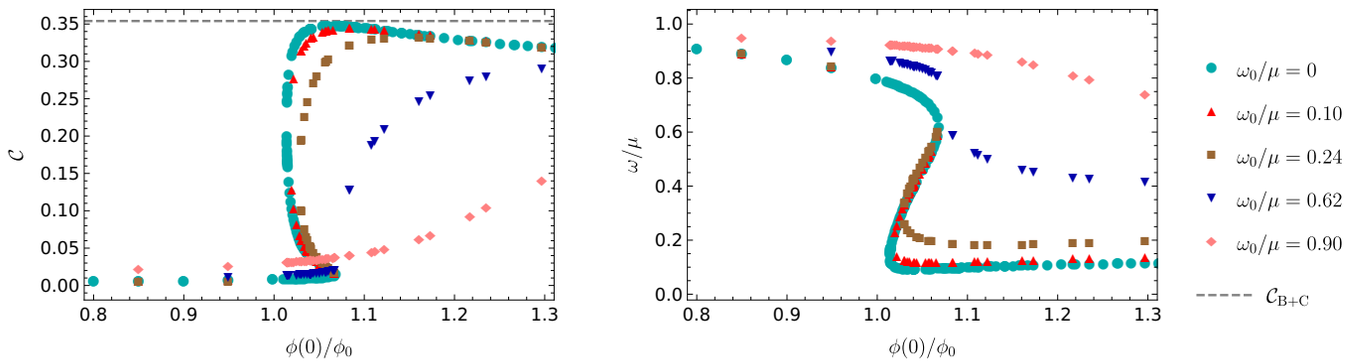

Figure 4.13: Compactness (left) and scalar frequency (right) of SBSs for the general sextic potential (4.89), in the $v(\infty) = 0$ gauge, as a function of the central field. Various values of the parameter ω_0 that describes the deviation from the degenerate vacuum case are considered, and we set $\Lambda = 0.186$, comparing also with the vanila case $\omega_0/\mu = 0$.

4.4.5 Non-polynomial quartic potential

As one last departure from the benchmark scenario of this work, we will now consider a real scalar field ϕ with the renormalizable potential

$$V_4(\phi) = \mu^2\phi^2 - g\phi^3 + \lambda\phi^4\,, \qquad g > 0\,, \quad \lambda > 0\,. \tag{4.99}$$

Q-balls with this effective potential can form in the presence of other fields [285, 180, 176], or we can consider this scenario as a proxy for a pseudo-soliton composed of real scalars. Formally (and in line with the rest of this work) we will take this model to originate from the non-polynomial potential of a $U(1)$ complex scalar

$$V_4(|\Phi|) = \mu^2|\Phi|^2 - g(|\Phi|^2)^{3/2} + \lambda|\Phi|^4\,, \tag{4.100}$$

with the ansatz (4.3) [$\Phi = \phi(r)e^{-i\omega t}$] giving a real scalar ϕ in Eq. (4.99).

Like for the generic sextic potential of Sec. 4.4.4, the potential of Eq. (4.99) admits false and degenerate vacua, and can be parameterized as a deviation from the degenerate case

$$V_4 = \phi_0^2\Big[(\mu^2-\omega_0^2)\varphi^2(1-\varphi)^2+\omega_0^2\varphi^2\Big]\,, \tag{4.101}$$
$$\varphi = \frac{|\Phi|}{\phi_0}\,, \quad \phi_0 = \frac{g}{2\lambda}\,, \quad w_0 = \frac{\omega_0}{\mu} = \sqrt{1-\frac{g^2}{4\lambda\mu^2}}\,,$$

or parameterizing the two vacua

$$\begin{aligned} V_4 &= \frac{\lambda\phi_{\rm F}^4}{3}\varphi_x^2\left(6x-4(x+1)\varphi_x+3\varphi_x^2\right)\,, \\ \varphi_x &\equiv \frac{\phi}{\phi_{\rm B}}\,, \quad \phi_{\rm F/B} = \frac{3g\pm\sqrt{9g^2-32\lambda\mu^2}}{8\lambda}\,, \quad \frac{1}{\mu^2\phi_{\rm F}^2}\frac{\lambda\phi_{\rm F}^4}{3} = \frac{1}{6x}\,, \\ x &\equiv \frac{\phi_{\rm B}}{\phi_{\rm F}} = \frac{3-\sqrt{1-8\mathsf{w}_0^2}}{3+\sqrt{1-8\mathsf{w}_0^2}}\,, \quad \mathsf{w}_0 = \frac{\omega_0}{\sqrt{\mu^2-\omega_0^2}}\,. \end{aligned} \tag{4.102}$$

In contrast to the V_6 case in flat spacetime, all configurations are (classically) stable provided that[9] $w_0^2 \geq 0$ [286, 261, 262]. Otherwise, the discussion is similar to the generic V_6 case: for $1 \gg w^2 \sim w_0^2$ Q-balls are in the thin wall regime, while for $w \sim 1$ they are in the thick wall one.

The gravitating case for this potential was considered in [257], but only for one value of (in our parametrization) $w_0 \approx 0.4$, which is in the intermediate thick wall regime. Expecting a similar phenomenology with respect to $w_0 \neq 0$ as in Sec. 4.4.4, we have focused only on the $w_0 = 0$ case (degenerate vacua), noting that the above parametrization allows for a straightforward systematic exploration with respect to the height of the false vacuum.

In the thin-wall gravitating limit, the relations among the macroscopic parameters are very similar to those of SBSs with V_6 [Eq. (4.1)], as can be seen in Fig. 4.14 for the mass and Fig. 4.15 for the compactnesses. This should come as no surprise as the presence of the non-trivial vacuum renders the equation of state linear in the thin-wall regime and the same arguments from Sec. 4.3.4 apply. For example, the estimate of the speed of sound, in analogy with the Eq. (4.46), is

$$(c_s^2)_a \approx \frac{\varphi_c(4\varphi_c-3)}{12\varphi_c^2-15\varphi_c+4}\,. \tag{4.103}$$

From the above and the LinEoS results (4.45) we can predict $\mathcal{C}_{\rm LinEoS} = 0.337$ for the

[9] Quantum effects can influence stability in part of the parameter space for small Q-balls [180]. Note that stable solutions (under small perturbations) can exist also for $w_0^2 < 0$ [261, 262].

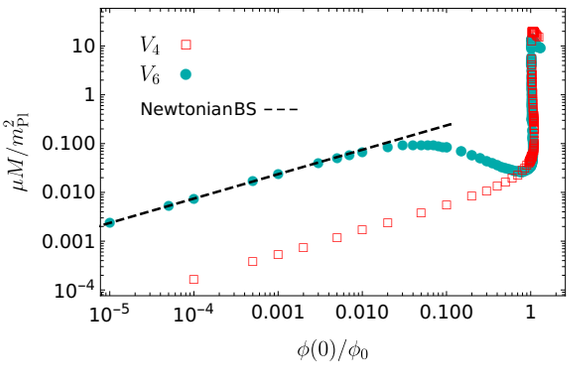

Figure 4.14: Mass vs central field of SBSs in the case of the quartic potential (4.99), compared with the benchmark case (4.1) for the same control parameter $\Lambda = 0.186$. We also show the NBS scaling (4.85) (black, dashed).

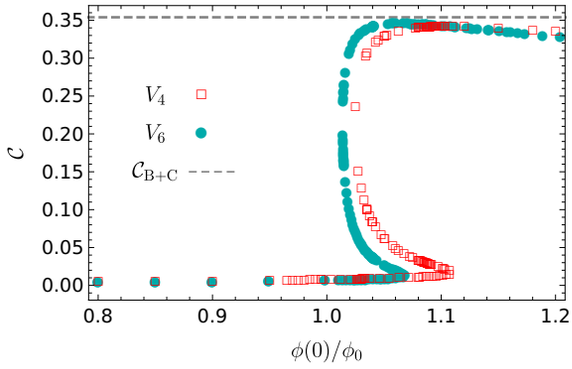

Figure 4.15: Compactness vs central field of SBSs in the case of the quartic potential (4.99), compared with the benchmark case (4.1) for the same control parameter $\Lambda = 0.186$. The causal Buchdahl bound $\mathcal{C}_{\rm B+C}$ is indicated as a gray and dashed line.

compactness of the maximaum mass configuration with $\Lambda = 0.186$ ($\varphi_c = 1.053$), whose true value is $\mathcal{C} = 0.331$.

The presence of only one turning point in the $\bar{M} - \varphi_c$ diagram [Fig. 4.14] indicates that only one stable branch is inherited from flat spacetime, in contrast with the V_6 case. This branch is, as in the V_6 case, succeeded by the compact unstable branch, as elaborated using catastrophe theory arguments in [257]. The fact that both SBSs with a quartic potential and MBSs have only one stable and one unstable branch, noted in [257], is in fact accidental, as the MBS stable zone originates from the quantum pressure, while the stable zone of SBSs with the V_4 potential is inherited from the corresponding Q-balls. This is the reason why the $\bar{M} - \varphi_c$ relation in the low compactness stable branch for the sextic potential is described by the NBS scaling (4.85) in Fig. 4.14, while the quartic is not. This difference can be also illustrated by the $w - \varphi$ diagram in Fig. 4.16: for the quartic potential one can observe a much sharper decline of the $w(\varphi_c)$ curve from $w = 1$ than with the V_6 potential. Convergence between the two potentials occurs, manifest in both $\bar{M} - \varphi_c$ and $w - \varphi_c$ representations (Figs. 4.14, 4.16), in the compact limit, where gravity does not discriminate between the highest powers of the scalar potential. In agreement with Sec. 4.3.5, the $\tilde{w}(\varphi_c)$ curve in the thin wall regime matches well the Q-ball result:

$$\tilde{w} = \sqrt{1 - 3\varphi_c + 2\varphi_c^2}\,. \tag{4.104}$$

4.5 Conclusion

In this work we have provided a comprehensive analysis of the self-gravitating solitonic objects made of complex scalars that obey potentials with false/degenerate vacua. We

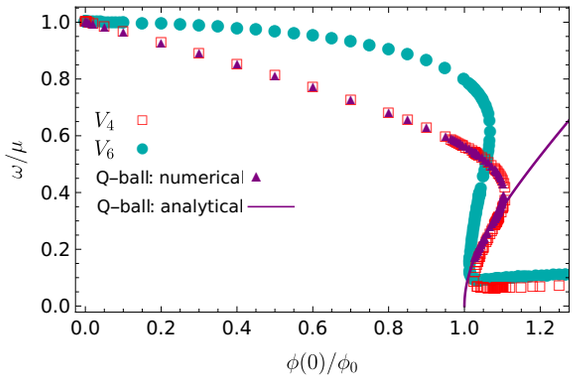

Figure 4.16: SBSs scalar frequency as a function of the central field in the case of the quartic potential (4.99), compared with the benchmark case (4.89) for $\Lambda = 0.186$. Q-ball (with the quartic potential) results, both numerical and analytical, are indicated with the purple triangles and the purple line, respectively.

have built on previous studies by reinterpreting and improving them, and also by providing novel results. In more detail, we find that in the thin wall regime, because of the presence of the non-trivial vacuum, these objects can achieve high compactness, saturating the Buchdahl limit with the causality constraint $\mathcal{C}_{\rm B+C} = 0.354$ (Sec. 4.3.4). These values are the highest that have been found so far for motivated ECO models. This results also provides a new perspective on SBSs - objects with an incredibly stiff equation of state, where the information on local disturbances is transmitted at almost the speed of light.

We have established the robustness of this picture by checking various potentials considered in the literature - general sextic, quartic and cosine potentials (Sec. 4.4). Although in this work we have stressed the general features of SBSs, particular models considered in the literature present some differences. For the ease of navigating amongst different models, we summarise in Table 4.2 the potentials that we have considered in this work. In addition, the bubble-like (in the thin-wall regime) behaviour of the scalar field allows for an analytic description of these configurations, which we have presented for the simplest case of degenerate vacua (Sec. 4.3.5), although we expect that this description can be extended (in a straightforward manner) to the other potentials considered in Sec. 4.4. This analytic solution can be used as an approximation to the numerical one, and it has helped us obtain analytic control of SBS solutions for arbitrarily small values of $\sigma_0/M_{\rm Pl}$.

In the low compactness limit, the configurations are stabilized either by gravity (thus behaving as MBS or NBS, cf. Sec. 4.4.2), or by self-interactions (like in the case of the quartic potential, cf. Sec. 4.4.5). For field values close to the Planck scale, the compact stable branch shrinks, and only the low-compactness one, described by the MBS model, survives (cf. Sec. 4.4.1).

One follow up to this project is to generalize our formalism to study scalar-fermion solitonic configurations as well as higher-spin fields and pseudo-solitions, motivated by

Boson star model	Potential	$M_{\rm Pl} \to \infty$	$\lvert\Phi\rvert \ll M_{\rm Pl}$	$\mathcal{C}_{\rm max}$
MBS	$\mu^2\lvert\Phi\rvert^2$	/	NBS	0.11
SIBS	$\mu^2\lvert\Phi\rvert^2 + \lvert\lambda\rvert\lvert\Phi\rvert^4$	/	NBS-SI	0.16
SBS: simplest	$\mu^2\lvert\Phi\rvert^2\left(1 - 2\frac{\lvert\Phi\rvert^2}{\sigma_0^2}\right)^2$	Q-ball: simplest	NBS/MBS	$\lesssim 0.354$
SBS: sextic	$\mu^2\lvert\Phi\rvert^2 - \lvert\beta\rvert\lvert\Phi\rvert^4 + \lvert\xi\rvert\lvert\Phi\rvert^6$	Q-ball: sextic	NBS/MBS	$\lesssim 0.354 - 0.06 w_0^2$
SBS: cosine	$\lvert\alpha\rvert\left[1 - \sqrt{1 - \lvert\beta\rvert \sin^2\left(\frac{\lvert\Phi\rvert}{\sigma_0}\right)}\right]$	Q-ball: cosine	NBS/MBS	$\lesssim 0.354$
SBS: quartic	$\mu^2\lvert\Phi\rvert^2 - \lvert g\rvert(\lvert\Phi\rvert^2)^{3/2} + \lvert\lambda\rvert\lvert\Phi\rvert^4$	Q-ball: quartic	Q-ball: quartic	$\lesssim 0.354 - 0.2 w_0^2$

Table 4.2: Models considered in this work, their potentials and main properties (including the non-gravitating limit $M_{\rm Pl} \to \infty$, the low compactness limit $|\Phi| \ll M_{\rm Pl}$ and the maximal compactness $\mathcal{C}_{\rm max}$). For the quartic SBS we have quoted $\mathcal{C}_{\rm max}$ for the general potential (4.101) and both general quartic and sextic potential expressions are valid for small w_0. Value for $\mathcal{C}_{\rm max}$[SIBS] is taken from [268]. Acronyms: mini BS (MBS), self-interacting BS (SIBS), soliton BS (SBS), Newtonian BS (NBS), self-interacting Newtonian BS (NBS-SI).

axion or vector DM [89, 84], which could form through different channels and possibly develop other interesting phenomenology [172, 173, 174, 175, 176]. From the astroparticle physics perspective, it is also important to understand what class of Q-ball production mechanisms can lead to a significant fraction of compact objects, and how can the presence or absence of SBS signatures in present and future GW detectors help us constrain their formation mechanism and possibly gain information on the early universe. On the phenomenological side, it is therefore imperative to systematically explore the behaviour of SBSs in binaries and their GW signatures [166], also for low-$\mathcal{C}$ configurations [287]. Work addressing the last topic is reported elsewhere [2].

Chapter 5

Gravitational waves and kicks from the merger of unequal mass, highly compact boson stars

5.1 Introduction

We are well into the era of gravitational wave (GW) astronomy with the rapidly growing catalog of GW events detected by the LIGO-Virgo collaboration [288, 289].

With the very recent release of the third GW transient catalog [290], the total number of reported coalescences increased to 90. Some of the more remarkable events detected to date include:

- GW190412 [291], a binary black hole (BBH) with asymmetric component masses, showing evidence for higher harmonics in its GW signal;
- GW190425 [292], identified with a binary neutron star (NS) merger lacking evidence of an electromagnetic counterpart;
- GW190521 [293], a BBH with a total mass greater than 150 solar masses, which is the most massive binary yet detected, in which the posterior distribution of the primary mass is nearly entirely in the pair-instability supernova mass gap where BHs are not expected to form from the collapse of massive stars;
- GW190814 [294], a highly asymmetric system consistent with the merger of a 23 solar mass black hole (BH) with a 2.6 solar mass compact object, making the latter either the lightest BH or the heaviest NS observed in a compact binary;
- GW200105 and GW200115 [295], which are the first detections consistent with a NS-BH merger.

The planned upgrades by the LIGO-Virgo collaboration and the addition of the KAGRA detector [296] promise even more exciting observations in the future.

A primary target of GW observations is the merger of very compact objects, with BHs and NSs being the most natural candidates. However, a number of other hypothetical compact objects have been proposed, called exotic compact objects (ECOs) [297, 146], discussed in Ch. 2. Phenomenological studies of ECOs are required to perform actual searches for their signatures. No evidence for such ECOs has yet been found, but, because they are expected to be too dim electromagnetically, it is mostly through GW detections that we can hope to observe them [146]. In particular, we will focus on (soliton) boson stars [(S)BS], extensively discussed in Ch. 4.

Collisions of BSs have been studied extensively, including: head-on and orbital mergers of mini-BSs [298, 299], head-on mergers of oscillatons [**?** **?**], orbital collisions of SBSs [253, 166, 254], and head-on and orbital mergers of Proca stars [300, 301, 302]. The merger of ECOs can be studied within various dark matter scenarios as well, as for example: mergers between a NSs and a star made of axions, [303, 105, 304] or mergers of binary NSs containing a small fraction of dark matter [305] modeled using fermion-BSs [306].

Motivated by the recent GW detections of very unequal mass binary mergers, we study here the coalescence of unequal mass BS binaries, focusing on their dynamics and GW radiation. As in our previous works [253, 166, 254], we adopt the nontopological SBS potential [167] to construct our asymmetric binaries because: (i) it allows for very compact configurations that reach a maximum compactness (see below for its definition) in the stable branch of approximately $\mathcal{C} \approx 0.35$ [1, 307] (see Ch. 4), and (ii) one can construct binaries with a large mass ratio. Indeed, defining the mass ratio $q \equiv m_1/m_2$ such that $m_1 > m_2$, we can produce compact binaries with a mass ratio ranging[1] approximately from 1 to 45. Here, we focus on binaries within the range $q \in [2, 23]$. We note that in contrast to the difficulties encountered when evolving BBH with large mass ratios [308, 309, 310, 311], these evolutions require no change to the choice of coordinates, namely gamma-driver shift condition, nor an exceptionally high resolution. The reason for this difference is because the radii of SBSs even with vastly different masses are of the same order, whereas the radius of the BH scales linearly with the mass, and therefore a large mass ratio in a BH binary necessarily implies a large separation of length scales.

Our mergers of unequal mass SBSs produce either a non-rotating BS or a spinning BH, as in the equal-mass cases [166]. In the former cases, all the angular momentum is emitted to infinity through scalar field and GW radiation, while in the latter case, after performing a very long-term simulation, we find no indication of a scalar cloud synchronized with the rotation of the remnant BH, as found in Ref. [312] (although such a

[1]SBSs in general admit two stable and two unstable branches [258, 1]. Here we focus on the more massive stable branch, while the other stable branch corresponds to the weak-field regime of mini BSs for our choice of the potential parameters [1]. See Ch. 4 for details.

cloud was produced from a fine-tuned initial conditions). For one of our simulations with large angular momentum, a blob of scalar field is ejected after the merger, producing a significant kick velocity of the remnant. Note that, this blob ejection has already been observed in SBS binaries of equal mass [166].

This work is organized as follows: in Sec. 5.2, we review the construction of initial data for binary BSs and numerical implementation. In Sec. 5.3, the coalescence of unequal-mass BS binaries is studied in detail. The GWs produced by these systems are explored in Sec. 5.4, in particular, analyzing the imprint of higher-order modes in the signal and the post-merger frequencies of the remnant's signal. In Sec. 5.5, we summarize our results. In contrast with the rest of this thesis, and as appropriate in numerical relativity, here we will use geometric units in which $G = c = 1$ unless otherwise stated, while $\hbar \neq 1$.

5.2 Setup

In this section, we briefly summarize the construction of binary BSs in quasicircular orbits that constitute the initial data. For a description of SBS structure, we refer the reader to Ch. 4. We also outline the numerical methods and grid setup employed to perform the simulations. Notice that our setup is very similar to the one used in Ref. [166] (in the rest of this Ch. we will refer to this reference as Paper I) for studying equal-mass binary BSs.

5.2.1 Binary initial data

The procedure to construct the initial data for a binary BS is the same as in Paper I, that is, a superposition of two boosted, isolated, SBSs.

The solution of a single SBS, whose potential is given by Eq. (4.96) is constructed as described in Ch. 4, by adopting the usual harmonic ansatz for the scalar field $\Phi = \phi(r)\, e^{-i\omega t}$ with a real frequency ω. For the ease of following, let us provide a short summary of such construction (see Ch. 4 for the detailed description): assuming stationarity and spherical symmetry, the EKG equations reduce to a set of ordinary differential equations which can be solved numerically with a shooting method. Integrating from the center with a given central value of the scalar field ϕ_c and frequency ω, one looks for solutions satisfying regularity and boundary conditions. The resulting BS equilibrium configurations can be characterized by their mass and radius. However, because the scalar field only vanishes asymptotically as it decays exponentially, the definition of its radius is necessarily somewhat ambiguous (see App. B.2). Following previous work and Ch. 4, we can define the effective radius R_M as the radius within which 99% of the total mass is contained, i.e. $m(R_M) = 0.99M$. Consequently, we define the compactness as $\mathcal{C} \equiv M/R_M$. As a reference, the compactness for a Schwarzschild BH is $\mathcal{C} = 0.5$ and $\mathcal{C} \approx 0.1 - 0.2$ for NSs. In numerical simulations, it is however more convenient to estimate the radius of the final

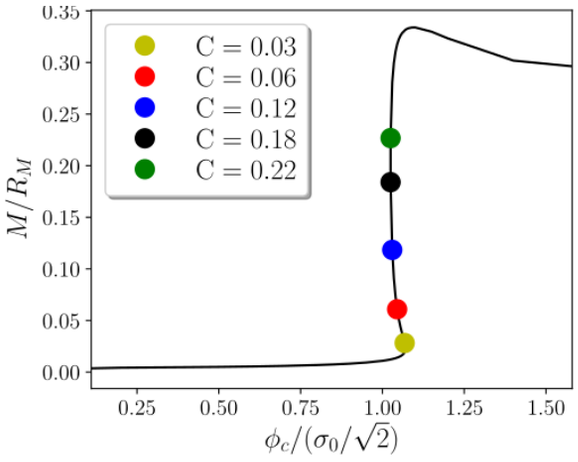

Figure 5.1: Compactness as a function of the central value of the scalar field ϕ_c for isolated, nonrotating BSs with $\sigma_0 = 0.05$. Circular markers refer to the equilibrium configurations used in this work to construct initial data for BS binaries [cf. Table 5.1]. The radius R_M is defined as that containing 99% of the mass of the star.

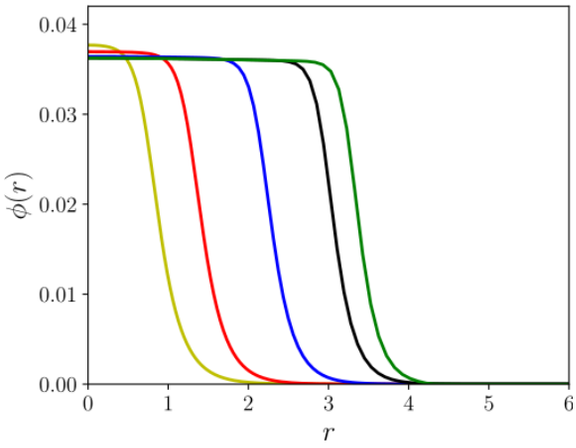

Figure 5.2: Profile of the scalar field as a function of the isotropic radius for the different configurations.

remnant through the radius that contains 99% of the Noether charge, R_N, so we will use this definition when required. The radius of the remnant is calculated with respect to its center of mass. Finally, let us note that in our units (in which the scalar field is dimensionless), m_b has the dimensions of an inverse length, $\mu = m_b\hbar$ is the bare mass of the scalar field, whereas σ_0 is dimensionless. We define $\lambda \equiv \sigma_0\sqrt{8\pi}$ and set $m_b\lambda = 1$ for the rest of the Ch.. However, in some occurrences we shall re-insert the proper factors of $m_b\lambda$.

The maximum mass of static configurations in this model is [see Eq. (4.31)]

$$M_{\rm max} \approx 5M_\odot \left[\frac{10^{-12}}{\sigma_0}\right]^2 \left[\frac{500\,{\rm GeV}}{m_b\hbar}\right] , \tag{5.1}$$

where the scaling with m_b^{-1} is exact, whereas the scaling with σ_0^{-2} is approximately valid only in the $\sigma_0 \ll 1$ limit. Thus, depending on (m_b, σ_0) the model supports self-gravitating configurations across a wide mass range.

Paper I presented a sequence of isolated BS solutions characterized by the central value of the scalar field ϕ_c that we use to construct our unequal mass binaries here. In the top panel of Fig. 5.1, the compactness $\mathcal{C}$ is shown as a function of ϕ_c. The circular markers denote the five representative BSs employed in this Ch. The bottom panel of Fig. 5.1 displays the radial profile of the scalar field for these isolated solutions, while Table 5.1 lists the key properties of these configurations.

Notice that these solutions can be rewritten in terms of the following dimensionless

$\mathcal{C}$	$\phi_c/(\sigma_0/\sqrt{2})$	$Mm_b\lambda$	$N(m_b\lambda)^2$	$(R_M, R_N)m_b\lambda$	$\omega/(m_b\lambda)$	I/M^3	$k_{\rm tidal}$
0.03	1.065	0.0463	0.01653	$(1.507, 1.380)$	2.129620346	245.3	136494
0.06	1.045	0.1238	0.0605	$(2.0334, 1.8288)$	1.545745909	84.9	8420
0.12	1.030	0.3650	0.2551	$(3.0831, 2.8360)$	1.066612350	27.8	332
0.18	1.025	0.7835	0.7193	$(4.2572, 3.9960)$	0.790449025	12.5	41
0.22	1.025	1.0736	1.1147	$(4.9647, 4.7068)$	0.685760351	8.34	20

Table 5.1: *Characteristics of SBS models with* $\sigma_0 = 0.05$. The table shows: • the compactness $\mathcal{C}$, • the central value of the scalar field $\phi_c/(\sigma_0/\sqrt{2})$, • the ADM mass $Mm_b\lambda$, • the Noether charge $N\left(m_b\lambda\right)^2$, • the radius of the star (the radius containing 99% of either the mass or of the Noether charge for R_M or R_N, respectively), and • the angular frequency of the field in the complex plane, $\omega/\left(m_b\lambda\right)$, in dimensionless units. In the last two columns, we give • the normalized, Newtonian, moment of inertia (where $I = \int \rho^2\, dm$, where ρ is the distance from the axis of rotation), and • the dimensionless tidal Love number, $k_{\rm tidal}$, as computed in Refs. [150, 252]. For a NS with an ordinary equation of state and $\mathcal{C} \approx 0.1$, $k_{\rm tidal} = \mathcal{O}(200)$ while $k_{\rm tidal} = 0$ for a BH.

quantities [248]

$$M(m_b\lambda), \quad N(m_b\lambda)^2, \quad r(m_b\lambda), \quad \omega/(m_b\lambda)\,, \tag{5.2}$$

recalling that $\lambda = \sigma_0\sqrt{8\pi}$. In terms of these parameters, the equations become independent of m_b, and hence m_b serves to set the units of the physical solution. Again, the linear scaling in m_b in the above expressions is exact, whereas that with respect to λ is approximately valid only in the $\sigma_0 \ll 1$ limit. For the chosen value, $\sigma_0 = 0.05$, this scaling is already a good approximation, and so smaller values of σ_0 can be studied simply by applying such a rescaling. Here we restrict ourselves to $\sigma_0 = 0.05$, which sufficiently fulfills the condition $\sigma_0 \ll 1$ and also allows for very compact, stable configurations. See Sec. 4.3.5 for the details.

The initial data for the BS binary follows the procedure described in Ref. [253] and Paper I. Once the isolated BSs are constructed in spherical coordinates, the solution is extended to Cartesian coordinates, with the centers of the stars located at along the y-axis at $(0, y_c^j, 0)$, so that the center of mass of the system is located at the origin.[2] A Lorentz transformation is performed to boost each star along the $\pm x$-directions, and finally the boosted solutions for both stars are superposed to obtain our binary initial data. Obviously, this superposition is only an approximate solution that does not satisfy exactly the constraints at the initial time (see Ref. [255] for a partial solution in case of equal mass binaries of BSs). However, our evolution scheme enforces an exponential decay of this constraint violation dynamically (e.g., see Fig. 10 in Ref. [253]).

[2]Here we define the center of mass using the masses of isolated configurations listed in Table 5.1. Constraint violation transient will change these masses, see the discussion of "effective" configurations below.

Binaries	q	ν	$y_{\rm c}^{(1)}$	$y_{\rm c}^{(2)}$	$v_x^{(1)}$	$v_x^{(2)}$	$M_0 m_b \lambda$	$J_0 (m_b \lambda)^2$	$t_{\rm c}$	$t_{\rm m}^{\rm ret}$
C003 - C022A	23.2	0.039	-9.58	0.42	-0.34	0.02	1.16	0.229	790	811
C003 - C022	23.2	0.039	-9.58	0.42	-0.34	0.02	1.16	0.229	790	808
C006 - C022	8.6	0.093	-8.96	1.04	-0.36	0.05	1.34	0.668	510	539
C012 - C022	2.9	0.189	-8.95	3.05	-0.33	0.136	1.90	2.388	370	402
C012 - C018	2.1	0.21	-8.18	3.81	-0.26	0.135	1.36	1.488	660	684

Binaries	remnant	$M_{\rm r} m_b \lambda$	$R_{\rm N} m_b \lambda$	$M_r \omega_{\rm r}^0$
C003 - C022A	BS	1.07	4.50	0.218
C003 - C022	BS	1.13	4.76	0.228
C006 - C022	BS	1.24	5.0	0.239
C012 - C022	BH	1.89	3.48	0.467
C012 - C018	BS	1.17	4.34	0.250

Table 5.2: *Properties of unequal binary BS models and of the final remnant.* Each case is characterized by: (Top) • the compactness $\mathcal{C}$ of the individual BSs in the binary, • the mass-ratio q, • the symmetric mass ratio ν, • the two initial centers $y_c^{(i)}$, • the initial velocities of the boost $v_x^{(i)}$, • the ADM mass M_0 of the system, and • the orbital ADM angular momentum J_0 of the system, after the constraint-violating transient respectively. The merger and remnant are characterized by: • the coordinate time of contact of the two stars t_c (defined as the time at which the individual Noether charge densities make contact for the first time), • the merger retarded time (defined as the time when the maximum of the modulus of the $\Psi_4^{2,2}$ is produced minus the travel time to the sphere where it is measured) (Bottom) • the type of final remnant, • the remnant mass $M_r m_b \lambda$, • the remnant radius $R_N m_b \lambda$ (i.e., containing 99% of the Noether charge), and • the main GW frequency $M_r \omega_r^0$ in the post-merger. When the final remnant is a BH, the radius is computed from the expression for Kerr BHs, $R_H = M_r(1+\sqrt{1-a^2})$, where $a = J_r/M_r^2 \approx 0.5$ is the dimensionless spin.

In contrast with Paper I where the positions and initial velocities of each binary were anti-symmetric (i.e., velocities with the same magnitude but opposite direction), for these unequal cases we have set those parameters as follows: given an initial separation we have calculated the 2nd order post-Newtonian orbital velocity [313] such that the system would be in quasicircular orbit and the velocity of the center of mass would be close to zero. Then, we modify these velocities by adding a tiny amount of linear drift velocity to account for the finite initial orbital distance and higher-order relativistic effects, and fix this drift velocity such that the velocity of the binary center of mass is close to zero. The positions and velocities of each binary system considered in this work, together with other parameters of our simulations, are presented in Table 5.2.

As mentioned, our binary initial data is only approximate, but constraint violations quickly propagate off the grid by our evolution scheme. Hence, it makes sense to evaluate the global characteristics of the initial data not at the initial time but instead just after the constraint-violating transient. We therefore extract numerically the ADM mass, M_0, of the spacetime after the transient, and, assuming that the mass ratio remains constant

through the transient, we decompose this mass into the constituent "effective" masses as

$$\tilde{M}_1 = \left(\frac{q}{q+1}\right) M_0\,, \quad \tilde{M}_2 = \left(\frac{1}{q+1}\right) M_0\,. \tag{5.3}$$

Notice that this calculation tacitly assumes that, even after the constraint violation transient (approximately) ends, stars are sufficiently separated so that GR nonlinearities are sub-leading. During this transient regime, we note that the masses of the constituent stars increase which results in a decrease in the number of orbits.

Furthermore, we can construct fitting formulae for the compactness, $\mathcal{C}(M)$, and particle number, $N(M)$, as functions of BS mass from the equilibrium configurations of isolated BSs (in particular, from the numerical results of Ch. 4). We obtain

$$\begin{aligned} \mathcal{C}(M) &\approx 0.0157 + 0.376M - 0.3M^2 + 0.136M^3 \\ &\quad -0.0195M^4\,, \end{aligned} \tag{5.4}$$

$$N(M) \approx -0.0187 + 0.6221M + 0.3872M^2\,. \tag{5.5}$$

With the above functions, one can calculate the "effective" Noether charges and compactnesses of the stars in our binaries as a function of their "effective" masses, respectively. In Table 5.3 , we provide this data for all configurations consider in this work and Paper I. We also provide the relative differences between the properties of the isolated initial data and the "effective" ones. Comparing the total Noether charge in the system, N_0, with the sum of the individually calculated charges, $N(\tilde{M}_1) + N(\tilde{M}_2)$, provides a test of the consistency of this approach. As explained below in Sec. 5.3.2, the "effective" initial data presented here agrees roughly with our initial data after the constraint-violating transient.

5.2.2 Numerical setup and analysis

The computational code, generated by the *Simflowny* platform [314, 315, 316, 317], runs under the SAMRAI infrastructure [318, 319, 320], which provides parallelization and the adaptive mesh refinement (AMR) required to resolve the different scales in the problem. We use fourth-order spatial, finite difference operators to discretize the EKG equations, which are evolved in time using a fourth-order Runge-Kutta integrator [321].

Our computational domain ranges within $[-264, 264]^3$ and contains 8 levels of refinement. Each level has twice the resolution of its coarser parent level, achieving a resolution of $\Delta x_8 = 0.03125$ on the finest grid. We use a Courant factor $\lambda_c \equiv \Delta t_l/\Delta x_l = 0.4$ on each refinement level l to ensure the stability of the numerical scheme.

We analyze some relevant global physical quantities from our simulations, such as the Arnowitt-Deser-Misner (ADM) and the Komar mass, the ADM angular momentum, and the Noether charge, computed as in Ref. [253]. We focus our attention mainly on

Binaries	$\tilde{M}_1 m_b \lambda$	$\Delta M_1/\tilde{M}_1$	$\tilde{C}_1$	$\Delta C_1/\tilde{C}_1$	$\tilde{N}_1(m_b\lambda)^2$	$\Delta N_1/\tilde{N}_1$
C006 - C006	0.13	0.066	0.061	0.0099	0.071	0.14
C012 - C012	0.43	0.15	0.13	0.093	0.32	0.21
C018 - C018	1.0	0.22	0.21	0.14	1.0	0.29
C022 - C022	1.6	0.32	0.28	0.20	1.9	0.42
C003 - C022	0.048	0.034	0.033	0.093	0.012	0.38
C006 - C022	0.14	0.11	0.063	0.044	0.076	0.20
C012 - C022	0.49	0.25	0.14	0.16	0.38	0.32
C012 - C018	0.44	0.17	0.13	0.10	0.33	0.23
Binaries	$\tilde{M}_2 m_b \lambda$	$\Delta M_2/\tilde{M}_2$	$\tilde{C}_2$	$\Delta C_2/\tilde{C}_2$	$\tilde{N}_2(m_b\lambda)^2$	$\Delta N_2/\tilde{N}_2$
C006 - C006	0.13	0.066	0.061	0.0099	0.071	0.14
C012 - C012	0.43	0.15	0.13	0.093	0.32	0.21
C018 - C018	1.0	0.22	0.21	0.14	1.0	0.29
C022 - C022	1.6	0.32	0.28	0.20	1.9	0.42
C003 - C022	1.1	0.035	0.22	0.0028	1.2	0.034
C006 - C022	1.2	0.11	0.23	0.044	1.3	0.13
C012 - C022	1.4	0.24	0.25	0.14	1.6	0.32
C012 - C018	0.92	0.15	0.20	0.10	0.88	0.19

Table 5.3: *Effective properties of the individual stars within the binary after the constraint violating transient.* Tildes represent "effective" quantities of the stars in the binary. For the equal mass binaries of Paper I and the unequal mass binaries studied here: • the mass from Eq. (5.3), • the compactness $\mathcal{C}$ from Eq. (5.4), • the Noether charge from Eq. (5.5), • for each of these, their fractional differences, $\Delta X/X$, with respect to the initial data for the isolated star used in the construction of the binary.

the gravitational radiation represented by the strain h, which is the quantity directly observable by GW detectors. We consider first the Newman-Penrose scalar Ψ_4, which can be expanded in terms of spin-weighted $s = -2$ spherical harmonics [322, 323] as

$$r\Psi_4(t, r, \theta, \phi) = \sum_{l,m} \Psi_4^{l,m}(t, r)\, {}^{-2}Y_{l,m}(\theta, \phi), \tag{5.6}$$

where the coefficients $\Psi_4^{l,m}$ are extracted and calculated on spherical surfaces at different extraction radii. The relation between this scalar and the two polarizations of the strain is given by $\Psi_4 = \ddot{h}_+ - i\,\ddot{h}_\times$. The components of the strain in the time domain can be calculated by performing the inverse Fourier transform of the strain in the frequency domain, $h^{l,m}(t) \equiv \mathcal{F}^{-1}[\tilde{h}^{l,m}(f)]$, where a high-pass filter has been applied in the frequency domain in order to attenuate the signal with frequencies lower than the initial orbital frequency [324, 253]. The instantaneous angular frequency of each GW mode can be calculated easily from Ψ_4 as

$$\omega_{\rm GW}^{l,m} = -\frac{1}{m}\mathfrak{Im}\left(\frac{\dot{\Psi}_4^{l,m}}{\Psi_4^{l,m}}\right) \ , \quad f_{\rm GW}^{l,m} = \frac{\omega_{\rm GW}^{l,m}}{2\pi}. \tag{5.7}$$

We will refer to $\omega_{\rm GW}$ as the one given by the dominant mode $l = m = 2$.

The mass, the angular momentum, and Ψ_4 are calculated on spherical surfaces at different extraction radii between $R_{\rm ext} = 100$ and $R_{\rm ext} = 200$, which are located far away from the sources in the wave zone.

5.3 Dynamics for unequal-mass BS binaries

We have evolved four unequal mass binary BS cases, {C003-C022, C006-C022, C012-C022, C012-C018}, covering mass ratios $q \equiv m_1/m_2$ roughly between 2 and 23. Additionally, we have studied a variation of the most extreme case, C003-C022A, in which the heavier BS has been transformed into an anti-BS (see Ref. [2] for the details). In what follows, we describe first qualitatively the dynamics for all the cases and then analyze the GWs produced by these mergers in the next section.

5.3.1 Binary dynamics in the inspiral

We display some representative snapshots along the equatorial plane to characterize the dynamics of these binary evolutions. In particular, the Noether charge densities in Fig. 5.3 show the dynamics of the condensed bosons, whereas the scalar field norm in Fig. 5.4 shows the dynamics of the scalar field generally.

The binaries in C003-C022A and C003-C022 complete five full orbits before colliding,

C006-C022 and C012-C018 complete three orbits, and C012-C022 performs just two. While such a short inspiral limits their use for guiding templates, the inspiral is long enough for constraint violations resulting from the construction of the initial data to propagate away.

During the inspiral, the spacetime curvature is dominated mainly by the heavier BS, which moves in a spiral trajectory very close to the origin (i.e., see the leftmost column of Fig. 5.3), while the lighter one induces a perturbation orbiting around the most massive object. This effect is especially pronounced in the four most unequal mass cases in which the heavier BS accounts for at least 75% of the binary mass. During the inspiral, the scalar field constituting each star has no significant overlap (see the first column of Fig. 5.4), and therefore nonlinear scalar interactions only play a significant role inside the stars. Roughly speaking, the BSs behave then like point particles with moderate deviations produced by the tidal deformations. As the mass ratio approaches unity, the binary behaves similarly to the equal-mass cases of Paper I. In particular, C012-C018 with $q = 2.1$ resembles those equal-mass cases.

The aforementioned deviations due to tidal deformations can be estimated by looking at the quadrupole-moment tensor $Q^{(i)}_{ab}$ of the i-th object induced by the tidal-field tensor $G^{(j)}_{ab}$ produced by the j-th object ($i, j = 1, 2$) [325, 326],

$$Q^{(i)}_{ab} = \lambda_i G^{(j)}_{ab} \sim \lambda_i \frac{m_j}{r^3}\,, \tag{5.8}$$

where r is the orbital distance and $\lambda_i = \frac{2}{3} m_i^5 k^{(i)}_{\rm tidal}$ is the tidal Love number of the i-th object, with $k^{(i)}_{\rm tidal}$ being its dimensionless counterpart. Hence, the dimensionless quadrupole moment, $\bar{Q}_i = |Q^{(i)}_{ab}|/m_i^3$, reads

$$\bar{Q}_1 \sim k^{(1)}_{\rm tidal} \frac{q^2}{(1+q)^3} \frac{M_0^3}{r^3}\,, \tag{5.9}$$

$$\bar{Q}_2 \sim k^{(2)}_{\rm tidal} \frac{q}{(1+q)^3} \frac{M_0^3}{r^3}\,, \tag{5.10}$$

where $M_0 = m_1 + m_2$ is the binary total mass. In the large mass-ratio limit, $q \gg 1$, the tidally-induced quadrupole moments of the primary and of the secondary are suppressed by a factor q^{-1} and q^{-2}, respectively. For example, for a fixed value of $k^{(i)}_{\rm tidal}$, the tidally-induced quadrupole moment of the primary for $q = 23$ is suppressed by a factor 3 relative to $q = 1$, whereas that of the secondary is even a factor ~ 100 smaller. Overall, tidal effects on the secondary object are less relevant than those on the primary.

5.3.2 Final fate of the binary merger

If the system is sufficiently massive such that the remaining mass after merger exceeds the maximum stable BS mass (i.e., $M_r \geq M_{\rm max} \approx 1.85/(m_b\lambda)$), one expects the system to

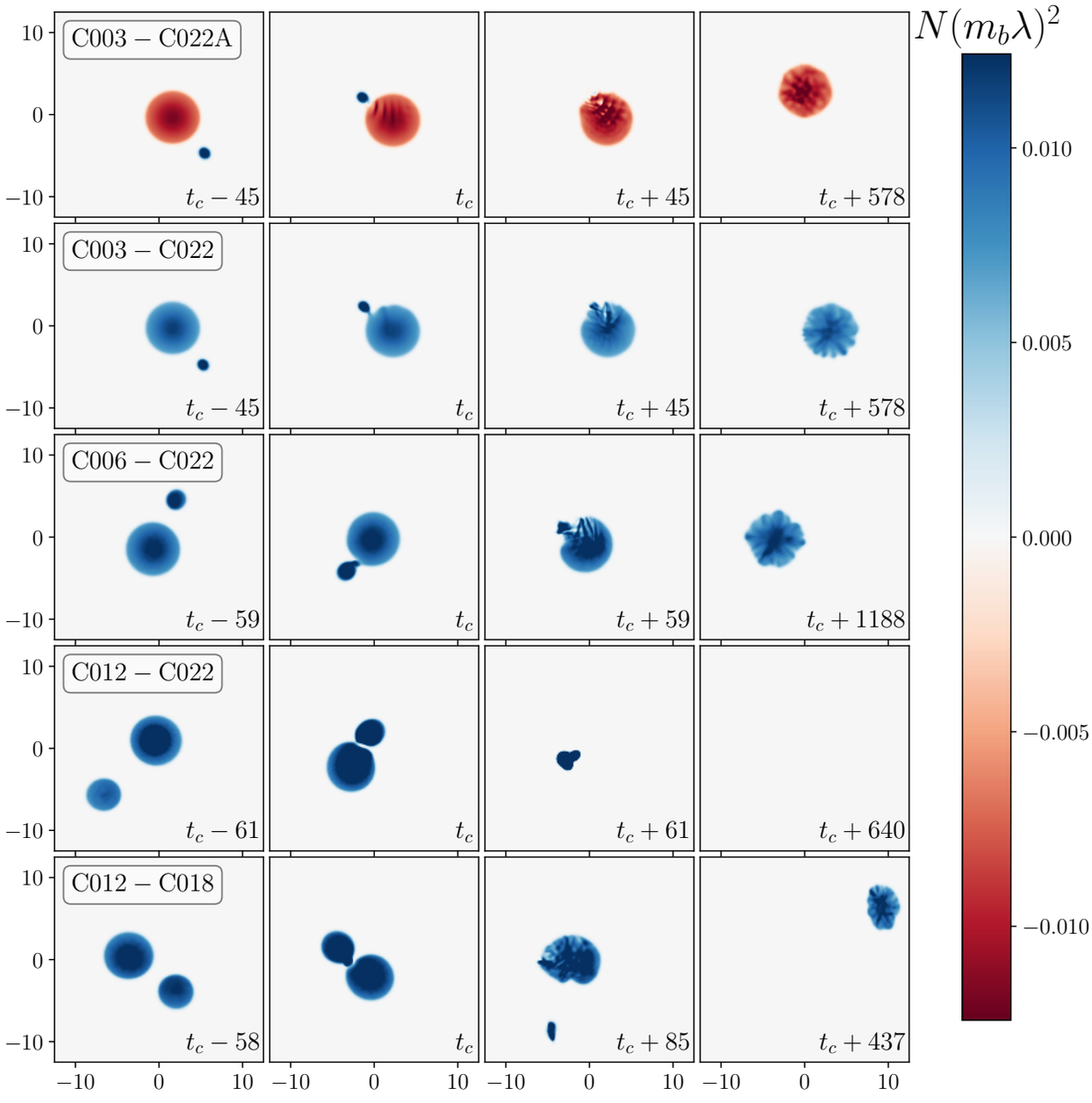

Figure 5.3: *Dynamics of the Noether charge.* Noether charge densities in the equatorial plane ($z = 0$) at representative times. Each row represents one of the cases (from top to bottom): {C003-C022A, C003-C022, C006-C022, C012-C022, C012-C018}. The first column illustrates a time roughly one orbit before the contact time t_c (defined as the time at which the individual Noether charge densities make contact for the first time), the second column occurs at contact time, the third is roughly an orbit after the contact time (except for the C012-C018 case, in order to visualize the ejected blob), and the fourth one occurs at the end of our simulations. Note that the final remnant for C012-C022 is a rotating BH which quickly engulfs the surrounding scalar field (i.e., not visible on this natural scale).

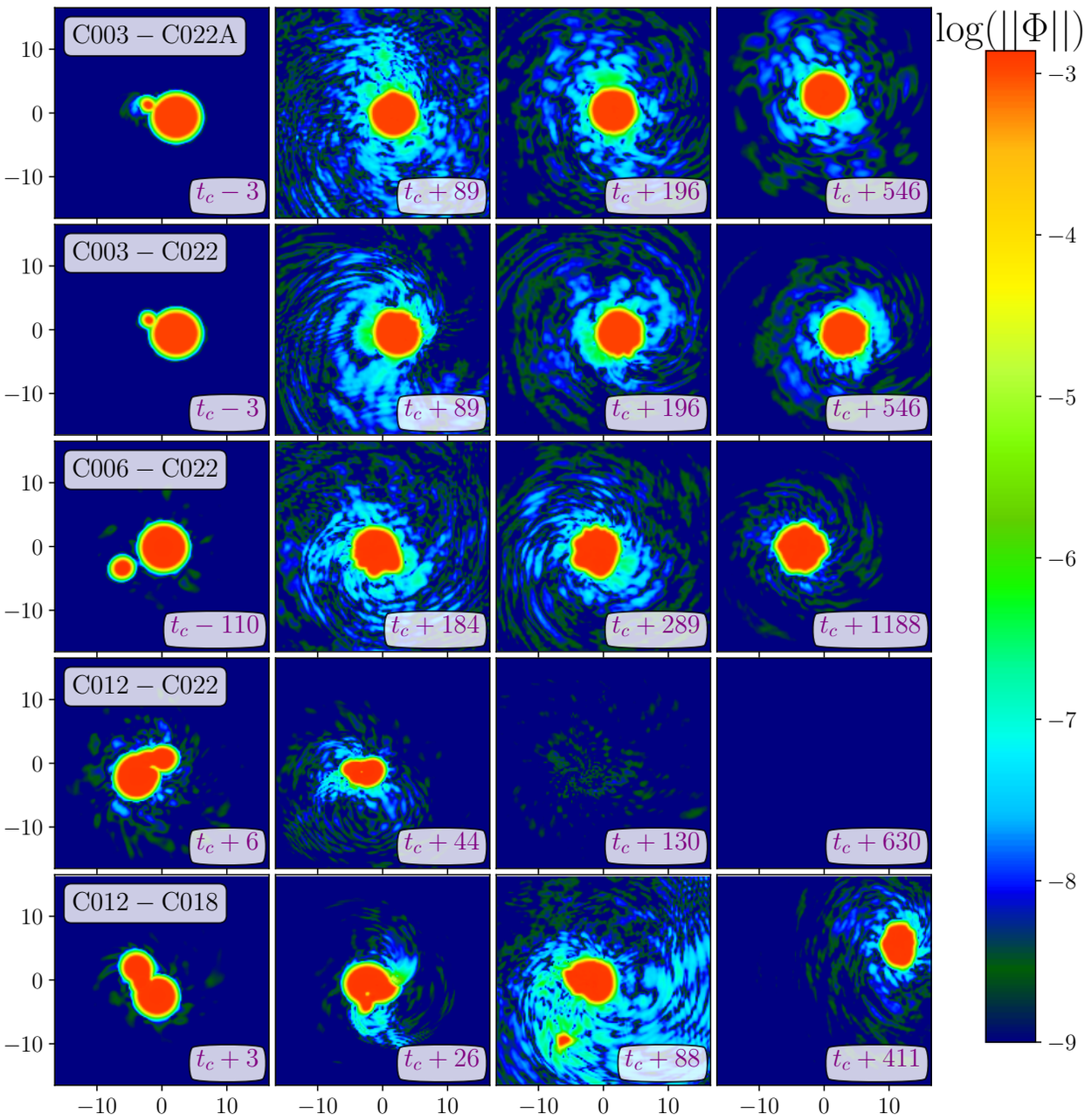

Figure 5.4: *Dynamics of the scalar field.* Logarithm of the modulus of the scalar field $||\Phi||$ in the equatorial plane ($z = 0$), at representative times. Each row represents the unequal cases considered. Notice that there is only some scalar emission around the contact time t_c (defined as the time at which the individual Noether charge densities make contact for the first time), suggesting that the final object is an almost stationary BS (except for the simulation on the third row, in which the remnant is a spinning BH).

collapse to a remnant BH. If instead the total mass is below this threshold, a remnant BS is expected. In the latter case, the possibility of forming a rotating BS should be considered. At least two conditions appear to be required for such formation: (i) because rotating BSs have quantized angular momentum, binaries need to have angular momentum at the point of contact at least slightly larger than or equal to the first discrete level of the rotating star,[3] and (ii) the rotating solution to which the remnant might settle must be stable.

Once the stars contact each other, one expects scalar field interactions to produce additional attractive forces that accelerate the merger (see the discussion of the effective force with just a massive potential in Appendix B of [299]). The newly formed, rotating object is initially largely nonaxisymmetric, and, even by the end of our simulations, the remnant is a highly perturbed BS (see the rightmost column of Fig. 5.3). Some general features of the dynamics can be found in certain global quantities (mass, Noether charge, and angular momentum) which are displayed in Fig. 5.5.

The mass and the Noether charge are unambiguously defined global quantities, in contrast to the radius of the star. In the case of a complex field, the $U(1)$ symmetry, which ensures the conservation of the Noether charge, significantly restricts the ways in which the remnants might relax. Fig. 5.6 shows the mass-Noether charge phase space for two representative cases C006-C012 and C012-C018. Here, we present several estimates of the initial and final data along with families of isolated BSs, to facilitate the understanding of the relaxation of the remnant.

The orange squares indicate the simplest estimate of the initial data, (M_1+M_2, N_1+N_2), obtained by adding the properties of the isolated BSs used to construct the binary. These two squares fall far from our two other estimates of the initial data. In particular, the total mass and Noether charge measured by the numerics after the transient is shown in black circles. We then construct the "effective" initial data (red crosses) by decomposing the numerically obtained total mass via Eq. (5.3) and computing the charge of each BSs from these individual masses (with Eq. (5.5) in Sec. 5.2.1).

We further note that, due to the nonlinearity of the function $N(M)$, some amount of scalar and/or GW emission is needed during the merger in order for the remnant to settle into either a static or rotating configuration. If the remnant is assumed to be a BS that relaxes only by the emission of GWs, namely no emission of scalar field to infinity, the evolutionary path of the binary would follow a horizontal line in the N-M phase space (blue dashed line on Fig. 5.6), ultimately settling into the remnant BS occurring at the intersection with the family of nonrotating BSs given by Eq. (5.5) (red dotted line). Our simulations indicate emission of scalar field, in addition to GWs, a process known as

[3]This argument excludes some exotic possibility in which, say, GWs with some opposite angular momentum are radiated copiously until the remnant achieves the sufficient amount of angular momentum.

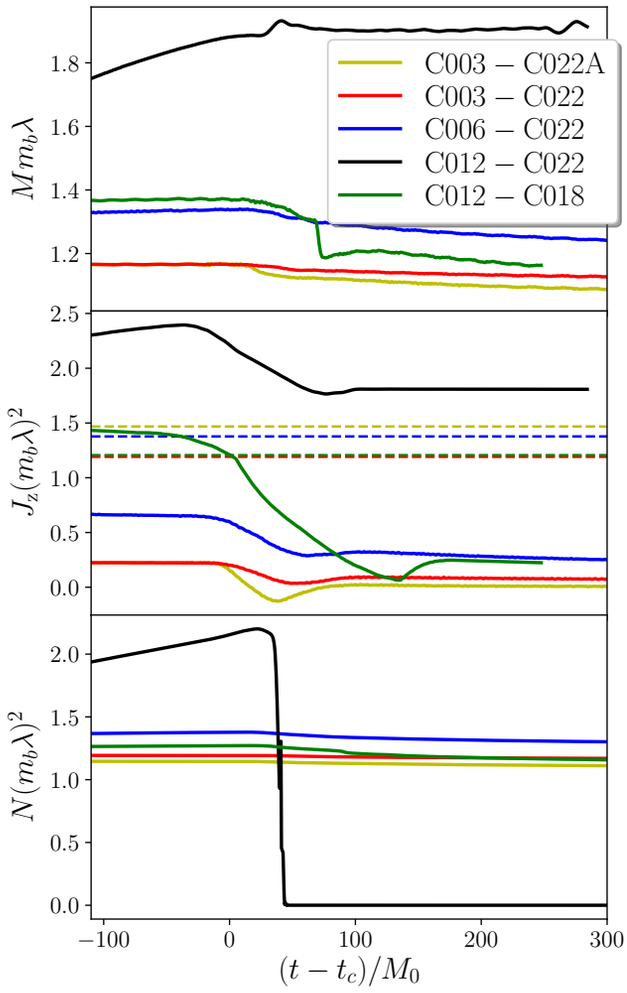

Figure 5.5: *Global quantities.* ADM mass (**top**) , angular momentum J_z (**middle**) and Noether charge (**bottom**) as functions of time. The time has been shifted such that contact time happens at $t = 0$ and rescaled with the initial total mass M_0 of each binary. Horizontal dashed lines in the middle panel indicate the angular momentum of the ground state rotating BS corresponding to the Noether charge measured at the contact time. Notice that the angular momentum decreases monotonically (although slowly) after merger for all remnants except for that of C012-C022 which collapses to a BH. This decrease in angular momentum along with the fact that these binaries (except C012-C022 which collapses to a BH) have less angular momentum than any rotating BS with the same Noether charge support our claim that all non-collapsed cases settle to a nonrotating BS. The non-monotonic, brief drops in the mass and angular momentum plots for the C003-C022A and C012-C018 cases correspond to the passage of transients across the extraction surface on which mass and angular momentum are calculated (the retarded time is used). The Noether charge is computed as a volume integral and therefore less subject to such errors.

"gravitational cooling" [165, 327]. Indeed, the path of the numerical evolution (green dots) indicates that the dynamics are driving each system toward a stationary BS (red-dotted line). Although most of these BS mergers ended before the remnant fully relaxed to stationarity, we have established for C003-C022 and C012-C012 that the point (M_r, N_r) (where $N_r \equiv N(t_{\rm end})$) indeed lies on the isolated BS curve. However, the near constancy of the Noether charge in the late postmerger (Fig. 5.5) and the close approach of the final simulation to the isolated BS curve (Fig. 5.6) both indicate that the mergers that do not collapse are forming a stable, nonrotating, SBS.

If the late stage evolution is dominated by GW emission (since most of the ambient scalar field has already been radiated), then we would expect the final object to be that represented by the black solid diamond, $(M_r, N(M_r))$, itself a stationary BS, because the Noether charge would not be changing.

An important unresolved question is whether a merger of two BSs can produce a rotating BS. The stability of rotating, SBSs has been studied recently. First, rotating BSs without scalar self-interactions were found to be unstable due to a non-axisymmetric instability [162]. However, a subsequent study showed that this instability was quenched for the solitonic model of the potential [163] (see also Ref. [164]) if $M > 0.13/(m_b\lambda)$, for the value $\sigma_0 = 0.05$ considered here. Without stability, one would not expect formation of such configurations from a merger.

Rotating BSs have quantized angular momentum, $J = kN$ for some integer k, and one can calculate the function $N(M)$ for the $k = 1$ family of rotating BSs following Ref. [163] (see also [249]). We display this family of solutions as a green solid curve in the right panel of Fig. 5.6 (case C012-C018) because this binary has angular momentum close to this first quantized level. Actually, only two cases among those studied in this work and Paper I (i.e., C012-C018 and C012-C012) are close to satisfying the quantization condition, namely that the angular momentum is greater than or equal to the Noether charge at the time of contact. In neither of these two cases do we find a rotating remnant, and the angular momentum is primarily reduced through emission of scalar "blobs."

The case C012-C018 is shown in the right panel of Fig. 5.6. We display the Noether charge equal to the binary's angular momentum at the time of contact with the horizontal, yellow dot-dashed line. However, as shown in the figure, the point of intersection of the dynamical path of the binary, $(M(t), N(t))$ shown in green dots, with the curve indicating the $k = 1$ family of rotating BSs (solid green curve) occurs above this yellow line. Because these rotating solutions have angular momentum equal to their charge, the evolution lacks sufficient angular momentum to form the rotating BS indicated by this point of intersection.

In an effort to understand the configuration space of binaries in terms of possible endstates, in particular including formation of a rotating remnant or a blob, we parame-

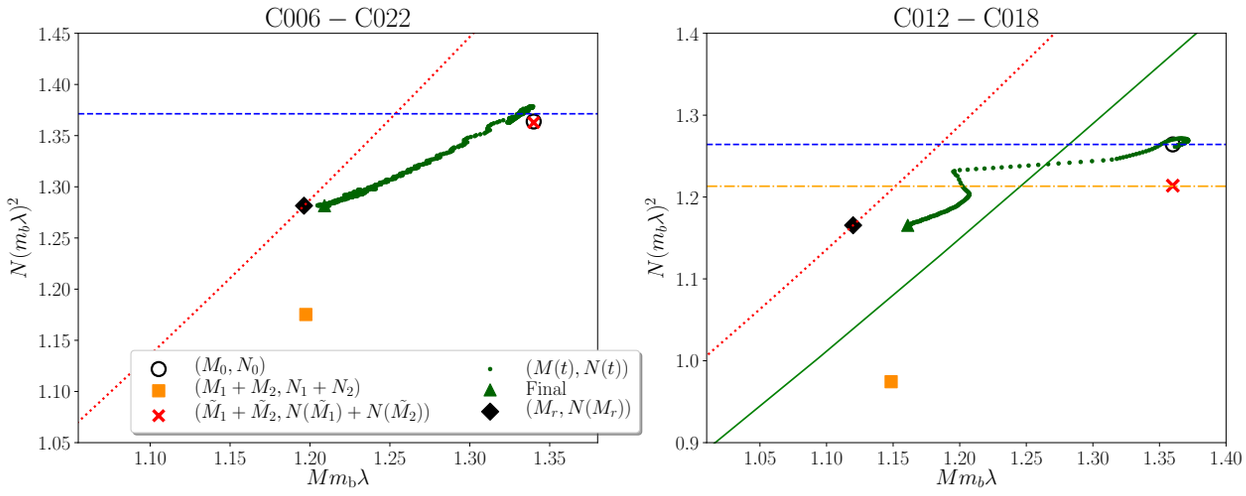

Figure 5.6: *Mass-Noether charge phase space.* Evolution of the total mass and charge of the system for two representative cases: C006-C012 (**left**) and C012-C018 (**right**) which ejects a blob of scalar field after merger. The orange square for each case represents the value of (M_1+M_2, N_1+N_2) obtained from the individual stars as listed in Table 5.1. The black, open circles are the masses and charges, (M_0, N_0), obtained from the numerical evolution just after the transient. The red crosses are the "effective" values $(\tilde{M}_1+\tilde{M}_2, N(\tilde{M}_1)+N(\tilde{M}_2))$, as explained in Sec. 5.2.1. The fact that the red crosses and black circles are close to each other supports the validity of this approach. The green dots trace the numerical evolution by showing the extracted quantities $(M(t), N(t))$. The values characterizing the final state, (M_r, N_r), of the simulation are represented by a green triangle. The black diamond is the point, $(M_r, N(M_r))$, with the same mass as the green triangle but with the charge obtained from the fit in Eq. (5.5). If one assumes that the remnant is a BS that relaxes only via emission of gravitational waves, one obtains a horizontal phase space trajectory (blue dashed line) through the initial data (namely the black circle here). The family of nonrotating BSs given by Eq. (5.5) are plotted with a (red dotted curve). Only the case on the right has angular momentum comparable to the first rotating solution, and so for this case we also show the family of $k = 1$ rotating BS configurations for our same potential from Ref. [163] with a solid green curve. Because $J = kN$ for such rotating BSs, we also show the value of N corresponding to the angular momentum of the binary at contact time with a horizontal, yellow dot-dashed line.

terize the quantization condition. We first compute a Keplerian estimate of the angular momentum either at the time of first contact $R_c = C_1/M_1 + C_2/M_2$ or when the binary reaches the innermost stable circular orbit, $R_{\rm ISCO} = 6M_0$, whichever occurs first. We then correct this estimate by including the relativistic effects of strong gravity. Due to the pre-contact scalar emission, the total Noether charge in the binary at the point of contact will be slightly smaller than the initial one. In addition, we have observed blob emission in both cases where the total charge of the binary is slightly higher than J_c. We incorporate these two effects in our quantization condition for rotating boson stars, $J \geq N$,

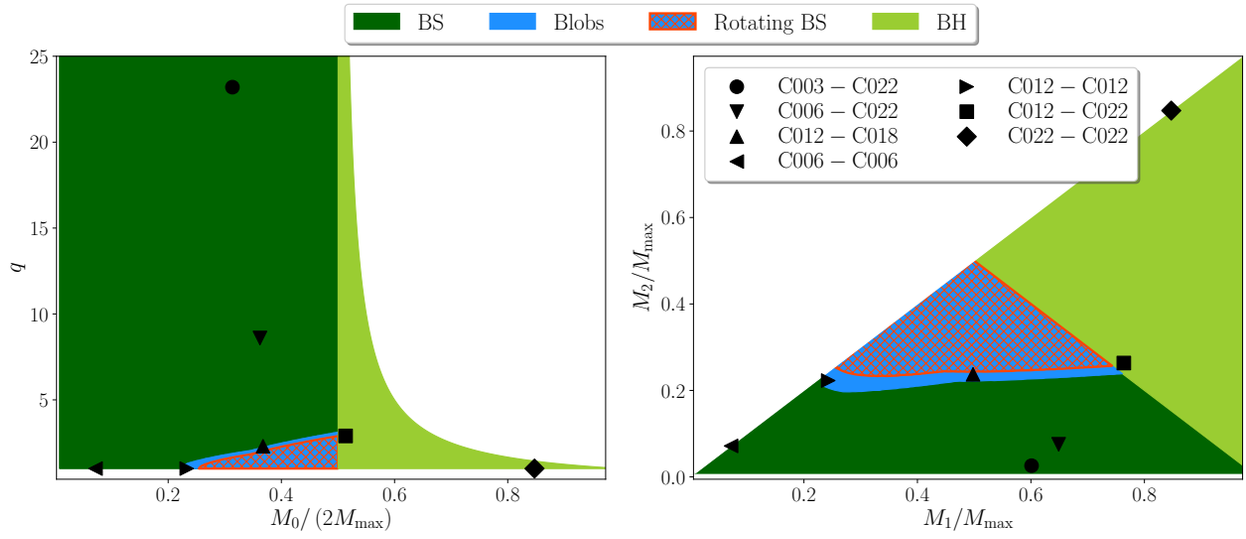

Figure 5.7: *Scenario classification.* The parameter space of solutions represented in two different ways: (**left**) mass ratio versus total mass, and (**right**) individual mass of one star versus the other. The outcomes of our simulations are consistent with $M_{\rm max}$ being the simple delineator for the BS/BH nature of the remnant. The blue region encloses configurations that satisfy the angular momentum requirement of Eq. (5.11) (informed by our evolutions that produce blobs), and thus we expect either blob ejection or the formation of a rotating boson star. The red hashed region is a subset of this region which we have not sampled, but where rotating BSs may form.

by introducing two new parameters $\{e_N\,, e_J\}$ in the following way

$$\frac{J_{c,K}(1+e_J)}{N(M_1)+N(M_2)} > 1+e_N, \tag{5.11}$$

where $J_{c,K}$ is the Keplerian estimate of the angular momentum at the contact time, e_N estimates either the amount of Noether charge radiated during the merger ($e_N > 0$) or the difference between the critical angular momentum and the charge at the point of contact that allows for blob emission ($e_N < 0$). Finally, e_J accounts for general relativistic corrections to the Keplerian angular momentum calculation.

We use the above cases to estimate the value for the parameters e_J, e_N. To estimate e_J, we compute the differences between the Keplerian estimate of the angular momentum at contact time and the numerical value, obtaining $\sim 25\%$ in scenarios where we observe blob formation: C012-C012 and C012-C018. In the low-mass regime, where SBSs are in the weak-field regime, we expect that $e_J \to 0$. Thus, we linearly interpolate e_J between 0 and 0.25 for $M_0/2 \in [M_{\rm min}, M_{\rm C012}]$ and take the constant value $e_J = 0.25$ up to $M_0 = M_{\rm max}$. Due to the initial data constraint violation, we cannot estimate reliably how much of the Noether charge is emitted before contact. For the sake of argument, we take $e_N = 0.01$ in this case, delineating a subset of the parameter space where the strict form of the quantization condition is satisfied and where rotating remnants may form. In addition, we

require that the remnant has surpassed the threshold mass estimate from Ref. [163].

In the two cases where the blobs are observed, one finds $e_N = \{-0.05, -0.02\}$ for C012-C018 and C012-C012, respectively. Thus, taking $e_N = -0.05$ would encompass both scenarios where blobs are found and indicate the part of the parameter space where one can expect blobs generically and even possibly rotating remnants (more restrictive condition). We sketch the configuration space for these mergers in Fig. 5.7 in two ways: the left panel plots the mass ratio versus the total mass, (q, M), whereas the right panel shows the space spanned by individual masses $(M_1 m_b \lambda, M_2 m_b \lambda)$. Solutions exist only for binaries constructed with stable BSs, $M_i < M_{\rm max}$, with regions outside this indicated in white. For binaries with $M_1 + M_2 < M_{\rm max}$, the formation of a rotating BS appears possible for the binaries that do not collapse to a BH and possess angular momentum satisfying Eq. (5.11), although we have not observed such formation (red hashed region).[4] The set where we expect blob emission based on the results of C012-C018 and C012-C012 cases (blue region) has a red hashed region as its subset. Note that lacking an understanding of the physics of the blob formation, the blue region should serve only for illustrative purposes. Both of these regions are determined approximately and require more simulations in order to understand their precise extent.

One expects qualitatively similar behavior near $M_0 \approx M_{\rm max}$ in the small λ regime ($\lambda \ll 1$). In contrast, when $M_0 \to M_{\rm min}$ BSs behave as thick-walled Q-balls (where "Q-balls" [168] refers to the flatspace limit of SBSs) [1], we can study the quantization condition (5.11) in detail in this regime. We consider an equal-mass ($q = 1$) binary with $N \approx \lambda M$ in which the objects collide at R_c (for $q = 1$ this happens when $\mathcal{C} < 0.17$). Taking $e_J \approx e_N \approx 0$ (in $m_b = \lambda^{-1}$ units) and setting the angular velocity to the Keplerian estimate, it can be shown with some algebra that Eq. (5.11) becomes

$$\mathcal{C} < \frac{M^2}{4\lambda^2}\,. \tag{5.12}$$

Thus, for sufficiently small λ (approximately an order of magnitude smaller than the value in this work $\lambda = 0.25$), the quantization condition will be satisfied. This simple expression does not change parametrically when a more precise description of the Q-balls is used [1]. Although rotating Q-ball solutions have been constructed [249], the non-axisymmetric instability (NAI) probably prevents one from dynamically forming, based on the results of Ref. [163]. Whether in those cases blobs form or the non-axisymmetric instability would kick in is an open question.

To conclude, we cannot rule out the formation of a rotating BS with the solitonic

[4]Because the maximal mass of rotating BSs is larger than that for non-rotating BSs, a priori, even binaries with total mass slightly higher than the maximum mass for static stars, $M_{\rm max}$, could allow for the formation of a rotating remnant. Note, however, that the effective mass of C012-C022 is slightly larger than the static maximum mass $M_{\rm max}$ and the configuration collapses to BH. Whether this also happens for $q \to 1$ is an open question.

potential although none has been formed. In any case, our parameter space analysis indicates that the initial conditions would need significant tuning, which may require more accurate initial data. Even in those cases where the formation of rotating BS might be feasible, as suggested in Paper I, the organization of the bosonic field into a rotating star from the very nonlinear merger may be too difficult, particularly because the rotating BS necessarily has a toroidal energy density [5].

5.3.3 Scalar blobs and kicks

We now consider the ejection of scalar blobs. As previously explained, the case C012-C018 is the only one with contact angular momentum close to that of the first quantized spinning BS configuration (namely, $J_z \gtrsim N$) that does not collapse to a BH. Instead, whether the spheroidal energy density formed in the merger somehow prevents the configuration from relaxing to the toroidal shape of the rotating BS or not, the system relaxes instead to a nonrotating BS. To do so, the system must shed its angular momentum.

In this case, the excess angular momentum is emitted in the form of a blob of scalar field that is ejected from the remnant soon after the merger (see the bottom row of Figs. 5.3 and 5.4). This blob travels outward on the grid, and its passage across the spherical surface (i.e., around $(t - t_c)/M_0 \approx 100$) at which the system mass and angular momentum are computed disrupts the assumptions of the calculation, seen as non-monotonicity in the global quantities shown in Fig. 5.5.

Using the values before and after the drop in mass, we can estimate the blob's mass as $M_{\rm blob} \approx 0.12$. Despite the blob containing only a small fraction of the total mass, it carries a significant fraction of the total angular momentum due to its large velocity, $v_{\rm blob} \approx 0.5$ directed nearly tangentially away from the remnant and its distance from the center of mass when ejected, $L \approx 7$. Indeed, using the same simple estimate for the angular momentum as in Paper I, we obtain $J_z \approx M_{\rm blob} v_{\rm blob} L \approx 0.4$, which is roughly equal to the sharp decrease of angular momentum observed in the middle panel of Fig. 5.5. On the time scale of our simulation, the blob appears bounded. In fact, the blob satisfies the stability condition (in $m_b = \lambda^{-1}$ units) $\lambda M_{\rm blob} < N_{\rm blob}$, with $N_{\rm blob} \approx 0.05/(m_b\lambda)^2$ (see Ref. [1] and references therein for a discussion of the stability regimes of SBSs).

In addition to the unequal mass case C012-C018 presented here, the ejection of condensed scalar field was observed in two equal-mass BS binary simulations, one in Ref. [253] and the other in Paper I. In those two cases, the symmetry of the binary resulted in two, identical blobs propagating along opposite directions. That three different studies found blob ejection suggests that such ejection might be typical in SBS binaries under certain conditions.

[5] Rotating Proca stars instead have a spheroidal energy density and yet none of these have been formed from a merger either [302].

The ejection of the blobs has important implications for the astrophysics of BS mergers should such systems (or similar systems such as axion stars) actually exist in nature. In contrast to the equal-mass case that ejects two blobs in opposite directions, the ejection of a single blob generates a kick on the remnant. For binaries with large enough mass ratios, the kick can be large; large even compared to the superkicks of binary BHs (which are as large as a few $\times 10^3$ km/s [328, 329, 330, 331]) and larger than the typical escape velocities of galaxies and of globular clusters (which are of $\mathcal{O}(10^2 - 10^3)$ km/s and $\mathcal{O}(10)$ km/s, respectively). For example, the linear momentum of the blob shown in the C012-C018 simulation is roughly $M_{\rm blob} v_{\rm blob} \approx 0.06/(m_b\lambda)$ which, by linear-momentum conservation, implies that the remnant with mass $M_r = 1.17/(m_b\lambda)$ recoils with a velocity $v_r \approx 0.05 \sim 1.4 \times 10^4$ km/s . In practice, since the ejected scalar blobs have a sizeable mass and relativistic speed, they induce remnant kicks much more efficiently than GW emission in asymmetric binary BH systems [328, 329, 330, 331]. These large kicks would have important implications for the merger rate of BS binaries in the universe, as they largely exceed the escape velocity from bound structures (e.g. nuclear star clusters [332] and galaxies [333]). As a result, the rate of successive generations of mergers (which is particularly important for supermassive objects, see e.g. Ref. [334]) may be suppressed relative to the BH case. Moreover, "'stray" BSs moving at high speeds may be present in the intergalactic medium as a result of ejections from the host galaxies.

Finally, one might be tempted to associate this disruption and blob ejection to the nonaxisymmetric instability present in some rotating BSs [162]. However, a recent study shows that the NAI should be quenched for the solitonic potential for sufficiently compact BSs [163, 75], which suggests that the NAI is not the cause of blob ejection.

5.4 Gravitational Wave Signal

We now turn our attention to the analysis of the gravitational radiation produced by unequal-mass BS binaries.

5.4.1 Late inspiral and merger

Some of the most relevant (l, m) modes of the gravitational radiation represented by the strain, together with the angular frequency of the $(2, 2)$ mode, are displayed in Fig. 5.8. A simple inspection of these profiles already confirms that the dominant mode during the inspiral is always the $l = m = 2$ for our wide range of mass ratios. As expected, mass ratios closer to unity (i.e., such as the C012-C018 case), when the mass quadrupole moment is stronger, displays a larger predominance of the $l = m = 2$ mode. On the other hand, for large mass ratios (i.e., such as the C003-C022 case), the importance of the higher-order

modes increases. It is interesting to note that after the merger the amplitudes of the various modes are of the same order, without one clearly dominating over the others.

Furthermore, as the mass ratio increases, the effects of tidal deformations on the waveform become less relevant. This can be understood as follows. A generic quadrupole-moment tensor, $Q_{ab}^{(i)}$, of the i-th object affects the GW phase starting at second post-Newtonian order. The extra $1/r^3$ dependence of the tidally-induced quadrupole moment [see Eq. (5.8)] implies that tidal effects enter the GW phase starting at the fifth post-Newtonian order, with a phase correction [325, 326]

$$\delta\phi_{\rm tidal} = -\frac{117}{8}\frac{(1+q)^2}{q}\frac{\Lambda}{M_0^5}v^5 \ , \tag{5.13}$$

where $v = (\pi M_0 f)^{1/3}$ is the orbital velocity, f is the GW frequency, and $\Lambda = \frac{1}{26}((1 + 12/q)\lambda_1 + (1 + 12q)\lambda_2)$ is the weighted tidal deformability. When $q = 1$, $\Lambda = (\lambda_1 + \lambda_2)/2$ is simply the average of the two tidal deformability parameters. However, in the large mass-ratio limit [335], we can write the correction as

$$\delta\phi_{\rm tidal} = -k_1\left(\frac{3}{8}v^5 q + \dots\right) - k_2\left(\frac{9}{2}v^5\frac{1}{q^3} + \dots\right) \ , \tag{5.14}$$

where we include for each of the tidal terms k_1 and k_2 only the leading-order term in the $q \gg 1$ expansion. The above equation shows that the tidal deformability of the primary is much more important than that of the secondary, which is suppressed by a relative factor $\sim q^{-4}$. Thus, the net contribution of the tidal deformability in the GW phase, compared to the point-particle phase, depends on two competing effects: on the one hand, less compact BSs have a large tidal Love number (see Table 5.1) but, on the other hand, for binaries with very disparate mass stars the tidal Love number of the secondary is negligible. The quantity Λ/M_0^5, which provides a measure of the relevance of the tidal contribution compared to the leading-order point particle phase, is presented in Table 5.4. For the binary systems under consideration, the suppressing effect of large mass ratio more than compensate for the large tidal Love number of the secondary, and hence the quantity Λ/M_0^5 is larger for the smallest mass-ratio system in the catalog.

5.4.2 Post-merger

We analyze the post-merger frequencies of the gravitational signal of the remnant, showing the power spectral density of the dominant $l = m = 2$ mode in Fig. 5.9. In Fig. 5.10, we display the frequency of the dominant mode for all the cases studied in this Ch. and Paper I, together with the fundamental mode for isolated BS stars (from Paper I) as a function of the remnant mass.

An analysis from Paper I indicates a correspondence between the frequency of the first

Binaries	q	k_1	k_2	Λ/M_0^5
C003 - C022A	23.2	20	136494	0.75
C003 - C022	23.2	20	136494	0.75
C006 - C022	8.6	20	8420	0.99
C012 - C022	2.9	20	332	0.94
C012 - C018	2.1	41	332	1.79

Table 5.4: *Tidal properties of unequal binary BS models considered in our simulations.* For each binary studied here, the weighted tidal deformability Λ is shown. Despite the large tidal Love numbers in the most unequal mass binaries, the binary deformability increases as $q \to 1$.

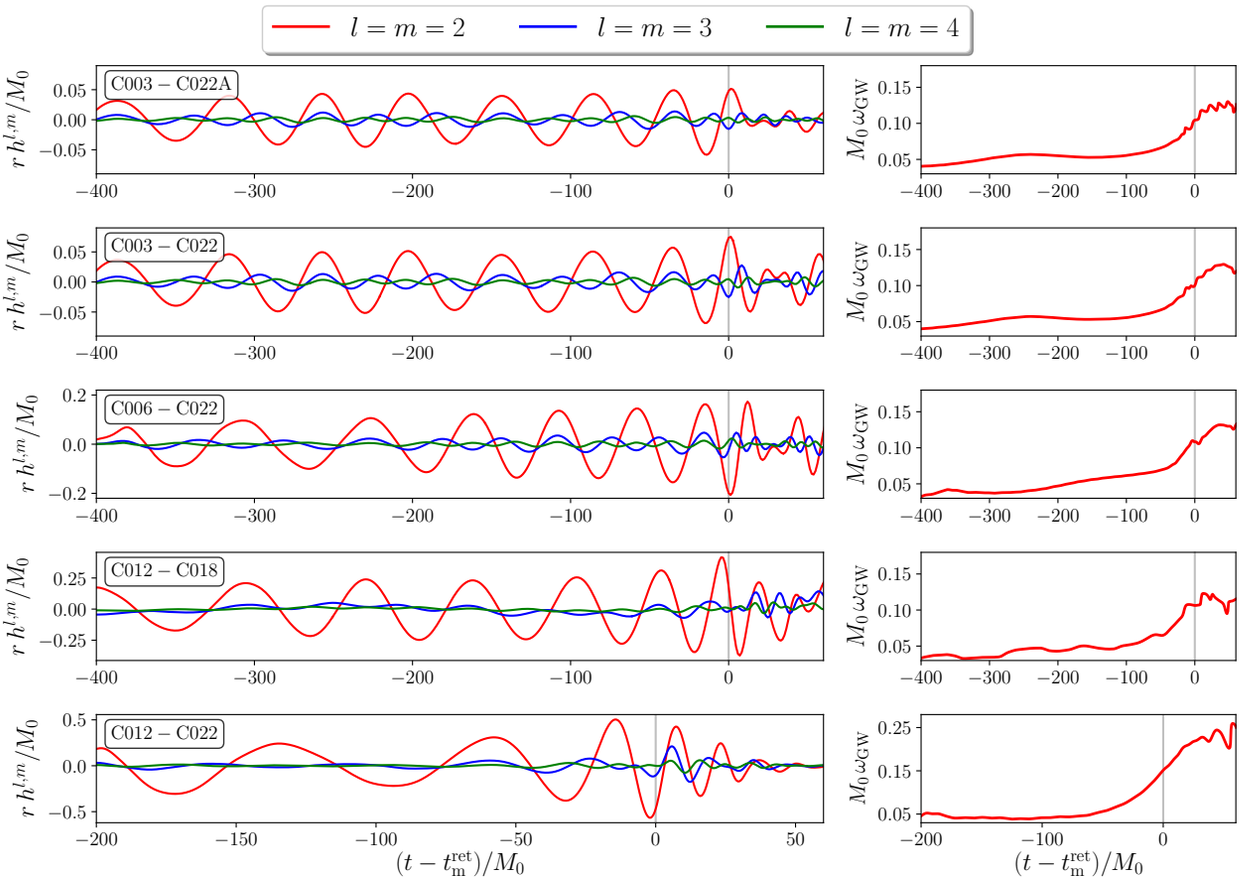

Figure 5.8: *GWs in the coalescence.* Different modes $l = m$ of the strain as a function of time, together with the frequency of the dominant mode $l = m = 2$. Clearly, the $l = m = 2$ mode is always much larger than the others, even for the largest mass ratio. The vertical, gray lines show the merger time.

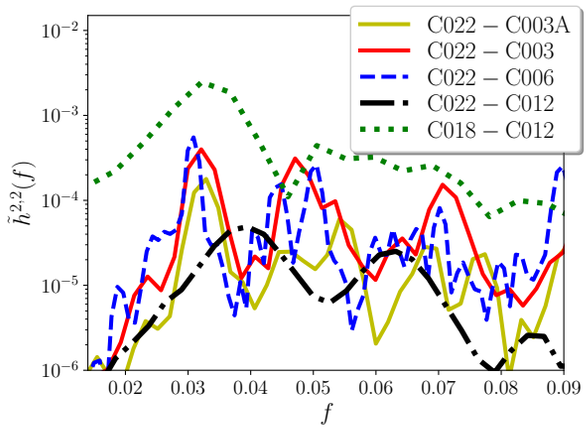

Figure 5.9: *GWs in the post-merger stage.* Power spectral density of the main mode (i.e., $l = m = 2$) of the strain for the post-merger.

peak with the quasi-normal mode (QNM) of isolated BSs. We scrutinize this hypothesis further by considering the post-merger behavior of all configurations from both work as well as the QNM of isolated SBSs with $\mathcal{C} = \{0.06, 0.12, 0.18, 0.22\}$ calculated in Paper I. We fit the spectral lines with a Lorentzian function, i.e.

$$\tilde{h}^{2,2}(\omega) \sim \frac{\omega_I}{(\omega_I^2 + (\omega - \omega_{\rm R})^2)} \tag{5.15}$$

to determine the peak frequency of the main mode $\omega_{\rm R}$ and the inverse decay time ω_I. In line with the discussion on the relaxation of the remnant from Sec. 5.3.2, one can construct quadratic fits for $\omega_{\rm R}(M_r)\,, \omega_{\rm I}(M_r)$, where $M_r = M(N_r)$ [Eq. (5.5)],

$$M_r\omega_{\rm R} \approx 0.05 + 0.3M_r - 0.13(M_r)^2\,, \tag{5.16}$$

$$M_r\omega_{\rm I} \approx 0.013 + 0.007M_r\,, \tag{5.17}$$

for isolated scenarios from Paper I. As shown in Fig. 5.10 (left panel), excluding the C018-C018 case from Paper I where the post-merger behavior is not reliable, real parts of the post-merger main mode frequencies agree well with the isolated SBS QNM fit.

However, in the case of the imaginary frequency (see Fig. 5.10, right panel) all remnants produced in the binary coalescence have an offset with respect to the isolated QNMs. We notice that the three configurations in which blobs do not form have lower imaginary frequencies (longer decay times) compared to the isolated configurations. In contrast, in the case of blob formation, frequencies are higher (shorter decay times) than expected from the isolated QNMs. Note the three cases with $m_b\lambda M_r \approx 1.07 - 1.1$ that have almost identical real frequencies but vastly different imaginary components. Understanding this peculiar behavior lies beyond the scope of this work. We speculate that the excess angular momentum requires longer decay times in contrast to the isolated configurations, except

in the case of blob formation that removes the excess (rotational) energy more efficiently than in the isolated case, thus shortening the decay time.

We have also compared the fits with the tabulated BH QNMs [336]. The BH remnant from Paper I, i.e. the C022-C022 case ($a = 0.698$), has tabulated value $(M_r\omega_R, M_r\omega_I) = (0.532, -0.081)$, while we find $(0.469, -0.083)$, which is close to the time-domain fit from Paper I where $(0.5, -0.07)$. For the C022-C012 case ($a = 0.5$), we find the tabulated value $(0.464, -0.086)$, while the fit gives $(0.475, -0.061)$. This mild discrepancy between the fit and the predicted ones for BHs may originate from the numerical precision of the ADM mass/angular momentum extraction and the fit, the presence of some remnant scalar surrounding the BH, or the fact that the frequency estimate depend on the choice of the post-merger time. Nonetheless, the overall agreement corroborates the conclusion that the remnant is a BH.

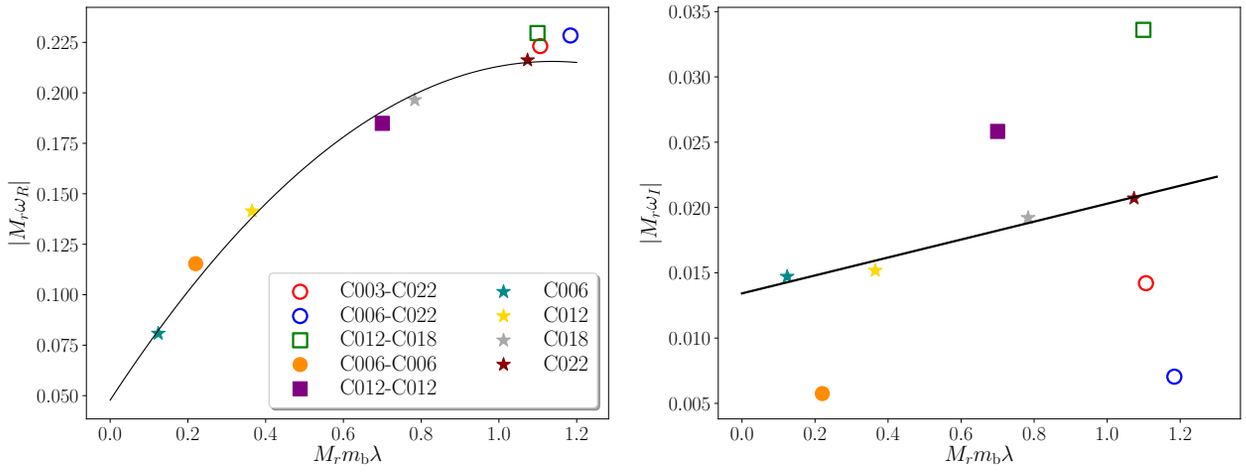

Figure 5.10: *QNMs and post-merger spectrum.* (**Left**) Real and (**right**) imaginary parts of the frequencies of the first peak of the $l = m = 2$ mode with respect to remnant mass M_r for binaries that form a remnant BS, with the equal mass binaries of Paper I (filled) and the unequal mass binaries studied here (open). Binaries that eject a blob are denoted with squares while circles denote those that do not. The frequencies of the QNMs of the four isolated BSs used for initial data are marked with stars, and the curves (solid) represent the fits to the real and imaginary components of these QNM frequencies from Eqs. (5.16) and (5.17).

5.4.3 Soliton BSs in the LIGO/Virgo band

In this subsection, we quantify the difference between the GW signal expected from BS binaries and from binary BHs, focusing on the LIGO/Virgo band. In particular, we assess whether analyzing LIGO/Virgo data with binary BH templates can lead to missed detections or to biases on the estimate of the parameters of the source, under the assumption that the latter consists of a BS binary.

As a preliminary test of this, we consider the BS binary waveforms extracted from the unequal-mass simulations of this Ch., focusing on the $l = m = 2$ mode alone. Actually, each of these simulations can be taken to represent a binary of any total mass, as long as frequencies and strain amplitudes are properly rescaled, i.e. each simulation actually corresponds to a one-parameter family of systems with varying binary mass M, but with fixed dimensionless product $m_b M/\hbar$. We choose therefore to vary M in a range likely to yield observable effects in the LIGO/Virgo frequency band, i.e. we choose M in the interval $[M_{\rm min}, 100]M_\odot$, where $M_{\rm min}$ is such that the smaller progenitor is always heavier than $\sim 3M_\odot$. For each BS waveform obtained in this way, we rescale the (2,2)-mode strain amplitude to correspond to a fiducial luminosity distance of 400 Mpc. (We recall that choosing a slightly different distance will simply rescale strains and signal-to-noise ratios by a linear factor, at leading order.) We then compare the BS signal obtained to SEOBNRv4 BH binary waveforms [337], as implemented in the `Pycbc` python package [338]. The component masses and luminosity distance of the BH binary waveform are chosen to match those of the BS binary, the component BH spins are set to zero, and the initial phase and merger time are chosen so as to minimize the "difference" of the two signals. In particular, we minimize the signal-to-noise ratio of the difference of the two signals,

$$\rho(\Delta) = \left[4 \int \frac{|\tilde{\Delta}(f)|^2}{S_n(f)} df \right]^{1/2} , \tag{5.18}$$

with $\Delta(t) \equiv h_{\rm BS}(t) - h_{\rm BH}(t)$ the residual, i.e. the difference between BS and BH signals (computed for optimal detector orientation and sky position), and with a tilde denoting a Fourier transform. The (single-sided) power spectral density of the noise, S_n, is chosen to be that of a single LIGO detector. More precisely, we consider both the case in which S_n corresponds to the Livingston detector in O3b [290], or to the zero-detuning, high laser power *design* sensitivity curve [339]. Accounting for the second LIGO interferometer and for Virgo will further increase the signal-to-noise ratio, roughly by a factor $\lesssim \sqrt{3}$ (with the $\lesssim$ due to the fact that the source can only be optimally placed relative to one detector at a time, and that Virgo is less sensitive than LIGO in O3b).

Two examples of BS binary waveforms, qualitatively representative of the two possible post-merger scenarios (i.e. BH or BS remnant), are shown in Fig. 5.11a, where they are compared to the "most similar" BH binary waveforms identified with this procedure.

The signal-to-noise ratio $\rho(h_{\rm BH})$ of the BH binary waveform best matching each BS signal is shown in the top panel of Fig. 5.11b, as a function of M and for both the O3b and design LIGO configurations. The signal-to-noise ratio is computed by using the aforementioned SEOBNRv4 waveforms, which (unlike our short BS signals) include inspiral, merger and ringdown. In the bottom panel, we show instead the residual signal-to-noise ratio $\rho(\Delta)$, minimized over initial phase and merger time for all the simulations that we

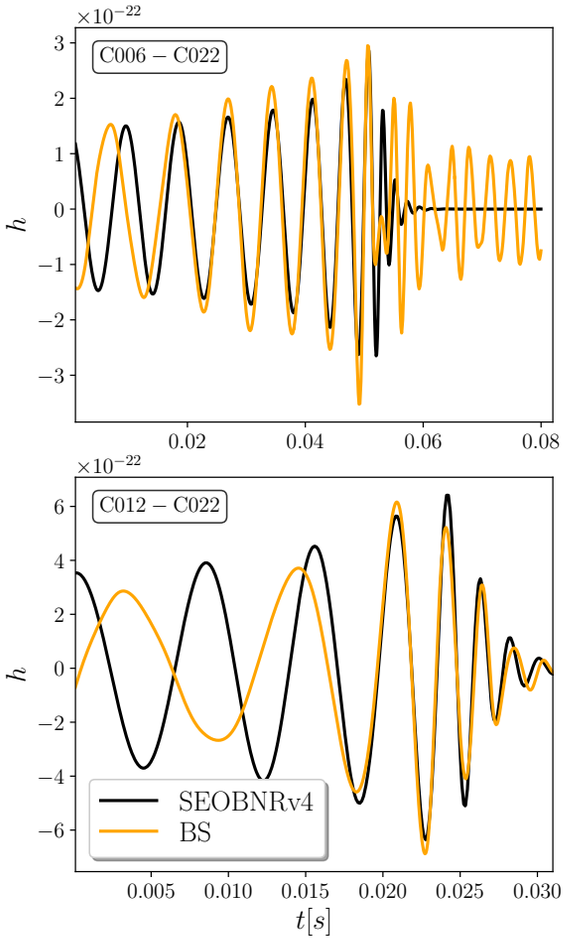

(a) Comparison between $(2,2)$-mode BS waveforms produced from our simulations and BH binary SEOBNRv4 templates, for a system leading to a BS ($q = 8.6$, $M = 28M_\odot$; **top**) or a BH ($q = 2.9$, $M = 30M_\odot$; **bottom**). The template's initial phase and merger time are chosen to minimize the residual signal-to-noise ratio. Both systems are optimally oriented at a luminosity distance of 400 Mpc, and the BH component masses and spins are set equal to the BS component masses and to zero, respectively.

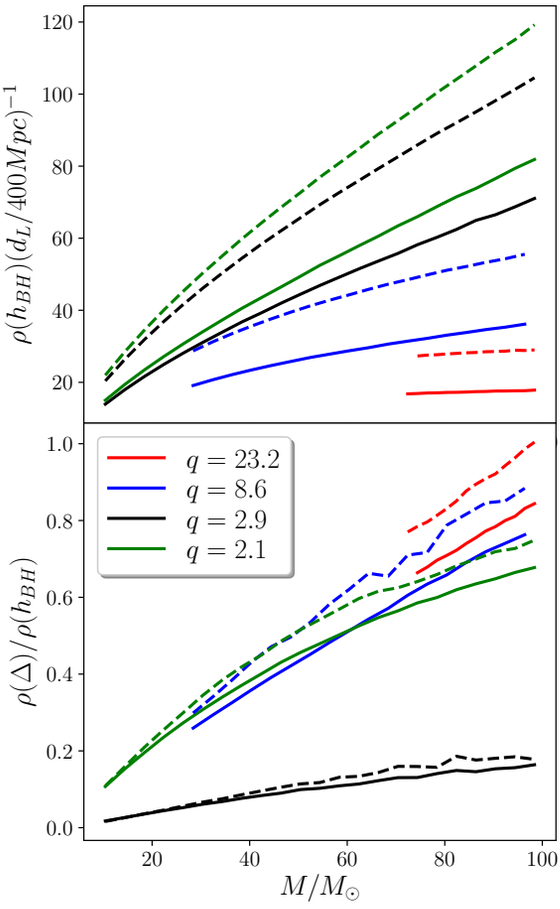

(b) Inspiral-merger-ringdown BH binary SEOBNRv4 signal-to-noise ratio $\rho(h_{\rm BH})$ (**top**) and residual signal-to-noise ratio $\rho(\Delta)$ between BS and BH waveforms (**bottom**), as functions of the total binary mass. The residual signal-to-noise ratio is minimized over initial phase and merger time and then normalized by $\rho(h_{\rm BH})$, for the BS waveforms extracted from our unequal mass simulations. Both the BS and BH binaries are optimally oriented at a luminosity distance of 400 Mpc, and the BH component masses and spins are set respectively to the BS component masses and to zero. For both signals and templates only the $(2,2)$ mode is included. The signal-to-noise ratios are computed with the O3b single-detector sensitivity (solid lines), and with the single-detector design LIGO sensitivity in the zero-detuning, high laser power configuration (dashed lines).

Figure 5.11: *Soliton BS vs. BH waveforms in the LIGO/Virgo band*

have at our disposal.

This residual signal-to-noise ratio is computed by comparing BH and BS waveforms that are both cut below the minimum frequency at which constraint violations are significant in our simulations, in order to avoid biasing the comparison. In this way, the residual signal-to-noise ratio includes differences between BH and BS waveforms that occur in the post-merger phase and also in the late inspiral, thus including at least some contribution from tidal effects, while keeping the impact of initial constraint violations subleading [6]. We then normalize $\rho(\Delta)$ by the *full* inspiral-merger-ringdown BH signal-to-noise ratio $\rho(h_{\rm BH})$, since we have no access to the full inspiral-merger-ringdown BS waveforms. As can be seen, $\rho(\Delta)/\rho(h_{\rm BH})$ is always very large and grows with M, as expected because for massive binaries only the merger signal is in the band of terrestrial interferometers (i.e. for those binaries the BS-BH differences in the post-merger have a larger relative impact). Also note that $\rho(\Delta)/\rho(h_{\rm BH})$ is smallest (although still quite significant) in the case where the remnant is a BH ($q = 2.9$). Again, this is expected: The collision of two non-rotating BHs with $q = 2.9$ leads to a rotating remnant with $a \approx 0.52$ [340], close to the value of the BH spin produced by the BS binary in our simulation ($a \approx 0.5$). As such, the differences in the merger-ringdown, where most of the in-band power resides (at least for moderately high masses), are small, c.f. e.g. Fig. 5.11a.

As a rough rule of thumb, residual signal-to-noise ratios $\rho(\Delta) \lesssim 8/\sqrt{3} \sim 5$ may allow for claiming a BS binary detection (as opposed to a BH binary one), provided that an accurate determination of the component masses and spins is available (e.g. thanks to a long inspiral). In the absence of a sufficiently long detected inspiral, large residual signal-to-noise ratios may merely lead to biases in the estimation of the parameters of the source (i.e. one could mistake a BS post-merger signal for a BH ringdown with remnant mass different from the actual one, and/or non-zero spin), or even missed detections. As can be seen from Fig. 5.11b, this second possibility seems the most likely at high masses, for which most of the inspiral is out of band and BH templates miss most of the signal's power for binaries producing a BS remnant. Whether this leads to a bias on the recovered parameters or just a missed detection should be ascertained by considering templates with varying BH progenitor spins. However, given the long duration of the BS post-merger signal (c.f. e.g. Fig. 5.11a), it seems unlikely that it can be detected by any one BH template, i.e. we expect mainly missed detections at high M, at least for second-generation detectors and for systems that lead to a BS remnant. For systems that instead lead to BH formation (e.g. the $q = 2.9$ case in Fig. 5.11b), using BH templates may simply produce a bias on the parameter estimation.

The situation will be more favorable for third-generation interferometers [341] such as

[6] Improvements in the initial data would change the residual signal-to-noise ratio only marginally at high masses, while at low masses they would allow for simulating a longer portion of the inspiral phase. Our residual signal-to-noise ratios should then be regarded as lower bounds.

the Einstein Telescope or Cosmic Explorer, which will observe many more inspiral cycles. Not only will this allow for a better measurement of progenitor masses and spins (which will reduce degeneracies when comparing the post-merger signal to BH templates), but it may also allow for measuring the tidal Love number in the late inspiral [150, 342, 343]. This will provide additional hints on the BS versus BH nature of the system. We will explore the discovery space of these detectors, and at the same time refine our analysis, in future work.

5.5 Conclusions

The coalescence of BSs allows us to study not only the binary dynamics of one of the most viable and better motivated models of ECOs, but also the two-body problem in General Relativity for large mass ratios. The soft dependence of the BS radius with its mass, at least for the solitonic potential used here, facilitates the numerical simulations of binaries with very different compactness, as compared to the more challenging case of asymmetric BH binaries. Taking advantage of this feature of SBSs, we have studied numerically the coalescence of unequal-mass binaries with mass ratios ranging between 2 and 23. The analysis of our simulations, which extends the equal-mass binaries considered in Paper I (i.e., Ref. [166]), confirms many of the findings obtained in that previous study.

The fate of these binary mergers is either a nonrotating BS or a Kerr BH, as confirmed not only by global quantities and by the structure of the solution, but also by the gravitational QNMs of the remnant. As in Paper I, we once again find no evidence that any of these binaries form a rotating BS. The asymmetry introduced by the unequal mass of the constituent stars perhaps makes the formation of either of these remnants less likely. An analysis of the parameter space indicates the need to refine the initial configurations to assess whether a rotating remnant can be formed.

For a certain range of the initial angular momentum, the remnant undergoes a process similar to a tidal disruption in NSs, and a blob of scalar field is ejected. This process has already been observed in the equal-mass binaries of Paper I, although the symmetry in that case induced the ejection of two blobs in opposite directions instead of a single blob observed here. The ejection of a single blob produces a large recoil of the remnant. In our C012-C018 case, the estimate of the recoil velocity is more than 10^4 km/s, larger than the superkicks of binary BHs and large enough to have significant implications for the expected dynamics of BSs in the universe. Because recent studies suggest that rotating SBSs should be stable against the nonaxisymmetric instability [163], the ejection of the scalar blob is not likely a result of such an instability.

Regarding the GWs emitted during the coalescence, we have found results comparable to those of binary BHs: the $l = m = 2$ mode of the strain is always dominant, although

higher-order modes become more relevant as the mass ratio increases.

We have also analyzed the prospect of detecting differences between binary BS and binary BH gravitational signals with ground interferometers. We have found that while the merger portion of the signal is significantly different between the two classes of sources (at least if the final merger remnant is a BS), distinguishing between the two might be difficult with second-generation detectors due to degeneracies between merger and inspiral parameters. However, this task will ease considerably with third-generation interferometers, such as Cosmic Explorer or the Einstein Telescope.

Many interesting questions remain to be addressed, especially regarding the final state of the remnant. Evolutions of SBSs have yet to produce either a spinning BS or a synchronized scalar cloud. More accurate and longer simulations together with improved initial data may shed light on such questions, or perhaps some a priori analysis will indicate whether and under what conditions such end states will result.

Part IV

Conclusions

In this thesis we have focused on the phenomenological consequences of "dark" bosonic fields in the context of gravitational physics. These bosons are either very light and mediate a fifth force between matter in the Universe (Part II) or are massive and may constitute exotic compact objects (Part III). Let us here provide a quick qualitative survey of the conclusions:

- Chapter 3: In screening, more is different. Due to the nonlinear nature of theories with derivative screening, going beyond staticity and/or spherical symmetry makes the scalar equations of motion difficult to solve. In particular, it is not a priori clear to what extent the screening is effective in realistic scenarios without high levels of symmetry. We have demonstrated that the Hodge-Helmholtz decomposition of the Noether current associated with the shift symmetry allows for analytic understanding of the non-relativistic two-body problem in good agreement with numerical results. The formalism developed in this work may be used to formulate a post-Newtonian expansion and obtain analytical control of problems such as binary coalescence and stellar collapse in theories with kinetic screening [58, 55]. Furthermore, Hodge-Helmholtz decomposition can also be applied at the perturbative level to theories that softly break shift symmetry [344].

  We have also found, at the phenomenological level, that the fifth force is screened slightly more efficiently in equal-mass systems than in extreme mass-ratio ones. However, systems with comparable masses also exhibit regions where screening is ineffective. These descreened spheroidal regions (bubbles) could in principle be probed in the solar system with sufficiently precise space accelerometers.

- Chapter 4: Soliton stars that have a false vacuum in the potential are effectively described by a linear equation of state, with the speed of sound asymptoting to the speed of light. In this way such configurations saturate the causal Buchdahl bound and constitute a well-defined toy model to study matter under extreme circumstances and demonstrate possibly the most compact exotic objects that can be looked for with gravitational wave probes. Furthermore, this property doesn't depend on the details of the potential but on the presence of a false vacuum.

  Our conclusions have been subsequently validated by other researchers - using different and independent methods [307, 345] and considering different boson star potentials [346]. Let us also note that recent work has analyzed the properties of causal elastic objects, that may have positive pressure anisotropicity, demonstrating that the anisotropic pressure can allow for $\mathcal{C}_{\rm max} \approx 0.389 > \mathcal{C}_{\rm B+C}$ if the radial stability of the object is required [277, 347, 348]. However, in contrast with the

causal Buchdahl bound and soliton boson stars, there are no explicit examples of solitonic objects that can have significant pressure anisotropies and saturate the causal elastic bound. Finally, let us note that compact objects may suffer other types of (non-linear) instabilities that may provide stronger bounds on maximal compactness. In particular, in the case of boson stars, light-ring instability [349] seems to be effective in capping maximal compactness at $\mathcal{C}_{\rm LR} \approx 0.33$ [350].

- Chapter 5: Boson stars abhor angular momentum. Spinning boson stars seems non-trivial as they tend to develop non-axisymmetric instability [162], although strong self-interactions can quench this instability [163]. However, the coalescence of non-rotating strongly-interacting boson stars fails to produce a rotating remnant and the excess orbital angular momentum is emitted in the form of "blobs" - small, apparently self-gravitating structures. We have shown that such a relaxation channel, established in the equal-mass case in Ref. [166], carries over to the non-equal mass case. Furthemore, in the non-equal mass case such blobs induce significant kicks to the remnant boson star.

We have also constructed a model that allows us to classify and predict possible end states of the binary boson star merger. This model has been consistent with the catalog of the binary boson star simulations that we had at our disposal. Our analysis has subsequently been further developed by other researchers. At the technical level, construction of the initial data for the binary boson star coalescence has been significantly improved in Refs. [351, 352]. This further allows quantitative study of gravitational waveforms of the binary coalescence that we have illustrated in our work. Secondly, if one allows for different phases of the scalar field in one of the stars, the rotating boson stars can in fact form [353]. Thus, in Ref. [353] our model for the binary coalescence parameter space has been augmented to include the phase condition. This development further shows that the phenomenology of (binary) boson stars is much richer than what would naively be expected from such simple objects.

Appendix A

Two-body problem in theories with kinetic screening: Details on analytics and numerics

A.1 Regime of validity of the Effective Field Theory

We have discussed the topic of the classical regime of validity of a polynomial $K(X)$ EFT in Sec. 1.2.1. Let us now briefly comment on a DBI case. As a reminder, the EFT description is valid as long as $r \gg r_{\rm UV}$, where $r_{\rm UV}$ is the scale where quantum corrections become significant and consequently the UV physics must play a role

$$r_{\rm UV}^{\rm DBI} \sim \frac{1}{\Lambda} \left(\Lambda r_{\rm sc}\right)^{2/3} . \tag{A.1}$$

In the polynomial case we have seen [discussion around Eq. (1.33)] that for cosmologically motivated values of Λ and any astrophysical object, one is clearly in the regime of validity of the EFT. As an extreme example, let us consider the LISA Pathfinder test mass (see Sec. 3.3.3), which is 2kg and has a size of 4.6cm [354]. From Eq. (3.27), the screening radius is $r_{\rm sc} \approx 10^{-4}$km, while $r_{\rm UV} \approx 10^{-13}$km. The $r_{\rm UV}$ scale is pushed to even smaller values as $N \gg 1$ (and even further for Galileons [22]). The presence of a second body will not change this conclusion, see Sec. 3.3.

Interestingly, the $r_{\rm UV}$ scale for screening in opposite DBI is significantly larger:

$$r_{\rm UV}^{\rm (DBI)} \approx 10^5 {\rm km} \left(\frac{\alpha}{0.1}\right)^{2/3} \left(\frac{\Lambda}{\rm meV}\right)^{-1} \left(\frac{m}{M_\odot}\right)^{2/3} . \tag{A.2}$$

Thus, as already noticed in Ref. [207], the opposite DBI EFT is not appropriate for describing screening around the Sun ($R_\odot = 7 \times 10^5$km), at least for $\Lambda \approx \Lambda_{\rm DE}$. The case becomes even worse for neutron stars, as $R_{\rm NS} \sim 10{\rm km} \ll r_{\rm UV}^{\rm DBI}$.

In the case of anti-screening[1] i.e. $1/2 < N < 1$ [see Eq. (3.76)], based on the results of Ref. [22], the rough condition for the regime of validity is $r_{\rm a-sc} \gg \Lambda^{-1}$, where $r_{\rm a-sc}$ is the anti-screening radius. This condition is easily satisfied for any relevant astrophysical scenario. The exception is the standard DBI anti-screening $N = 1/2$, where the classical description breaks down around the anti-screening radius.

A.2 Regularized Newtonian/FJBD potential

The leading order energy for a system of two point particles can be found from Eq. (3.64), when $N = 1$, by integrating by parts to substitute X with the source T:

$$E_\psi = \frac{\alpha}{2M_{\rm Pl}}[m_a\psi(z_a) + m_b\psi(z_b)]\,. \tag{A.3}$$

Substituting ψ [taking $\Lambda \to \infty$ in Eq. (3.30)], this expression diverges due to the self-energies of the two particles. Even classically, however, these self-energy contributions are actually finite due to the finite size of the two bodies (for which point particles are just a model valid in the IR). If the bodies have a finite size, the total binary energy is therefore regular and reads

$$E_{\psi,\varepsilon} = -\frac{1}{4\pi}\left(\frac{\alpha}{M_{\rm Pl}}\right)^2\left[\frac{m_a^2}{\varepsilon} + \frac{m_b^2}{\varepsilon} + \frac{m_a m_b}{D}\right]\,, \tag{A.4}$$

where ϵ is a regularization parameter of the order of the size of the two bodies. Note that the self energy contributions $\propto 1/\epsilon$ are constant and thus not observable, as the fifth force is given by the energy's gradient. For instance, in the FJBD case the force reads

$$\frac{dE_{\psi,\varepsilon}}{da} = \frac{1}{4\pi}\left(\frac{\alpha}{M_{\rm Pl}}\right)^2\frac{m_a m_b}{D^2} \tag{A.5}$$

which is finite and manifestly independent of the regulator ε.

For numerical purposes, however, we need to specify concrete a "UV completion" of the point particle model. The Gaussian source that we use in this work admits an analytical solution for the Poisson equation, i.e.

$$\psi_{\sigma_i} = -\frac{m\alpha}{4\pi M_{\rm Pl}}{\rm Erf}\Big(\frac{|\boldsymbol{r} - \boldsymbol{r}_i|}{\sqrt{2}\sigma_i}\Big)\,. \tag{A.6}$$

One of course needs to establish that the results do not depend on the choice of σ, as the Gaussian distribution above is not a physically motivated "UV model"[2]. Indeed, we find

[1] We thank the authors of Ref. [196] for pointing out a small error in the previous version of this manuscript.

[2] For example, in order to model a star, one would need to solve the Einstein-Klein-Gordon system for a realistic matter equation of state, as done e.g. in Refs. [36, 198, 58, 196].

that the relative difference between the FJBD force for Dirac-delta and Gaussian sources is less than 1% when $a/\sigma \gtrsim 2$.

A.2.1 Calculation of the fifth force in the irrotational approximation

As the integrals in Sec. 3.3.4 have poles for the point-particle source, we have used the aforementioned Gaussian regularization to calculate them. Consider first the integral $I_N(q)$ of the fifth force in the deep screening regime [Eq. (3.67)], which depends only on q. As the integrand scales as $\sim \mathsf{r}^{(1+2n)/(1-2n)}$ near infinity, we can formally identify the screening region with the whole space. Using the Gaussian regularization, we have $I_N(q) \to \tilde{I}_N(q,\mathsf{R})$, and we have calculated $\tilde{I}_N(q,\mathsf{R})$ for a few values of R. These results are well described by a functional form $\tilde{I}_N(q,\mathsf{R}) = I_N(q)\mathsf{R}^p$ when $\mathsf{R} \ll 1$. Using this fact, we can extract $I_N(q)$, verifying that $p \approx 0$ i.e. that our results are independent of the details of the regularization.

Regarding the calculation of the full energy/force in the irrotational approximation, the volume integral of Eq. (3.65) can be split as

$$\mathcal{E} \approx -\int d\Omega \Big[\int_0^{\mathcal{R}} d\mathsf{r} \sum_{n=1}^{N} \Big(\frac{2n-1}{2n}\Big) \mathcal{X}^n + \frac{1}{2}\int_{\mathcal{R}}^{\infty} d\mathsf{r} \mathcal{X}_\Psi \Big] \mathsf{r}^2 \,,$$

where we have assumed that $\mathcal{X} = \mathcal{X}(\mathcal{X}_\Psi)$ [given by Eq. (3.47) for the quadratic kinetic function], $\mathcal{R} \gg c_2\sqrt{\kappa}\mathsf{D}$ and $d\Omega = \sin\theta d\theta d\vartheta$. The second integral can be found in closed form using Mathematica [355]. Differentiating the integrand with respect to D before fixing the scale $\mathsf{D} = 1$, we obtain the magnitude of the fifth force. As we perform all calculations with the Gaussian regularization, differentiation with respect to D and the integral commute. In order for these results to be independent of the details of the regularization, one must consider the limit $\mathsf{R} \ll 1$. In practice, we find that already at $D \simeq 4R$ the relative difference between the deep screening approximation and the full calculation is smaller than 1%. This difference then gradually increases with D/R, because of the worsening of the deep screening approximation, up to $\sim 50\%$ when $D \approx r_{\rm sc}$.

A.3 Classical dual vs. Helmholtz decomposition

In Ref. [213] it was shown that the theory described by Eq. (2.15), with $\beta = -1$ and $\gamma = 0$ and in the decoupling limit of the scalar and tensor degrees of freedom, can be reformulated, at the classical level, as

$$\mathcal{L}_{\rm dual} = -\frac{1}{2}(\partial\varphi)^2 + \frac{3}{4}\Lambda^{4/3}(\Gamma_\mu\Gamma^\mu)^{2/3} - \Gamma^\mu\partial_\mu\varphi \,, \tag{A.7}$$

where one has introduced the new vector field Γ_μ. The equations of motion that follow from this action are

$$\Box\varphi + \partial_\mu \Gamma^\mu = -\frac{\alpha}{M_{\rm Pl}} T \,, \tag{A.8}$$

$$\Lambda^{4/3} (\Gamma_\mu \Gamma^\mu)^{-1/3} \Gamma_\mu = \partial_\mu \varphi \,. \tag{A.9}$$

Using the latter, the auxiliary vector Γ_μ can be integrated out and the original action is recovered. The appeal of this formulation is that none of the coupling constants in the dual action given by Eq. (A.7) have a negative mass dimension (except for the scalar-matter coupling). This in turn allows for a controlled perturbative expansion in the non-linear regime of the original theory. This formulation was shown to originate from a Legendre transformation and is generalizable to a large class of self-interacting theories [214].

Let us now Hodge-Helmholtz decompose the vector and redefine the scalar as

$$\Gamma_\mu = (-2) B_\mu + \partial_\mu \tilde{\Gamma} \,, \quad \partial_\mu B^\mu = 0 \,, \quad \varphi = \psi - \tilde{\Gamma} \,, \tag{A.10}$$

where B_μ, ψ are for now generic objects. Substituting this decomposition into Eq. (A.8) we obtain Eq. (3.10), i.e.

$$\Box\psi = -\frac{1}{2M_{\rm Pl}} T \,. \tag{A.11}$$

Squaring Eq. (A.9) and substituting the above decomposition, we reconstruct Eq. (3.8) for the quadratic k-essence, i.e.

$$-\frac{1}{2}\Big(1 + \frac{X}{\Lambda^4}\Big) \partial_\mu \varphi = -\frac{1}{2} \partial_\mu \psi + B_\mu \,. \tag{A.12}$$

Thus, the dual formulation of quadratic k-essence is equivalent to the Hodge-Helmholtz decomposition.

In Ref. [213] a different decomposition was used instead of Eq. (A.10):

$$\begin{aligned} &\Gamma_i = (-2) B_i + \partial_i \tilde{\Gamma} \,, \quad \Gamma_0 = \omega \,, \quad \partial_i B^i = 0 \,, \\ &\varphi = \psi - \tilde{\Gamma} \,. \end{aligned} \tag{A.13}$$

It is easy to show that in the static regime, this decomposition is also equivalent to the $\mathbb{R}^3$ Helmholtz one in Eq. (3.18). It was then argued in Ref. [213] that one can consistently choose an ansatz where $B_i = 0$. This however is not the case, as we have elaborated in the main body of this work. The reason why this inconsistency has not been noticed in Ref. [213] is that the dual formulation was applied to isolated systems in spherical and cylindrical symmetry, where the solenoidal component vanishes as argued in Sec. 3.2.2,

	κ	q	R	D/R	$\varrho_{\rm fin}$	$\mathsf{z}_{\rm fin}$
(i)	6	∞	1.6	4	6	12
(ii)	4.8	1	1.6	1.25	8.4	23.04

Table A.1: Parameters of the systems considered for the numerical tests, in units given by Eq. (3.35).

3.2.3.

Finally, let us note an advantage of the Helmholtz-decomposition program over the perturbative expansion in $\tilde{\Gamma}$ that was performed in Ref. [213], for scenarios where the solenoidal component is zero. Instead of expanding, one can solve for the square of the scalar gradient to all orders in the perturbative expansion (see Sec. 3.3.1). If one is interested in the fifth force or the force acting on test bodies, the scalar gradient is the relevant object and the full scalar profile is not necessary (Sec. 3.3.4). However, the dual formulation at the level of action can have other advantages, e.g. allowing for constructing analogues of the irrotational approximation in other types of theories, like Galileons.

A.4 Code validation

We start by testing our code against the known solution for a single isolated body. Because our Newton-Raphson/Broyden method needs an initial guess for the solution, we start from the "linear" solution given by Eq. (A.6), while the exact solution to which we compare is known analytically up to integration of the ordinary differential equation gievn by Eq. (3.47). As a test of our non-linear elliptic solver, we have then solved numerically for the one-body system (i) given in Tab. A.1, for different grid resolutions.

In Fig. A.1, we show the relative difference between the numerical and the semi-analytic results as a function of ϱ, with $\mathsf{z} = \mathsf{z}_c$ fixed to the center of the matter source (where the numerical error is the largest). Results for grid resolutions $\mathsf{h}/R \lesssim 0.15$ have sub-percent errors with respect to the semi-analytic ones. The plot also shows that the relative difference between the initial guess, i.e. the FJBD scalar sourced by a Gaussian [Eq. (A.6)], and the semi-analytic solution that be as large as $\sim 30\%$. Finally, we have checked that the solenoidal vector $\boldsymbol{B}$ is zero (Sec. 3.2.3), up to a numerical errors.

We have also checked the convergence of our residuals (from the semi-analytic solution). In more detail, in Fig. A.2 (left) we show the L^2 norm of the residuals (throughout the grid) vs the grid resolution, alonside a power law fit (red line). The fitted power law exponent ($p = 1.91$) is very close to $p = 2$, as expected from our discretization scheme. By using instead the L^1 norm of the residuals, we obtain $p = 1.99$.

In the two-body case, we do not have a semi-analytic exact solution to compare our numerical results with. However, we can test convergence by considering three different

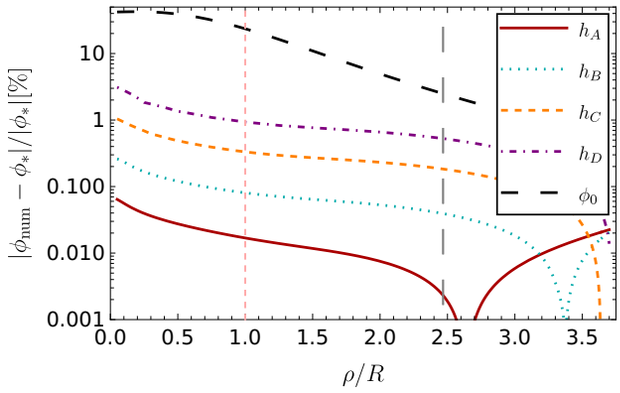

Figure A.1: Relative difference of our numerical results $\phi_{\rm num}$ from the semi-analytic solution ϕ_*, for a one-body system and four different resolutions $h/R = \{0.0375, 0.075, 0.15, 0.25\}$ (corresponding respectively to A, B, C, D), at the center of the source and as function of ϱ. The black long-dashed line represents the difference between the initial guess (FJBD scalar sourced by a Gaussian) and the semi-analytic solution. The screening radius $r_{\rm sc} = 2.47R$ is shown by a gray, long dashed line, and the effective radius of the Gaussian source is $R = 2\sigma$ (pink, short dashed line).

resolutions ($\mathsf{h}_1 = 0.32, \mathsf{h}_2 = 0.16, \mathsf{h}_3 = 0.08$), and estimating the convergence order as

$$p = \log_2 \left(\frac{|\phi_1 - \phi_3|}{|\phi_2 - \phi_3|} - 1 \right) \tag{A.14}$$

where ϕ_1, ϕ_2 and ϕ_3 are the numerical solutions. For the scenario (ii) in Tab. A.1, Fig. A.2 (right) shows $p(\varrho, \mathsf{z})$ at two radial points and demonstrates that the results are consistent with the expected second order convergence.

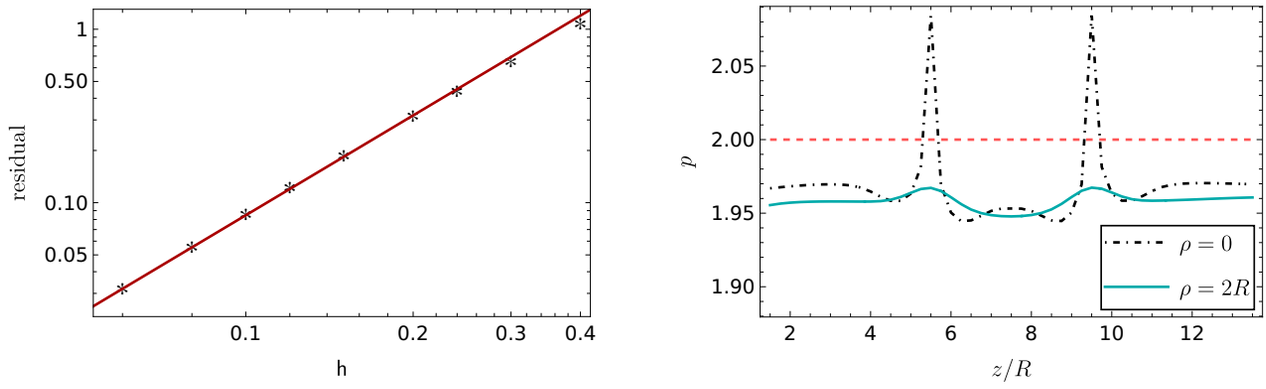

Figure A.2: Grid resolution convergence tests: (left) L^2 norm of the residuals from the semi-analytic solution for a single isolated object (i) in Table A.1, as a function of the resolution. The fitted power law (solid line) corresponds to an exponent $p = 1.91$; (right) Effective convergence order p for the two-body system (ii) in Table A.1, evaluated at $\rho = 0$ and $\rho = 2R$ and as function of z, is consistent with the implemented second order convergence scheme.

Appendix B

Soliton Boson Stars: Details on analytics and numerics

B.1 Numerical solutions of Einstein-Klein-Gordon system

In the following, we present the technical details regarding the well-posedness and numerical solution of the Einstein-Klein-Gordon system given by Eqs. (4.34), (4.35) and (4.36), which we reproduce here for clarity:

$$\frac{1}{r^2}\left(r\,e^{-u}\right)' - \frac{1}{r^2} = -\frac{1}{M_{\rm Pl}^2}\rho\,, \tag{B.1}$$

$$e^{-u}\left(\frac{v'}{r}+\frac{1}{r^2}\right) - \frac{1}{r^2} = \frac{1}{M_{\rm Pl}^2}P_{\rm rad}\,, \tag{B.2}$$

$$\phi'' + \left(\frac{2}{r}+\frac{v'-u'}{2}\right)\phi' = e^{u}\left(\frac{dV}{d|\Phi|^2}-\omega^2 e^{-v}\right)\phi. \tag{B.3}$$

First, let us notice that the structure equations have poles at $r=0$, and we thus have to impose regularity there. In addition, we require solutions to be asymptotically flat. The resulting boundary eigenvalue problem uniquely determines the eigenvalue ω. In fact, on the one hand, a local expansion of the fields around $r=0$ up to $\mathcal{O}(\epsilon^4)$ yields

$$u(\epsilon) \approx 0+\frac{1}{6}\Lambda^2\epsilon^2\varphi_c^2\left(1+e^{-v_c}w^2+\varphi_c^4-2\varphi_c^2\right)\,, \tag{B.4}$$

$$v(\epsilon) \approx v_c-\frac{1}{6}\Lambda^2\epsilon^2\varphi_c^2\left(1-2e^{-v_c}w^2+\varphi_c^4-2\varphi_c^2\right)\,, \tag{B.5}$$

$$\varphi(\epsilon) \approx \varphi_c+\frac{1}{6}\epsilon^2\varphi_c\left(1-e^{-v_c}w^2+3\varphi_c^4-4\varphi_c^2\right)\,, \tag{B.6}$$

where we can set $\tilde{v}_c=0$ and $w\to\tilde{w}$ with a rescaling of the time coordinate. On the other hand, the leading order asymptotic behaviour, as discussed in Sec. 4.3.5.1, is given by Eqs.

(4.49), (4.50), (4.53), which we reproduce here for the reader's convenience:

$$u_{>} = -\log\left(1-\frac{2\bar{M}}{\mathsf{r}}\right), \tag{B.7}$$

$$\tilde{v}_{>} = \tilde{v}_{\infty}+\log\left(1-\frac{2\bar{M}}{\mathsf{r}}\right) \tag{B.8}$$

$$\varphi_{\infty} \simeq \frac{\mathcal{A}}{\mathsf{r}^{1+\beta_{>}}}e^{-\alpha_{>}\mathsf{r}}, \tag{B.9}$$

$$\alpha_{>} = \sqrt{1-e^{-\tilde{v}_{\infty}}\tilde{w}^2}, \tag{B.10}$$

$$\beta_{>} = \frac{\bar{M}}{\alpha_{>}}(1-2e^{-\tilde{v}_{\infty}}\tilde{w}^2), \tag{B.11}$$

One can then match the numerical solution from the interior, obtained with the initial conditions determined by (B.4)-(B.6) at some small but non-zero radius ϵ, with the asymptotic expansion at the infinity, at a finite but sufficiently large matching radius ("direct shooting"). This can be done by solving the four junction conditions

$$\Delta u|_{\bullet}=0\,,\quad \Delta v|_{\bullet}=0\,,\quad \Delta\varphi|_{\bullet}=0\,,\quad \Delta\varphi'|_{\bullet}=0\,, \tag{B.12}$$

where $\Delta x \equiv x_{>}-x_{<}$ and $\mathsf{r}_{\bullet}$ is the matching radius, in the unknowns φ_c, $\tilde{w}$, $\mathcal{A}$ and $\tilde{v}_{\infty}$. Numerical integrations were performed using `Mathematica`'s [355] default stiff solver. The stiffness of the system in the thin wall regime requires an extraordinary amount of fine tuning for the eigenvalues. Examples of the precision levels needed in order to produce compact configurations with a shooting method are given in [248].

Note that this procedure is applicable to SBSs, MBSs, to the potentials considered in Sec. 4.4, and by taking $v\to 0$, $u\to 0$ also to Q-balls. (The asymptotics of Q-balls are discussed in Sec. 4.2.1). Note that the local expansion (B.4)-(B.6) is given for the SBS model and is different for the other potentials. We have validated our results by successfully reproducing the MBS and SBS configurations of [248] and by verifying that the static configurations that we find do not change when used as initial data in the evolution code of [2]. The radius of our solutions is found by inverting $\bar{M}(\mathsf{R})=0.99\bar{M}$ (using bisection) and the Noether charge is calculated numerically by integrating Eq. (4.43). An alternative method for numerical calculation is outlined in [249, 163].

B.2 Definitions of boson star radius

As the radius of boson stars is not well defined, various definitions have been used in the literature [158]. Besides the definition used in this work (corresponding to 99% enclosed mass), the radius R_{95} enclosing 95% of the total mass has also been used [280], as well as

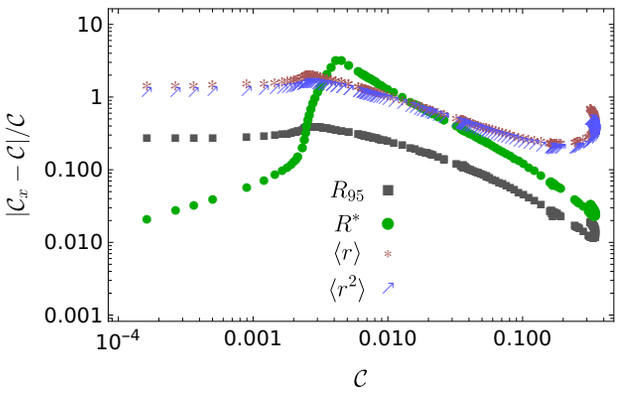

Figure B.1: Relative difference between $\mathcal{C}$ calculated with the benchmark definition of the radius enclosing 99% of the mass and $\mathcal{C}_x = M/R_x$, where $R_x = \{R_{95}, R^*, \langle r \rangle, \sqrt{\langle r^2 \rangle}\}$.

the following moments of the density distribution:

$$\langle r \rangle = \frac{1}{M} \int_0^\infty r \rho(r) dV \,, \tag{B.13}$$

$$\sqrt{\langle r^2 \rangle} = \sqrt{\frac{1}{M} \int_0^\infty r^2 \rho(r) dV} \,. \tag{B.14}$$

Some authors have also considered radii enclosing a given fraction (95% or 99%) of the total Noether charge Q [166], or the moments of j^t [250]. We will not discuss these definitions, because in this Ch. we are interested in the behaviour of Q-balls/SBSs as compact objects, for which energy density based radii are more relevant. Finally, the inflection point R^* was also taken as a Q-ball radius in [263, 278].

In Fig. B.1, we show the difference between our benchmark definition of compactness $\mathcal{C} = M/R$ and the compactness calculated with (respectively) R_{95} , R^* , $\langle r \rangle$, $\sqrt{\langle r^2 \rangle}$ for $\Lambda = 0.186$. The cutoff for the numerical integrals in Eqs. (B.13) and (B.14) was taken to be the domain of the integration. As can be seen, while R_{95} and R^* produce relative differences in the value of the compactness in the compact stable branch of respectively $\sim 10^{-1} - 10^{-2}$ and $\sim 3 \cdot 10^{-1} - 2 \cdot 10^{-2}$ for $\mathcal{C} \gtrsim 0.05$, $\langle r \rangle$ and $\langle r^2 \rangle$ yield $\sim 0.2 - 0.7$ relative differences. This difference can be understood in the following way: in the flat space-time and $\omega \to 0$ limit, the scalar profile approaches a step function and R^* approaches the hard surface radius. Neglecting the surface tension and the potential in that limit, one finds $\langle r \rangle \approx (3/4) R^*$ and $\sqrt{\langle r^2 \rangle} \approx \sqrt{(3/5)} R^*$.

B.3 Analytic construction of Soliton Boson stars: technical details

Here we provide some additional information on the analytic construction of SBS.

B.3.1 u_B metric coefficient on the boundary

On the basis of the discussion from Sec. 4.3.5.3 we find the $\ln(g_{tt})$ metric coefficient jump:

$$
\begin{aligned}
u_B = \quad & -2\mathsf{m}_*\mathsf{R}_* + v_<(\mathsf{R}^*) - \log\left[\frac{\Lambda^2}{r}(e^{-2\mathsf{m}_*\mathsf{R}_*+v_<(\mathsf{R}^*)}\{\chi_0+\chi_1 r+\chi_2 r^2+\chi_2 r^3\}+c_{\rm int})\right], \qquad \text{(B.1}\\
\chi_0 = \quad & \frac{1}{24}\left(-\frac{3e^{-v_<(\mathsf{R}^*)}w^2\mathrm{Li}_3\left(-2e^{2\mathsf{m}_*(r-\mathsf{R}_*)}\right)}{\mathsf{m}_*^3}+\frac{3\mathrm{Li}_2\left(-2e^{2\mathsf{m}_*(r-\mathsf{R}_*)}\right)}{\mathsf{m}_*^3}+\frac{3\log\left(2e^{2\mathsf{m}_*(r-\mathsf{R}_*)}+1\right)}{\mathsf{m}_*^3}\right),\\
\chi_1 = \quad & \frac{1}{24}\Big(\frac{24}{\Lambda^2}+\frac{6e^{-v_<(\mathsf{R}^*)}w^2\mathrm{Li}_2\left(-2e^{2\mathsf{m}_*(r-\mathsf{R}_*)}\right)}{\mathsf{m}_*^2}+\frac{6}{\mathsf{m}_*^2\left(2e^{2\mathsf{m}_*(r-\mathsf{R}_*)}+1\right)}\\
& +\frac{6\log\left(2e^{2\mathsf{m}_*(r-\mathsf{R}_*)}+1\right)}{\mathsf{m}_*^2}-\frac{6}{\mathsf{m}_*^2}\Big),\\
\chi_2 = \quad & \frac{1}{24}\left(\frac{6e^{-v_<(\mathsf{R}^*)}w^2\log\left(2e^{2\mathsf{m}_*(r-\mathsf{R}_*)}+1\right)}{\mathsf{m}_*}-\frac{6}{\mathsf{m}_*\left(2e^{2\mathsf{m}_*(r-\mathsf{R}_*)}+1\right)^2}+\frac{12}{2\mathsf{m}_*e^{2\mathsf{m}_*(r-\mathsf{R}_*)}+\mathsf{m}_*}-\frac{6}{\mathsf{m}_*}\right)\\
\chi_3 = \quad & -\frac{1}{6}e^{-v_<(\mathsf{R}^*)}w^2\,.
\end{aligned}
$$

The integration constant $c_{\rm int}$ is determined by matching the previous solution to $u_<$ at $\mathsf{R}_<$ and Li_n is the polylogarithm function.

B.3.2 Details of the energy balance calculation

Here we provide details on obtaining analytic approximations in Sec. 4.3.5.4 . We will first approximate the complicated algebraic expressions (4.69) - (4.73). The sum $B_{\mathcal{E}}+C_{\mathcal{E}}+D_{\mathcal{E}B}$ is subleading, as the dominant contribution, proportional to $\mathsf{m}_*^2\Lambda^2\mathsf{R}^{*2}$, cancels out. In the Q-ball limit, one also has $\mathsf{m}_*^2\sim 1$, which suppresses the term proportional to $(1-\mathsf{m}_*^2)$. In the more compact branch, we have numerically established that $(1-\mathsf{m}_*^2)\lesssim 2.5$; however, in that regime the terms $\sim 1/\mathsf{R}^*$ are subdominant relative to the volume originating terms in $D_{\mathcal{E}<}$, because $(\mathsf{R}^*\Lambda\tilde{w})^2\sim 4$, while $1/\mathsf{R}^*\sim\Lambda\tilde{w}/2\ll 1$. Finally, the contributions with $w^2e^{-v_*}$ are suppressed, both due to $v_*>0$ and to the numerical pre-factors.

Leaving only the terms $A_{\mathcal{E}}+D_{\mathcal{E}<}$ on the right hand side of our master equation Eq. (4.69), approximating $\mathsf{m}_*\approx\exp\left(u_<(\mathsf{R}^*)/2\right)$ and expanding in Λ, we the find Eq. (4.77)

which we reproduce here

$$\tilde{w} \approx \Lambda \frac{\sqrt{-\frac{T^4}{5} + 6T^2 + 36}\,(T^4 + 10T^2 + 30)}{T\,(-T^4 + 30T^2 + 180)}\,. \tag{B.16}$$

Inverting this equation, we find complicated expressions for the two branches, which can be approximated as

$$T \approx T(\tilde{w}_\cup/\Lambda) \pm \sqrt{3.1\,(\tilde{w} - \tilde{w}_\cup)/\Lambda}\,, \tilde{w} \sim \tilde{w}_\cup \tag{B.17}$$

where $T(\tilde{w}_\cup/\Lambda) \approx 1.6$. Using Eq. (B.17), the simple expectation for $v_\infty \approx v_<(\mathsf{R}^*) + u_<(\mathsf{R}^*)$ allows us to find an approximate behaviour for w, given in Eq. (4.78).

B.3.3 On the errors of estimating the radius

In Section 4.3.5.5, the semi-analytic calculation develops a few percent systematic error near the maximum mass. There are two reasons for this. First, the expansion of u and v in the interior [expressions (4.56)-(4.57)] works well only for small $\tilde{w}$, i.e. for configurations similar to II. In the thick-wall regime, the perturbative expansion outlined in Section 4.3.5.2 does not work well by construction. Although the frequency $\tilde{w}$ is higher for the configurations similar to III, the field derivative is still exponentially suppressed and physically these configurations have even thinner walls than the ones similar to II. Thus, one can expect that some different perturbative scheme could improve the analytic description of the metric coefficients for the configurations similar to III.

The second reason for the systematic error is that Eq. (4.21), which describes the deviation between R and R^*, does the best job for the configurations similar to II. For configurations similar to III, we have established numerically that the choice

$$\lambda_{\rm III} = \frac{4}{2}\frac{2.66}{\delta} \tag{B.18}$$

is the most appropriate one, while for configurations similar to I:

$$\lambda_{\rm I} = \frac{2}{2}\frac{2.66}{\delta}\,. \tag{B.19}$$

This issue can be circumvented by performing the (cheap) numerical inversion $4\pi \int_0^R dr\, r^2 \rho(r) = 0.99M$ around the trial value determined by the semi-analytic algorithm, with a piecewise analytic approximation for ρ (obtained from the field and the metric coefficients approximants). Finally, the limits of the analytic description of the thin-wall Q-ball-like region in the parameter space (i.e. configurations similar to I) are discussed in [263].

Regarding the compact unstable branch: the numerical calculations indicate additional

step-like features in the bulk of the scalar profile. This feature, not accounted for in our analytical description, is probably the origin of the increasing error in this branch.

Bibliography

[1] M. Bošković and E. Barausse, "Soliton boson stars, Q-balls and the causal Buchdahl bound," *JCAP*, vol. 02, no. 02, p. 032, 2022.

[2] M. Bezares, M. Bošković, S. Liebling, C. Palenzuela, P. Pani, and E. Barausse, "Gravitational waves and kicks from the merger of unequal mass, highly compact boson stars," *Phys. Rev. D*, vol. 105, no. 6, p. 064067, 2022.

[3] M. Bošković and E. Barausse, "Two-body problem in theories with kinetic screening," 5 2023.

[4] S. Weinberg, "On the Development of Effective Field Theory," *Eur. Phys. J. H*, vol. 46, no. 1, p. 6, 2021.

[5] J. F. Donoghue, M. M. Ivanov, and A. Shkerin, "EPFL Lectures on General Relativity as a Quantum Field Theory," 2 2017.

[6] R. Penco, "An Introduction to Effective Field Theories," 6 2020.

[7] C. P. Burgess, *Introduction to Effective Field Theory*. Cambridge University Press, 12 2020.

[8] M. D. Schwartz, *Quantum Field Theory and the Standard Model*. Cambridge University Press, 3 2014.

[9] C. P. Burgess and M. Williams, "Who You Gonna Call? Runaway Ghosts, Higher Derivatives and Time-Dependence in EFTs," *JHEP*, vol. 08, p. 074, 2014.

[10] C. Rovelli, *Quantum gravity*. Cambridge Monographs on Mathematical Physics, Cambridge, UK: Univ. Pr., 2004.

[11] R. P. Feynman, *Feynman lectures on gravitation*. 1996.

[12] S. Weinberg, *The Quantum theory of fields. Vol. 1: Foundations*. Cambridge University Press, 6 2005.

[13] M. Blagojevic, *Gravitation and gauge symmetries*. 2002.

[14] S. Deser, "Selfinteraction and gauge invariance," *Gen. Rel. Grav.*, vol. 1, pp. 9–18, 1970.

[15] S. Deser, "Gravity from self-interaction redux," *Gen. Rel. Grav.*, vol. 42, pp. 641–646, 2010.

[16] S. Weinberg, "What is quantum field theory, and what did we think it is?," in *Conference on Historical Examination and Philosophical Reflections on the Foundations of Quantum Field Theory*, pp. 241–251, 3 1996.

[17] N. Arkani-Hamed, L. Rodina, and J. Trnka, "Locality and Unitarity of Scattering Amplitudes from Singularities and Gauge Invariance," *Phys. Rev. Lett.*, vol. 120, no. 23, p. 231602, 2018.

[18] J. F. Donoghue, "Quantum General Relativity and Effective Field Theory," 11 2022.

[19] G. Goon, K. Hinterbichler, A. Joyce, and M. Trodden, "Aspects of Galileon Non-Renormalization," *JHEP*, vol. 11, p. 100, 2016.

[20] A. Joyce, A. Nicolis, A. Podo, and L. Santoni, "Integrating out beyond tree level and relativistic superfluids," *JHEP*, vol. 09, p. 066, 2022.

[21] A. Nicolis and R. Rattazzi, "Classical and quantum consistency of the DGP model," *JHEP*, vol. 06, p. 059, 2004.

[22] C. de Rham and R. H. Ribeiro, "Riding on irrelevant operators," *JCAP*, vol. 11, p. 016, 2014.

[23] P. Brax and P. Valageas, "Quantum field theory of K-mouflage," *Phys. Rev. D*, vol. 94, no. 4, p. 043529, 2016.

[24] A. O. Barvinsky and G. A. Vilkovisky, "Beyond the Schwinger-Dewitt Technique: Converting Loops Into Trees and In-In Currents," *Nucl. Phys. B*, vol. 282, pp. 163–188, 1987.

[25] A. O. Barvinsky and G. A. Vilkovisky, "Covariant perturbation theory. 2: Second order in the curvature. General algorithms," *Nucl. Phys. B*, vol. 333, pp. 471–511, 1990.

[26] A. Codello and O. Zanusso, "On the non-local heat kernel expansion," *J. Math. Phys.*, vol. 54, p. 013513, 2013.

[27] A. Zee, *Einstein Gravity in a Nutshell.* New Jersey: Princeton University Press, 2013.

[28] P. Creminelli, A. Nicolis, M. Papucci, and E. Trincherini, "Ghosts in massive gravity," *JHEP*, vol. 09, p. 003, 2005.

[29] Y. Aharonov, A. Komar, and L. Susskind, "Superluminal behavior, causality, and instability," *Phys. Rev.*, vol. 182, pp. 1400–1403, 1969.

[30] A. Joyce, B. Jain, J. Khoury, and M. Trodden, "Beyond the Cosmological Standard Model," *Phys. Rept.*, vol. 568, pp. 1–98, 2015.

[31] H. S. Reall and C. M. Warnick, "Effective field theory and classical equations of motion," *J. Math. Phys.*, vol. 63, no. 4, p. 042901, 2022.

[32] A. R. Solomon and M. Trodden, "Higher-derivative operators and effective field theory for general scalar-tensor theories," *JCAP*, vol. 02, p. 031, 2018.

[33] A. Nicolis, R. Rattazzi, and E. Trincherini, "The Galileon as a local modification of gravity," *Phys. Rev. D*, vol. 79, p. 064036, 2009.

[34] J. L. Ripley, "Numerical relativity for Horndeski gravity," *Int. J. Mod. Phys. D*, vol. 31, no. 13, p. 2230017, 2022.

[35] L. Bernard, L. Lehner, and R. Luna, "Challenges to global solutions in Horndeski's theory," *Phys. Rev. D*, vol. 100, no. 2, p. 024011, 2019.

[36] C. Armendariz-Picon and E. A. Lim, "Haloes of k-essence," *JCAP*, vol. 08, p. 007, 2005.

[37] A. D. Rendall, "Dynamics of k-essence," *Class. Quant. Grav.*, vol. 23, pp. 1557–1570, 2006.

[38] J.-P. Bruneton, "On causality and superluminal behavior in classical field theories: Applications to k-essence theories and MOND-like theories of gravity," *Phys. Rev. D*, vol. 75, p. 085013, 2007.

[39] E. Babichev, V. Mukhanov, and A. Vikman, "k-Essence, superluminal propagation, causality and emergent geometry," *JHEP*, vol. 02, p. 101, 2008.

[40] P. Brax and P. Valageas, "Small-scale Nonlinear Dynamics of K-mouflage Theories," *Phys. Rev. D*, vol. 90, no. 12, p. 123521, 2014.

[41] M. Bezares, M. Crisostomi, C. Palenzuela, and E. Barausse, "K-dynamics: well-posed 1+1 evolutions in K-essence," *JCAP*, vol. 03, p. 072, 2021.

[42] M. P. Hertzberg, J. A. Litterer, and N. Shah, "Acausality in superfluid dark matter and MOND-like theories," *JCAP*, vol. 11, p. 015, 2021.

[43] J. Cayuso, N. Ortiz, and L. Lehner, "Fixing extensions to general relativity in the nonlinear regime," *Phys. Rev. D*, vol. 96, no. 8, p. 084043, 2017.

[44] G. Lara, M. Bezares, and E. Barausse, "UV completions, fixing the equations, and nonlinearities in k-essence," *Phys. Rev. D*, vol. 105, no. 6, p. 064058, 2022.

[45] E. Barausse, M. Bezares, M. Crisostomi, and G. Lara, "The well-posedness of the Cauchy problem for self-interacting vector fields," 7 2022.

[46] A. Kovacs, *The Cauchy problem and the initial data problem in effective theories of gravity*. PhD thesis, University of Cambridge, 2021.

[47] E. Witten, "Light Rays, Singularities, and All That," *Rev. Mod. Phys.*, vol. 92, no. 4, p. 045004, 2020.

[48] A. D. Kovács and H. S. Reall, "Well-Posed Formulation of Scalar-Tensor Effective Field Theory," *Phys. Rev. Lett.*, vol. 124, no. 22, p. 221101, 2020.

[49] A. D. Kovács and H. S. Reall, "Well-posed formulation of Lovelock and Horndeski theories," *Phys. Rev. D*, vol. 101, no. 12, p. 124003, 2020.

[50] W. E. East and J. L. Ripley, "Dynamics of Spontaneous Black Hole Scalarization and Mergers in Einstein-Scalar-Gauss-Bonnet Gravity," *Phys. Rev. Lett.*, vol. 127, no. 10, p. 101102, 2021.

[51] W. E. East and F. Pretorius, "Binary neutron star mergers in Einstein-scalar-Gauss-Bonnet gravity," *Phys. Rev. D*, vol. 106, no. 10, p. 104055, 2022.

[52] A. Fienga and O. Minazzoli, "Testing GR and alternative theories with planetary ephemerides," 3 2023.

[53] P. Figueras and T. França, "Black hole binaries in cubic Horndeski theories," *Phys. Rev. D*, vol. 105, no. 12, p. 124004, 2022.

[54] E. Poisson and C. M. Will, *Gravity: Newtonian, Post-Newtonian, Relativistic*. Cambridge University Press, 2014.

[55] M. Bezares, R. Aguilera-Miret, L. ter Haar, M. Crisostomi, C. Palenzuela, and E. Barausse, "No Evidence of Kinetic Screening in Simulations of Merging Binary Neutron Stars beyond General Relativity," *Phys. Rev. Lett.*, vol. 128, no. 9, p. 091103, 2022.

[56] M. Gerhardinger, J. T. Giblin, Jr., A. J. Tolley, and M. Trodden, "Well-posed UV completion for simulating scalar Galileons," *Phys. Rev. D*, vol. 106, no. 4, p. 043522, 2022.

[57] G. Allwright and L. Lehner, "Towards the nonlinear regime in extensions to GR: assessing possible options," *Class. Quant. Grav.*, vol. 36, no. 8, p. 084001, 2019.

[58] M. Bezares, L. ter Haar, M. Crisostomi, E. Barausse, and C. Palenzuela, "Kinetic screening in nonlinear stellar oscillations and gravitational collapse," *Phys. Rev. D*, vol. 104, no. 4, p. 044022, 2021.

[59] L.-Y. Chen, N. Goldenfeld, and Y. Oono, "The Renormalization group and singular perturbations: Multiple scales, boundary layers and reductive perturbation theory," *Phys. Rev.*, vol. E54, pp. 376–394, 1996.

[60] J. T. Gálvez Ghersi and L. C. Stein, "Numerical renormalization-group-based approach to secular perturbation theory," *Phys. Rev. E*, vol. 104, no. 3, p. 034219, 2021.

[61] A. Adams, N. Arkani-Hamed, S. Dubovsky, A. Nicolis, and R. Rattazzi, "Causality, analyticity and an IR obstruction to UV completion," *JHEP*, vol. 10, p. 014, 2006.

[62] K. Aoki, S. Mukohyama, and R. Namba, "Positivity vs. Lorentz-violation: an explicit example," *JCAP*, vol. 10, p. 079, 2021.

[63] M. Tomašević, "On the Inaccessibility of Time Machines," *Universe*, vol. 9, no. 4, p. 159, 2023.

[64] C. de Rham and A. J. Tolley, "Causality in curved spacetimes: The speed of light and gravity," *Phys. Rev. D*, vol. 102, no. 8, p. 084048, 2020.

[65] N. Arkani-Hamed, T.-C. Huang, and Y.-t. Huang, "The EFT-Hedron," *JHEP*, vol. 05, p. 259, 2021.

[66] C. Y. R. Chen, C. de Rham, A. Margalit, and A. J. Tolley, "A cautionary case of casual causality," *JHEP*, vol. 03, p. 025, 2022.

[67] M. Carrillo Gonzalez, C. de Rham, V. Pozsgay, and A. J. Tolley, "Causal effective field theories," *Phys. Rev. D*, vol. 106, no. 10, p. 105018, 2022.

[68] M. Carrillo González, C. de Rham, S. Jaitly, V. Pozsgay, and A. Tokareva, "Positivity-causality competition: a road to ultimate EFT consistency constraints," 7 2023.

[69] T. Grall, *Symmetries, unitarity and positivity of cosmological effective field theories*. PhD thesis, Department of Applied Mathematics And Theoretical Physics, Cambridge U., University of Cambridge, 2023.

[70] B. Bellazzini, F. Riva, J. Serra, and F. Sgarlata, "Beyond Positivity Bounds and the Fate of Massive Gravity," *Phys. Rev. Lett.*, vol. 120, no. 16, p. 161101, 2018.

[71] C. de Rham, S. Melville, A. J. Tolley, and S.-Y. Zhou, "Positivity bounds for scalar field theories," *Phys. Rev. D*, vol. 96, no. 8, p. 081702, 2017.

[72] M. Herrero-Valea, R. Santos-Garcia, and A. Tokareva, "Massless positivity in graviton exchange," *Phys. Rev. D*, vol. 104, no. 8, p. 085022, 2021.

[73] M. Herrero-Valea, A. S. Koshelev, and A. Tokareva, "UV graviton scattering and positivity bounds from IR dispersion relations," *Phys. Rev. D*, vol. 106, no. 10, p. 105002, 2022.

[74] A.-C. Davis and S. Melville, "Scalar fields near compact objects: resummation versus UV completion," *JCAP*, vol. 11, p. 012, 2021.

[75] P. Creminelli, O. Janssen, and L. Senatore, "Positivity bounds on effective field theories with spontaneously broken Lorentz invariance," *JHEP*, vol. 09, p. 201, 2022.

[76] D. Baumann, *Cosmology*. 2017.

[77] D. Baumann, *Cosmology*. Cambridge University Press, 7 2022.

[78] P. J. E. Peebles, "Large scale background temperature and mass fluctuations due to scale invariant primeval perturbations," *Astrophys. J. Lett.*, vol. 263, pp. L1–L5, 1982.

[79] N. Aghanim *et al.*, "Planck 2018 results. VI. Cosmological parameters," *Astron. Astrophys.*, vol. 641, p. A6, 2020. [Erratum: Astron.Astrophys. 652, C4 (2021)].

[80] M. M. Ivanov, M. Simonović, and M. Zaldarriaga, "Cosmological Parameters from the BOSS Galaxy Power Spectrum," *JCAP*, vol. 05, p. 042, 2020.

[81] G. Bertone and D. Hooper, "History of dark matter," *Rev. Mod. Phys.*, vol. 90, no. 4, p. 045002, 2018.

[82] G. Bertone and T. Tait, M. P., "A new era in the search for dark matter," *Nature*, vol. 562, no. 7725, pp. 51–56, 2018.

[83] J. S. Bullock and M. Boylan-Kolchin, "Small-Scale Challenges to the ΛCDM Paradigm," *Ann. Rev. Astron. Astrophys.*, vol. 55, pp. 343–387, 2017.

[84] L. Hui, "Wave Dark Matter," 2021.

[85] M. Lisanti, "Lectures on Dark Matter Physics," in *Proceedings, Theoretical Advanced Study Institute in Elementary Particle Physics: New Frontiers in Fields and Strings (TASI 2015): Boulder, CO, USA, June 1-26, 2015*, pp. 399–446, 2017.

[86] D. J. E. Marsh, "Axion Cosmology," *Phys. Rept.*, vol. 643, pp. 1–79, 2016.

[87] A. Hook, "TASI Lectures on the Strong CP Problem and Axions," 2018.

[88] A. Arvanitaki, S. Dimopoulos, S. Dubovsky, N. Kaloper, and J. March-Russell, "String Axiverse," *Phys. Rev.*, vol. D81, p. 123530, 2010.

[89] L. Hui, J. P. Ostriker, S. Tremaine, and E. Witten, "Ultralight scalars as cosmological dark matter," *Phys. Rev.*, vol. D95, no. 4, p. 043541, 2017.

[90] D. J. Kaup, "Klein-Gordon Geon," *Phys. Rev.*, vol. 172, pp. 1331–1342, 1968.

[91] P.-H. Chavanis and T. Harko, "Bose-Einstein Condensate general relativistic stars," *Phys. Rev.*, vol. D86, p. 064011, 2012.

[92] H. Năstase, *Classical Field Theory*. Cambridge University Press, 2019.

[93] E. Seidel and W. M. Suen, "Oscillating soliton stars," *Phys. Rev. Lett.*, vol. 66, pp. 1659–1662, 1991.

[94] T. Helfer, D. J. E. Marsh, K. Clough, M. Fairbairn, E. A. Lim, and R. Becerril, "Black hole formation from axion stars," *JCAP*, vol. 1703, no. 03, p. 055, 2017.

[95] M. Bošković, F. Duque, M. C. Ferreira, F. S. Miguel, and V. Cardoso, "Motion in time-periodic backgrounds with applications to ultralight dark matter haloes at galactic centers," *Phys. Rev.*, vol. D98, p. 024037, 2018.

[96] S. Kasuya, M. Kawasaki, and F. Takahashi, "I-balls," *Phys. Lett. B*, vol. 559, pp. 99–106, 2003.

[97] M. P. Hertzberg, "Quantum Radiation of Oscillons," *Phys. Rev.*, vol. D82, p. 045022, 2010.

[98] H.-Y. Zhang, M. A. Amin, E. J. Copeland, P. M. Saffin, and K. D. Lozanov, "Classical Decay Rates of Oscillons," *JCAP*, vol. 07, p. 055, 2020.

[99] N. Bar, D. Blas, K. Blum, and S. Sibiryakov, "Galactic rotation curves versus ultralight dark matter: Implications of the soliton-host halo relation," *Phys. Rev.*, vol. D98, no. 8, p. 083027, 2018.

[100] N. Bar, K. Blum, T. Lacroix, and P. Panci, "Looking for ultralight dark matter near supermassive black holes," 2019.

[101] N. Bar, K. Blum, and C. Sun, "Galactic rotation curves versus ultralight dark matter: A systematic comparison with SPARC data," *Phys. Rev. D*, vol. 105, no. 8, p. 083015, 2022.

[102] D. G. Levkov, A. G. Panin, and I. I. Tkachev, "Gravitational Bose-Einstein condensation in the kinetic regime," *Phys. Rev. Lett.*, vol. 121, no. 15, p. 151301, 2018.

[103] J. Y. Widdicombe, T. Helfer, D. J. E. Marsh, and E. A. Lim, "Formation of Relativistic Axion Stars," *JCAP*, vol. 1810, no. 10, p. 005, 2018.

[104] A. Arvanitaki, S. Dimopoulos, M. Galanis, L. Lehner, J. O. Thompson, and K. Van Tilburg, "Large-misalignment mechanism for the formation of compact axion structures: Signatures from the QCD axion to fuzzy dark matter," *Phys. Rev.*, vol. D101, no. 8, p. 083014, 2020.

[105] T. Dietrich, F. Day, K. Clough, M. Coughlin, and J. Niemeyer, "Neutron star–axion star collisions in the light of multimessenger astronomy," *Mon. Not. Roy. Astron. Soc.*, vol. 483, no. 1, pp. 908–914, 2019.

[106] J. Bekenstein and M. Milgrom, "Does the missing mass problem signal the breakdown of Newtonian gravity?," *Astrophys. J.*, vol. 286, pp. 7–14, 1984.

[107] B. Famaey and S. McGaugh, "Modified Newtonian Dynamics (MOND): Observational Phenomenology and Relativistic Extensions," *Living Rev. Rel.*, vol. 15, p. 10, 2012.

[108] S. McGaugh, F. Lelli, and J. Schombert, "Radial Acceleration Relation in Rotationally Supported Galaxies," *Phys. Rev. Lett.*, vol. 117, no. 20, p. 201101, 2016.

[109] J. D. Bekenstein, "Relativistic gravitation theory for the MOND paradigm," *Phys. Rev. D*, vol. 70, p. 083509, 2004. [Erratum: Phys.Rev.D 71, 069901 (2005)].

[110] T. G. Zlosnik, P. G. Ferreira, and G. D. Starkman, "Modifying gravity with the Aether: An alternative to Dark Matter," *Phys. Rev. D*, vol. 75, p. 044017, 2007.

[111] L. Blanchet and S. Marsat, "Modified gravity approach based on a preferred time foliation," *Phys. Rev. D*, vol. 84, p. 044056, 2011.

[112] M. Bonetti and E. Barausse, "Post-Newtonian constraints on Lorentz-violating gravity theories with a MOND phenomenology," *Phys. Rev. D*, vol. 91, p. 084053, 2015. [Erratum: Phys.Rev.D 93, 029901 (2016)].

[113] P. M. Chesler and A. Loeb, "Constraining Relativistic Generalizations of Modified Newtonian Dynamics with Gravitational Waves," *Phys. Rev. Lett.*, vol. 119, no. 3, p. 031102, 2017.

[114] J. M. Ezquiaga and M. Zumalacárregui, "Dark Energy After GW170817: Dead Ends and the Road Ahead," *Phys. Rev. Lett.*, vol. 119, no. 25, p. 251304, 2017.

[115] S. Dodelson, "The Real Problem with MOND," *Int. J. Mod. Phys.*, vol. D20, pp. 2749–2753, 2011.

[116] J. Khoury, "Alternative to particle dark matter," *Phys. Rev. D*, vol. 91, no. 2, p. 024022, 2015.

[117] L. Berezhiani and J. Khoury, "Theory of dark matter superfluidity," *Phys. Rev.*, vol. D92, p. 103510, 2015.

[118] S. M. Carroll, "The Cosmological constant," *Living Rev. Rel.*, vol. 4, p. 1, 2001.

[119] C. P. Burgess, "The Cosmological Constant Problem: Why it's hard to get Dark Energy from Micro-physics," in *100e Ecole d'Ete de Physique: Post-Planck Cosmology*, pp. 149–197, 2015.

[120] P. Brax, "What makes the Universe accelerate? A review on what dark energy could be and how to test it," *Rept. Prog. Phys.*, vol. 81, no. 1, p. 016902, 2018.

[121] S. Weinberg, "The Cosmological Constant Problem," *Rev. Mod. Phys.*, vol. 61, pp. 1–23, 1989.

[122] R. Bousso, "TASI Lectures on the Cosmological Constant," *Gen. Rel. Grav.*, vol. 40, pp. 607–637, 2008.

[123] S. Weinberg, "Anthropic Bound on the Cosmological Constant," *Phys. Rev. Lett.*, vol. 59, p. 2607, 1987.

[124] G. Cabass, M. M. Ivanov, M. Lewandowski, M. Mirbabayi, and M. Simonović, "Snowmass White Paper: Effective Field Theories in Cosmology," in *2022 Snowmass Summer Study*, 3 2022.

[125] M. Fierz, "On the physical interpretation of P.Jordan's extended theory of gravitation," *Helv. Phys. Acta*, vol. 29, pp. 128–134, 1956.

[126] P. Jordan, "The present state of Dirac's cosmological hypothesis," *Z. Phys.*, vol. 157, pp. 112–121, 1959.

[127] C. Brans and R. H. Dicke, "Mach's principle and a relativistic theory of gravitation," *Phys. Rev.*, vol. 124, pp. 925–935, 1961.

[128] B. Bertotti, L. Iess, and P. Tortora, "A test of general relativity using radio links with the Cassini spacecraft," *Nature*, vol. 425, pp. 374–376, 2003.

[129] A. I. Vainshtein, "To the problem of nonvanishing gravitation mass," *Phys. Lett. B*, vol. 39, pp. 393–394, 1972.

[130] E. Babichev, C. Deffayet, and R. Ziour, "k-Mouflage gravity," *Int. J. Mod. Phys. D*, vol. 18, pp. 2147–2154, 2009.

[131] E. Babichev and C. Deffayet, "An introduction to the Vainshtein mechanism," *Class. Quant. Grav.*, vol. 30, p. 184001, 2013.

[132] P. Brax and C. Burrage, "Constraining Disformally Coupled Scalar Fields," *Phys. Rev. D*, vol. 90, no. 10, p. 104009, 2014.

[133] P. Brax and A.-C. Davis, "Gravitational effects of disformal couplings," *Phys. Rev. D*, vol. 98, no. 6, p. 063531, 2018.

[134] K. Hinterbichler and J. Khoury, "Symmetron Fields: Screening Long-Range Forces Through Local Symmetry Restoration," *Phys. Rev. Lett.*, vol. 104, p. 231301, 2010.

[135] J. Khoury and A. Weltman, "Chameleon fields: Awaiting surprises for tests of gravity in space," *Phys. Rev. Lett.*, vol. 93, p. 171104, 2004.

[136] G. W. Horndeski, "Second-order scalar-tensor field equations in a four-dimensional space," *Int. J. Theor. Phys.*, vol. 10, pp. 363–384, 1974.

[137] J. Gleyzes, D. Langlois, F. Piazza, and F. Vernizzi, "Healthy theories beyond Horndeski," *Phys. Rev. Lett.*, vol. 114, no. 21, p. 211101, 2015.

[138] J. Ben Achour, M. Crisostomi, K. Koyama, D. Langlois, K. Noui, and G. Tasinato, "Degenerate higher order scalar-tensor theories beyond Horndeski up to cubic order," *JHEP*, vol. 12, p. 100, 2016.

[139] G. Tambalo, *Gravitational Wave Decay: Implications for cosmological scalar-tensor theories*. PhD thesis, SISSA, Trieste, 2020.

[140] L. Santoni, E. Trincherini, and L. G. Trombetta, "Behind Horndeski: structurally robust higher derivative EFTs," *JHEP*, vol. 08, p. 118, 2018.

[141] P. Creminelli and F. Vernizzi, "Dark Energy after GW170817 and GRB170817A," *Phys. Rev. Lett.*, vol. 119, no. 25, p. 251302, 2017.

[142] P. Creminelli, M. Lewandowski, G. Tambalo, and F. Vernizzi, "Gravitational Wave Decay into Dark Energy," *JCAP*, vol. 12, p. 025, 2018.

[143] P. Creminelli, G. Tambalo, F. Vernizzi, and V. Yingcharoenrat, "Dark-Energy Instabilities induced by Gravitational Waves," *JCAP*, vol. 05, p. 002, 2020.

[144] P. Creminelli, G. Tambalo, F. Vernizzi, and V. Yingcharoenrat, "Resonant Decay of Gravitational Waves into Dark Energy," *JCAP*, vol. 10, p. 072, 2019.

[145] G. Bertone *et al.*, "Gravitational wave probes of dark matter: challenges and opportunities," *SciPost Phys. Core*, vol. 3, p. 007, 2020.

[146] V. Cardoso and P. Pani, "Testing the nature of dark compact objects: a status report," *Living Rev. Rel.*, vol. 22, no. 1, p. 4, 2019.

[147] M. Visser, *Lorentzian wormholes: From Einstein to Hawking*. 1995.

[148] P. O. Mazur and E. Mottola, "Gravitational condensate stars: An alternative to black holes," 2001.

[149] G. Raposo, P. Pani, M. Bezares, C. Palenzuela, and V. Cardoso, "Anisotropic stars as ultracompact objects in General Relativity," *Phys. Rev.*, vol. D99, no. 10, p. 104072, 2019.

[150] V. Cardoso, E. Franzin, A. Maselli, P. Pani, and G. Raposo, "Testing strong-field gravity with tidal Love numbers," *Phys. Rev. D*, vol. 95, no. 8, p. 084014, 2017. [Addendum: Phys.Rev.D 95, 089901 (2017)].

[151] H. S. Chia, T. D. P. Edwards, D. Wadekar, A. Zimmerman, S. Olsen, J. Roulet, T. Venumadhav, B. Zackay, and M. Zaldarriaga, "In Pursuit of Love: First Templated Search for Compact Objects with Large Tidal Deformabilities in the LIGO-Virgo Data," 5 2023.

[152] A. Toubiana, S. Babak, E. Barausse, and L. Lehner, "Modeling gravitational waves from exotic compact objects," *Phys. Rev. D*, vol. 103, no. 6, p. 064042, 2021.

[153] E. Barausse, V. Cardoso, and P. Pani, "Can environmental effects spoil precision gravitational-wave astrophysics?," *Phys. Rev.*, vol. D89, no. 10, p. 104059, 2014.

[154] V. Cardoso, E. Franzin, and P. Pani, "Is the gravitational-wave ringdown a probe of the event horizon?," *Phys. Rev. Lett.*, vol. 116, no. 17, p. 171101, 2016. [Erratum: Phys. Rev. Lett.117,no.8,089902(2016)].

[155] V. Cardoso, S. Hopper, C. F. B. Macedo, C. Palenzuela, and P. Pani, "Gravitational-wave signatures of exotic compact objects and of quantum corrections at the horizon scale," *Phys. Rev.*, vol. D94, no. 8, p. 084031, 2016.

[156] T. Lee and Y. Pang, "Nontopological solitons," *Phys.Rept.*, vol. 221, pp. 251–350, 1992.

[157] P. Jetzer, "Boson stars," *Phys.Rept.*, vol. 220, pp. 163–227, 1992.

[158] F. Schunck and E. Mielke, "General relativistic boson stars," *Class.Quant.Grav.*, vol. 20, pp. R301–R356, 2003.

[159] S. L. Liebling and C. Palenzuela, "Dynamical Boson Stars," *Living Rev. Rel.*, vol. 20, p. 5, 2017.

[160] L. Visinelli, "Boson Stars and Oscillatons: A Review," 9 2021.

[161] E. Seidel and W.-M. Suen, "Dynamical Evolution of Boson Stars. 1. Perturbing the Ground State," *Phys. Rev.*, vol. D42, pp. 384–403, 1990.

[162] F. Di Giovanni, N. Sanchis-Gual, P. Cerdá-Durán, M. Zilhão, C. Herdeiro, J. A. Font, and E. Radu, "Dynamical bar-mode instability in spinning bosonic stars," *Phys. Rev. D*, vol. 102, no. 12, p. 124009, 2020.

[163] N. Siemonsen and W. E. East, "Stability of rotating scalar boson stars with nonlinear interactions," *Phys. Rev. D*, vol. 103, no. 4, p. 044022, 2021.

[164] A. S. Dmitriev, D. G. Levkov, A. G. Panin, E. K. Pushnaya, and I. I. Tkachev, "Instability of rotating Bose stars," *Phys. Rev. D*, vol. 104, no. 2, p. 023504, 2021.

[165] E. Seidel and W.-M. Suen, "Formation of solitonic stars through gravitational cooling," *Phys. Rev. Lett.*, vol. 72, pp. 2516–2519, 1994.

[166] C. Palenzuela, P. Pani, M. Bezares, V. Cardoso, L. Lehner, and S. Liebling, "Gravitational Wave Signatures of Highly Compact Boson Star Binaries," *Phys. Rev.*, vol. D96, no. 10, p. 104058, 2017.

[167] R. Friedberg, T. D. Lee, and Y. Pang, "Scalar Soliton Stars and Black Holes," *Phys. Rev.*, vol. D35, p. 3658, 1987.

[168] S. R. Coleman, "Q Balls," *Nucl. Phys.*, vol. B262, p. 263, 1985. [Erratum: Nucl. Phys.B269,744(1986)].

[169] T. D. Lee, "Soliton Stars and the Critical Masses of Black Holes," *Phys. Rev.*, vol. D35, p. 3637, 1987.

[170] R. Friedberg, T. D. Lee, and Y. Pang, "MINI - SOLITON STARS," *Phys. Rev.*, vol. D35, p. 3640, 1987.

[171] T. D. Lee and Y. Pang, "Fermion Soliton Stars and Black Holes," *Phys. Rev.*, vol. D35, p. 3678, 1987.

[172] T. D. Lee, "Soliton Stars and Black Holes," *Comments Nucl. Part. Phys.*, vol. 17, no. 5, pp. 225–238, 1987.

[173] S. Bahcall, B. W. Lynn, and S. B. Selipsky, "FERMION Q STARS," *Nucl. Phys. B*, vol. 325, pp. 606–618, 1989.

[174] J.-P. Hong, S. Jung, and K.-P. Xie, "Fermi-ball dark matter from a first-order phase transition," *Phys. Rev. D*, vol. 102, no. 7, p. 075028, 2020.

[175] C. Gross, G. Landini, A. Strumia, and D. Teresi, "Dark Matter as dark dwarfs and other macroscopic objects: multiverse relics?," *JHEP*, vol. 09, p. 033, 2021.

[176] L. Del Grosso, G. Franciolini, P. Pani, and A. Urbano, "Fermion soliton stars," *Phys. Rev. D*, vol. 108, no. 4, p. 044024, 2023.

[177] E. Cotner, A. Kusenko, M. Sasaki, and V. Takhistov, "Analytic Description of Primordial Black Hole Formation from Scalar Field Fragmentation," *JCAP*, vol. 1910, p. 077, 2019.

[178] M. A. Amin and P. Mocz, "Formation, gravitational clustering, and interactions of nonrelativistic solitons in an expanding universe," *Phys. Rev.*, vol. D100, no. 6, p. 063507, 2019.

[179] E. Krylov, A. Levin, and V. Rubakov, "Cosmological phase transition, baryon asymmetry and dark matter Q-balls," *Phys. Rev. D*, vol. 87, no. 8, p. 083528, 2013.

[180] M. Postma, "Solitosynthesis of Q balls," *Phys. Rev. D*, vol. 65, p. 085035, 2002.

[181] D. Croon, A. Kusenko, A. Mazumdar, and G. White, "Solitosynthesis and Gravitational Waves," *Phys. Rev. D*, vol. 101, no. 8, p. 085010, 2020.

[182] V. A. Rubakov and D. S. Gorbunov, *Introduction to the Theory of the Early Universe: Hot big bang theory*. Singapore: World Scientific, 2017.

[183] S. Krippendorf, F. Muia, and F. Quevedo, "Moduli Stars," *JHEP*, vol. 08, p. 070, 2018.

[184] S. Troitsky, "Supermassive dark-matter Q-balls in galactic centers?," *JCAP*, vol. 11, p. 027, 2016.

[185] Z. Nazari, M. Cicoli, K. Clough, and F. Muia, "Oscillon collapse to black holes," *JCAP*, vol. 05, p. 027, 2021.

[186] F. Muia, M. Cicoli, K. Clough, F. Pedro, F. Quevedo, and G. P. Vacca, "The Fate of Dense Scalar Stars," *JCAP*, vol. 1907, p. 044, 2019.

[187] R. Brito, V. Cardoso, C. F. B. Macedo, H. Okawa, and C. Palenzuela, "Interaction between bosonic dark matter and stars," *Phys. Rev.*, vol. D93, no. 4, p. 044045, 2016.

[188] M. A. Amin, M. P. Hertzberg, D. I. Kaiser, and J. Karouby, "Nonperturbative Dynamics Of Reheating After Inflation: A Review," *Int. J. Mod. Phys.*, vol. D24, p. 1530003, 2014.

[189] J. C. Niemeyer and R. Easther, "Inflaton clusters and inflaton stars," *JCAP*, vol. 2007, p. 030, 2020.

[190] J. C. Aurrekoetxea, K. Clough, and F. Muia, "Oscillon formation during inflationary preheating with general relativity," *Phys. Rev. D*, vol. 108, no. 2, p. 023501, 2023.

[191] C. Armendariz-Picon, V. F. Mukhanov, and P. J. Steinhardt, "A Dynamical solution to the problem of a small cosmological constant and late time cosmic acceleration," *Phys. Rev. Lett.*, vol. 85, pp. 4438–4441, 2000.

[192] C. Armendariz-Picon, V. F. Mukhanov, and P. J. Steinhardt, "Essentials of k essence," *Phys. Rev. D*, vol. 63, p. 103510, 2001.

[193] P. Brax, C. Burrage, and A.-C. Davis, "Screening fifth forces in k-essence and DBI models," *JCAP*, vol. 01, p. 020, 2013.

[194] R. J. Scherrer, "Purely kinetic k-essence as unified dark matter," *Phys. Rev. Lett.*, vol. 93, p. 011301, 2004.

[195] D. Giannakis and W. Hu, "Kinetic unified dark matter," *Phys. Rev. D*, vol. 72, p. 063502, 2005.

[196] M. P. Hertzberg, J. A. Litterer, and N. Shah, "Causal modifications of gravity and their observational bounds," *Phys. Rev. D*, vol. 107, no. 2, p. 024037, 2023.

[197] E. Babichev, "Formation of caustics in k-essence and Horndeski theory," *JHEP*, vol. 04, p. 129, 2016.

[198] L. ter Haar, M. Bezares, M. Crisostomi, E. Barausse, and C. Palenzuela, "Dynamics of Screening in Modified Gravity," *Phys. Rev. Lett.*, vol. 126, p. 091102, 2021.

[199] M. Shibata and D. Traykova, "Properties of scalar wave emission in a scalar-tensor theory with kinetic screening," *Phys. Rev. D*, vol. 107, no. 4, p. 044068, 2023.

[200] F. Dar, C. De Rham, J. T. Deskins, J. T. Giblin, and A. J. Tolley, "Scalar Gravitational Radiation from Binaries: Vainshtein Mechanism in Time-dependent Systems," *Class. Quant. Grav.*, vol. 36, no. 2, p. 025008, 2019.

[201] P. Figueras and T. França, "Gravitational Collapse in Cubic Horndeski Theories," *Class. Quant. Grav.*, vol. 37, no. 22, p. 225009, 2020.

[202] L. Aresté Saló, K. Clough, and P. Figueras, "Well-Posedness of the Four-Derivative Scalar-Tensor Theory of Gravity in Singularity Avoiding Coordinates," *Phys. Rev. Lett.*, vol. 129, no. 26, p. 261104, 2022.

[203] T. Hiramatsu, W. Hu, K. Koyama, and F. Schmidt, "Equivalence Principle Violation in Vainshtein Screened Two-Body Systems," *Phys. Rev. D*, vol. 87, no. 6, p. 063525, 2013.

[204] A. Kuntz, "Two-body potential of Vainshtein screened theories," *Phys. Rev. D*, vol. 100, no. 2, p. 024024, 2019.

[205] N. C. White, S. M. Troian, J. B. Jewell, C. J. Cutler, S.-w. Chiow, and N. Yu, "Robust numerical computation of the 3D scalar potential field of the cubic Galileon gravity model at solar system scales," *Phys. Rev. D*, vol. 102, no. 2, p. 024033, 2020.

[206] J. Braden, C. Burrage, B. Elder, and D. Saadeh, "φenics: Vainshtein screening with the finite element method," *JCAP*, vol. 03, p. 010, 2021.

[207] C. Burrage and J. Khoury, "Screening of scalar fields in Dirac-Born-Infeld theory," *Phys. Rev. D*, vol. 90, no. 2, p. 024001, 2014.

[208] J. H. Taylor and J. M. Weisberg, "A new test of general relativity: Gravitational radiation and the binary pulsar PS R 1913+16," *Astrophys. J.*, vol. 253, pp. 908–920, 1982.

[209] C. M. Will, "The Confrontation between General Relativity and Experiment," *Living Rev. Rel.*, vol. 17, p. 4, 2014.

[210] E. Berti *et al.*, "Testing General Relativity with Present and Future Astrophysical Observations," *Class. Quant. Grav.*, vol. 32, p. 243001, 2015.

[211] M. Kramer *et al.*, "Strong-Field Gravity Tests with the Double Pulsar," *Phys. Rev. X*, vol. 11, no. 4, p. 041050, 2021.

[212] R. Abbott *et al.*, "Tests of General Relativity with GWTC-3," 12 2021.

[213] G. Gabadadze, K. Hinterbichler, and D. Pirtskhalava, "Classical Duals of Derivatively Self-Coupled Theories," *Phys. Rev. D*, vol. 85, p. 125007, 2012.

[214] A. Padilla and P. M. Saffin, "Classical Duals, Legendre Transforms and the Vainshtein Mechanism," *JHEP*, vol. 07, p. 122, 2012.

[215] L. Hui, A. Nicolis, and C. Stubbs, "Equivalence Principle Implications of Modified Gravity Models," *Phys. Rev. D*, vol. 80, p. 104002, 2009.

[216] G. Lara, M. Bezares, M. Crisostomi, and E. Barausse, "Robustness of kinetic screening against matter coupling," *Phys. Rev. D*, vol. 107, no. 4, p. 044019, 2023.

[217] M. Nakahara, *Geometry, topology and physics*. 2003.

[218] V. Chandrasekaran, G. N. Remmen, and A. Shahbazi-Moghaddam, "Higher-Point Positivity," *JHEP*, vol. 11, p. 015, 2018.

[219] M. Milgrom, "Solutions for the modified Newtonian dynamics field equation," *Astrophys. J.*, vol. 302, pp. 617–625, 1986.

[220] J. Bekenstein and J. Magueijo, "Mond habitats within the solar system," *Phys. Rev. D*, vol. 73, p. 103513, 2006.

[221] D. J. Griffiths, *Introduction to Electrodynamics*. 2017.

[222] J. K. Bloomfield, C. Burrage, and A.-C. Davis, "Shape dependence of Vainshtein screening," *Phys. Rev. D*, vol. 91, no. 8, p. 083510, 2015.

[223] R. McManus, L. Lombriser, and J. Peñarrubia, "Parameterised Post-Newtonian Expansion in Screened Regions," *JCAP*, vol. 12, p. 031, 2017.

[224] C. Renevey, J. Kennedy, and L. Lombriser, "Parameterised post-Newtonian formalism for the effective field theory of dark energy via screened reconstructed Horndeski theories," *JCAP*, vol. 12, p. 032, 2020.

[225] C. Renevey, R. McManus, C. Dalang, and L. Lombriser, "Effect of screening mechanisms on black hole binary inspiral waveforms," *Phys. Rev. D*, vol. 105, no. 8, p. 084059, 2022.

[226] M. Andrews, Y.-Z. Chu, and M. Trodden, "Galileon forces in the Solar System," *Phys. Rev. D*, vol. 88, p. 084028, 2013.

[227] S. Mazumder, *Numerical Methods for Partial Differential Equations: Finite Difference and Finite Volume Methods*. Academic Press, 2016.

[228] W. H. Press, S. A. Teukolsky, W. T. Vetterling, and B. P. Flannery, *Numerical Recipes in FORTRAN: The Art of Scientific Computing*. 1992. ISBN-9780521430647.

[229] J. Magueijo and A. Mozaffari, "The case for testing MOND using LISA Pathfinder," *Phys. Rev. D*, vol. 85, p. 043527, 2012.

[230] P. Pucci and J. Serrin, *The Maximum Principle*, vol. 73. 01 2007.

[231] A. Barreira, P. Brax, S. Clesse, B. Li, and P. Valageas, "K-mouflage gravity models that pass Solar System and cosmological constraints," *Phys. Rev. D*, vol. 91, no. 12, p. 123522, 2015.

[232] M. Vallisneri *et al.*, "Modeling the uncertainties of solar-system ephemerides for robust gravitational-wave searches with pulsar timing arrays," 1 2020.

[233] A. Hees, B. Famaey, G. W. Angus, and G. Gentile, "Combined Solar System and rotation curve constraints on MOND," *Mon. Not. Roy. Astron. Soc.*, vol. 455, no. 1, pp. 449–461, 2016.

[234] G. Dvali, G. F. Giudice, C. Gomez, and A. Kehagias, "UV-Completion by Classicalization," *JHEP*, vol. 08, p. 108, 2011.

[235] L. Hui and A. Nicolis, "No-Hair Theorem for the Galileon," *Phys. Rev. Lett.*, vol. 110, p. 241104, 2013.

[236] T. P. Sotiriou and S.-Y. Zhou, "Black hole hair in generalized scalar-tensor gravity," *Phys. Rev. Lett.*, vol. 112, p. 251102, 2014.

[237] A. A. H. Graham and R. Jha, "Nonexistence of black holes with noncanonical scalar fields," *Phys. Rev. D*, vol. 89, no. 8, p. 084056, 2014. [Erratum: Phys.Rev.D 92, 069901 (2015)].

[238] P. Creminelli, N. Loayza, F. Serra, E. Trincherini, and L. G. Trombetta, "Hairy Black-holes in Shift-symmetric Theories," *JHEP*, vol. 08, p. 045, 2020.

[239] L. Capuano, L. Santoni, and E. Barausse, "Black hole hairs in scalar-tensor gravity (and lack thereof)," 4 2023.

[240] C. M. Will and H. W. Zaglauer, "Gravitational Radiation, Close Binary Systems, and the Brans-dicke Theory of Gravity," *Astrophys. J.*, vol. 346, p. 366, 1989.

[241] T. Damour and G. Esposito-Farese, "Tensor multiscalar theories of gravitation," *Class. Quant. Grav.*, vol. 9, pp. 2093–2176, 1992.

[242] L. Bernard, "Dynamics of compact binary systems in scalar-tensor theories: Equations of motion to the third post-Newtonian order," *Phys. Rev. D*, vol. 98, no. 4, p. 044004, 2018.

[243] A. Kuntz, F. Piazza, and F. Vernizzi, "Effective field theory for gravitational radiation in scalar-tensor gravity," *JCAP*, vol. 05, p. 052, 2019.

[244] L. Bernard, L. Blanchet, and D. Trestini, "Gravitational waves in scalar-tensor theory to one-and-a-half post-Newtonian order," *JCAP*, vol. 08, no. 08, p. 008, 2022.

[245] C. de Rham, A. J. Tolley, and D. H. Wesley, "Vainshtein Mechanism in Binary Pulsars," *Phys. Rev. D*, vol. 87, no. 4, p. 044025, 2013.

[246] E. Ya. Nugaev and A. V. Shkerin, "Review of Nontopological Solitons in Theories with $U(1)$-Symmetry," *J. Exp. Theor. Phys.*, vol. 130, no. 2, pp. 301–320, 2020.

[247] M. Kesden, J. Gair, and M. Kamionkowski, "Gravitational-wave signature of an inspiral into a supermassive horizonless object," *Phys.Rev.*, vol. D71, p. 044015, 2005.

[248] C. F. B. Macedo, P. Pani, V. Cardoso, and L. C. B. Crispino, "Astrophysical signatures of boson stars: quasinormal modes and inspiral resonances," *Phys. Rev.*, vol. D88, no. 6, p. 064046, 2013.

[249] B. Kleihaus, J. Kunz, and M. List, "Rotating boson stars and Q-balls," *Phys. Rev.*, vol. D72, p. 064002, 2005.

[250] B. Kleihaus, J. Kunz, and S. Schneider, "Stable Phases of Boson Stars," *Phys. Rev.*, vol. D85, p. 024045, 2012.

[251] D. Guerra, C. F. B. Macedo, and P. Pani, "Axion boson stars," *JCAP*, vol. 1909, no. 09, p. 061, 2019. [Erratum: JCAP2006,no.06,E01(2020)].

[252] N. Sennett, T. Hinderer, J. Steinhoff, A. Buonanno, and S. Ossokine, "Distinguishing Boson Stars from Black Holes and Neutron Stars from Tidal Interactions in Inspiraling Binary Systems," *Phys. Rev. D*, vol. 96, no. 2, p. 024002, 2017.

[253] M. Bezares, C. Palenzuela, and C. Bona, "Final fate of compact boson star mergers," *Phys. Rev. D*, vol. 95, no. 12, p. 124005, 2017.

[254] M. Bezares and C. Palenzuela, "Gravitational Waves from Dark Boson Star binary mergers," *Class. Quant. Grav.*, vol. 35, no. 23, p. 234002, 2018.

[255] T. Helfer, U. Sperhake, R. Croft, M. Radia, B.-X. Ge, and E. A. Lim, "Malaise and remedy of binary boson-star initial data," *Class. Quant. Grav.*, vol. 39, no. 7, p. 074001, 2022.

[256] T. Multamaki and I. Vilja, "Limits on Q ball size due to gravity," *Phys. Lett. B*, vol. 542, pp. 137–146, 2002.

[257] T. Tamaki and N. Sakai, "Unified picture of Q-balls and boson stars via catastrophe theory," *Phys. Rev.*, vol. D81, p. 124041, 2010.

[258] T. Tamaki and N. Sakai, "How does gravity save or kill Q-balls?," *Phys. Rev.*, vol. D83, p. 044027, 2011.

[259] T. Tamaki and N. Sakai, "What are universal features of gravitating Q-balls?," *Phys. Rev.*, vol. D84, p. 044054, 2011.

[260] A. M. Safian, S. R. Coleman, and M. Axenides, "SOME NONABELIAN Q BALLS," *Nucl. Phys.*, vol. B297, pp. 498–514, 1988.

[261] F. Paccetti Correia and M. G. Schmidt, "Q balls: Some analytical results," *Eur. Phys. J.*, vol. C21, pp. 181–191, 2001.

[262] N. Sakai and M. Sasaki, "Stability of Q-balls and Catastrophe," *Prog. Theor. Phys.*, vol. 119, pp. 929–937, 2008.

[263] J. Heeck, A. Rajaraman, R. Riley, and C. B. Verhaaren, "Understanding Q-Balls Beyond the Thin-Wall Limit," *Phys. Rev.*, vol. D103, no. 4, p. 045008, 2021.

[264] M. I. Tsumagari, E. J. Copeland, and P. M. Saffin, "Some stationary properties of a Q-ball in arbitrary space dimensions," *Phys. Rev. D*, vol. 78, p. 065021, 2008.

[265] K. S. Thorne, "NONSPHERICAL GRAVITATIONAL COLLAPSE: A SHORT REVIEW," in *Magic Without Magic*, pp. 231–258, 1972.

[266] A. Burrows and J. P. Ostriker, "The Astronomical Reach of Fundamental Physics," *Proc. Nat. Acad. Sci.*, vol. 111, p. 2409, 2014.

[267] B. Freivogel, T. Gasenzer, A. Hebecker, and S. Leonhardt, "A Conjecture on the Minimal Size of Bound States," *SciPost Phys.*, vol. 8, no. 4, p. 058, 2020.

[268] P. Amaro-Seoane, J. Barranco, A. Bernal, and L. Rezzolla, "Constraining scalar fields with stellar kinematics and collisional dark matter," *JCAP*, vol. 1011, p. 002, 2010.

[269] W.-C. Chen and J. Piekarewicz, "Compactness of Neutron Stars," *Phys. Rev. Lett.*, vol. 115, no. 16, p. 161101, 2015.

[270] J. Balakrishna, E. Seidel, and W.-M. Suen, "Dynamical evolution of boson stars. 2. Excited states and selfinteracting fields," *Phys. Rev. D*, vol. 58, p. 104004, 1998.

[271] L. G. Collodel, B. Kleihaus, and J. Kunz, "Excited Boson Stars," *Phys. Rev. D*, vol. 96, no. 8, p. 084066, 2017.

[272] N. Sanchis-Gual, C. Herdeiro, and E. Radu, "Self-interactions can stabilize excited boson stars," *Class. Quant. Grav.*, vol. 39, no. 6, p. 064001, 2022.

[273] S. Carroll, *Spacetime and Geometry: An Introduction to General Relativity*. San Francisco: Addison-Wesley, 2004.

[274] H. A. Buchdahl, "General Relativistic Fluid Spheres," *Phys. Rev.*, vol. 116, p. 1027, 1959.

[275] A. Urbano and H. Veermäe, "On gravitational echoes from ultracompact exotic stars," *JCAP*, vol. 1904, p. 011, 2019.

[276] J. Guven and N. O'Murchadha, "Bounds on 2m / R for static spherical objects," *Phys. Rev.*, vol. D60, p. 084020, 1999.

[277] A. Alho, J. Natário, P. Pani, and G. Raposo, "Compact elastic objects in general relativity," *Phys. Rev. D*, vol. 105, no. 4, p. 044025, 2022. [Erratum: Phys.Rev.D 105, 129903 (2022)].

[278] J. Heeck, A. Rajaraman, R. Riley, and C. B. Verhaaren, "Mapping Gauged Q-Balls," *Phys. Rev.*, vol. D103, no. 11, p. 116004, 2021.

[279] F. Kling and A. Rajaraman, "Towards an Analytic Construction of the Wavefunction of Boson Stars," *Phys. Rev. D*, vol. 96, no. 4, p. 044039, 2017.

[280] J. Barranco, J. Chagoya, A. Diez-Tejedor, G. Niz, and A. A. Roque, "Horndeski stars," *JCAP*, vol. 10, p. 022, 2021.

[281] F. S. Guzman and L. A. Urena-Lopez, "Newtonian collapse of scalar field dark matter," *Phys. Rev.*, vol. D68, p. 024023, 2003.

[282] L. Annulli, V. Cardoso, and R. Vicente, "Response of ultralight dark matter to supermassive black holes and binaries," *Phys. Rev. D*, vol. 102, no. 6, p. 063022, 2020.

[283] F. Kling and A. Rajaraman, "Profiles of boson stars with self-interactions," *Phys. Rev. D*, vol. 97, no. 6, p. 063012, 2018.

[284] J. F. M. Delgado, C. A. R. Herdeiro, and E. Radu, "Rotating Axion Boson Stars," *JCAP*, vol. 2006, p. 037, 2020.

[285] A. Kusenko, "Solitons in the supersymmetric extensions of the standard model," *Phys. Lett. B*, vol. 405, p. 108, 1997.

[286] A. Kusenko, "Small Q balls," *Phys. Lett. B*, vol. 404, p. 285, 1997.

[287] H. S. Chia and T. D. P. Edwards, "Searching for General Binary Inspirals with Gravitational Waves," *JCAP*, vol. 11, p. 033, 2020.

[288] J. Aasi *et al.*, "Advanced LIGO," *Class. Quant. Grav.*, vol. 32, p. 074001, 2015.

[289] F. Acernese *et al.*, "Advanced Virgo: a second-generation interferometric gravitational wave detector," *Class. Quant. Grav.*, vol. 32, no. 2, p. 024001, 2015.

[290] R. Abbott *et al.*, "GWTC-3: Compact Binary Coalescences Observed by LIGO and Virgo During the Second Part of the Third Observing Run," 11 2021.

[291] R. Abbott *et al.*, "GW190412: Observation of a Binary-Black-Hole Coalescence with Asymmetric Masses," *Phys. Rev. D*, vol. 102, no. 4, p. 043015, 2020.

[292] B. P. Abbott *et al.*, "GW190425: Observation of a Compact Binary Coalescence with Total Mass $\sim 3.4 M_{\odot}$," *Astrophys. J. Lett.*, vol. 892, no. 1, p. L3, 2020.

[293] R. Abbott *et al.*, "GW190521: A Binary Black Hole Merger with a Total Mass of $150 M_{\odot}$," *Phys. Rev. Lett.*, vol. 125, no. 10, p. 101102, 2020.

[294] R. Abbott *et al.*, "GW190814: Gravitational Waves from the Coalescence of a 23 Solar Mass Black Hole with a 2.6 Solar Mass Compact Object," *Astrophys. J. Lett.*, vol. 896, no. 2, p. L44, 2020.

[295] R. Abbott *et al.*, "Observation of Gravitational Waves from Two Neutron Star–Black Hole Coalescences," *Astrophys. J. Lett.*, vol. 915, no. 1, p. L5, 2021.

[296] T. Akutsu *et al.*, "Overview of KAGRA: Calibration, detector characterization, physical environmental monitors, and the geophysics interferometer," *PTEP*, vol. 2021, no. 5, p. 05A102, 2021.

[297] G. F. Giudice, M. McCullough, and A. Urbano, "Hunting for Dark Particles with Gravitational Waves," *JCAP*, vol. 1610, p. 001, 2016.

[298] C. Palenzuela, I. Olabarrieta, L. Lehner, and S. L. Liebling, "Head-on collisions of boson stars," *Phys.Rev.*, vol. D75, p. 064005, 2007.

[299] C. Palenzuela, L. Lehner, and S. L. Liebling, "Orbital Dynamics of Binary Boson Star Systems," *Phys.Rev.*, vol. D77, p. 044036, 2008.

[300] R. Brito, V. Cardoso, C. A. R. Herdeiro, and E. Radu, "Proca stars: Gravitating BoseEinstein condensates of massive spin 1 particles," *Phys. Lett.*, vol. B752, pp. 291–295, 2016.

[301] N. Sanchis-Gual, C. Herdeiro, E. Radu, J. C. Degollado, and J. A. Font, "Numerical evolutions of spherical Proca stars," *Phys. Rev. D*, vol. 95, no. 10, p. 104028, 2017.

[302] N. Sanchis-Gual, C. Herdeiro, J. A. Font, E. Radu, and F. Di Giovanni, "Head-on collisions and orbital mergers of Proca stars," *Phys. Rev. D*, vol. 99, no. 2, p. 024017, 2019.

[303] T. Dietrich, S. Ossokine, and K. Clough, "Full 3D numerical relativity simulations of neutron star–boson star collisions with BAM," *Class. Quant. Grav.*, vol. 36, no. 2, p. 025002, 2019.

[304] K. Clough, T. Dietrich, and J. C. Niemeyer, "Axion star collisions with black holes and neutron stars in full 3D numerical relativity," *Phys. Rev.*, vol. D98, no. 8, p. 083020, 2018.

[305] M. Bezares, D. Viganò, and C. Palenzuela, "Gravitational wave signatures of dark matter cores in binary neutron star mergers by using numerical simulations," *Phys. Rev. D*, vol. 100, no. 4, p. 044049, 2019.

[306] S. Valdez-Alvarado, C. Palenzuela, D. Alic, and L. A. Ureña López, "Dynamical evolution of fermion-boson stars," *Phys. Rev. D*, vol. 87, no. 8, p. 084040, 2013.

[307] V. Cardoso, C. F. B. Macedo, K.-i. Maeda, and H. Okawa, "ECO-spotting: looking for extremely compact objects with bosonic fields," 12 2021.

[308] J. A. Gonzalez, U. Sperhake, and B. Bruegmann, "Black-hole binary simulations: The Mass ratio 10:1," *Phys. Rev. D*, vol. 79, p. 124006, 2009.

[309] C. O. Lousto, H. Nakano, Y. Zlochower, and M. Campanelli, "Intermediate-mass-ratio black hole binaries: Intertwining numerical and perturbative techniques," *Phys. Rev. D*, vol. 82, p. 104057, 2010.

[310] C. O. Lousto and Y. Zlochower, "Orbital Evolution of Extreme-Mass-Ratio Black-Hole Binaries with Numerical Relativity," *Phys. Rev. Lett.*, vol. 106, p. 041101, 2011.

[311] D. Müller, *Numerical Simulations of Black Hole Binaries with Unequal Masses*. PhD thesis, PhD Thesis, 2011, 2011.

[312] N. Sanchis-Gual, M. Zilhão, C. Herdeiro, F. Di Giovanni, J. A. Font, and E. Radu, "Synchronized gravitational atoms from mergers of bosonic stars," *Phys. Rev. D*, vol. 102, no. 10, p. 101504, 2020.

[313] S. Mirshekari and C. M. Will, "Compact binary systems in scalar-tensor gravity: Equations of motion to 2.5 post-Newtonian order," *Phys. Rev. D*, vol. 87, no. 8, p. 084070, 2013.

[314] A. Arbona, A. Artigues, C. Bona-Casas, J. Massó, B. Miñano, A. Rigo, M. Trias, and C. Bona, "Simflowny: A general-purpose platform for the management of physical models and simulation problems," *Computer Physics Communications*, vol. 184, no. 10, pp. 2321–2331, 2013.

[315] A. Arbona, B. Miñano, A. Rigo, C. Bona, C. Palenzuela, A. Artigues, C. Bona-Casas, and J. Massó, "Simflowny 2: An upgraded platform for scientific modelling and simulation," *Computer Physics Communications*, vol. 229, pp. 170–181, 2018.

[316] C. Palenzuela, B. Miñano, A. Arbona, C. Bona-Casas, C. Bona, and J. Massó, "Simflowny 3: An upgraded platform for scientific modeling and simulation," *Computer Physics Communications*, vol. 259, p. 107675, 2021.

[317] "Simflowny project website.," 2021.

[318] R. D. Hornung and S. R. Kohn, "Managing application complexity in the samrai object-oriented framework," *Concurrency and Computation: Practice and Experience*, vol. 14, no. 5, pp. 347–368, 2002.

[319] B. T. Gunney and R. W. Anderson, "Advances in patch-based adaptive mesh refinement scalability," *Journal of Parallel and Distributed Computing*, vol. 89, pp. 65 – 84, 2016.

[320] "Samrai project website.," 2021.

[321] C. Palenzuela, B. Miñano, D. Viganò, A. Arbona, C. Bona-Casas, A. Rigo, M. Bezares, C. Bona, and J. Massó, "A Simflowny-based finite-difference code for high-performance computing in numerical relativity," *Class. Quant. Grav.*, vol. 35, no. 18, p. 185007, 2018.

[322] B. Bruegmann, J. A. Gonzalez, M. Hannam, S. Husa, U. Sperhake, and W. Tichy, "Calibration of Moving Puncture Simulations," *Phys. Rev. D*, vol. 77, p. 024027, 2008.

[323] N. T. Bishop and L. Rezzolla, "Extraction of Gravitational Waves in Numerical Relativity," *Living Rev. Rel.*, vol. 19, p. 2, 2016.

[324] C. Reisswig and D. Pollney, "Notes on the integration of numerical relativity waveforms," *Classical and Quantum Gravity*, vol. 28, p. 195015, Oct. 2011.

[325] E. E. Flanagan and T. Hinderer, "Constraining neutron star tidal Love numbers with gravitational wave detectors," *Phys. Rev. D*, vol. 77, p. 021502, 2008.

[326] E. Poisson and C. M. Will, *Gravity: Newtonian, Post-Newtonian, Relativistic*. Cambridge: Cambridge University Press, 1st ed., 2014.

[327] F. S. Guzman and L. A. Urena-Lopez, "Gravitational cooling of self-gravitating Bose-Condensates," *Astrophys. J.*, vol. 645, pp. 814–819, 2006.

[328] L. Boyle, M. Kesden, and S. Nissanke, "Binary black hole merger: Symmetry and the spin expansion," *Phys. Rev. Lett.*, vol. 100, p. 151101, 2008.

[329] M. Campanelli, C. O. Lousto, Y. Zlochower, and D. Merritt, "Maximum gravitational recoil," *Phys. Rev. Lett.*, vol. 98, p. 231102, 2007.

[330] J. A. Gonzalez, M. D. Hannam, U. Sperhake, B. Bruegmann, and S. Husa, "Supermassive recoil velocities for binary black-hole mergers with antialigned spins," *Phys. Rev. Lett.*, vol. 98, p. 231101, 2007.

[331] C. O. Lousto and Y. Zlochower, "Hangup Kicks: Still Larger Recoils by Partial Spin/Orbit Alignment of Black-Hole Binaries," *Phys. Rev. Lett.*, vol. 107, p. 231102, 2011.

[332] F. Antonini and F. A. Rasio, "Merging black hole binaries in galactic nuclei: implications for advanced-LIGO detections," *Astrophys. J.*, vol. 831, no. 2, p. 187, 2016.

[333] T. Bogdanovic, C. S. Reynolds, and M. C. Miller, "Alignment of the spins of supermassive black holes prior to merger," *Astrophys. J. Lett.*, vol. 661, p. L147, 2007.

[334] E. Barausse and A. Lapi, "Massive Black Hole Mergers," 11 2020.

[335] P. Pani and A. Maselli, "Love in Extrema Ratio," *Int. J. Mod. Phys. D*, vol. 28, no. 14, p. 1944001, 2019.

[336] Webpage with Mathematica notebooks and numerical quasinormal mode Tables:
`http://centra.tecnico.ulisboa.pt/network/grit/files/`
`http://www.phy.olemiss.edu/~berti/ringdown/`
`http://www.roma1.infn.it/~pani/` .

[337] A. Bohé *et al.*, "Improved effective-one-body model of spinning, nonprecessing binary black holes for the era of gravitational-wave astrophysics with advanced detectors," *Phys. Rev. D*, vol. 95, no. 4, p. 044028, 2017.

[338] A. Nitz, I. Harry, D. Brown, C. M. Biwer, J. Willis, T. D. Canton, C. Capano, T. Dent, L. Pekowsky, A. R. Williamson, G. S. C. Davies, S. De, M. Cabero, B. Machenschalk, P. Kumar, D. Macleod, S. Reyes, dfinstad, F. Pannarale, T. Massinger, S. Kumar, M. Tápai, L. Singer, S. Khan, S. Fairhurst, A. Nielsen, S. Singh, K. Chandra, shasvath, and B. U. V. Gadre, "gwastro/pycbc:," Aug. 2021.

[339] "Advanced LIGO anticipated sensitivity curves : LIGO document T0900288-v3." `https://dcc.ligo.org/LIGO-T0900288/public`.

[340] F. Hofmann, E. Barausse, and L. Rezzolla, "The final spin from binary black holes in quasi-circular orbits," *Astrophys. J. Lett.*, vol. 825, no. 2, p. L19, 2016.

[341] V. Kalogera *et al.*, "The Next Generation Global Gravitational Wave Observatory: The Science Book," 11 2021.

[342] C. Pacilio, M. Vaglio, A. Maselli, and P. Pani, "Gravitational-wave detectors as particle-physics laboratories: Constraining scalar interactions with a coherent inspiral model of boson-star binaries," *Phys. Rev. D*, vol. 102, no. 8, p. 083002, 2020.

[343] C. Pacilio, A. Maselli, M. Fasano, and P. Pani, "Ranking the Love for the neutron star equation of state: the need for third-generation detectors," 4 2021.

[344] M. Bošković and M. Herrero-Valea, "work in progress," 2023.

[345] L. G. Collodel and D. D. Doneva, "Solitonic boson stars: Numerical solutions beyond the thin-wall approximation," *Phys. Rev. D*, vol. 106, no. 8, p. 084057, 2022.

[346] S. L. Pitz and J. Schaffner-Bielich, "Generating ultra compact boson stars with modified scalar potentials," 8 2023.

[347] A. Alho, J. Natário, P. Pani, and G. Raposo, "Compactness bounds in general relativity," *Phys. Rev. D*, vol. 106, no. 4, p. L041502, 2022.

[348] A. Alho, J. Natário, P. Pani, and G. Raposo, "Spherically symmetric elastic bodies in general relativity," 7 2023.

[349] P. V. P. Cunha, E. Berti, and C. A. R. Herdeiro, "Light-Ring Stability for Ultra-compact Objects," *Phys. Rev. Lett.*, vol. 119, no. 25, p. 251102, 2017.

[350] P. V. P. Cunha, C. Herdeiro, E. Radu, and N. Sanchis-Gual, "Exotic Compact Objects and the Fate of the Light-Ring Instability," *Phys. Rev. Lett.*, vol. 130, no. 6, p. 061401, 2023.

[351] T. Evstafyeva, U. Sperhake, T. Helfer, R. Croft, M. Radia, B.-X. Ge, and E. A. Lim, "Unequal-mass boson-star binaries: initial data and merger dynamics," *Class. Quant. Grav.*, vol. 40, no. 8, p. 085009, 2023.

[352] N. Siemonsen and W. E. East, "Generic initial data for binary boson stars," 6 2023.

[353] N. Siemonsen and W. E. East, "Binary boson stars: Merger dynamics and formation of rotating remnant stars," *Phys. Rev. D*, vol. 107, no. 12, p. 124018, 2023.

[354] M. Armano *et al.*, "Sub-Femto- g Free Fall for Space-Based Gravitational Wave Observatories: LISA Pathfinder Results," *Phys. Rev. Lett.*, vol. 116, no. 23, p. 231101, 2016.

[355] W. R. Inc., "Mathematica, Version 12.3.1." Champaign, IL, 2021.